

UNIVERSITÀ DEGLI STUDI DI TRIESTE

DEPARTMENT OF PHYSICS

Doctoral School of Physics

XXIX Cycle

School Coordinator: Prof. Livio LANCERI



Chemical evolution of galaxies:
from the Local Group to the Local Universe

Supervisor:
Prof. Maria Francesca MATTEUCCI



PhD candidate:
Fiorenzo VINCENZO



ACADEMIC YEAR 2015/2016

PHD CANDIDATE: **Fiorenzo Vincenzo**

SUPERVISOR: **Prof. Francesca Matteucci**

SCHOOL DIRECTOR:
Prof. Livio Lanceri

REFEREES:
Dr. Marcella Marconi
Dr. Stefania Salvadori

DEFENCE COMMITTEE:
Prof. Stefano Borgani
Prof. Domenico Di Bari
Prof. Raffaella Schneider

DEFENCE DATE: 13TH APRIL 2017

©2017 – FIORENZO VINCENZO
ALL RIGHTS RESERVED.

to Martina

Chemical evolution of galaxies:
from the Local Group to the Local Universe

SUMMARY

The chemical composition of the galaxy interstellar medium continuously evolves as a function of time because of many environmental physical processes. Restitution of metals from dying stars, astration of metals due to the star formation activity, gas inflows and outflows, radial mixing of both gas and stars are all fundamental mechanisms in driving the *chemical evolution* of the interstellar medium of galaxies. Such mechanisms can have very different relative contributions as functions of time when considering galaxies of different morphological type; that is the main reason why spiral galaxies display different chemical abundance patterns with respect to elliptical galaxies or dwarf galaxies: they had different star formation and gas mass growth histories, as well as different mass distributions of the stars at their birth (the so-called “initial mass function”). Finally, not all the chemical species are affected in the same way by the aforementioned physical processes and this fact can introduce complexity within the models.

Astronomers try to constrain and reconstruct the past evolutionary history of galaxies, by looking at their present-day observed physical and chemical properties. Chemical evolution models are very useful tools in this respect, because they can draw a complete physical description of the galaxy evolution, by solving a set of physically motivated differential equations. In fact, by assuming the galaxy gas mass assembly history, initial mass function and stellar nucleosynthetic products, chemical evolution models can predict not only the temporal evolution of the galaxy chemical abundances, but also the evolution of the galaxy stellar and gas masses with time and the star formation history.

In the first part of the Thesis, I introduce the basic concepts lying at the basis of the galaxy chemical evolution modeling (**Chapter 1**) and present my original contributions in the foundation of this field (**Chapter 2**). In particular, I have explored – for the first time – the effect of the metallicity and initial mass function on the stellar yield of oxygen and metals per stellar generation. This quantity is usually assumed as a free parameter in the analytical models, adjusted to reproduce the data, without realizing that it is the outcome of stellar evolutionary models, depending on a variety of factors. One of the main conclusions is that changing the initial mass function can easily reconcile observations with the theoretical expectations. Finally, I present a new simple (but effective) method for solving the chemical evolution of galaxies, by assuming the so-called “instantaneous recycling approximation” for the chemical elements synthesized and restored by massive stars and the Delay Time Distribution formalism for the delayed chemical enrichment by Type Ia Supernovae. I apply this method to reproduce the observed $[O/Fe]$ and $[Si/Fe]$ versus $[Fe/H]$ abundance patterns in the Milky Way. This method can be

very useful because it can be easily included in other complementary stellar population synthesis models, enabling them to take into account chemical elements – such as iron – which are restored with a distribution of delay times from the star formation event.

The second part of the Thesis is devoted to the study of the classical and ultra-faint dwarf spheroidal galaxies, satellites of the Milky Way. In particular, in **Chapter 3**, I present updated chemical evolution models for two classical dwarf spheroidals (*Sculptor* and *Carina*) and the first detailed chemical evolution models for two ultra-faint dwarfs (*Hercules* and *Boötes I*), reproducing and explaining most of the chemical and physical properties which are observed at the present time in these galaxies. The models for the dwarf spheroidals assume a very slow star formation rate and relatively high rate of galactic winds, and these characteristics are more marked in the ultra-faint dwarfs. One of the main conclusions is that it is unlikely that the actual ultra-faint dwarfs have been the building blocks of the whole Galactic halo, although more accurate data are necessary to draw firm conclusions.


In **Chapter 4**, I explore the effect of the so-called integrated galactic initial mass function (IGIMF) on the chemical evolution of the Sagittarius dwarf spheroidal galaxy. The IGIMF theory predicts less massive stars in the regime of very low star formation rates of dwarf spheroidal galaxies; hence its assumption may leave peculiar features in the predicted chemical abundance patterns, which can be directly compared with observations. I explore also different yield prescriptions for Eu, including the Eu production by neutron star mergers, never tested before for explaining the Eu abundances in dwarf galaxies. The results of my models support the idea that the initial mass function in Sagittarius is truncated, hence favouring the IGIMF theory; moreover, I conclude that the observed Eu abundances can be reproduced only by assuming a completely alternative channel for the Eu nucleosynthesis (merging neutron stars) than the usual rapid neutron-capture process in massive stars.


In **Chapter 5**, I present chemical evolution models for the Milky Way, which assume that the the Galaxy stellar halo assembled by accreting gas and metals from the surrounding classical and ultra-faint dwarf spheroidal galaxies, through their galactic outflows. I also show that barium might be the best chemical element to test the theories suggesting dwarf spheroidal and ultra-faint dwarf galaxies to be the evolved building blocks of the Galaxy halo; in fact, this chemical element can be (relatively) easily measured in low metallicity stars. One of the main conclusions is that the assumptions of the model about the the typical halo formation time-scale and the threshold for the star formation activity strongly affect our results.

In **Chapter 6**, I present the results of a novel *photochemical evolution model*, which I have developed during my PhD research activity and applied to the study of the stellar populations in the Sculptor dwarf spheroidal galaxy. This new stellar population synthesis model starts from the predictions of chemical evolution models and “lights up” the stars with different mass, metallicity and age of galaxies. In this way, we can understand how the assumed underlying galaxy formation and evolution scenario affects the final configuration of the synthetic color-magnitude diagram.

In the third part of my Thesis, I pass from the chemical evolution of the Local Group dwarf galaxies to the star forming galaxies in the Local Universe. In particular, in **Chapter 7**, I present detailed chemical evolution models to explain the nitrogen and oxygen abundances, which have been inferred in a sample of Sloan Digital Sky Survey galaxies in the Local Universe. The dataset – integrated with the nitrogen and oxygen abundances derived in metal-poor, star forming dwarf galaxies – spans a wide metallicity range, enabling us to recover the trend of the (N/O) vs. (O/H) relation with a precision never reached before. In particular, this collection of data clearly demonstrates the existence of a plateau in the (N/O) ratio at very low metallicity, followed by an increase of this ratio which steepens as the metallicity increases. The conclusions are that primary nitrogen production by massive stars is always needed to reproduce the plateau at very low metallicity, together with differential galactic winds, which are responsible for the steepening of the (N/O) vs. (O/H) relation at large metallicities. I conclude also that the secondary nitrogen component by low- and intermediate-mass stars, increasing as a function of the metallicity, is also necessary to explain the final high (N/O) ratios in the data. Finally, in **Chapter 8**, I show how – by making use of an analytical chemical evolution model, which assumes the gas infall history to obey a decaying exponential law with time – we can characterize the local population of star forming and passive galaxies, in terms of their typical ages, gas accretion time scales, infall masses, star formation efficiencies and wind loading factors.

The natural prosecution of this Thesis work would be to exploit the recently released MaNGA data, which resolve a sample of Sloan Digital Sky Survey galaxies in very great detail. In particular, we can derive the metallicity as a function of the galactocentric distance for a large statistical sample of galaxies, representative of the Local Universe. In this way, we can study variations in the metallicity profile for galaxies with different stellar mass and we will better constrain the main physical mechanisms shaping the galaxy chemical evolution across the cosmic epochs.

VISTO

(L. LANCERI)

VISTO

(F. MATTEUCCI)

Contents

I	Introduction: foundations of the chemical evolution of galaxies	1
1	PRELIMINARY CONCEPTS	3
1.1	Overview	3
1.2	Basic ingredients	7
1.2.1	Fundamental stellar parameters	7
1.2.2	The stellar lifetimes	11
1.2.3	Simple and composite stellar populations	12
1.2.4	The nucleosynthetic stellar yields	17
1.2.5	Type Ia Supernovae	24
1.2.6	The stellar delay time distribution	27
1.3	The galaxy chemical evolution models	28
1.3.1	The differential equations for the galaxy chemical evolution	29
1.3.2	Numerical methods to solve the equations	37
	References	42
2	ANALYTICAL MODELS OF CHEMICAL EVOLUTION	43
2.1	Introduction	43
2.2	Basic assumptions	44
2.3	Models with the infall rate proportional to the galaxy star formation rate	46
2.4	Models with the exponential infall law	48
2.5	Modern yields per stellar generation: the effect of the IMF and metallicity	49
2.5.1	Definitions and assumptions	51
2.5.2	Results	55
2.6	Including the delayed production of iron by Type Ia Supernovae within analytical models: a novel method	59
2.6.1	The galaxy star formation history	61
2.6.2	The observed data set	65
2.6.3	Results: the Milky Way chemical evolution	67
2.6.4	Conclusions and discussion	70
	References	73

II	Chemical evolution of the Milky Way dwarf spheroidal galaxy satellites	75
3	CHEMICAL EVOLUTION OF CLASSICAL AND ULTRA-FAINT DWARF SPHEROIDAL GALAXIES	77
3.1	Introduction	77
3.2	Assumptions of the model	79
3.3	Data sample	80
3.4	Results	83
3.4.1	Chemical evolution of the Sculptor dSph	83
3.4.2	Chemical evolution of the Carina dSph	89
3.4.3	Chemical evolution of the Hercules UFD	93
3.4.4	Chemical evolution of the Boötes I UFD	101
3.5	Conclusions	103
	References	108
4	THE INTEGRATED GALACTIC INITIAL MASS FUNCTION AND NEUTRON STAR MERGERS IN THE SAGITTARIUS DWARF SPHEROIDAL GALAXY	109
4.1	Introduction	109
4.2	The integrated galactic initial mass function	111
4.3	Data sample	112
4.4	The chemical evolution model	113
4.4.1	The general model for dSphs	113
4.4.2	The model for Sagittarius	116
4.5	Results	118
4.5.1	MDF and chemical abundances	121
4.5.2	Exploring the parameter space	129
4.6	Conclusions	130
	References	134
5	ARE ANCIENT DWARF SATELLITES THE BUILDING BLOCKS OF THE GALACTIC HALO?	135
5.1	Introduction	135
5.2	The assumed chemical evolution models	137
5.2.1	The Milky Way	137
5.2.2	The dSph and UFD galaxies	140
5.2.3	Nucleosynthesis prescriptions	140
5.3	Milky Way models with an enriched infall of gas	141
5.4	Results	144
5.4.1	Results: the Galactic halo in the model 2IM	144
5.4.2	Results: the Galactic halo in the model 2IMW	152
5.5	Conclusions	156
	References	160

6	LIGHTNING UP STARS IN CHEMICAL EVOLUTION MODELS: THE CMD OF SCULPTOR	161
6.1	Introduction	161
6.2	The observed dataset	162
6.3	Model, assumptions and methods	163
6.3.1	Database of stellar isochrones and stellar lifetimes	163
6.3.2	Modelling the chemical evolution of Sculptor	164
6.3.3	The photo-chemical model	167
6.4	Results	169
6.5	Conclusions and discussion	173
	References	175
 III Chemical evolution of galaxies in the Local Universe		177
7	NITROGEN AND OXYGEN ABUNDANCES IN THE LOCAL UNIVERSE	179
7.1	Introduction	179
7.2	Overview of the data	182
7.2.1	Estimating the dust depletion	183
7.3	The nucleosynthetic origin of nitrogen	184
7.3.1	Primary and secondary nucleosynthetic products	185
7.3.2	The production of nitrogen in the CNO cycle	185
7.3.3	Nitrogen yields in low- and intermediate-mass stars	185
7.3.4	Nitrogen yields in massive stars	186
7.3.5	Empirically fixing the nitrogen yield from massive stars at low metallicity	187
7.4	Summary and reminder of the chemical evolution framework	188
7.4.1	Star formation and chemical evolution	188
7.4.2	The infall rate	189
7.4.3	The outflow model	189
7.4.4	Summary of the stellar yields for O and N	189
7.5	Modelling the SDSS data	191
7.5.1	The reference model	191
7.5.2	Exploring the parameter space	192
7.6	Modelling the low metallicity tail	197
7.7	Conclusions	198
	References	203
8	CHARACTERIZING THE LOCAL POPULATION OF STAR-FORMING AND PASSIVE GALAXIES WITH ANALYTICAL MODELS OF CHEMICAL EVOLUTION	205
8.1	Introduction	205
8.2	The MZ relation of the SDSS sample of star-forming and passive galaxies	206
8.2.1	Summary of the analytical solutions	208
8.3	Methods	209

Contents

8.3.1	Passive galaxies	210
8.3.2	Star-Forming galaxies	210
8.3.3	Summary of the free parameters and constraints	210
8.4	Results	212
8.5	The predicted Fundamental Relation of the local star-forming and passive galaxies	217
8.6	Conclusions	218
	References	220
IV	Concluding remarks	221
9	CONCLUSIONS AND PERSPECTIVES	223
	LIST OF PUBLICATIONS	231
	ACKNOWLEDGMENTS	233

Part I

Introduction: foundations of the chemical evolution of galaxies

*Oh, but if I had the stars from the darkest night
And the diamonds from the deepest ocean
I'd forsake them all for your sweet kiss
For that's all I'm wishin' to be ownin'*

“Boots Of Spanish Leather”, Bob Dylan

1

Preliminary concepts

1.1 Overview

The term “metals” for astronomers include all the chemical elements in the periodic table which are heavier than helium; accordingly, the “metallicity”, Z , is defined as the observed total abundance by mass of all the metals present in the gas mixture of an astrophysical source, as follows:

$$Z = \frac{M_Z}{M_{\text{gas}}}, \quad (1.1)$$

where the numerator represents the total gas mass of metals and the denominator the total gas mass, which include all the chemical elements in the gas mixture from hydrogen to the heaviest ones.

Chemical abundances can be directly measured in the atmospheres of the stars in the Milky Way and its dwarf galaxy satellites, starting from the analysis of the absorption lines in the stellar spectra (see [Nissen 2011](#) for an interesting discussion on the topic). Beyond our Galaxy and its nearby satellites, we still cannot resolve single stars for high resolution spectroscopic studies. Historically, in extragalactic systems, the chemical abundances of carbon, nitrogen, oxygen, sulphur, and some other elements, have been mostly measured from the emission lines in the HII regions; this method turns out to be very accurate and straightforward when dealing with the weak “auroral” lines, such as [OIII] λ 4363 or [NII] λ 5755 (see, for example, [Pagel et al. 1992](#); [Izotov et al. 2006](#)), however, it is strongly biased by the assumed calibration (either empirical or theoretical, by making use of photoionisation models) when only strong emission lines are available (e.g., [Kewley & Ellison 2008](#)). Nevertheless, quite accurate chemical abundances in some extragalactic systems

can also be obtained from the spectral analysis of the so-called red and blue supergiant stars, which are very luminous and evolved stars, lying in the upper part of the color-magnitude diagram of galaxies (Kudritzki et al., 2008; Gazak et al., 2015).

Many calibrations have been determined in the years between distinctive features in the integrated spectrum of galaxies (usually, absorption line strengths) and the metallicity of the dominant galaxy stellar populations; the most used in the literature are the so-called “Lick indices”, such as the Mg_2 or Fe5270 indices (Faber, 1973; Faber et al., 1985; Worthey et al., 1994; Thomas et al., 2010). Although largely approximate, these calibrations have been instrumental in the past to show, for example, that the most massive elliptical galaxies in the Universe formed – on average – at high redshift, on very short typical time-scales, and experienced an initial very intense burst of star formation (Matteucci, 1994). Finally, at high redshift, the abundances of several chemical elements in the gas-phase of the galaxy interstellar medium can be measured with very high resolution, when absorption systems lie along the line of sight towards a quasar; such systems are called Damped Ly α , because of the higher neutral hydrogen column densities which characterize them with respect to the most common Ly α systems in the quasar spectra (see Wolfe et al. 2005 for a review on the topic).

In summary, chemical abundances in galaxies can be measured either within the gas-phase of the galaxy interstellar medium or within the stellar atmospheres. Although the gas can be observed only because it is lightened up by the surrounding stars (we observe the emission lines superimposed on the integrated galaxy spectrum), gas-phase and stellar chemical abundances can be significantly different between each other, and not only because of the effect of the dust depletion, which efficiently removes part of the so-called “refractory” elements (mainly silicon and carbon) from the gas-phase.

The main reasons why gas-phase and stellar chemical abundances are conceptually different can be summarized as follows.

- The abundance patterns in the gas-phase represent a snapshot of the chemical composition of the galaxy interstellar medium at the present time. We cannot obtain any direct information about the past chemical composition of the interstellar medium only by measuring gas-phase abundances; in particular, in order to reconstruct the chemical evolution of the galaxy interstellar medium with time, we have to rely on the results of models, which must be able to reproduce many other observed physical properties beyond the chemical abundances, such as – for example – the galaxy gas and stellar mass and the galaxy spectro-photometric properties.
- The chemical abundances as derived in the stellar photospheres represent a fossil record of the chemical composition of the galaxy interstellar medium when the stars originated (this is particularly true for F and G main sequence stars and, with more caution, for K sub-giants). Since the stars we observe at the present time have a distribution of ages, they display different chemical abundance patterns with respect to each other and hence they sample the chemical composition of the interstellar medium at different epochs of the

galaxy evolution.

The chemical composition of the galaxy interstellar medium continuously evolves as a function of time because of many environmental physical processes acting on it, which can be summarized as follows: **a)** returned metals from dying stars; **b)** astration of metals due to the star formation activity itself; **c)** gas inflows and outflows; **d)** radial mixing of both gas and stars. All these physical processes can have very different relative contributions when passing from a galaxy to an other, according also to the galaxy morphological type; for example, that is the main reason why spiral galaxies display different chemical abundance patterns with respect to elliptical galaxies or dwarf galaxies. Finally, not all the chemical elements are affected in the same way by the aforementioned physical processes; this fact introduces complexity in chemical evolution models and must be taken into account if we want to reproduce the abundance pattern of each single chemical element in detail.

In the case of unresolved stellar systems, the estimate of the average galaxy *gas-phase metallicity*, $\langle Z_{\text{gas}} \rangle$, is a measure of the global metal budget in the galaxy at the present-time, while the average galaxy *stellar metallicity*, $\langle Z_{\star} \rangle$, is mostly sensitive to the physical properties of the stellar populations which dominate in the integrated light of the galaxy at the present time. Therefore, $\langle Z_{\star} \rangle$ can be as complex and uncertain to estimate as $\langle Z_{\text{gas}} \rangle$, both because of inherent completeness limits in the galaxy surveys and because of possible degeneracies (e.g., there is a well-known age-metallicity degeneracy for red giant branch stars). The quantity $\langle Z_{\star} \rangle$ is, in fact, strongly model-dependent, since it depends not only on the assumptions about the galaxy star formation history and mass distribution function of the stars at their birth (the so-called “initial mass function”), but also on the assumed database of isochrones and stellar spectra.

It is worth remarking that, although we often speak about “average galaxy metallicity”, the metallicity is a *local* physical quantity; in fact, the metallicity can vary when investigating different regions of a stellar system, both in the gas and in the stellar components. For example, we observe a systematic variety in metallicity among the main stellar constituents of our Galaxy; in particular, Bulge stars display a different metallicity distribution function with respect to Halo but also disc stars. Furthermore, metallicity gradients can be measured within the interstellar medium of galaxies in the Local Universe thanks to the most recent surveys working with Integral Field Unit, such as CALIFA or MaNGa (see, for example, [Belfiore et al. 2015](#); [Zinchenko et al. 2016](#); [Ibarra-Medel et al. 2016](#)). Moreover, the metallicity is also observed to vary within single HII regions, such as the Orion Nebula. Finally, there is growing observational evidence – from both photometric and spectroscopic studies – that globular clusters host multiple stellar populations, characterized by different ages and metallicities, at variance with the findings of the earliest studies.

Oxygen is the most abundant chemical element in galaxies beyond hydrogen and helium; for this reason, oxygen represents the best proxy for the stellar and gas-phase metallicity. An other chemical element which is frequently taken as a metallicity indicator in stars is iron, mainly because its abundance is much more straightforward to derive in stars than the oxygen abundance. In fact, iron atoms leave in the stellar spectrum a variety of well defined absorption lines, which can

be eventually used all together in the abundance analysis. Nevertheless, the iron enrichment history of the interstellar medium is more complex than the oxygen one, and hence the two chemical elements do not trace in the same way the evolution of the metal content during most of the lifetime of galaxies.

The amount of metals is observed to be – on average – relatively low everywhere and at every time in the Universe; in particular, the metallicity in the stellar photospheres or in the interstellar medium of galaxies is always $\lesssim 4\text{--}5$ per cent, with the exact value changing according to the degree of evolution of the object under study. For example, one of the most comprehensive and cited studies in the literature on the chemical composition of the Sun is given by [Asplund et al. \(2009\)](#), which measured a solar metallicity $Z_{\odot} = 0.0134$, mostly dominated by the oxygen and carbon contributions; the remaining mass fraction, as derived in the present-day solar photosphere, is given by the hydrogen ($X = 0.7381$) and helium ($Y = 0.2485$) contents. On the other hand, Big Bang nucleosynthesis predicts the early cosmic plasma to be essentially free of metals, which hence must have been synthesized later as the first population of stars eventually appeared. Therefore, the terrestrial and solar abundance of chemical elements like carbon, nitrogen, oxygen or silicon – which are fundamental for life on Earth and predominate in the atmosphere and crust of our planet – can be explained only by invoking a sequence of stellar generations which increasingly polluted the interstellar medium from which, between 4 and 5 Gyr ago, the Sun and Earth originated.

Stellar interiors represent the best place in the Universe where to find the right physical conditions for fusion reactions to occur; in principle, by means of this kind of mechanism (i.e. hydrostatic or explosive thermonuclear burning within stars), one can explain the origin of all the chemical elements from carbon to iron. The lighter chemical elements, in particular hydrogen and helium, were almost entirely synthesized during the primordial nucleosynthesis and later destroyed inside stars – stellar generation by stellar generation – for the production of the heavier chemical elements. Chemical elements with atomic weight $A > 56$ cannot be synthesized via thermonuclear burning, since this process is not convenient for their production in terms of energy balance. In particular, for $A > 56$, the binding energy per nucleon almost continuously diminishes and the nuclear reactions would require large energy consumption at the expense of the environment to occur. Therefore, an other physical process must be invoked for the production of the heavy elements which lie in the periodic table beyond iron.

The main physical mechanism for the nucleosynthesis of the chemical elements heavier than iron is given by the so-called “neutron-capture process” inside stars, namely by a series of neutron-captures onto an increasingly heavier atomic nucleus, followed by β^- decays of the captured neutrons. If the neutron-captures proceed with an higher rate with respect to the β^- decays (condition of high neutron fluxes), then the reactions give rise to an *r-process element*, where the letter “r” stands for “rapid”; otherwise, the reactions give rise to an *s-process element*, where “s” obviously stands for “slow”. Each neutron-capture element can have both an s- and r-process channel of nucleosynthesis; europium is predominantly produced as an r-process element, while barium is mostly an s-process element.

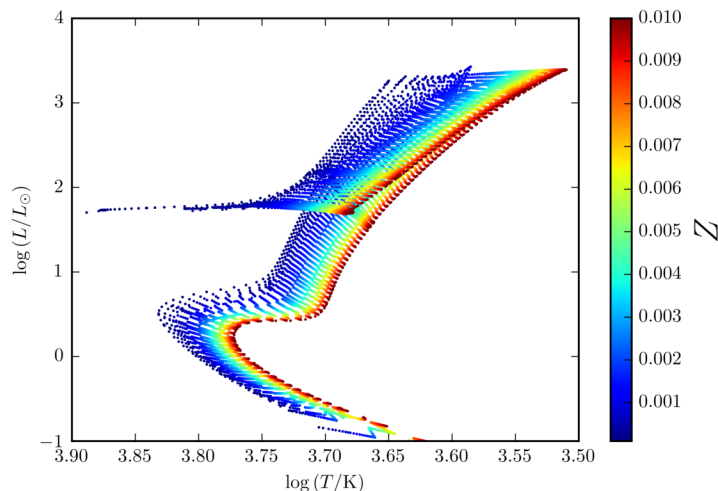


Figure 1.1: In this Figure, we show how the stellar isochrones move in the (T_{eff}, L) plane when continuously varying the initial stellar metallicity, Z . The age of all the isochrones is assumed to be 12.6 Gyr. The isochrone database is PARSEC (Bressan et al., 2012; Tang et al., 2014; Chen et al., 2015).

Notation. In this thesis, we will extensively use the following notation for the chemical abundance ratios in stars:

$$\left[\frac{X}{Y} \right] = \log \left(\frac{N_X}{N_Y} \right)_* - \log \left(\frac{N_X}{N_Y} \right)_\odot, \quad (1.2)$$

where N_X and N_Y represent the number density of atoms in the form of the chemical species X and Y , respectively. Therefore, for example, if we measure $[\text{Fe}/\text{H}] \approx -1.0$ dex in the photosphere of a given red giant star in our Galaxy, then the ratio $N_{\text{Fe}}/N_{\text{H}}$ in the star is nearly one order of magnitude lower than in the Sun.

1.2 Basic ingredients

We can think at galaxies as *composite stellar populations*, namely as a collection of stars which are characterized by a present-day distribution of masses, ages and metallicities. In this Section, many theoretical concepts and notions about stars and galaxies – which are extensively used in astrophysics for interpreting observations and are fundamental for the study of the chemical evolution of galaxies – will be introduced and summarized.

1.2.1 Fundamental stellar parameters

From a theoretical point of view, the main three fundamental parameters which define the photometric and spectroscopic properties of stars are the following.

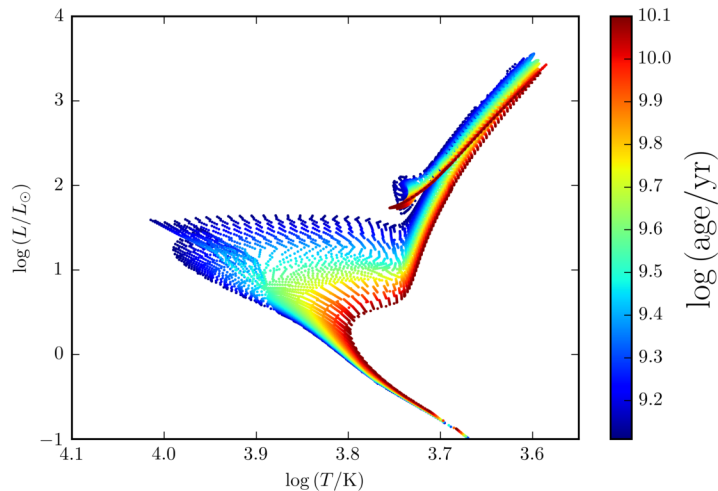


Figure 1.2: In this Figure, we show the effect of continuously varying the age of the stellar isochrones for a fixed value of the stellar metallicity $Z = 1.0 \times 10^{-3}$. The isochrone database is PARSEC (Bressan et al., 2012; Tang et al., 2014; Chen et al., 2015).

Stellar mass. It is probably the most important stellar parameter, strongly determining the evolution of the internal structure of the star as a function of time, as well as its final fate. Since stars with different mass have different lifetimes and enrich the interstellar medium at their death with different fractions of a given chemical element, different chemical elements enrich the interstellar medium of galaxies on different typical time-scales. Such a process lies at the core of galaxy chemical evolution models and it is basically driven by the mass of the stars. On the one hand, massive stars (with $m \gtrsim 8 M_{\odot}$) are the most important metal-producers in the Universe; in particular, most of the so-called α -elements (O, Mg, Ne, Si, S, Ca, and Ti) have been synthesized by massive stars, on short typical time scales. On the other hand, low- and intermediate-mass stars (with $0.8 \lesssim m \lesssim 8 M_{\odot}$) provide most of the carbon, nitrogen and heavy s-process elements (e.g., Ba, Sr, Zr) and pollute the galaxy interstellar medium on relatively long typical time scales. Although iron is mostly synthesized by Type Ia Supernovae, a significant amount of iron is also synthesized by massive stars during the explosive Si burning (roughly $\sim 1/3$ of the total, with standard Salpeter-like initial mass functions).

Stellar age. As a star evolves along its various different evolutionary stages, its luminosity, effective temperature and surface gravity can strongly vary, influencing the distribution of the emitted energy flux at the various wavelengths. Main sequence stars do not shine as red-giant branch stars or horizontal branch stars. The stellar age is a fundamental stellar parameter, particularly important for the construction of spectro-photometric population synthesis models.

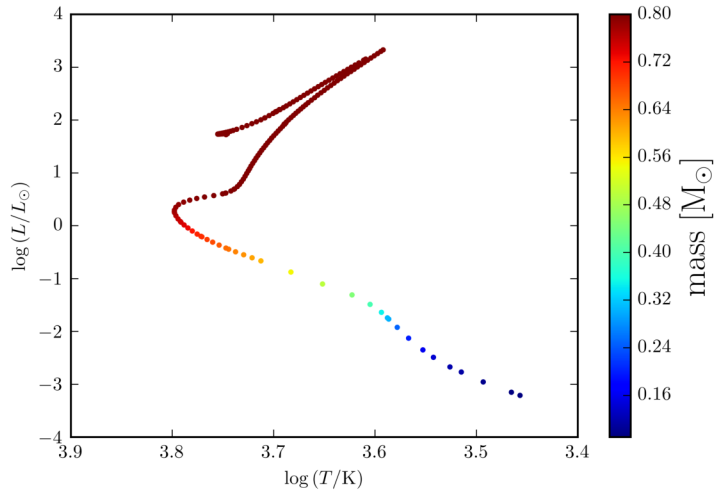


Figure 1.3: In this Figure, we show how the stellar mass varies when moving along a single stellar isochrone. The age of the isochrone is 12.6 Gyr, while the metallicity of the stars is $Z = 1.0 \times 10^{-3}$. The isochrone database is PARSEC (Bressan et al., 2012; Tang et al., 2014; Chen et al., 2015).

Stellar metallicity. It can have a strong influence on the effective temperature and compactness of the stellar object. For example, by increasing the metallicity, the radiative opacity in the stellar atmosphere becomes higher and higher, and hence the star becomes at the same time colder and less luminous, eventually having larger lifetimes (the turn-off mass increases by only increasing the stellar metallicity). The stellar metallicity is a fundamental parameter both for the construction of spectro-photometric population synthesis models and for chemical evolution models.

Most of the predictions and results of stellar evolutionary models are given in terms of the aforementioned fundamental stellar parameters. For example, the stellar nucleosynthetic products are usually computed by stellar models over a discrete two-dimensional grid of different initial stellar masses and metallicities (see Section 1.2.4). An other example is given by the stellar isochrones, which provide the results of the stellar models about the photometric properties of the stars. Stellar isochrones are usually computed over a discrete two-dimensional grid of different stellar ages and metallicities; one moves along each single isochrone by increasing the initial mass of the star. In particular, the larger the stellar mass, the later is the evolutionary stage experienced by the star along the isochrone. This is due to the fact that massive stars evolve faster than low-mass stars (namely, stellar lifetimes decrease as functions of the stellar mass). In Figures 1.1, 1.2, and 1.3, we show how the stars move in the (T_{eff}, L) plane, when varying the initial stellar metallicity, age and mass, respectively; the database of stellar isochrones assumed to produce these figures is PARSEC (Bressan et al., 2012; Tang et al., 2014; Chen et al., 2015). Finally, the most recent databases of stellar spectra are

computed over a discrete three-dimensional grid of different metallicities, effective temperatures, and surface gravities. Nevertheless, one can easily pass from the (m, g, T_{eff}) space of the stellar spectra to the more theoretical (m, Z, τ) space by using stellar evolutionary tracks or isochrones. Incidentally, a further parameter which is usually taken into account to compute even more precise stellar spectra is given by the $[\alpha/\text{Fe}]$ abundance ratio in the star.

By starting from the distribution of the fundamental stellar parameters in galaxies, we can introduce three fundamental ingredients for galaxy formation and evolution models, as follows.

- The distribution of the stellar ages reflects the *galaxy star formation history*.
- The distribution of the stellar masses is determined by the so-called *initial mass function*.
- The distribution of the stellar metallicities is a direct consequence of the *galaxy chemical evolution*.

The three aforementioned ingredients do not lie at the same level in the models; in particular, the chemical evolution can be computed only if we know the galaxy star formation history and initial mass function. In fact, to compute the galaxy chemical evolution, we have to reconstruct the birth time and the number of all the stars which are dying at each time of the galaxy evolution: the time of formation of the dying stars comes from the past galaxy star formation history, while their number comes from the assumed initial mass function. This is due to the fact that – as the stars die – they expel metals into the galaxy interstellar medium and hence crucially contribute to the galaxy chemical evolution. Chemical evolution models enter in the broad area of studies, which is called in the literature as *galaxy Astro-Archaeology*; roughly speaking, we struggle to reconstruct the past evolutionary history of galaxies, starting from their observed physical and chemical properties at the present time.

We remark on the fact that numerical codes of chemical evolution can provide – in principle – a complete physical description of the galaxy evolution; by only starting from the assumption of a galaxy gas mass assembly history, they are capable of predicting the run of the galaxy stellar and gas masses with time, as well as the galaxy star formation history, hence not only the evolution of the galaxy chemical abundances with time.

The star formation history is regulated by all the physical processes which alter the gas content within galaxies, and chemical evolution itself must be included in these processes. As the star formation proceeds, the gas is continuously locked up into stars. Then, as the stars die, part of the “locked” gas is re-injected into the galaxy interstellar medium. From the expelled gas by dying stars, further stars in the future will form, causing a continuous recycling of the galaxy interstellar medium. Such a recycling has an influence on the galaxy star formation history, which must be taken into account. In summary, the chemical evolution is strictly coupled with the galaxy star formation history: one cannot fully understand the former without precisely knowing the latter, and viceversa.

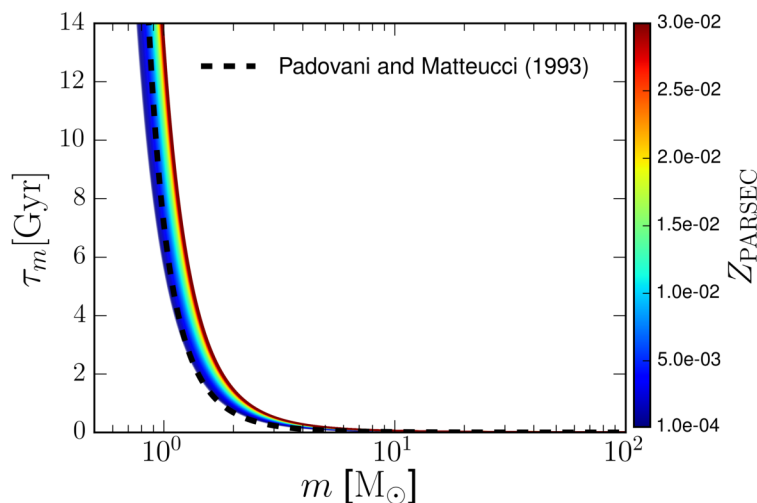


Figure 1.4: In this figure, we show how the stellar lifetimes we have derived from the PARSEC stellar evolutionary tracks vary as functions of the stellar mass and metallicity. The dashed black curve corresponds to the stellar lifetimes of [Padovani & Matteucci \(1993\)](#).

1.2.2 The stellar lifetimes

When dealing with the chemical evolution of galaxies, we have always to take into account the delay time which elapses between the star formation event and the moment at which the stars die and hence enrich the galaxy interstellar medium. This distribution of delay times defines the so-called *stellar lifetimes*, τ_m , which are basically driven by the initial stellar mass and metallicity. In reality, stars continuously enrich the galaxy interstellar medium through winds as they evolve; nevertheless, for the sake of simplicity, chemical evolution models consider the restitution of chemical elements by stars only at the stellar death, in a cumulative way. That is the reason why the age of the stars is not a fundamental parameter for chemical evolution models.

The stellar lifetimes can be computed from the isochrone tables, by associating the maximum stellar mass of each single isochrone with the age of the isochrone itself. In [Vincenzo, Matteucci, de Boer, Cignoni & Tosi \(2016\)](#), we have derived the stellar lifetimes from the PARSEC database of stellar evolutionary tracks ([Bressan et al., 2012](#); [Tang et al., 2014](#); [Chen et al., 2015](#)), by assuming the following fitting function:

$$\tau_m(Z) = A(Z) \times \exp \left[B(Z) m^{-C(Z)} \right], \quad (1.3)$$

where $A(Z)$, $B(Z)$ and $C(Z)$ are the fitting parameters as functions of the metallicity Z . In [Fig. 6.2](#) we compare our derived stellar lifetimes with the ones of [Padovani & Matteucci \(1993\)](#), which do not depend on metallicity and are extensively used in chemical evolution models.

1.2.3 Simple and composite stellar populations

Let us assume that a galaxy \mathcal{G} experienced star formation activity over a finite period of time $\Delta t_{\text{SF}} = [t_1, t_2]$ in the past. At every short time interval $\Delta t_{\text{SSP}} \ll \Delta t_{\text{SF}}$ during the star formation activity, a *simple stellar population* is assumed to originate, namely a population of stars which were born during a burst of star formation (namely as a response to a Dirac delta function in the star formation activity), all characterized by the same age and metallicity. The best examples of simple stellar populations in the Universe are the oldest globular clusters in the Galaxy halo, which host stars with nearly constant age and metallicity, likely originating from a single bursty episode of star formation. From a theoretical point of view, simple stellar populations are represented by the stellar isochrones in the color-magnitude diagram.

We can define a galaxy as a linear combination of simple stellar populations with continuously increasing ages and different metallicities. For this reason, galaxies are defined as *composite stellar populations*. By varying the weight of any given simple stellar population in the linear combination, the galaxy can be significantly different, at any time of its evolution. Such weights, w_{SSP} , in the linear combination define in a unique way both the galaxy star formation history – since we can reconstruct how many stars form as a function of time (and hence the present-day distribution of the stellar ages, if we know the stellar lifetimes) – and the metallicity evolution of the galaxy interstellar medium – which is represented by the metallicity of the stars at their birth.

In summary, from a theoretical point of view, any given galaxy physical property, $\hat{\mathcal{O}}_{\mathcal{G}}$, can be expressed in the following way:

$$\hat{\mathcal{O}}_{\mathcal{G}}(t) = \sum_{t_i < t} w_{\text{SSP}}(t_i) \hat{\mathcal{O}}_{\text{SSP}}(t - t_i, Z(t_i)), \quad (1.4)$$

where the sum is made over all the times t_i of star formation, which are prior to the current one; $w_{\text{SSP}}(t_i)$ represents the weight associated to the stellar population born at t_i ; finally, $\hat{\mathcal{O}}_{\text{SSP}}(\tau, Z)$ is the given physical property, as predicted for a simple stellar population with age τ and metallicity $Z = Z(\tau)$. We remind the reader that equation (1.4) describes unresolved galaxies, where only the cumulative effect of the stars alive at the present time can be studied.

In equation (1.4), the mass of the stars (which is the third fundamental stellar parameter beyond the stellar age and metallicity) is hidden in the computation of the quantity $\hat{\mathcal{O}}_{\text{SSP}}(\tau, Z)$. Very generally, $\hat{\mathcal{O}}_{\text{SSP}}$ can be computed as follows:

$$\hat{\mathcal{O}}_{\text{SSP}}(\tau, Z) = \sum_{m_k} f_{\star}(m_k, \tau, Z) \hat{\mathcal{O}}_{\star}(m_k, \tau, Z), \quad (1.5)$$

where the quantities $f_{\star}(m_k, \tau, Z)$ physically represents the total number of stars in the simple stellar population with mass m_k , age τ and metallicity Z , with $\hat{\mathcal{O}}_{\star}(m_k, \tau, Z)$ being their corresponding predicted physical property under examination, as given – for example – by stellar isochrones.

In the astrophysics literature, the quantity $f_{\star}(m, \tau, Z)$ in equation (1.5) – which

represents the contribution of all the stars with mass m , metallicity Z and age τ to the quantity $\hat{O}_{\text{SSP}}(\tau, Z)$ – is assumed to depend only upon the mass, m , of the star. This is a very strong assumption. In practice, it means that the mass distribution function of the stars of a simple stellar population is a universal function and hence it does not depend upon the place or time of birth of the stars of the simple stellar population^{*}.

By inserting equation (1.5) into equation (1.4) and by assuming that $f_{\star} = f_{\star}(m)$, we can eventually find the following equation for the generic galaxy physical property, $\hat{O}_{\mathcal{G}}$:

$$\hat{O}_{\mathcal{G}}(t) = \sum_{t_i < t} \sum_{m_k} w_{\text{SSP}}(t_i) f_{\star}(m_k) \hat{O}_{\star}(m_k, t - t_i, Z(t_i)). \quad (1.6)$$

By looking at equation (1.6), the quantity $f_{\star}(m_k)$ physically represents the fraction of $w_{\text{SSP}}(t_i)$ contributed by the stars with mass m_k .

Let us assume that $\hat{O}_{\mathcal{G}}$ in equation (1.6) is the total galaxy stellar mass, \mathcal{M}_{\star} . Historically, this particular case is used to define the normalization of the quantity f_{\star} and the physical dimensions of w_{SSP} . In particular, by accordingly assuming $\hat{O}_{\star}(m_k, \tau, Z) = m_k$, we have the following equation:

$$\mathcal{M}_{\star}(t) = \left(\sum_{t_i < t} w_{\text{SSP}}(t_i) \right) \times \left(\sum_{m_k} f_{\star}(m_k) m_k \right). \quad (1.7)$$

In order to have physically consistent results we have to assume what follows.

- $w_{\text{SSP}}(t_i)$ physically represents the total mass of stars which were born at t_i , namely the total mass of the simple stellar population with age $\tau = t - t_i$ and metallicity $Z(t_i)$. Therefore, it has the dimensions of a mass (hence the units of M_{\odot}).
- The quantity $f_{\star}(m_k)$ is directly proportional to the number of stars which were born with mass m_k in a simple stellar population. It is normalized such that $\sum_{m_k} m_k f_{\star}(m_k) = 1$.

As we will see in the following discussion, the quantities w_{SSP} and f_{\star} are directly related to the star formation rate and initial mass function, respectively; their product in equation (1.6) is also strictly related to the so-called “stellar birthrate function”, which we will introduce in what follows.

^{*}A further – very subtle – assumption is made, which is not recognized in the literature: f_{\star} should depend – in principle – also on the observable \hat{O}_{\star} , but we always neglect this effect. For example, this means that we subtly assume that the stars in a given mass range $m_1 \leq m \leq m_2$ contribute to any physical quantity of their simple stellar population with always the same amount (it could be the B-band luminosity, the I-band one, or the total stellar mass itself). This is not obvious.

The stellar birthrate function

The number of stars which were born in the time interval $t, t + dt$ and with mass in the range $m, m + dm$ represents, by definition, the so-called *stellar birthrate function*, $\mathcal{B}(t, m)$. This quantity is assumed to be the product of the initial mass function, $\phi(m)$, with the galaxy star formation rate, $\psi(t)$, according to the following formula:

$$\mathcal{B}(t, m) = \psi(t) \phi(m) dt dm. \quad (1.8)$$

There is no physical reason for such a factorization in the time and mass dependence of the stellar birthrate function, except our ignorance about the star formation process in galaxies. The physical definitions of star formation rate and initial mass function are the following ones.

The star formation rate. It is defined as the amount of mass within the galaxy interstellar medium which is converted into stars per unit time. It is usually expressed in terms of $M_{\odot} \text{ yr}^{-1}$. Star formation rate is observed to correlate in galaxies with many fundamental physical quantities, such as the total galaxy stellar mass and the average metallicity of the galaxy interstellar medium. Nevertheless, the best example of correlation is the so-called *Schmidt-Kennicutt law* (Schmidt, 1959; Kennicutt, 1998) between the density of star formation rate and the galaxy gas mass density. Historically, based on the suggestions of the early work by Schmidt (1959), galaxy formation and evolution models have always assumed the following empirical law for modeling the star formation process: $\psi(r, t) \propto \nu \rho_g(r, t)^k$, where ρ_g represents the volume (or surface) gas mass density of the galaxy interstellar medium, the index k lies in the interval $[1, 2]$, and ν represents the so-called *star formation efficiency*, whose dimensions are the inverse of a time. As aforementioned, this law was originally proposed by Schmidt (1959) to fit observational data. Later, Kennicutt (1998) derived $k = 1.4 \pm 0.15$ for star-forming spiral and starburst galaxies in the Local Universe. Other parametrizations of the star formation law have been explored in the literature; they make use – for example – of the dynamical timescale or the angular rotation speed (Boissier, 2013).

The initial mass function. It represents the mass spectrum with which stars distribute in mass at their birth. The initial mass function is usually normalized in mass such that $\int_{0.1 M_{\odot}}^{100 M_{\odot}} dm m \phi(m)$. Most of the initial mass functions which have been proposed in the literature to fit Solar neighborhood data are defined as a single- or multi-slope power law of the form: $\phi(m) \propto m^{-(1+x)}$. The most famous initial mass function is the one by Salpeter (1955), which assumes $x = 1.35$. The assumption of different initial mass functions can strongly affect the chemical evolution of galaxies, since this quantity determines the relative numbers of stars which lie in different mass ranges and hence the amount of the restitution of chemical elements by dying stars. The initial mass function is observed to be strongly biased towards low-mass stars, since they have the largest lifetimes and hence the largest probability to be observed at the present time.

Fundamental galaxy integrated properties

By starting from the galaxy star formation history and assuming a particular initial mass function, one can compute the temporal evolution of many fundamental galaxy properties. In what follows, some examples are given to illustrate this.

The total galaxy stellar mass. By assuming that $m_{\max}(t', t)$ represents the mass of a star having lifetime $\tau = |t - t'|$ (all the stars born at t' , having mass larger than m_{\max} , are already dead at t), the run of the total galaxy stellar mass with time can be computed by means of the following equation:

$$\mathcal{M}_*(t) = \int_0^t dt' \psi(t') \int_{0.1 M_\odot}^{m_{\max}(t', t)} dm \phi(m) m, \quad (1.9)$$

where the integral over mass represents the mass fraction of the stars which formed at the time t' and can be still observed as alive at the time t , namely all the stars with mass $m \leq m_{\max}(t', t)$, born at the time t' , can be still observed as alive at the time t . The functional behavior of m_{\max} is simply given by the inverse function of the stellar lifetimes.

The galaxy integrated spectrum. Similarly, the integrated galaxy spectrum at the time t can be computed as follows.

$$\mathcal{F}_\lambda(t) = \int_0^t dt' \psi(t') \int_{0.1 M_\odot}^{m_{\max}(t', t)} dm \phi(m) f_\lambda(m, t', Z(t')), \quad (1.10)$$

where $f_\lambda(m, t', Z(t'))$ is the spectrum of a star with mass m , age $|t - t'|$, and initial metallicity $Z(t')$. In equation (1.10), the integrated galaxy spectrum is computed by summing up only the contribution of the stars which can be still observed as alive at the time t .

The rate of death of stars. A fundamental quantity for chemical evolution models is the rate of death of the stars as a function of the galaxy lifetime. This quantity can be computed if we know the behavior of the galaxy star formation rate as a function of time, the initial mass function and the stellar lifetimes. In particular, the rate of death of the stars having mass in the range $m_1 \leq m \leq m_2$, at the time t of the galaxy evolution, is given by the following formula:

$$\mathcal{R}(t) = \int_{m_1}^{m_2} dm \phi(m) \psi(t - \tau_m), \quad (1.11)$$

where – with the purpose of simplifying the formula – we have assumed that the galaxy has undergone a continuous star formation activity over its entire lifetime

and that the time t is such that $m_{\max}(0, t) < m_1$. We remind the reader that the quantity τ_m in equation (1.11) represents the lifetime of a star with mass m .

The physical meaning of equation (1.11) is that each single time $t' < t$ of the galaxy evolution is univocally associated to a particular star, which was born at the time t' and dies at the time t , having mass m such that its corresponding lifetime is $\tau_m = |t - t'|$. Stars with very small stellar masses are associated to the earliest stages of the galaxy evolution, while massive stars can only come from epochs which are very close to the present time.

The monotonic (continuously decreasing) relation between the stellar lifetimes and stellar mass allows us to rewrite the integral over mass in equation (1.11) as an integral over all the previous times of star formation; in fact, as aforementioned, each star dying at the time t originated at a given previous time $t' < t$, which is univocally determined by the initial stellar mass. In particular, we can rewrite equation (1.11) as follows.

$$\mathcal{R}(t) = \int_{\tau_1}^{\tau_2} d\tau \left| \frac{dm(\tau)}{d\tau} \right| \phi(m) \psi(t - \tau), \quad (1.12)$$

where the quantity $m(\tau)$ represents the inverse stellar lifetimes, namely the mass of a star with lifetime τ . Usually, chemical evolution models compute the quantity $\mathcal{R}(t)$ by using equation (1.12).

The stellar restitution rate of chemical elements. Let us assume that $p_X(m, Z)$ represents the *stellar nucleosynthetic yields* of the chemical element X , namely the mass in the form of the chemical element X which is freshly synthesized by a star with mass m and metallicity Z , and later ejected into the galaxy interstellar medium at the stellar death (see also Section 1.2.4). The rate of restitution of the newly produced quantity of X , by all the stars with mass in the range $m_1 \leq m \leq m_2$, at the time t , can be computed by means of the following formula:

$$\mathcal{R}_X(t) = \int_{m_1}^{m_2} dm \phi(m) \psi(t - \tau_m) p_X(m, Z(t - \tau_m)). \quad (1.13)$$

In equation (1.13), the initial mass function plays a fundamental role, together with the stellar lifetimes. In particular, the initial mass function gives different weights to stars (and hence stellar yields) belonging to different mass ranges, whereas the stellar lifetimes regulate the delay time with which stars enrich the interstellar medium at their death. Low-mass stars have the highest weights in the initial mass function but also the largest typical lifetimes; hence low-mass stars are expected to heavily pollute the interstellar medium with their nucleosynthetic products on long typical time-scales. On the other hand, massive stars enrich the interstellar medium on very short typical time scales from the star formation event.

In chemical evolution models, it is customary to assume:

- $m_1 = m_{\max}(0, t) \equiv m_D(t)$, which is the minimum mass of the stars dying

at the time t (“D” stands for “dead”) or, equivalently, the maximum mass of the stars alive at the time t . This quantity continuously decreases as a function of the galaxy lifetime.

- $m_2 = 100 M_{\odot}$, which is the assumed maximum stellar mass that can be formed in the star formation process.

By comparing equation (1.13) with equation (1.10), lying at the basis of chemical and spectro-photometric galaxy evolutionary codes, respectively, we can appreciate that the population of stars contributing to the galaxy chemical enrichment are complementary with respect to the stars contributing to the galaxy integrated light. In particular, chemical evolution is determined by all the stars dying at the time t , while the integrated galaxy light is given by all the stars still alive at t .

1.2.4 The nucleosynthetic stellar yields

As already anticipated in the discussion above, the amount of mass of the newly formed chemical element X , as synthesized by a star during its various evolutionary phases, is called *stellar yield of the chemical element X* . The assumed stellar yield database is probably the most important quantity for the development of an accurate galaxy chemical evolution model.

Stellar yields are provided by stellar evolutionary models; many groups in the astronomical community compete in the development of these models. The complexity and accuracy of stellar models have reached nowadays very high levels, since they are capable of taking into account most of the relevant physical processes influencing the production and diffusion of the chemical elements within stars, together with a very accurate treatment of the thermodynamics of the stellar interiors. For example, the most advanced stellar models take into account the combined effect of stellar rotation, convection and mass loss. Most of the stellar models are able to compute the explosive nucleosynthesis of the chemical elements, by assuming a particular Supernova explosion mechanism and by including a comprehensive network of nuclear reactions which are solved together with the differential equations for the stellar evolution.

Although a lot of progress has been made in the development of the stellar models in the last decades, there is still not a consensus in the literature about the precise values of the nucleosynthetic stellar yields; the typical difference in the final chemical abundances, as introduced by the assumptions of different stellar yield compilations, is of the order of ~ 0.2 dex. Although the uncertainty is still not negligible for most of the chemical elements, the majority of the works in the literature agree about the production mechanism and site of the various chemical elements within stars. Nevertheless, concerning this point, there are still few (important) open problems, such as the primary nitrogen production in massive stars, at very low metallicity; the Eu nucleosynthesis (recently, an alternative scenario with respect to the classical r-process in massive stars has been proposed, namely the Eu nucleosynthesis in neutron star mergers); the chemical elements produced by the first Population III of stars. In summary, there are chemical elements (like oxygen) for which stellar models converge towards an agreement for their stellar

yields; for other chemical elements (like titanium, and some other α -elements) the situation is still critical and their stellar yields are not reliable.

Chemical elements can be produced by stars either during the hydrostatic thermonuclear burnings (this is valid both for low- and intermediate-mass stars and massive stars), or through the final explosive thermonuclear burnings, occurring as massive stars eventually explode as core-collapse Supernovae. Although the release of the chemical elements into the galaxy interstellar medium might be continuous as the star evolves towards the latest evolutionary phases and stellar winds develop, chemical evolution models assume that the chemical enrichment occurs at the “stellar death”, namely at the end of the stellar lifetime, in a cumulative way.

As aforementioned, the stellar yields are provided in the literature as functions of the stellar mass and metallicity. There is still some confusion in the literature about the exact definition of “stellar yield”; in particular – although the original works define the stellar yields by including only the fresh chemical elements as newly formed by the star – many works define it as the total amount of X which is expelled by the star at its death. The two quantities are conceptually different; in this Thesis, we will conform to the original definition.

The following equation explains how to recover the stellar yield of the chemical element X from the total amount of X which is expelled by the star:

$$p_X(m, Z) = \mathcal{M}_{\text{ej},X}(m, Z) - Z_X (m - M_{\text{rem}}(m, Z)), \quad (1.14)$$

where p_X represents the stellar yield of X ; the quantity $\mathcal{M}_{\text{ej},X}$ is the total amount of X ejected by the star at its death; Z_X is the abundance by mass of X in the original gas mixture from which the star originated; finally, M_{rem} represents the stellar remnant, as left by the star at its death. The second addend in the right-hand side of equation (1.14) represents the original quantity of X which is ejected without being nuclearly processed by the star.

In chemical evolution models, stars are broadly sub-divided into two main classes, according to their initial mass and hence their final fate: **a)** low- and intermediate-mass stars ($0.8 \lesssim m \lesssim 8 M_{\odot}$), which end their lives as white dwarfs; **b)** massive stars ($m > 8 M_{\odot}$), exploding as core-collapse Supernovae and leaving a neutron star or a black hole as a remnant. We remind the reader that stars with $m \lesssim 0.8 M_{\odot}$ have lifetimes equal or larger than the Hubble time and hence they play a marginal role in chemical evolution models, since they do not contribute to the galactic chemical enrichment.

In what follows, we schematically summarize the contribution of the two classes to the chemical enrichment of galaxies.

Low- and intermediate-mass stars

The stars with $0.8 \lesssim m \lesssim 8 M_{\odot}$ are the most important producers of ^4He , ^{12}C , ^{13}C , ^{14}N , ^{17}O and s-process elements like Ba, La, Sr and Zr in the Universe. Low- and intermediate-mass stars play also a fundamental role in the dust production, from the asymptotic giant branch to the planetary nebula phase. Their atmosphere starts being very diffuse during the asymptotic giant branch phase, along which

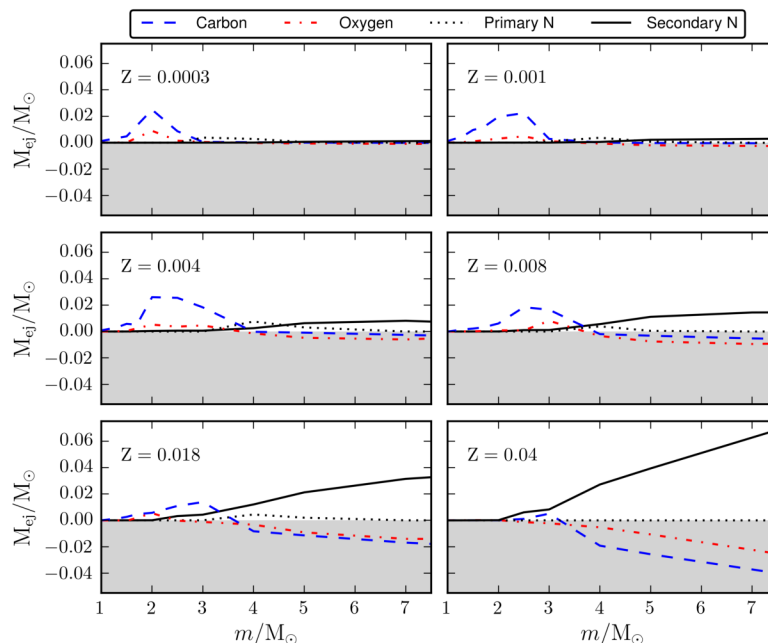


Figure 1.5: In this figure, we show the Ventura et al. (2013) stellar yields of low- and intermediate-mass stars for carbon (dashed blue line), oxygen (dashed-dotted red line), primary nitrogen (dotted black line) and secondary nitrogen (solid black line), as computed at $Z = 0.0003, 0.001, 0.004, 0.008, 0.018,$ and 0.04 . The various quantities do not include the amount of ejected mass which was initially present in the star and has not been nucleary processed; so the finding of negative values for the stellar yields means that the final total ejected amount of the generic element X is smaller than the one which was initially present in the star at its birth and has been later ejected into the interstellar medium without any nuclear processing.

these stars move towards very high luminosities and low effective temperatures; then, intense stellar winds can develop and the chemically enriched material in the outer atmosphere can diffuse into the interstellar medium, crucially contributing to the galaxy chemical enrichment.

An important role during the evolution of asymptotic giant branch stars is played by the so-called “dredge-up” episodes, which are due to a deeper surface convection in the star, establishing itself after each thermal pulse and bringing the nucleosynthetic products from the inner burning zones towards the outer envelope. Particularly important for chemical evolution studies is the *third dredge-up* in asymptotic giant branch stars, since it can occur in conjunction with the so-called “hot-bottom burning”, which is the CNO burning at the base of the convective envelope in the outer shell of the star: in this way, the C and O nuclei, as synthesized in the inner He burning zone, can be brought by convection towards the outer CNO burning zone, where ^{13}C and ^{14}N can be later synthesized.

The amount of ^{14}N which is produced during hot-bottom burning is called to have a *primary origin*, since it is synthesized only at the expense of the H and He

originally present in the star at its birth; in fact, the C and O nuclei – after being produced by the star through the triple- α process in the inner He-burning zone – migrate to the outer H-burning shell where they are used to synthesize “primary” N. Nevertheless, ^{14}N has mostly a *secondary origin* in low- and intermediate-mass stars, since in the majority of the cases the CNO cycle involves C and O nuclei which were already present in the stars at its birth.

In summary, the stellar yields of the secondary elements scale with the initial metallicity of the star, since their nucleosynthesis crucially depends upon the initial amount of metals in the star (they act as seeds for the production of the secondary elements), while the stellar yields of the primary elements do not correlate with metallicity, since the metals which might be necessary for their production are synthesized by the star itself.

Beyond nitrogen, the other very important chemical element which is synthesized by low- and intermediate-mass stars is carbon. In particular, the most important carbon producers are the stars with mass in the range $1 \lesssim m \lesssim 3 M_{\odot}$, which – incidentally – also significantly contribute to the initial mass function. Stars within that mass range are also responsible for the production of Ba and other heavy s-process elements, like Sr or La.

In summary:

- Low-mass stars with mass in the range $0.08 \lesssim m \lesssim 0.5 M_{\odot}$ only ignite H in their core. They die as He-white dwarfs and their helium core is supported against further collapse by the electron-degeneracy pressure. Their core becomes electron-degenerate before reaching the necessary temperatures for the He burning.
- Low-mass stars with mass in the range $0.5 \lesssim m \lesssim 2.25 M_{\odot}$ end their lives as CO white dwarfs. Before leaving the red giant branch, they are characterized by a highly electron-degenerate helium core. At the tip of the red giant branch, namely at the time of the He ignition, the helium core has grown up to a value which is predicted to be always around $\sim 0.48\text{--}0.50 M_{\odot}$. Then, as first triple- α reactions start in the core, they cause a sudden increase in the central temperature of the star, which is not accompanied by an expansion of the core, since it is still highly electron-degenerate. Therefore, stellar models predict a sort of positive feedback between the central temperature and the triple- α reaction rate; in particular, they predict a “thermal runaway” together with a very large release of nuclear energy over very a short amount of time (few seconds). Roughly speaking, a spike is predicted to occur in the light curve of these stars (that is the so-called *helium flash*), as they start burning helium in their core and hence start moving towards the blue horizontal branch.
- Intermediate-mass stars with mass in the range $2.25 \lesssim m \lesssim 8 M_{\odot}$ end their lives as CO white dwarfs. They are predicted to leave the red giant branch with a non-degenerate helium core, without any helium flash.

The first widely assumed stellar yield compilation for low- and intermediate-mass stars is the one by [Renzini & Voli \(1981\)](#). Then, the work by [van den Hoek](#)

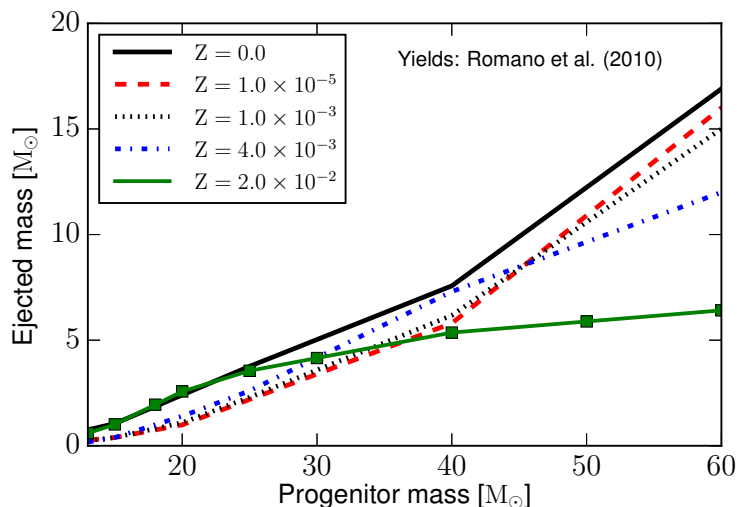


Figure 1.6: In this figure, we report the ejected mass of oxygen as a function of the progenitor mass, for different initial stellar metallicities. This set of stellar yields is from [Romano et al. \(2010\)](#). The solid line in black corresponds to the stellar yields at $Z = 1.0 \times 10^{-10}$; the dashed line in red to $Z = 1.0 \times 10^{-5}$; the black dotted line to $Z = 1.0 \times 10^{-3}$; the dashed-dotted line in blue to $Z = 3 \times 10^{-3}$, and the green squares to the stellar yields at $Z = 2.0 \times 10^{-2}$.

& [Groenewegen \(1997\)](#) provided a detailed compilation of stellar yields for stars with mass in the range $0.8 \leq m \leq 8 M_{\odot}$ and metallicities $Z = 0.001, 0.004, 0.008, 0.02, \text{ and } 0.04$. A more recent compilation of stellar yields for low- and intermediate-mass stars is the one by [Karakas \(2010\)](#), which is assumed by almost all the current chemical evolution models which are capable of reproducing the Milky Way chemical abundance patterns ([Romano et al., 2010](#)). Finally, a recent stellar yield compilation is the one provided by the Paolo Ventura’s group at the Astronomical Observatory of Rome (see, for example, [Ventura et al. 2013](#)), which has been assumed by [Vincenzo et al. \(2016b\)](#) to reproduce the N and O abundances as observed in a sample of Sloan Digital Sky Survey galaxies.

In [Fig. 1.5](#), we show how the stellar yields of [Ventura et al. \(2013\)](#) for C, O, and primary and secondary N vary as functions of the initial stellar mass, for different metallicities. The stellar yield of a given chemical element X is defined as the ejected amount of mass of the newly formed X . By looking at the figure, the stellar yields of secondary N increase with metallicity, by means of the consumption of the C and O nuclei originally present in the star. In fact, during the CNO cycle, the global abundance of the CNO nuclei remains constant, while the relative abundances of each CNO element can significantly vary. By looking at [Fig. 1.5](#), the stellar producers of primary N have masses in the range between $\sim 3 M_{\odot}$ and $6 M_{\odot}$. Furthermore, the production of primary N does not show any correlation with the consumption of the original C and O in the star, as expected.

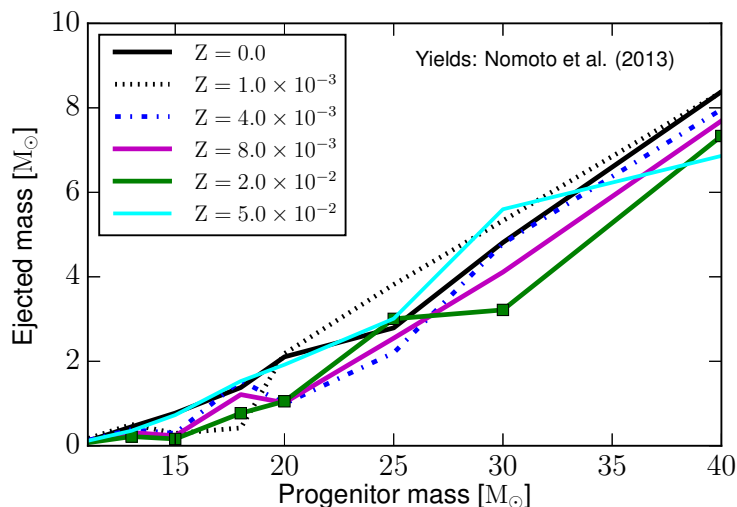


Figure 1.7: In this figure, we show how the ejected mass of oxygen vary as a function of the progenitor mass, for different initial stellar metallicities, when assuming the [Nomoto et al. \(2013\)](#) stellar yields. The solid line in black corresponds to the stellar yields at $Z = 0.0$; the dotted line in black to $Z = 1.0 \times 10^{-3}$; the dashed-dotted line in blue to $Z = 4.0 \times 10^{-3}$; the solid line in magenta to $Z = 8.0 \times 10^{-3}$; the solid line in green to $Z = 2.0 \times 10^{-2}$, and the solid line in cyan to the stellar yields at $Z = 5.0 \times 10^{-2}$.

Massive stars

Massive stars are defined as having mass $m \gtrsim 8 M_{\odot}$, although the limiting mass is still highly uncertain. In summary:

- Stars with mass $8 \lesssim m \lesssim 10 M_{\odot}$ give rise to the so-called “super asymptotic giant branch stars” and develop an electron-degenerate O-Ne-Mg core; as the core reaches a critical density of the order of $\sim 4 \times 10^9 \text{ g cm}^{-3}$, corresponding to a mass around $\sim 1.38 M_{\odot}$, e-captures onto the Mg nuclei cause the degenerate pressure to decrease and the core to collapse; then, the O explosively ignites, giving eventually rise to an *e-capture Supernova*.
- Stars with mass in the range $10 M_{\odot} \lesssim m < M_{\text{WR}}(Z)$ give rise to Type II Supernovae and are the most important metal-producers in the Universe, despite the fact that their contribution in the initial mass function is much minor with respect to low-mass stars. M_{WR} is the minimum mass for the formation of a Wolf-Rayet star, which is highly uncertain since it depends on the prescriptions about the stellar mass loss, which in turn depend both on the initial stellar mass and on the metallicity (the higher the metallicity, the lower turns out to be M_{WR}). Massive stars, before exploding as Type II Supernovae, develop an onion-like structure with a central non-degenerate iron core and a series of surrounding burning shells (Si, O, Ne, C, He, and H, from inside out). As the iron core reaches the Chandrasekhar’s mass limit $M_{\text{Ch}} \sim 1.44 M_{\odot}$, because of the continuous accretion of iron-group elements

from the surrounding Si burning shell, the electron-degeneracy pressure cannot prevent anymore the core from the gravitational collapse. The iron core – as it collapses and reaches always higher densities – passes through the stages of “photo-disintegration” of the iron nuclei and α -particles, and finally “neutronization”. At the end, these stars can leave either a neutron star or – if the degeneracy pressure of the neutrons cannot sustain the core (this occurs for core masses $\gtrsim 3 M_{\odot}$) – a black hole as remnants. During the violent core-collapse, a Supernova explosion of Type II takes place. They can enrich the interstellar medium either through stellar winds, as the star evolves in its “normal” evolutionary stages, or at the very final explosive stages, as the burning shells are partly blown away by the shockwaves originating from the so-called “core bounce”, which takes place when the collapsing core reaches so extremely high densities that the strong nuclear forces suddenly halt the collapse; the mass expulsion is later reinforced by high-energy neutrinos. The limiting initial mass of the star for the formation of a black hole is still highly uncertain; it is thought to be of the order of $\sim 40 M_{\odot}$. The presence of a black hole as a remnant might cause the fallback of a substantial part of the expelled material, hence strongly reducing the stellar yields. Concerning the nucleosynthesis of the chemical elements, ^{16}O is mostly produced during the hydrostatic He burning; ^{23}Na during the hydrostatic C, Ne and H burnings; ^{24}Mg and ^{27}Al during the hydrostatic C and Ne burnings; ^{28}Si and ^{40}Ca can be produced both during the hydrostatic and during the explosive O burning; finally, chemical elements like ^{48}Ti , ^{52}Cr , ^{55}Mn , and ^{56}Fe are mainly synthesized during the explosive Si burning. A fraction of the neutrons produced by the iron photo-disintegration could be successively involved in the production of r-process elements like Eu.

- Stars with mass in the range $M_{\text{WR}}(Z) \lesssim m \leq 100 M_{\odot}$ undergo very intense stellar winds which remove their external H-rich envelopes. They become Wolf-Rayet stars and are expected to die by eventually exploding as Type Ib/c Supernovae, which are currently thought to be directly linked to long Gamma Ray Bursts, because of the observed similarity of their spectra. These stars contribute to the galaxy chemical enrichment mainly with ^4He , ^{12}C , ^{13}C , ^{22}Ne , ^{14}N , and ^{18}O , concerning the hydrostatic chemical elements; the heavier chemical elements are synthesized during the final Supernova explosion.

The most widely used compilation of stellar yields for massive stars is the one by [Woosley & Weaver \(1995\)](#). A recent compilation of stellar yields for massive stars is the one assumed by [Romano et al. \(2010\)](#), where the He, C, N and O stellar yields are taken from the results of the Geneva stellar models of massive stars, taking into account the combined effect of mass loss and rotation, but only assuming hydrostatic burning ([Meynet & Maeder, 2002](#); [Hirschi et al., 2005](#); [Hirschi, 2007](#); [Ekström et al., 2008](#)); for heavier elements, [Romano et al. \(2010\)](#) assume the stellar yields of massive stars by [Kobayashi et al. \(2006\)](#), which do include standard mass loss and the explosive nucleosynthesis but not the effect of rotation.

The mass loss driven by rotation turns out to be particularly important at

almost solar metallicity and above in depressing the oxygen stellar yields of the most massive stars ($M \gtrsim 30\text{-}40 M_{\odot}$). In fact, mass loss increases with stellar metallicity and stars of high metal content lose H, He, but also C, through radiatively line driven winds. Therefore, the C production is increased by mass loss whereas the oxygen production is decreased, since part of C which would have been transformed into O, is lost from the star (Maeder, 1992). Finally, the effect of rotation is to produce mixing and enhances mass loss, with the efficiency of the mixing process being larger at lower metallicities (see also Chiappini et al. 2008, and references therein).

An other compilation of stellar yields of massive stars is the one by Nomoto et al. (2013), which is a review, combining the results of the works by Nomoto et al. 2006; Kobayashi et al. 2006, 2011. Finally, an other group working on stellar evolutionary models of massive stars is the one of Marco Chieffi and Paolo Limongi at the Astronomical Observatory of Rome, who include in their models the combined effect of mass and rotation and take into account also the final explosive nucleosynthesis (Chieffi & Limongi, 2013).

In Figures 1.6 and 1.7, we show how the oxygen stellar yields of Romano et al. (2010) and Nomoto et al. (2013), respectively, vary as functions of the initial stellar mass and for different metallicities. The Geneva stellar yields are available only up to $60 M_{\odot}$ and we therefore assume in our standard case that the yields from 60 to $100 M_{\odot}$ are constant. On the other hand, the stellar yields of massive stars of Kobayashi et al. (2006, included in Romano et al. 2010, for the elements heavier than oxygen) and Nomoto et al. (2013) are available only up to $40 M_{\odot}$ and thus we keep them constant for stars with larger initial mass. We remark on the fact that very massive stars are expected to leave a black hole as a remnant; therefore, a significant fraction of the stellar nucleosynthetic products in the ejecta of very massive stars may eventually fall back onto the black hole. This process might cause a reduction of the stellar yields of very massive stars.

1.2.5 Type Ia Supernovae

Type Ia Supernovae play a fundamental role both in the pollution and in the heating of the interstellar medium of galaxies. Each Type Ia Supernova releases an amount of energy which is $\sim 10^{51}$ erg; moreover, Type Ia Supernovae are responsible for the nucleosynthesis of most of the iron and iron-peak elements in galaxies, together with a significant amount of silicon, calcium and other light elements. Therefore, the effect of Type Ia Supernovae must be taken into account by the galaxy evolution models which aim at being accurate and complete.

Type Ia Supernovae are observed to explode in all kind of galaxies, from the early to the late morphological types, at variance with Type II Supernovae which are preferentially observed to explode in the late-type star-forming ones. Furthermore, as Type Ia Supernovae explode, they do not leave any remnant and almost all the material is explosively synthesized to eventually produce large amounts of iron; in Type II Supernovae, the majority of the iron remains “locked up” in the remnant. That explains why Type II Supernovae do not contribute to the iron chemical enrichment as Type Ia Supernovae.

Type Ia Supernovae have been extensively used as standard candles in the past because they display a nearly universal light curve profile, which is powered by the decay of almost $\sim 0.6 M_{\odot}$ of ^{56}Ni into ^{56}Co (it takes nearly 9 days), which eventually decays into ^{56}Fe after roughly 114 days. From an observational point of view, the spectra of Type Ia Supernovae do not show any evidence of H or He lines and – at the peak of the light curve – they clearly display silicon and sulphur lines; later on, strong iron lines appear.

Two alternative models have been proposed in the literature to explain the origin of Type Ia Supernovae. Both scenarios involve an (electron-degenerate) CO white dwarf, belonging to a binary system and exceeding – at a certain point of its evolution – the Chandrasekhar mass limit; this happens **(a)** either because of the mass transfer from a main sequence or red-giant companion (this is the so-called *single-degenerate scenario*), or **(b)** because of the coalescence with another CO white dwarf, which lost angular momentum via gravitational wave emission and eventually collided with the companion, undergoing the same process (*double-degenerate scenario*). In both cases, deflagration rather than detonation is needed to ignite carbon and propagate the burning front; in fact, deflagration is the only mechanism with which there is a significant nucleosynthesis of chemical elements lighter than the iron-peak ones, in agreement with what is observed in the spectra of all Type Ia Supernovae.

In summary, the mechanism for the explosion of Type Ia Supernovae involves low- and intermediate-mass stars, which must have masses in the range $0.8 \lesssim m \lesssim 8 M_{\odot}$, in order to have a CO white dwarf in a Hubble time. Therefore, Type Ia Supernovae can explode over a large range of typical time-scales from the star formation event, from a minimum time delay which is nearly ~ 30 Myr (this is almost the lifetime of an $8 M_{\odot}$ star) to a Hubble time. In the single-degenerate scenario, we have two low- and intermediate-mass stars: the most massive one is the so-called *primary star*, which becomes an electron-degenerate CO white dwarf and accretes material from the companion; the less massive one is the so-called *secondary star*, which evolves more slowly and feeds the (primary) CO white dwarf with its stellar wind. The main parameter which regulates the “clock” for the explosion is given by the mass of the secondary star, since the mass primarily determines the lifetime of the star.

The Type Ia Supernova rate in galaxies can be theoretically recovered if we know the galaxy star formation history and the distribution function of the delay times with which Type Ia Supernovae explode since the formation of the original binary system. Many Delay Time Distributions have been proposed in the literature to reproduce the Type Ia Supernova rate in galaxies.

By definition, the Delay Time Distribution of Type Ia Supernovae, $\text{DTD}_{\text{Ia}}(\tau)$, is the response of the Type Ia Supernova rate to a burst of star formation (namely, to a Dirac delta function in the star formation history): after a time τ from the burst of star formation, it gives the number of Type Ia Supernovae exploding per unit time. By following the formalism originally developed by [Ruiz-Lapuente & Canal \(1998\)](#), the Type Ia Supernova rate, $\mathcal{R}_{\text{Ia}}(t)$, is defined as the convolution of

the galaxy star formation rate with a suitable Delay Time Distribution, as follows.

$$\mathcal{R}_{\text{Ia}}(t) = C_{\text{Ia}} \int_{\tau_1}^{\min(t, \tau_2)} d\tau \text{DTD}_{\text{Ia}}(\tau) \psi(t - \tau), \quad (1.15)$$

where τ_1 and τ_2 are suitable values depending on the adopted scenario for the DTD. The normalization constant C_{Ia} is related to the fraction of stars in the binary systems giving rise to Type Ia Supernovae and it can vary from galaxy to galaxy and is usually determined by fitting the observed present-day Type Ia Supernova rate in galaxies, when observed.

In [Vincenzo, Matteucci & Spitoni \(2016\)](#), we have proposed an alternative method to compute the constant C_{Ia} in the models, providing an excellent agreement with the observed chemical abundance patterns of the Milky Way. In particular, observations suggest an integrated number of Type Ia Supernovae in galaxies, which is ~ 1 Supernova per $M_{\star} = 10^3 M_{\odot}$ of stellar mass formed, with a scatter of about 2-10 around this value ([Bell et al., 2003](#); [Maoz et al., 2014](#)). Therefore, the normalization constants of the Delay Time Distributions can be chosen so as to fulfill this criterium; in particular, the constant C_{Ia} in equation (1.15) can be computed by requiring the following constraint:

$$\frac{\int_0^{t_G} dt' R_{\text{Ia}}(t')}{\int_0^{t_G} dt' \psi(t')} = \frac{2 \text{ Supernovae}}{10^3 M_{\odot}}, \quad (1.16)$$

where the numerator represents the integrated number of Type Ia Supernovae and the denominator the total galaxy stellar mass formed.

In what follows, we briefly summarize the main ways which have been proposed in the literature for modeling the Type Ia Supernova rate in galaxies.

Double degenerate scenario According to [Greggio \(2005\)](#), the double degenerate scenario – in which Type Ia Supernovae originate from binary systems of white dwarfs losing angular momentum via gravitational wave emission – can be modeled by assuming $\text{DTD}_{\text{Ia}}(\tau) \propto 1/\tau$ (see also [Totani et al. 2008](#)), which provides almost the same final results for the Type Ia Supernova rate in galaxies as the Delay Time Distribution proposed by [Schönrich & Binney \(2009\)](#).

Bimodal Delay Time Distribution An other widely used Delay Time Distribution often assumed in the literature is the so-called “bimodal Delay Time Distribution” as determined by [Mannucci et al. \(2006\)](#). It was originally defined with the following functional form:

$$\text{DTD}_{\text{Ia}}(\tau) = C_{\text{Ia}} \left[A_1 \exp\left(-\frac{(\tau - \tau')^2}{2\sigma'^2}\right) + A_2 \exp(-\tau/\tau_D) \right], \quad (1.17)$$

where the constants $A_1 \approx 19.95$ and $A_2 \approx 0.17$ guarantee that the two terms in the equation equally contribute by 50 per cent; the parameters determining the

prompt Gaussian function are $\tau' = 0.05$ Gyr and $\sigma' = 0.01$ Gyr; finally, the time scale of the tardy declining exponential component is $\tau_D = 3$ Gyr.

Single degenerate scenario If Type Ia Supernovae are assumed to originate from the C-deflagration of a white dwarf accreting material from a red giant or main sequence companion (the single degenerate scenario), then the Type Ia Supernova rate can be computed by means of the following theoretical formula (Greggio & Renzini, 1983; Matteucci, 1986; Matteucci & Recchi, 2001):

$$\mathcal{R}_{\text{Ia}}(r, t) = A_B \int_{3 M_\odot}^{16 M_\odot} dM_B \phi(M_B) \int_{0.158}^{0.5} d\mu f(\mu) \psi(r, t - \tau_{m_2}), \quad (1.18)$$

where the binary fraction A_B can be determined with equation (1.16) and can span the range ~ 0.01 - 0.1 , according to the assumed initial mass function and the galaxy under study; $M_B = m_1 + m_2$ is the total mass of the binary system; $\mu = m_2/M_B$ is the mass fraction of the secondary star, the ‘‘clock’’ for the explosion, and $f(\mu) = 2^{1+\gamma} (1 + \gamma) \mu^\gamma$ represents the mass distribution of the secondary star, with $\gamma = 2$. Therefore, in this formalism, the primary star (the most massive and finally exploding one) has mass $m_1 = (1 - \mu)M_B$, while the secondary (less massive) star is characterized by $m_2 = \mu M_B$ and lifetime $\tau = \tau_{m_2}$. Both m_1 and m_2 are usually defined in the mass range $1.5 \leq m \leq 8.0 M_\odot$ to ensure the Chandasekhar mass to be reached at the final evolutionary stage of both stars.

1.2.6 The stellar delay time distribution

We can rewrite equation (1.12), to define the *stellar delay time distribution* (Vincenzo, Matteucci & Spitoni, 2016). In particular, if a given chemical element X is restored into the galaxy interstellar medium by long-lived stars with mass in the range $m_1 \leq m \leq m_2$, the rate of death of its stellar producers at a given time t of the galaxy evolution and at a given galactocentric radius r can be written by the following formula:

$$\begin{aligned} \mathcal{R}_X(t) &= \int_{\tau_1}^{\tau_2} d\tau \left| \frac{dm(\tau)}{d\tau} \right| \phi(m) \psi(t - \tau) = \\ &= \int_{\tau_1}^{\tau_2} d\tau \text{DTD}_*(\tau) \psi(t - \tau), \end{aligned} \quad (1.19)$$

where τ_m represents the lifetime of a star with mass m ; $m(\tau)$ the mass of a star with lifetime τ ; $\phi(m)$ the assumed initial mass function and, finally, $\psi(t)$ the star formation rate. By looking at equation (1.19), the delay time distribution of long-lived stars is a universal function and it only depends upon the inverse stellar lifetimes and the initial mass function, according to the following formula (see also

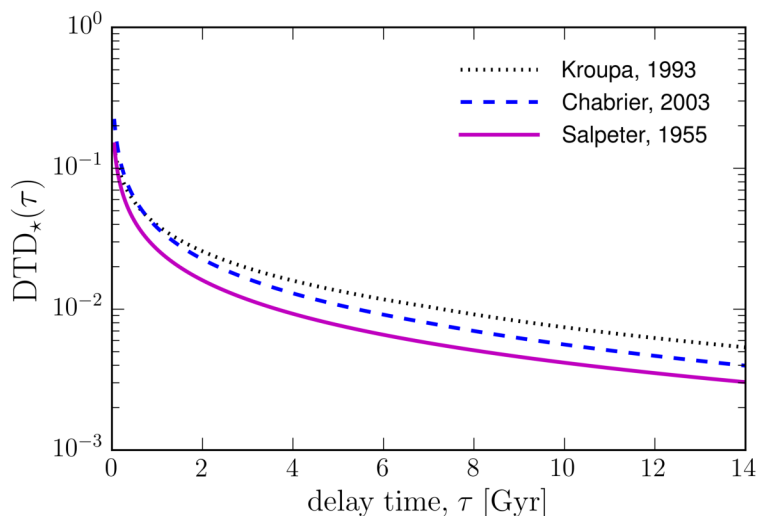


Figure 1.8: In this figure, we show how the stellar delay time distribution varies as a function of the delay time, for different initial mass functions. Bottom-heavy initial mass functions like the one by [Kroupa et al. \(1993\)](#), hosting a large number of low- and intermediate-mass stars) predict large delay times for the chemical enrichment to be more frequent than top-heavy initial mass functions like the one by [Chabrier \(2003\)](#), with a large number of massive stars).

[Ciotti et al. 1991](#); [Greggio 2005](#)):

$$\text{DTD}_*(\tau) = \left| \frac{dm(\tau)}{d\tau} \right| \phi(m(\tau)). \quad (1.20)$$

The quantity $\text{DTD}_*(\tau)$ physically represents the number of stars with mass m and lifetime $\tau_m = \tau$, which are expected to die at the time $t = \tau$ from a burst of star formation at $t = 0$, per unit mass of the simple stellar population and per unit time of duration of the burst. In [Figure 1.8](#), we show how $\text{DTD}_*(\tau)$ is predicted to evolve as a function of the delay time τ , for different initial mass functions. As expected, large delay times turn out to be more frequent if the assumed initial mass function contains also larger numbers of low- and intermediate-mass stars. In [Figure 1.8](#), we assume the stellar lifetimes of [Padovani & Matteucci \(1993\)](#). An example of bottom-heavy initial mass function is the one by [Kroupa et al. \(1993\)](#), which is usually assumed for modeling the chemical evolution of the Milky Way (see also [Romano et al. 2010](#)).

1.3 The galaxy chemical evolution models

In this Section, we review the differential equations which are solved by numerical codes of chemical evolution, we describe in detail the various terms in the equations and the method to solve them. The books by [Matteucci \(2001, 2012\)](#) and [Pagel \(2009\)](#) present an exhaustive and detailed description of chemical evolution models.

1.3.1 The differential equations for the galaxy chemical evolution

By defining $\sigma_X(r, t)$ as the surface gas mass density of the generic chemical element X within the galaxy interstellar medium at the time t and galactocentric radius r , the chemical evolution models solve the following integro-differential equation:

$$\frac{d\sigma_X(r, t)}{dt} = \underbrace{-Z_X(r, t) \psi(r, t)}_{\text{star formation}} + \underbrace{\mathcal{R}_X(r, t)}_{\text{yields}} - \underbrace{\mathcal{O}_X(r, t)}_{\text{outflows}} + \underbrace{\mathcal{I}_X(r, t)}_{\text{infall}} + \underbrace{\mathcal{F}_X(r, t)}_{\text{radial gas flows}} + \underbrace{\mathcal{M}_X(r, t)}_{\text{stellar migrations}}, \quad (1.21)$$

where $Z_X(r, t) = \sigma_X(r, t)/\sigma_{\text{ISM}}(r, t)$ is the abundance by mass of the chemical element X within the galaxy interstellar medium, defined such that $\sum_i Z_i(r, t) = 1$, where the sum is over all the metals. The quantity $\psi(r, t)$ represents the galaxy star formation rate with the units of $\text{M}_\odot \text{yr}^{-1} \text{pc}^{-2}$. We remark on the fact that equation (1.21) refers to the evolution of the chemical abundances within the galaxy interstellar medium; we can make direct comparisons between the predictions of the models and the observed stellar abundances both because stars have a distribution of ages at the present time and because their atmosphere is assumed to retain the chemical composition of the galaxy interstellar medium at the stellar birth. The physical meaning of the various terms in the right-hand side of equation (1.21) are summarized in the following subsections.

Astration of metals due to the star formation activity

The first term in the right-hand side of equation (1.21) represents the amount of the chemical element X which is removed per unit time and surface from the galaxy interstellar medium because of the star formation activity. Usually, chemical evolution models assume for the star formation rate a Schmidt-Kennicutt law, namely

$$\psi(r, t) \propto \nu(r) \sigma_{\text{gas}}(r, t)^k, \quad (1.22)$$

where $\nu(r)$ is the so-called *star formation efficiency*, a free parameter of the model, which has the units of Gyr^{-1} and physically represents the inverse of the typical time-scale over which the gas mass within the galaxy would be consumed if only the star formation activity process were present. The total galaxy surface gas mass density $\sigma_{\text{gas}}(r, t)$ is computed as the sum of the surface gas mass densities of all the chemical elements X , from hydrogen to the heaviest ones. Many works assume a threshold in the surface gas mass density below which the star formation is suppressed; such a threshold is about $\sigma_{\text{gas,th}} \sim 5\text{-}10 \text{M}_\odot \text{pc}^{-2}$ for the Galaxy disc, according also to the works of Kennicutt (1989, 1998); Martin & Kennicutt (2001); Boissier et al. (2003); Schaye (2004).

Restitution rate of metals from dying stars and Supernovae

The second term in the right-hand side of equation (1.21) lies at the core of chemical evolution models, since it represents the rate with which the chemical element X is returned back into the galaxy interstellar medium by dying stars (low- and intermediate-mass stars through their asymptotic giant branch phase and core-collapse Supernovae) and Type Ia Supernovae. Hence this term subsumes all the prescription about the Supernova progenitor models and stellar nucleosynthetic yields. Its mathematical form consists in a sum of integrals, each having the same form as equation (1.13) and corresponding to the contribution of the stars in a given mass range.

Most of chemical evolution models assume for the restitution rate of the chemical element X the following sum of integrals, where the single degenerate scenario is assumed for modeling Type Ia Supernovae (see also equation 1.18):

$$\begin{aligned}
 \mathcal{R}_X(r, t) = & \int_{m_{\text{low}}(t)}^{3 M_{\odot}} dm \phi(m) \psi(t - \tau_m) p_X(m, Z(t - \tau_m)) + \\
 & + (1 - A_B) \int_{3 M_{\odot}}^{16 M_{\odot}} dm \phi(m) \psi(t - \tau_m) p_X(m, Z(t - \tau_m)) + \\
 & + \int_{16 M_{\odot}}^{100 M_{\odot}} dm \phi(m) \psi(t - \tau_m) p_X(m, Z(t - \tau_m)) + \\
 & + \langle p_{X, \text{Ia}} \rangle \mathcal{R}_{\text{Ia}}(r, t), \quad (1.23)
 \end{aligned}$$

where the quantity $p_X(m, Z)$ corresponds to the nucleosynthetic stellar yield of the chemical element X of a star with initial mass m and metallicity Z ; the stellar yields represent a fundamental assumption of the models.

The first and the third integrals in equation (1.23) represent the contribution of low-mass stars (ending their lives as CO white dwarfs) and massive stars (exploding as core-collapse Supernovae), which are not in the same mass range of the binary systems giving rise to Type Ia Supernovae (which is $3 \leq M_B \leq 16 M_{\odot}$, see also equation 1.18); the quantity $m_{\text{low}}(t)$ represents the minimum mass of the stars which can die at the time t : this quantity diminishes as a function of the galaxy lifetime and cannot be lower than $0.8 M_{\odot}$. Furthermore, the last term in the right-hand side of equation (1.23) corresponds to the restitution rate of the chemical element X by Type Ia Supernovae, with $\langle p_{X, \text{Ia}} \rangle$ being the nucleosynthetic products of Type Ia Supernovae; in the most sophisticated models, like the one of the Matteucci's group, the last term includes also the chemical elements which are restituted by the primary (most massive) star of the binary system during the asymptotic giant branch phase, before becoming a CO white dwarf and exploding as Type Ia Supernova.

Finally, the third integral in equation (1.23) represents the chemical enrichment

by single stars which have the same mass as the whole binary systems giving rise to Type Ia Supernovae and end their lives either as CO white dwarfs or as core-collapse Supernovae.

Galactic winds

The third term in the right-hand side of equation (1.21) takes into account the possibility for the galaxy to lose gas via galactic winds, which are assumed to develop when the thermal energy of the gas – as heated by Type II and Type Ia Supernovae, and stellar winds from low- and intermediate-mass stars – exceeds the binding energy of the gas to the galaxy potential well, according to the formulation as presented in [Bradamante et al. \(1998\)](#), see also [Pipino et al. 2002](#)).

The outflow rate is assumed to be directly proportional to the star formation rate, namely

$$\mathcal{O}_X(r, t) = \omega_X \psi(r, t), \quad (1.24)$$

where the parameter ω_X represents the so-called *mass loading factor*. Observations generally suggest that star-forming galaxies experience time-averaged outflow loading factors of order unity ([Lilly et al., 2013](#); [Peng et al., 2015](#); [Belfiore et al., 2015](#); [Lu et al., 2015](#)) at stellar masses around $\log(M_*/M_\odot) \sim 10$, close to the knee of the luminosity function. It is, however, likely that less massive galaxies experience much higher loading factors. The mass loading factor might be the same for all the chemical elements (in this case we refer to a “normal wind”), or preferentially carry out of the galaxy potential well some chemical elements rather than others (“differential wind”); nevertheless, the assumption of a differential galactic wind is highly uncertain and it does not rely on firm theoretical and observational findings; further detailed investigations are needed, by looking – for example – at the chemical abundances in the halo of the MW or in quasar absorption lines, which were also related in the past to galactic winds.

The assumption of a differential outflow enhanced in the α -elements might be justified by the fact that massive stars (the progenitors of core-collapse Supernovae and the most important oxygen producers in the Universe) are observed to be highly clustered and so, as they explode, they create a region of the interstellar medium in which the filling factor closely approaches to unity; hence the ejecta of Type II Supernovae might gain enough thermal energy to escape from the galaxy potential well (see [Marconi et al. 1994](#); [Recchi et al. 2001](#)). An opposite result has been obtained by [Recchi et al. \(2001\)](#), by simulating the effect of a burst of star formation on the chemical and hydrodynamical evolution of a dwarf irregular galaxy. In particular, [Recchi et al. \(2001\)](#) found that iron should be lost easier than α -elements, firstly because Type Ia Supernovae can inject into the galaxy interstellar medium more energy than Type II Supernovae; secondly, Type Ia Supernovae are characterized by longer typical time scales than Type II Supernovae and hence they release their nucleosynthetic products in an interstellar medium which has been already perturbed and heated by a large number of Type II Supernovae. Nevertheless, the results of [Recchi et al. \(2001\)](#) might not be correct for the case of a continuous star formation activity, lasting several billion years as in most of the galaxies in the Universe.

As aforementioned, galactic winds are assumed to develop when the gas thermal energy, $E_{\text{gas}}^{\text{th}}(t)$, exceeds its binding energy, $E_{\text{gas}}^{\text{b}}(t)$, namely when:

$$E_{\text{gas}}^{\text{th}}(t) \geq E_{\text{gas}}^{\text{b}}(t). \quad (1.25)$$

The gas thermal energy is computed by summing up the contributions of Type Ia and Type II Supernovae and stellar winds, according to the following formula:

$$E_{\text{gas}}^{\text{th}}(t) = E_{\text{SNIa}}^{\text{th}}(t) + E_{\text{SNII}}^{\text{th}}(t) + E_{\text{sw}}^{\text{th}}(t), \quad (1.26)$$

where $E_{\text{sw}}^{\text{th}}(t)$, $E_{\text{SNIa}}^{\text{th}}(t)$ and $E_{\text{SNII}}^{\text{th}}(t)$ are the energy fraction deposited in the gas by stellar winds from massive stars and by Type Ia and Type II Supernova explosions, respectively. Not all the energy produced in these events is stored into the galaxy interstellar medium, since a fraction of it can be lost by cooling. The supernova contributions are given by:

$$E_{\text{SNII}}^{\text{th}}(t) = \int_0^t dt' \epsilon_{\text{SNII}} R_{\text{SNII}}(t'), \quad (1.27)$$

and:

$$E_{\text{SNIa}}^{\text{th}}(t) = \int_0^t dt' \epsilon_{\text{SNIa}} R_{\text{SNIa}}(t'), \quad (1.28)$$

with $R_{\text{SNII}}(t)$ and $R_{\text{SNIa}}(t)$ being the rates of Type II and Type Ia Supernova explosions, respectively, and ϵ_{SNII} and ϵ_{SNIa} being the energy injected and effectively thermalized from Supernovae explosions, defined by:

$$\epsilon_{\text{SNII}} = \eta_{\text{SNII}} E_0, \quad (1.29)$$

$$\epsilon_{\text{SNIa}} = \eta_{\text{SNIa}} E_0. \quad (1.30)$$

The quantity $E_0 = 10^{51}$ erg is the assumed total energy released by a Supernova explosion, while $\eta_{\text{SNII}} \sim 0.03$ and $\eta_{\text{SNIa}} \sim 1.00$ are the adopted efficiencies of the energy transfer from the Supernova explosions into the galaxy interstellar medium (Bradamante et al., 1998).

The different values of η assigned to the two types of Supernovae are easily explained by the fact that Type Ia Supernovae explode in a hotter and more rarefied medium, already warmed up by Type II Supernovae; consequently, the efficiency of the energy transfer from Type Ia Supernovae is higher than the one from Type II Supernovae. We remark on the fact that this formulation depicts an ideal case when the interstellar medium is uniform and had no interaction with other Supernova remnants or interstellar clouds. In particular, when a Supernova explodes, the stellar material is assumed to be violently ejected into the galaxy interstellar medium, gradually slowing down.

In the case of the stellar winds, one has:

$$E_{\text{sw}}^{\text{th}}(t) = \int_0^t dt' \psi(t') \int_{8.0 M_{\odot}}^{100 M_{\odot}} dm \phi(m) \epsilon_{\text{sw}}, \quad (1.31)$$

where:

$$\epsilon_{\text{sw}} = \eta_{\text{sw}} E_{\text{sw}} \quad (1.32)$$

is the energy injected and effectively thermalized from stellar winds by massive stars, assuming $E_{\text{sw}} = 10^{49}$ erg and $\eta_{\text{sw}} = \eta_{\text{SNII}} = 0.03$ (Bradamante et al., 1998).

To compute $E_{\text{gas}}^{\text{b}}(t)$, the binding energy of the gas, we follow the assumptions of Bradamante et al. (1998). In particular, each galaxy has been assumed to be made up by a dark matter halo, with the binding energy of the gas described as:

$$E_{\text{gas}}^{\text{b}} = W_{\text{L}}(t) + W_{\text{LD}}(t), \quad (1.33)$$

where:

$$W_{\text{L}}(t) = -0.5 \cdot G \cdot \frac{M_{\text{gas}}(t) M_{\text{L}}(t)}{r_{\text{L}}} \quad (1.34)$$

represents the potential well due to the *luminous* (baryonic) matter, and:

$$W_{\text{LD}}(t) = -G \cdot w_{\text{LD}} \frac{M_{\text{gas}}(t) M_{\text{dark}}}{r_{\text{L}}} \quad (1.35)$$

represents the potential well due to the interaction between the dark and the luminous matter. The quantity w_{LD} has is defined as follows:

$$w_{\text{LD}} \sim \frac{1}{2\pi} S (1 + 1.37 S), \quad (1.36)$$

where $S = r_{\text{L}}/r_{\text{D}}$ is the ratio between the galaxy effective radius (the quantity r_{L}) and the radius of the dark matter core (the quantity r_{D}); typically, $S \approx 0.3$.

The equations above for the binding energy of the gas have been originally developed by Bertin et al. (1992) and – in principle – are valid only for S defined in the range $0.10 \lesssim S \lesssim 0.45$. Moreover, it is worth noting that the original formulation of Bertin et al. (1992) was thought only for the massive elliptical galaxies.

The galaxy gas mass assembly history

The fourth term in the right-hand side of equation (1.21) represents the galaxy gas mass assembly history, namely the infall rate of gas, which is accreted as a function of time into the galaxy potential well from an external reservoir. The infall material can be either of primordial chemical composition or pre-enriched with metals by previous stellar generations. Chemical evolution models customarily assume the infall rate to be composed of several accretion episodes, each obeying a decaying exponential law. In particular, in most of the cases, we assume for the infall rate the following law:

$$\mathcal{I}_X(r, t) = A_X(r) \exp\left(-t/\tau_{\text{inf}}(r)\right), \quad (1.37)$$

where $\tau_{\text{inf}}(r)$ is the so-called *infall time scale* at the galactocentric radius r , a free parameter of the model, and $A_X(r)$ is a normalization constant such that

$$\sum_X \int_0^{t_G} dt \mathcal{I}_X(r, t) = \sigma_{\text{tot}}(r, t_G), \quad (1.38)$$

where $\sigma_{\text{tot}}(r, t_G)$ is the radial profile of the total surface mass density, as observed at the present time. In the case of primordial infall material, the quantity $A_X(r)$ is different from zero only for H and He.

The abundance gradients in disc galaxies can be well reproduced only by assuming that the gas accretion history differs as a function of the galactocentric radius; this can be simulated by the models by assuming, for example, an exponential profile for the present-day total surface mass density, namely

$$\sigma_{\text{tot}}(r, t_G) = \sigma_0 e^{-r/r_D} \quad (1.39)$$

and an *inside-out formation* for the galactic disc (Larson, 1976), in which the innermost regions are assumed to assemble on much shorter typical time-scales than the outermost ones; hence $\tau_{\text{inf}} = \tau_{\text{inf}}(r)$ in equation (1.37) is a monotonically increasing function of the galactocentric distance r .

By assuming an inside-out formation for spiral galaxies, chemical evolution models can simulate that the galaxy disc continuously grows both in size and in mass, naturally leading also to abundance gradients in the galaxy interstellar medium (see, for example, Matteucci & François 1989; Boissier & Prantzos 1999). We remark on the fact that the present-day abundance gradients in the outermost disc regions can be reproduced only by assuming a threshold in the star formation rate together with the inside-out growth of the galaxy, as shown – for example – by Colavitti et al. (2009).

Radial gas flows

Most of the chemical evolution models in the literature only assume the first four terms in equation (1.21). This means that, in the majority of the works, the galaxy is assumed to be composed of several concentric *shells* (or *annuli* in the case of disc galaxies) which do not interact with each other, with the gas mass (and metals) accreted at a certain radius r remaining there over the whole galaxy lifetime, together with all the gas mass (and metals) returned by dying stars.

The fifth term in equation (1.21) physically represents *radial gas flows*, which mix the metals coming from different galactic zones. The most interesting recent works in the literature including radial gas flows in chemical evolution models are those of Portinari & Chiosi (2000); Schönrich & Binney (2009); Spitoni & Matteucci (2011); Bilitewski & Schönrich (2012); Mott et al. (2013); Pezzulli & Fraternali (2016), which refer to the theoretical framework as presented in the very early work by Lacey & Fall (1985).

From a physical point of view, radial gas flows are thought to establish themselves as a consequence of the different angular momenta between the infalling

material and the disc, in order to re-establish the conservation of the total angular momentum; in fact, it is highly improbable that the infalling material has the same rotational velocity component as the one of the disc at the moment – and point – of the impact. Also large-scale shocks induced by the spiral arms – as they interact with the gas on the disc – may cause dissipation and hence the gas to drift inward (Bertin & Lin, 1996). Although radial gas flows cannot be invoked as the only mechanism responsible for the abundance gradients in the galactic discs, they should be taken into account for a complete physical description of the galaxy chemical evolution.

The quantity $\mathcal{F}_X(r, t)$ in the right-hand side of equation (1.21) physically represents the amount of the chemical element X , which flows per unit time and surface through the shell at the radius r and time t ; it can be expressed as follows:

$$\mathcal{F}_X(r, t) = v_{\text{flow}}(r, t) \frac{\partial \sigma_X(r, t)}{\partial r}, \quad (1.40)$$

where $v_{\text{flow}}(r, t)$ is the velocity of the net radial motion of gas through the galaxy disc. Typical values of the velocities of the radial gas flows are between -1 and -5 km s^{-1} , hence very low and difficult to observe directly.

By imposing the angular momentum conservation, Bilitewski & Schönrich (2012) have been able to relate the accreted gas mass onto the disc, $\delta M_{\text{inf}}(r, t)$, in a short time-step δt and at the radius r , with the net total gas mass radially flowing from (and into) the adjacent rings in the same interval of time and through the same annulus ($\delta M_{\text{rad}}(r, t)$); in particular, they have found the following equation for the k -th annulus:

$$\frac{\delta M_{\text{flow}}(r_k, t)}{\delta M_{\text{inf}}(r_k, t)} = -\frac{2a(4k^3 + 6k^2 + 4k + 1)}{4N(2k + 1)} + \frac{2(1 - b)(3k^2 + 3k + 1)}{3(2k + 1)}, \quad (1.41)$$

where N is the total number of rings, and the parameters a and b follow from the assumption of the following velocity profile for the infalling material:

$$v_{\text{inf}}(r) = V_{\text{circ}} \left(b + a \frac{R}{R_{\text{out}}} \right), \quad (1.42)$$

where V_{circ} and R_{out} are the galaxy circular velocity (at sufficiently large radii) and the outermost galactocentric distance, respectively. All the aforementioned quantities have been shown by Bilitewski & Schönrich (2012) to obey the same equations, which were originally derived by Lacey & Fall (1985) for the radial gas flows in the chemical evolution models; these equations can be summarized as follows:

$$\delta M_{\text{flow}}(r, t) = 2\pi r \sigma_{\text{gas}}(r, t) \times v_{\text{flow}}(r, t) \delta t \quad (1.43)$$

$$v_{\text{flow}}(r, t) = \frac{\delta M_{\text{flow}}}{2\pi r \sigma_{\text{gas}} \delta t} = -\frac{\dot{\sigma}_{\text{inf}}}{\sigma_{\text{gas}}} r \frac{(v_{\text{inf}} - V_{\text{circ}})}{V_{\text{circ}}}. \quad (1.44)$$

We remark on the fact that the inclusion of radial gas flows in the chemical evolution models can modify the normalization criterium for the galaxy gas ac-

cretion history at a given radius r , as expressed by equation (1.38). As pointed out by Pezzulli & Fraternali (2016), it should be the so-called *effective accretion* to constrain the present-day total surface mass density of the galaxy disc, rather than the “pure” accretion, which is not corrected for the gas mass flowing through each given annulus. In particular, by following the work by Pitts & Tayler (1989), Pezzulli & Fraternali (2016) define the “effective accretion” by including both the external contribution from the intergalactic medium (the original accretion term) and the internal contribution from the radial motions due to gas flows, which can modify the evolution of the surface gas mass density at a given radius. This fact has been also acknowledged by Portinari & Chiosi (2000), which claimed that the predicted present-day total surface mass densities with or without radial gas flows do not deviate substantially, because of the very low typical velocities of the gas flows themselves.

The main effect of radial gas flows is to steepen the abundance gradients in the outer parts of the disc of spiral galaxies with respect to the models without radial gas flows, where only the inside-out growth of the galaxy is assumed to produce the gradients. Typical values of the gas flow velocity are of the order of -1 km s^{-1} , hence they are typically directed inwards; this is due to the fact that – on average – there is a deficit in the angular momentum of the infalling material with respect to the galactic disc. The steepest abundance gradients can be obtained by assuming a radial velocity pattern where the modulus of the velocity increases as a function of the galactocentric distance (see also (Mott et al., 2013)).

Stellar migrations

The last term in the right-hand side of equation (1.21) is related to the effect of stellar migrations on the chemical evolution of galaxies. The seminal works on this topic are the ones by Schönrich & Binney (2009); Minchev et al. (2013); Wang & Zhao (2013); Kubryk et al. (2015a,b); Spitoni (2015). Stellar migration can have a significant effect on the evolution and distribution of the chemical elements which are produced by long-lived stellar sources, such as iron – mainly produced by Type Ia Supernovae – carbon, nitrogen, as well as s-process elements, which are mainly synthesized by low- and intermediate-mass stars. The main effect of stellar migration is that stars die and pollute the interstellar medium at a different place with the respect to the one they were born, causing a mixing of the stellar populations born at different radii.

The effect of stellar migration at the galactocentric radius r can be studied by means of the following formula, which computes the death rate of the stellar producers of the chemical element X, by assuming them to possess mass in the range $m_1 \leq m \leq m_2$ and corresponding lifetimes $\tau_2 \leq \tau(m) \leq \tau_1$:

$$\mathcal{M}_X(r, t) = \mathcal{M}_{\text{migr,in}}(r, t) - \mathcal{M}_{\text{migr,out}}(r, t), \quad (1.45)$$

where the first term in the right-hand side of equation (1.45) corresponds to the contribution from outside to the number of stars dying at the radius r and can be

computed as follows:

$$\mathcal{M}_{\text{migr,in}}(r, t) = \int_0^{R_{\text{max}}} dr' \int_{\tau_1}^{\tau_2} d\tau \psi(r', t - \tau) \text{DTD}_*(\tau) \mathcal{P}_{\text{migr}}(r', r, t - \tau); \quad (1.46)$$

the quantity $\mathcal{P}_{\text{migr}}(r_{\text{in}}, r_{\text{fin}}, t_{\text{in}})$ appearing in equation (1.46) is of fundamental importance and it represents the probability for a star born at the time t_{in} of the galaxy evolution to migrate from the initial radius r_{in} to the final radius r_{fin} ; it is given by dynamical models for the galaxy formation and evolution; the function $\mathcal{P}_{\text{migr}}$ is usually asymmetric in the radial dependence, whereas its time-dependence mainly resides within its width parameter, which increases as a function of time (see Wang & Zhao 2013 and references therein). Moreover, the quantity $\text{DTD}_*(r, t)$ in equation (1.46) is the so-called “stellar delay-time distribution”, as defined in equation (1.20).

The second term in the right-hand side of equation (1.45) removes the stars which were born at r and then migrate towards the other galaxy zones; in particular, it can be computed as follows:

$$\mathcal{M}_{\text{migr,out}}(r, t) = \int_0^{R_{\text{max}}} dr' \int_{\tau_1}^{\tau_2} d\tau \psi(r, t - \tau) \text{DTD}_*(\tau) \mathcal{P}_{\text{migr}}(r, r', t - \tau). \quad (1.47)$$

By suitably adjusting the extremes of the integrals in the various equations which define the quantity $\mathcal{M}_X(r, t)$ and assuming the correct Delay Time Distribution, one could also take into account the effect of migration of the Type Ia Supernova progenitor systems. This work has never been done in the context of chemical evolution models and could provide interesting results. In fact, an excess of the radial distribution of the Type Ia Supernova remnants in the outer galaxy zones might be explained as an effect of radial migration of the Type Ia Supernova progenitor systems; this might have an effect on the chemical evolution of iron, since it is the chemical element mostly produced by Type Ia Supernovae.

1.3.2 Numerical methods to solve the equations

In this Section, we briefly summarize the numerical methods which are employed by chemical evolution models to solve equation (1.21).

If we normalize the “physical” gas mass with respect to the present-day total surface mass density, then we can rewrite equation (1.21) for a given radius in the following way:

$$\frac{dG_i(t)}{dt} = -\tilde{\nu}(t) G_i(t) + W_i(t), \quad (1.48)$$

where $G_i(t) = \sigma_i(r, t) / \sigma_{\text{tot}}(r, t_G)$ is the normalized surface gas mass density in the form of the chemical element i . The first term in the right-hand side of equation (1.48) takes into account the amount of mass which is removed per unit time and surface by the star formation activity and galactic winds; in particular, the

parameter $\tilde{\nu}$ is defined as follows:

$$\tilde{\nu} = \frac{\psi(r, t) + \mathcal{O}(r, t)}{G(t)} = (\nu + \omega) G^{k-1}(t), \quad (1.49)$$

where the star formation rate, $\psi(t) \propto \nu G^k(t)$, is expressed in terms of the normalized total surface gas mass density, $G(t) = \sigma_{\text{gas}}(r, t)/\sigma_{\text{tot}}(r, t_G)$, and ν and ω represent the star formation efficiency and mass loading factor, respectively.

The quantity $\tilde{\nu}$, as defined in equation (1.49), include the free parameters of all the physical processes whose intensity is assumed to be directly proportional to the star formation rate; that is the reason why we include in the definition of $\tilde{\nu}$ also the effect of the galactic wind, $\mathcal{O}(r, t)$.

Finally, the second term in the right-hand side of equation (1.48), $W_i(r, t)$, include all the physical processes which are not directly proportional to the star formation rate, including all the integrals defining the returned mass rate from dying stars (see equation 1.23).

Equation (1.48) is an equation of the following form:

$$\frac{dy(t)}{dt} = a(t) y(t) + b(t), \quad (1.50)$$

for which the formal analytical solution is

$$y(t) = y(t_0) \exp\left(\int_{t_0}^t d\xi a(\xi)\right) + \int_{t_0}^t d\xi b(\xi) \exp\left(\int_{\xi}^t d\theta a(\theta)\right), \quad (1.51)$$

where $y(t_0)$ is the initial condition at the time $t = t_0$. By making use of equations (1.48) and (1.51), we can compute the advancement in the solution for the surface gas mass density of the chemical element i , as follows:

$$G_i(t + \delta t) = G_i(t) e^{-\chi(t, t+\delta t)} + \int_t^{t+\delta t} dt' W_i(t') e^{-\chi(t', t+\delta t)}, \quad (1.52)$$

where

$$\chi(t_1, t_2) = \int_{t_1}^{t_2} dt' \tilde{\nu}(t'). \quad (1.53)$$

By assuming that the time step δt is sufficiently small such that the quantities $\tilde{\nu}(t)$ and $W_i(t)$ can be considered as constant (we take their average values at the midpoint of the time step, namely $\bar{\nu}$ and \bar{W}_i), then the equation (1.52) can be rewritten in the following way:

$$G_i(t + \delta t) = G_i(t) e^{-\bar{\nu} \delta t} + \bar{W}_i \frac{1 - e^{-\bar{\nu} \delta t}}{\bar{\nu}}. \quad (1.54)$$

Since both $\bar{\nu}$ and \bar{W}_i crucially depend on the value of $G_i(t + \delta t)$ itself, an iteration procedure is required so as to converge towards the exact solution within a fixed tolerance. Hence we have to solve equation (1.54) with respect to $G_i(t + \delta t)$, namely

we have to find the roots of the following function:

$$f(x) = G_i(t) e^{-\bar{\nu}(x) \delta t} + \bar{W}_i \frac{1 - e^{-\bar{\nu}(x) \delta t}}{\bar{\nu}(x)} - x, \quad (1.55)$$

where $x = G_i(t + \delta t)$. Since $f(x)$ only depends linearly upon \bar{W}_i , the iteration over \bar{W}_i can be neglected; this is also due to the fact that the quantity \bar{W}_i includes the convolution integral of the stellar yields and stellar birthrate function over all the past galaxy star formation history, hence it is less sensitive to the exact value of $G_i(t + \delta t)$. By applying the Newton-Raphson method, the $(j + 1)$ -th correction for the solution can be found as follows:

$$x^{(j+1)} = x^{(j)} - \frac{f(x^{(j)})}{f'(x^{(j)})}; \quad (1.56)$$

with some algebraic passages, one can find:

$$f'(x) = \left[-\delta t G_i(t) e^{-\bar{\nu} \delta t} - \bar{W}_i \frac{1 - e^{-\bar{\nu}(x) \delta t}}{\bar{\nu}^2} + \bar{W}_i \delta t \frac{1 - e^{-\bar{\nu}(x) \delta t}}{\bar{\nu}} \right] \frac{\partial \bar{\nu}}{\partial x} - 1. \quad (1.57)$$

The explicit solution for the $(j + 1)$ -th iteration is the following one:

$$\mathcal{G}_i^{(j+1)} = \mathcal{G}_i^{(j)} (1 + \delta_i^{(j)}), \quad (1.58)$$

where, for sake of simplicity, we assume $\mathcal{G}_i \equiv G_i(t + \delta t)$, and the (j) -th correction, $\delta_i^{(j)}$, can be computed according to the following equations:

$$\begin{cases} \delta_i^{(j)} = \frac{\mathcal{G}_i^{(j)} - A_i}{B_i - \mathcal{G}_i^{(j)}}; \\ A_i = e^{-\bar{\nu} \delta t} \left(G_i(t) - \frac{\bar{W}_i}{\bar{\nu}} \right) + \frac{\bar{W}_i}{\bar{\nu}}; \\ B_i = \frac{1}{2} \frac{\partial \ln \eta}{\partial \ln G} \left[(e^{-\bar{\nu} \delta t} - 1) \frac{\bar{W}_i}{\bar{\nu}} - \bar{\nu} \delta t e^{-\bar{\nu} \delta t} \left(G_i(t) - \frac{\bar{W}_i}{\bar{\nu}} \right) \right]. \end{cases} \quad (1.59)$$

One can easily demonstrate that, in equation (1.59), the quantity $\frac{\partial \ln \eta}{\partial \ln G} = k - 1$, where k represents the power index of the assumed Schmidt-Kennicutt law. The iteration stops when $\delta_i^{(j)} < \delta_{\max}$; we usually assume $\delta_{\max} = 10^{-4}$.

Including radial gas flows in the numerical code

The numerical prescriptions to include radial gas flows in chemical evolution codes can be found in [Portinari & Chiosi \(2000\)](#); [Spitoni & Matteucci \(2011\)](#), where we address the reader for further details.

The variation of the surface gas mass density of the chemical element X at the radius r_j , because of the effect of radial gas flows, can be expressed in the following

way:

$$\left(\frac{d\sigma_X}{dt}\right)_{\text{flow}} = -\frac{1}{\pi\left(r_{j+\frac{1}{2}}^2 - r_{j-\frac{1}{2}}^2\right)} \left[F_X(r_{j+\frac{1}{2}}, t) - F_X(r_{j-\frac{1}{2}}, t)\right], \quad (1.60)$$

where $F(r)$ represents the gas flow at the radius r_j , which can be expressed as

$$F_X(r_j, t) = 2\pi r_j v(r_j, t) \sigma_X(r_j, t). \quad (1.61)$$

The quantity $v(r_j, t)$ in equation (1.61) represents the velocity of the net radial gas motion, which is usually assumed to be negative if directed inward.

Since all the quantities in the numerical code of chemical evolution are normalized with respect to the present-day total mass density (see also equation 1.48), it can be demonstrated with some algebraic passages that equation (1.60) can be rewritten as

$$\left(\frac{dG_X(r_j, t)}{dt}\right)_{\text{flow}} = -\beta_j G_X(r_j, t) + \gamma_j G_X(r_{j+1}, t), \quad (1.62)$$

where

$$\begin{cases} \beta_j = -\frac{2}{r_j + \frac{r_{j+1} + r_{j+1}}{2}} \times \left[v_{j-\frac{1}{2}} \frac{r_{j-1} + r_j}{r_{j+1} - r_{j-1}} \right] \\ \gamma_j = -\frac{2}{r_j + \frac{r_{j+1} + r_{j+1}}{2}} \times \left[v_{j+\frac{1}{2}} \frac{r_j + r_{j+1}}{r_{j+1} - r_{j-1}} \right] \times \frac{\sigma_{\text{tot}}(r_{j+1}, t_G)}{\sigma_{\text{tot}}(r_j, t_G)}. \end{cases} \quad (1.63)$$

In practice, one re-defines the quantitis $\tilde{\nu}$ in equation (1.49) in the following way:

$$\tilde{\nu} = (\nu + \omega) G^{k-1}(r_j, t) + \beta_j, \quad (1.64)$$

while the second term in the right-hand side of equation (1.62), namely the product $\gamma_j G_X(r_{j+1}, t)$, is included in the definition of $W_X(r_j, t)$, which is the second term in the right-hand side of equation (1.48).

References

- Asplund M., Grevesse N., Sauval A. J., Scott P., 2009, ARA&A, 47, 481
 Belfiore F., Maiolino R., Bundy K., et al., 2015, MNRAS, 449, 867
 Bell, E. F., McIntosh, D. H., Katz, N., & Weinberg, M. D. 2003, ApJ, 149, 289
 Bertin, G., Saglia, R. P., & Stiavelli, M. 1992, ApJ, 384, 423
 Bertin, G., & Lin, C. C. 1996, Cambridge, MA MIT Press
 Bilitewski, T., & Schönrich, R. 2012, MNRAS, 426, 2266
 Boissier, S., & Prantzos, N. 1999, MNRAS, 307, 857
 Boissier, S., Prantzos, N., Boselli, A., & Gavazzi, G. 2003, MNRAS, 346, 1215
 Boissier, S., 2013, Springer Science+Business Media Dordrecht
 Bradamante F., Matteucci F., D’Ercole A., 1998, A&A, 337, 338
 Bressan A., Marigo P., Girardi L., et al., 2012, MNRAS, 427, 127
 Chabrier, G., 2003, PASP, 115, 763
 Chen Y., Bressan A., Girardi L., et al., 2015, MNRAS, 452, 1068

- Chiappini, C., Matteucci, F., & Gratton, R. 1997, *ApJ*, 477, 765
- Chiappini C., Ekström S., Meynet G., et al., 2008, *A&A*, 479, L9
- Chieffi, A., & Limongi, M. 2013, *ApJ*, 764, 21
- Ciotti, L., D’Ercole, A., Pellegrini, S., & Renzini, A. 1991, *ApJ*, 376, 380
- Colavitti, E., Cescutti, G., Matteucci, F., & Murante, G. 2009, *A&A*, 496, 429
- Ekström S., Meynet G., Chiappini C., Hirschi R., Maeder A., 2008, *A&A*, 489, 685
- Faber, S. M. 1973, *ApJ*, 179, 731
- Faber, S. M., Friel, E. D., Burstein, D., & Gaskell, C. M. 1985, *ApJ*, 57, 711
- Gazak, J. Z., Kudritzki, R., Evans, C., et al. 2015, *ApJ*, 805, 182
- Greggio, L., & Renzini, A. 1983, *A&A*, 118, 217
- Greggio, L. 2005, *A&A*, 441, 1055
- Hirschi R., Meynet G., Maeder A., 2005, *A&A*, 433, 1013
- Hirschi R., 2007, *A&A*, 461, 571
- Ibarra-Medel, H. J., Sánchez, S. F., Avila-Reese, V., et al. 2016, arXiv:1609.01304
- Iwamoto, K., Brachwitz, F., Nomoto, K., et al. 1999, *ApJ*, 125, 439
- Izotov, Y. I., Stasińska, G., Meynet, G., Guseva, N. G., & Thuan, T. X. 2006, *A&A*, 448, 955
- Karakas, A. I. 2010, *MNRAS*, 403, 1413
- Kennicutt, R. C., Jr. 1989, *ApJ*, 344, 685
- Kennicutt R. C., Jr., 1998, *ApJ*, 498, 541
- Kewley, L. J., & Ellison, S. L. 2008, *ApJ*, 681, 1183-1204
- Kobayashi C., Umeda H., Nomoto K., Tominaga N., Ohkubo T., 2006, *ApJ*, 653, 1145
- Kobayashi C., Karakas A. I., Umeda H., 2011, *MNRAS*, 414, 3231
- Kroupa, P., Tout, C. A., & Gilmore, G. 1993, *MNRAS*, 262, 545
- Kubryk, M., Prantzos, N., & Athanassoula, E. 2015, *A&A*, 580, A126
- Kubryk, M., Prantzos, N., & Athanassoula, E. 2015, *A&A*, 580, A127
- Kudritzki, R. P., Urbaneja, M. A., Bresolin, F., & Przybilla, N. 2008, *Physica Scripta* Volume T, 133, 014039
- Lacey, C. G., & Fall, S. M. 1985, *ApJ*, 290, 154
- Larson, R. B. 1976, *MNRAS*, 176, 31
- Lilly S. J., Carollo C. M., Pipino A., Renzini A., Peng Y., 2013, *ApJ*, 772, 119
- Lu Y., Blanc G. A., Benson A., 2015, *ApJ*, 808, 129
- Maeder A., 1992, *A&A*, 264, 105
- Mannucci, F., Della Valle, M., & Panagia, N. 2006, *MNRAS*, 370, 773
- Marconi G., Matteucci F., Tosi M., 1994, *MNRAS*, 270, 35
- Martin, C. L., & Kennicutt, R. C., Jr. 2001, *ApJ*, 555, 301
- Matteucci, F., & Greggio, L. 1986, *A&A*, 154, 279
- Matteucci, F., & Francois, P. 1989, *MNRAS*, 239, 885
- Matteucci, F. 1994, *A&A*, 288, 57
- Matteucci, F., & Recchi, S. 2001, *A&A*, 558, 351
- Matteucci F., 2001, *Astrophysics and Space Science Library*, Kluwer Academic Publishers
- Matteucci F., 2012, *Astronomy and Astrophysics Library*, Springer-Verlag Berlin Heidelberg
- Maoz, D., Mannucci, F., & Nelemans, G. 2014, *ARA&A*, 52, 107
- Meynet G., Maeder A., 2002, *A&A*, 390, 561
- Minchev, I., Chiappini, C., & Martig, M. 2013, *A&A*, 558, A9
- Mott, A., Spitoni, E., & Matteucci, F. 2013, *MNRAS*, 435, 2918
- Nissen, P. E. 2011, arXiv:1109.4010
- Nomoto K., Tominaga N., Umeda H., Kobayashi C., & Maeda K., 2006, *Nuclear Physics* A, 777, 424

- Nomoto K., Kobayashi C., Tominaga N., 2013, *ARA&A*, 51, 457
- Padovani, P., & Matteucci, F. 1993, *ApJ*, 416, 26
- Pagel, B. E. J., Simonson, E. A., Terlevich, R. J., & Edmunds, M. G. 1992, *MNRAS*, 255, 325
- Pagel, B. E. J. 2009, *Nucleosynthesis and Chemical Evolution of Galaxies*, Cambridge University Press
- Peng Y., Maiolino R., Cochrane R., 2015, *Nature*, 521, 192
- Pezzulli, G., & Fraternali, F. 2016, *MNRAS*, 455, 2308
- Pilyugin L. S., 1993, *A&A*, 277, 42
- Pipino, A., Matteucci, F., Borgani, S., & Biviano, A. 2002, *New Astronomy*, 7, 227
- Pitts, E., & Tayler, R. J. 1989, *MNRAS*, 240, 373
- Portinari, L., & Chiosi, C. 2000, *A&A*, 355, 929
- Recchi S., Matteucci F., D’Ercole A., 2001, *MNRAS*, 322, 800
- Recchi S., Spitoni E., Matteucci F., Lanfranchi G. A., 2008, *A&A*, 489, 555
- Renzini, A., & Voli, M. 1981, *A&A*, 94, 175
- Romano, D., Karakas, A. I., Tosi, M., & Matteucci, F. 2010, *A&A*, 522, A32
- Ruiz-Lapuente, P., & Canal, R. 1998, *ApJL*, 497, L57
- Salpeter E. E., 1955, *ApJ*, 121, 161
- Schaye, J. 2004, *ApJ*, 609, 667
- Schmidt M., 1959, *ApJ*, 129, 243
- Schönrich, R., & Binney, J. 2009, *MNRAS*, 396, 203
- Spitoni, E., & Matteucci, F. 2011, *A&A*, 531, A72
- Spitoni, E. 2015, *MNRAS*, 451, 1090
- Tang J., Bressan A., Rosenfield P., et al., 2014, *MNRAS*, 445, 4287
- Thomas, D., Maraston, C., Schawinski, K., Sarzi, M., & Silk, J. 2010, *MNRAS*, 404, 1775
- Totani, T., Morokuma, T., Oda, T., Doi, M., & Yasuda, N. 2008, *PASJ*, 60, 1327
- Wang, Y., & Zhao, G. 2013, *ApJ*, 769, 4
- Weinberg, D. H., Andrews, B. H., & Freudenburg, J. 2016, *arXiv:1604.07435*
- Wolfe, A. M., Gawiser, E., & Prochaska, J. X. 2005, *ARA&A*, 43, 861
- Woolsey, S. E., & Weaver, T. A. 1995, *ApJ*, 101, 181
- Worthey, G., Faber, S. M., Gonzalez, J. J., & Burstein, D. 1994, *ApJ*, 94, 687
- van den Hoek, L. B., & Groenewegen, M. A. T. 1997, *A&A*, 123
- Ventura, P., Di Criscienzo, M., Carini, R., & D’Antona, F. 2013, *MNRAS*, 431, 3642
- Vincenzo, F., Belfiore, F., Maiolino, R., Matteucci, F., & Ventura, P. 2016, *MNRAS*, 458, 3466
- Vincenzo, F., Matteucci, F., de Boer, T. J. L., Cignoni, M., & Tosi, M. 2016, *MNRAS*, 460, 2238
- Vincenzo, F., Matteucci, F., & Spitoni, E. 2016, *arXiv:1606.08469*
- Zinchenko, I. A., Pilyugin, L. S., Grebel, E. K., Sánchez, S. F., & Vílchez, J. M. 2016, *MNRAS*, 462, 2715

2

Analytical models of chemical evolution

2.1 Introduction

Analytical models of chemical evolution have been widely used in the past by theorists and observers to predict the metallicity evolution of a stellar system in a simplified but, at the same time, highly predictive fashion. In fact, although these models have many intrinsic assumptions (the most famous one is the so-called “instantaneous recycling approximation”; see the discussion below), they provide a very good approximation for the evolution of chemical elements like oxygen, which are restored on short typical time scales from the star formation event. Incidentally, oxygen is also the dominant chemical species among the metals in the galaxy interstellar medium, since it is mainly synthesized by massive stars, with lifetimes $\tau \lesssim 30$ Myr, dying as core-collapse Supernovae.

Beyond the metallicity evolution, analytical models of chemical evolution are able to predict also the evolution of the galaxy stellar and gas mass with time; hence they can draw – in principle – an approximate but complete physical picture for the evolution of the various galaxy mass components. We remind the reader that the galaxy star formation history simply follows from the gas mass evolution, because of the Schmidt-Kennicutt law which is always assumed in the models.

In the literature, in order to solve the set of differential equations for the galaxy gas mass, total mass and metallicity and hence obtain analytical solutions for these quantities, most of the works assume an infall rate of gas which is directly proportional to the star formation rate over the entire galaxy evolution; historically, the first work making this assumption was [Matteucci & Chiosi \(1983\)](#). We remark on the fact that this assumption is not physical and it represents a strong simplification in the models. Nevertheless, by exploring the effect of different prescriptions for the infall term in the equations, the final predicted physical properties of the

galaxy with an infall rate proportional to the galaxy star formation rate have been found not to deviate substantially from the case of a generic “exponential” infall law (Recchi et al., 2008), as assumed in almost all the detailed chemical evolution models.

A remarkable advancement in the assumptions of analytical chemical evolution models is represented by the recent work by Spitoni, Vincenzo & Matteucci (2017), where we find analytical solutions for the galaxy metallicity, star formation history and total mass with an “exponential” infall law. This work represents a step forward for the galaxy chemical evolution models, because any assumed (smooth) infall law can be expressed with good approximation in terms of a finite sum of exponentials, and the solutions for the star formation history associated to the various exponentials simply add up, thanks to the mathematical properties of first order linear differential equations.

In the first two Sections of this Chapter, we summarize the main assumptions and equations at the basis of analytical models of chemical evolution. Then, in the third and fourth Sections, we present our contribution in this field. In particular, **(a)** we have shown in Vincenzo, Matteucci, Belfiore & Maiolino (2016) that the so-called *yield per stellar generation* – which is a fundamental quantity assumed in all analytical models of chemical evolution, often treated as a free parameter, adjusted to reproduce the data – is the outcome of stellar models and depends on the assumed IMF and stellar metallicity; **(b)** we have developed a novel method to follow the chemical evolution of galaxies in a “semi-analytical” fashion, by assuming the *instantaneous recycling approximation* and the Delay Time Distribution formalism for the chemical enrichment by Type Ia Supernovae; by means of our new model, we are able to follow chemical elements which are restored with a certain delay time from the star formation event (see also Section 1.2.5).

2.2 Basic assumptions

The main assumptions of analytical models of chemical evolution are the following (Tinsley, 1980):

- The initial mass function (IMF) is constant in time and space, which means that every galaxy stellar generation hosts stars with mass sampling an universal distribution, whatever is the age, metallicity and birthplace of the stellar generation.
- The gas is well mixed at any time of the galaxy evolution (*instantaneous mixing approximation*).
- Stars with mass $m \geq 1 M_{\odot}$ die instantaneously, as soon as they form (*instantaneous recycling approximation*), while stars with mass $m < 1 M_{\odot}$ have infinite lifetime. This way, the effect of stellar lifetimes in the equations can be neglected and the effect subsumed into a net *return fraction* (R ; see the further discussion).

By making these simplifying assumptions, one can derive analytical formulas for the evolution of the main galaxy physical properties, such as the metallicity Z , star formation rate, gas and stellar mass; the two following quantities appear in the various differential equations:

$$R = \int_{1M_{\odot}}^{\infty} dm (m - M_R) \phi(m), \quad (2.1)$$

which represents the so-called *returned mass fraction*, where $\phi(m)$ is the IMF and M_R the mass of the stellar remnant, and

$$y_Z = \frac{1}{1 - R} \int_{1M_{\odot}}^{\infty} dm m p_Z(m) \phi(m) \quad (2.2)$$

which represents the so-called yield of metals per stellar generation, with $p_Z(m)$ being the fraction of the newly produced and ejected metals by a star of mass m . The values of y_Z and R might depend both on the IMF and metallicity of the stellar generation, as shown by [Vincenzo, Matteucci, Belfiore & Maiolino \(2016\)](#) (see Section 2.5).

Although the instantaneous recycling approximation is strong, it still represents a good approximation for those chemical elements produced and restored by stars with short lifetimes. The best example of such chemical elements is given by oxygen, which is also representative of the global metallicity Z , since it is the most abundant heavy element by mass. On the other hand, the evolution of chemical elements produced by long-lifetime sources cannot be followed by analytical models working with the instantaneous recycling approximation. Examples of such chemical elements are nitrogen and carbon, which are mainly synthesized by low- and intermediate-mass stars, and iron, mainly produced by Type Ia Supernovae. To take into account the stellar lifetimes with a high level of detail, numerical models of chemical evolution should be used (see [Matteucci 2012](#)).

The star formation rate is usually assumed to follow a linear [Schmidt \(1959\)](#) law of the following form:

$$\psi(t) = \nu M_{\text{gas}}(t), \quad (2.3)$$

where here $\psi(t)$ has the units of $M_{\odot} \text{Gyr}^{-1}$, $M_{\text{gas}}(t)$ is the galaxy gas mass at the time t , and ν is the so-called *star formation efficiency*, a free parameter of our model which has the units of Gyr^{-1} . The infall rate is usually assumed to be directly proportional to the galaxy star formation rate, according to the suggestions of the early work by [Matteucci & Chiosi \(1983\)](#); nevertheless, solutions have been found both for a constant infall law, which gives rise to the so-called *bathtub* or *gas regulatory models* ([Bouché et al., 2010](#); [Lilly et al., 2013](#)), and for a (more physical) decaying exponential law with time ([Spitoni, Vincenzo & Matteucci, 2017](#)).

In the models, outflow gas episodes in galaxies are usually taken into account. The outflow rate is always assumed to be directly proportional to the SFR in the galaxy (see [Matteucci 2012](#)):

$$\mathcal{O}(t) \propto \lambda \psi(t), \quad (2.4)$$

with the wind parameter λ being a dimensionless quantity and representing the

so-called *mass loading factor*. In analytical models, the galactic wind is assumed to be active over the whole galaxy lifetime; physically, we can justify it, by considering the outflow as moving the gas from the cold phase of the interstellar medium to the diffuse hot phase.

2.3 Models with the infall rate proportional to the galaxy star formation rate

Analytical chemical evolution models with the infall rate directly proportional to the galaxy star formation rate are still widely used in the literature to interpret the observed metallicity in galaxies. The most recent works are the ones by [Kudritzki et al. \(2015, 2016\)](#), which were able to characterize the chemical evolution of a sample of nearby star forming disc galaxies within a complete simple analytical framework; in particular, they were able to derive from the model the predicted radial profile of the galaxy metallicity, by starting only from the observed radial profile of the $(M_{\text{gas}}/M_{\star})$ ratio in their assumed sample of galaxies. Other recent works are the ones by [Hunt et al. \(2016a,b\)](#), where they assumed an analytical chemical evolution model with the gas mass assembly history being directly proportional to the galaxy star formation history, to interpret the fundamental metallicity relation which their sample of galaxies have been observed to exhibit up to redshift $z = 3.7$.

One of the first works in the literature using this kind of models, with the infall rate proportional to the star formation rate, aimed at characterizing the physical and chemical properties of galaxies in the Local Universe, is given by [Spitoni et al. \(2010\)](#), where the readers can also find a summary of most of the solutions of analytical models of chemical evolution. Finally, in [Spitoni \(2015\)](#), analytical solutions for the metallicity evolution of a stellar system, accreting enriched material from a companion galaxy satellite, are presented for the first time.

In the models with the infall rate proportional to the star formation rate, to simplify the analytical expressions for the solutions, the infall and outflow rates are usually expressed in the following way:

$$\mathcal{I}(t) = \Lambda (1 - R) \psi(t) \quad (\text{infall}); \quad (2.5)$$

$$\mathcal{O}(t) = \lambda (1 - R) \psi(t) \quad (\text{outflow}), \quad (2.6)$$

where Λ and λ are the infall and wind parameters, respectively, and R represents the return mass fraction, as defined in equation (2.1).

The set of differential equations to be solved for the total galaxy gas mass, $M_{\text{gas}}(t)$, metallicity, $Z(t)$, and total mass, $M_{\text{tot}}(t)$, are the following ones:

$$\frac{dM_{\text{gas}}(t)}{dt} = -\psi(t) + \mathcal{R}(t) + \mathcal{I}(t) - \mathcal{O}(t); \quad (2.7)$$

$$\frac{d\left(Z(t) M_{\text{gas}}(t)\right)}{dt} = -Z(t) \psi(t) + \mathcal{R}_Z(t) + Z_{\text{inf}} \mathcal{I}(t) - Z(t) \mathcal{O}(t); \quad (2.8)$$

2.3. Models with the infall rate proportional to the galaxy star formation rate

$$\frac{dM_{\text{tot}}(t)}{dt} = \mathcal{I}(t) - \mathcal{O}(t), \quad (2.9)$$

where $\mathcal{R}(t)$ and $\mathcal{R}_Z(t)$ represent the restitution rates of gas and metals from dying stars, respectively, including both processed and unprocessed material; in particular, these quantities are defined as follows:

$$\mathcal{R}(t) = \int_{m_{\text{low}}(t)}^{\infty} dm (m - M_R) \psi(t - \tau_m) \phi(m); \quad (2.10)$$

$$\mathcal{R}_Z(t) = \int_{m_{\text{low}}(t)}^{\infty} dm \left[(m - M_R) Z(t - \tau_m) + m p_Z(m) \right] \psi(t - \tau_m) \phi(m), \quad (2.11)$$

where $m_{\text{low}}(t)$ is the minimum mass of the star dying at the time t . By means of the instantaneous recycling approximation, equations (2.10) and (2.11) can be simplified as follows:

$$\mathcal{R}(t) = \psi(t) R; \quad (2.12)$$

$$\mathcal{R}_Z(t) = \psi(t) R Z(t) + y_Z (1 - R) \psi(t), \quad (2.13)$$

where R and y_Z are defined by the equations (2.1) and (2.2), respectively.

It can be demonstrated that the general solution for the galaxy metallicity is the following one (Recchi et al., 2008):

$$Z = \frac{\Lambda Z_{\text{inf}} + y_Z}{\Lambda} \left\{ 1 - [(\Lambda - \lambda) - (\Lambda - \lambda - 1)\mu^{-1}]^{\frac{\Lambda}{\Lambda - \lambda - 1}} \right\}, \quad (2.14)$$

where $\mu = M_{\text{gas}}/(M_{\text{gas}} + M_{\star})$ represents the gas mass fraction.

By assuming a linear Schmidt-Kennicutt law, namely $\psi(t) = \nu M_{\text{gas}}(t)$, with ν being the assumed star formation efficiency, the solutions for the total galaxy gas mass and stellar mass are the following ones:

$$M_{\text{gas}}(t) = M_{\text{gas}}(0) \exp \left\{ -\nu (1 - R) [1 - (\Lambda - \lambda)] t \right\} \quad (2.15)$$

$$M_{\star}(t) = M_{\star}(0) + \frac{M_{\text{gas}}(0)}{1 - (\Lambda - \lambda)} \left[1 - \exp \left\{ -\nu (1 - R) [1 - (\Lambda - \lambda)] t \right\} \right]. \quad (2.16)$$

Equations (2.14), (2.15) and (2.16) enable us – in principle – to draw a detailed physical and chemical description for the galaxy evolution. One can predict also abundance gradients, by assuming the gas mass fraction, μ , to vary as a function of the galactocentric distance, according to the observations. As aforementioned, this has been done – for the first time – by Kudritzki et al. (2015), which have been able to obtain very good agreements between models and the observed metallicity gradients in a sample of nearby galaxies.

2.4 Models with the exponential infall law

Most of the detailed numerical codes of chemical evolution assume a decaying exponential infall rate of gas with time over the entire galaxy lifetime, namely:

$$\mathcal{I}(t) = A e^{-t/\tau_{\text{inf}}}, \quad (2.17)$$

where τ_{inf} is the so-called infall time scale, which determines the typical time scale over which the galaxy is assumed to assemble, and A is a constant constrained by the total infall gas mass (M_{inf}) by means of the following equation:

$$\int_0^{t_G} dt A e^{-t/\tau_{\text{inf}}} = M_{\text{inf}} \quad \Rightarrow \quad A = \frac{M_{\text{inf}}}{\tau(1 - e^{-t_G/\tau_{\text{inf}}})}, \quad (2.18)$$

where the quantity M_{inf} represents the so-called *infall mass*, namely the external reservoir of gas, accreted into the galaxy potential well, from which the galaxy is assumed to assemble.

As aforementioned, any smooth complex galaxy gas mass assembly history could be well approximated with a sum of exponentials; for example, by assuming the gas infall histories as inferred by [Faucher-Giguère et al. \(2011\)](#) from the analysis of cosmological hydrodynamical simulations, the galaxy gas mass assembly history of a present-day dark matter halo with mass $M_{\text{DM}} = 10^{12} M_{\odot}$ can be well fitted with a sum of three exponentials, which have similar fitting parameters as the ones assumed in the so-called *three-infall model* for the chemical evolution of the Milky Way, as developed by [Micali et al. \(2013\)](#). Therefore, if we know the analytical solution for the galaxy metallicity, gas mass and stellar mass for a generic model with an exponential infall law, then the solutions for a sum of exponentials can be easily retrieved.

The first work in the literature showing analytical solutions for a decaying exponential infall rate of gas is given by [Spitoni, Vincenzo & Matteucci \(2017\)](#), which aim at characterizing the local population of star-forming and passive galaxies in terms of the free parameters of the model. It can be demonstrated that, by assuming a linear Schmidt-Kennicutt law for the galaxy star formation rate and the following law for the galactic wind:

$$\mathcal{O}(t) = \lambda \psi(t), \quad (2.19)$$

where there is not the extra factor $(1 - R)$ as in equation (2.6) (it is often included as a mathematical trick to simplify the solutions), the galaxy metallicity evolves according to the following equation:

$$\begin{aligned} Z(t) = & \frac{y_Z \nu (1 - R)}{\alpha \tau_{\text{inf}} - 1} \times \\ & \times \frac{M_{\text{gas}}(0) t (\alpha \tau_{\text{inf}} - 1)^2 + A \tau_{\text{inf}} \left[t - \tau_{\text{inf}} (1 + \alpha t) + \tau_{\text{inf}} e^{\alpha t - t/\tau_{\text{inf}}} \right]}{A \tau_{\text{inf}} (e^{\alpha t - t/\tau_{\text{inf}}} - 1) + M_{\text{gas}}(0) (\alpha \tau - 1)}. \end{aligned} \quad (2.20)$$

2.5. Modern yields per stellar generation: the effect of the IMF and metallicity

The evolution of the galaxy gas mass in presence of a decaying exponential infall rate is given by the following equation:

$$M_{\text{gas}}(t) = e^{-\alpha t} \left(\frac{A [e^{-t/\tau_{\text{inf}} + \alpha t} - 1] \tau_{\text{inf}}}{\alpha \tau_{\text{inf}} - 1} + M_{\text{gas}}(0) \right). \quad (2.21)$$

Finally, the run of the galaxy total mass with time is given as follows:

$$M_{\text{tot}}(t) = M_{\text{gas}}(0) \frac{\nu}{\alpha} \left(\lambda e^{-\alpha t} + 1 - R \right) + \frac{\nu}{\alpha} (1 - R) A \tau_{\text{inf}} - A \tau_{\text{inf}} e^{-t/\tau_{\text{inf}}} + \frac{\nu}{\alpha} \frac{\lambda A \tau_{\text{inf}} \left(\tau_{\text{inf}} \alpha e^{-t/\tau_{\text{inf}}} - e^{-\alpha t} \right)}{(\alpha \tau_{\text{inf}} - 1)}. \quad (2.22)$$

The quantity $\alpha = (1 - \lambda + R) \nu \equiv 1/\tau_{\text{eq}}$ in the equations above turns out to be the inverse of the so-called “equilibrium time-scale” of the *bathtub models* (Lilly et al., 2013) or *gas regulatory models* (Bouché et al., 2010), which has been shown by Peng & Maiolino (2014) to be the typical time-scale over which galaxies tend to reach their asymptotic physical and chemical properties under the condition of a constant infall rate of gas. Nevertheless, we remark on the fact that the assumption of a constant infall rate of gas over the entire galaxy lifetime – although motivated by “cosmological” reasons – is unphysical and contrary to the observations in the Local Universe.

It can be demonstrated that the asymptotic equilibrium condition for the models with a decaying exponential infall rate of gas occurs over a “critical” time-scale τ_{c} , which involves the following harmonic mean between the parameter $\tau_{\text{eq}} = 1/\alpha$ and the infall time-scale τ_{inf} :

$$\tau_{\text{c}} = \left(\frac{1}{\tau_{\text{inf}}} - \frac{1}{\tau_{\text{eq}}} \right)^{-1}; \quad (2.23)$$

it turns out that galaxies with larger values of τ_{c} have also larger metallicities, Z_{eq} , when the equilibrium is reached.

The system of equations (2.20), (2.21) and (2.22) can be used also to mimic an inside-out growth of galaxies in the context of analytical models of chemical evolution. In particular, this can be obtained – for example – by assuming that each galaxy annulus is characterized by a typical infall time-scale, which increases as a function of the galactocentric distance. In this way, one can eventually predict also metallicity gradients within the galaxy interstellar medium.

2.5 Modern yields per stellar generation: the effect of the IMF and metallicity

The blooming of extensive spectroscopic surveys of local and distant galaxies have fostered the use of metallicities to constrain the star formation history, feedback

processes (outflows) and gas inflows across the cosmic epoch, by comparing the observations with the expectations of analytical and numerical models of chemical evolution. One key element in such a comparison is the yield per stellar generation, y_Z , i.e. the quantity of metals that a stellar population releases into the interstellar medium, which is often assumed as a fixed fiducial value, or varied as a free parameter to reproduce the observed data, without realizing that it is the outcome of stellar evolutionary models, depending on a variety of factors.

For example, a net yield of oxygen $y_O = 0.015$ is assumed in [Peeples et al. \(2014\)](#), whereas $y_O = 5.7 \times 10^{-3}$ in [Zahid et al. \(2014\)](#) and $y_O = 3.13 \times 10^{-3}$ in [Ho et al. \(2015\)](#); particularly high are the values $y_O = 0.040$ - 0.045 assumed in [De Lucia et al. \(2004\)](#), $y_O = 0.03$ in [Croton et al. \(2006\)](#), and $y_O = 0.04$ in [Bower et al. \(2008\)](#). However, since the net yield is a combination of yields from different stellar masses, it is clear that it must depend on the IMF. This has sometimes been acknowledged (e.g. [Henry et al. 2000](#); [Kobayashi et al. 2011](#); [Ho et al. 2015](#)), but never really taken into consideration when using the net yield in the various models. In particular, several works derive the stellar mass and star formation rate by assuming a given IMF and then adopt a fiducial net yield that is derived from a completely different IMF. Moreover, there is some evidence that the IMF may vary in different classes of galaxies. This implies that different yields per stellar generation should be used. Finally, since the stellar nucleosynthetic yield have a metallicity dependence, it is important to check the effect of metallicity on the integrated net yield.

In the literature, deviations of the observed metallicity from the expected value of y_Z are often used to quantify the effect of outflows or inflows of gas, or even as evidence for biased metallicity calibrations or inaccurate metallicity diagnostics. Nevertheless, if the yield associated with the appropriate IMF is not used, this can produce inconsistent results and large systematic errors; fortunately, the dependence on the metallicity of the yield is reassuringly small.

In [Vincenzo, Matteucci, Belfiore & Maiolino \(2016\)](#), we calculate yields per stellar generation for the most commonly adopted IMFs and investigate their metallicity dependence, by comparing the results for two modern compilations of nucleosynthetic yields ([Romano et al., 2010](#); [Nomoto et al., 2013](#)), which have been thoroughly tested in the past against the best available data for galaxies, although we remark on the fact that each of them is still affected by specific limitations. We mostly focus on the yield of oxygen, which is the element most commonly used as a tracer of the global metallicity, and for which the instantaneous recycling approximation is appropriate. However, we also provide the yield per stellar generation for the total mass of metals, although this should be used with caution, given the enrichment delay of various elements (e.g. iron, nitrogen, carbon, etc...), for which the instantaneous recycling approximation is arguable.

2.5.1 Definitions and assumptions

Yield per stellar generation and return mass fraction

We recall that the *yield per stellar generation* $y_i(Z)$, or *net yield*, is defined as the ratio of the global gas mass in the form of a given chemical element i newly produced and restored into the interstellar medium by a simple stellar population with initial metallicity Z to the amount of mass locked up in low mass stars and stellar remnants (Tinsley, 1980; Maeder, 1992; Matteucci, 2001):

$$y_i(Z) = \frac{1}{1 - R(Z)} \frac{\int_{m_{\text{long-liv}}}^{m_{\text{up}}} m p_i(m, Z) \phi(m) dm}{\int_{0.1 M_{\odot}}^{m_{\text{up}}} m \phi(m) dm}, \quad (2.24)$$

where:

- $p_i(m, Z) = \frac{M_{\text{ej},i}(m, Z)}{m}$ is the *stellar yield*, which is defined such that $m \cdot p_i(m, Z)$ represents the mass in the form of the i -th chemical element newly formed and ejected into the interstellar medium by stars with initial mass m and metallicity Z ;
- $\phi(m)$ is the IMF, namely the mass-spectrum over which the stars of each single stellar generation are distributed at their birth;
- $m_{\text{long-liv}} = 1.0 M_{\odot}$ is the maximum mass of the so-called long-lived stars, which do not pollute the interstellar medium, within the framework of the instantaneous recycling approximation;
- m_{up} is the upper mass cutoff of the initial mass function; in our standard case, we assume $m_{\text{up}} = 100 M_{\odot}$, however in the second part of the article we will also investigate the effect of varying m_{up} .

Finally, we recall that R represents the *return mass fraction*, which is defined as the total mass fraction (including both processed and unprocessed material) returned into the interstellar medium by a stellar generation:

$$R(Z) = \frac{\int_{m_{\text{long-liv}}}^{m_{\text{up}}} (m - M_R(m, Z)) \phi(m) dm}{\int_{0.1 M_{\odot}}^{m_{\text{up}}} m \phi(m) dm}, \quad (2.25)$$

with $M_R(m, Z)$ being the mass of the stellar remnant left by a stars with initial mass m and metallicity Z .

If one changes the quantity $m_{\text{long-liv}}$ in accordance to the age of the galaxy, then one would obtain equations very similar to the ones numerically solved by current models of chemical evolution (see, for example, Matteucci 2012). In principle, the assumption of $m_{\text{long-liv}} = 1.0 M_{\odot}$ provides correct results only for stellar populations which are older than ≈ 7.1 Gyr, which corresponds to the lifetime of an $1 M_{\odot}$ star, according to Padovani & Matteucci (1993), although the lifetimes of low-mass stars can also be influenced by metallicity, particularly at very low Z (Gibson, 1997).

Table 2.1: In this Table, we report the numerical values of $\langle P_{\text{O}} \rangle$, which is defined as the IMF-averaged stellar yield of oxygen in the mass range $M = 10\text{-}40 M_{\odot}$, for different metallicities Z . 'MM02' and 'HMM05' stand for [Meynet & Maeder \(2002\)](#) and [Hirschi et al. \(2005\)](#), respectively, which correspond to the results of the Geneva stellar models also included in [Romano et al. \(2010\)](#). 'NKT13' stands for [Nomoto et al. \(2013\)](#).

Stellar yields	v_{rot} [km s ⁻¹]	Z	$\langle P_{\text{O}} \rangle$	$\langle P_{\text{O}} \rangle$	$\langle P_{\text{O}} \rangle$	$\langle P_{\text{O}} \rangle$
			Salpeter (1955)	Chabrier (2003)	Kroupa et al. (1993)	Kroupa (2001)
MM02	0	4.0×10^{-3}	0.004	0.007	0.002	0.007
	300		0.006	0.010	0.003	0.010
HMM05	0	2.0×10^{-2}	0.006	0.010	0.003	0.010
	300		0.009	0.015	0.005	0.014
NKT13	no	4.0×10^{-3}	0.007	0.011	0.004	0.010
	no		2.0×10^{-2}	0.006	0.009	0.003

Stellar yields and initial mass function

We use a numerical code of chemical evolution to explore the effect of the metallicity and IMF on the yields of oxygen per stellar generation and on the return mass fraction. We provide our results for the following sets of stellar yields:

- the set provided by [Romano et al. \(2010\)](#), which assume the stellar yields of [Karakas \(2010\)](#) for LIM stars, and the He, C, N and O stellar yields of the Geneva stellar models for massive stars ([Meynet & Maeder, 2002](#); [Hirschi et al., 2005](#); [Hirschi, 2007](#); [Ekström et al., 2008](#)); for heavier elements, which are not relevant for this study, [Romano et al. \(2010\)](#) assume the stellar yields of massive stars of [Kobayashi et al. \(2006\)](#);
- the stellar yields of [Nomoto et al. \(2013\)](#), which include the stellar yields of LIM stars of [Karakas \(2010\)](#), and the stellar yields of [Nomoto et al. \(2006\)](#), [Kobayashi et al. \(2006\)](#), [Kobayashi et al. \(2011\)](#), [Tominaga et al. \(unpublished\)](#) for core-collapse supernovae (SNe).

The mass of the stellar remnants have been collected by [Romano et al. \(2010\)](#) from the work of [Kobayashi et al. \(2006\)](#). Nevertheless, according to the [Talbot & Arnett \(1973\)](#) formalism, we compute the return mass fraction with the [Romano et al. \(2010\)](#) stellar yields, by summing the ejecta of all the chemical elements (both the processed and the unprocessed ones) for each stellar mass, and this quantity turns out to be dominated by the H and He contributions.

The [Romano et al. \(2010\)](#) compilation of stellar yields for He, C, N and O include the results of models which take into account the combined effect of mass loss and rotation (see also [Maeder 2009](#) for a detailed discussion), whereas the [Nomoto et al. \(2013\)](#) stellar yields have been computed by models which do include standard mass loss but not the effect of rotation. With standard mass loss, only C and N have been lost before supernova explosions. However, the mass loss driven by rotation turns out to be particularly important at almost solar metallicity and above in depressing the oxygen stellar yields of the most massive stars ($M \gtrsim 30\text{-}40 M_{\odot}$, see also [Fig. 1.6](#)). In fact, mass loss increases with stellar metallicity and

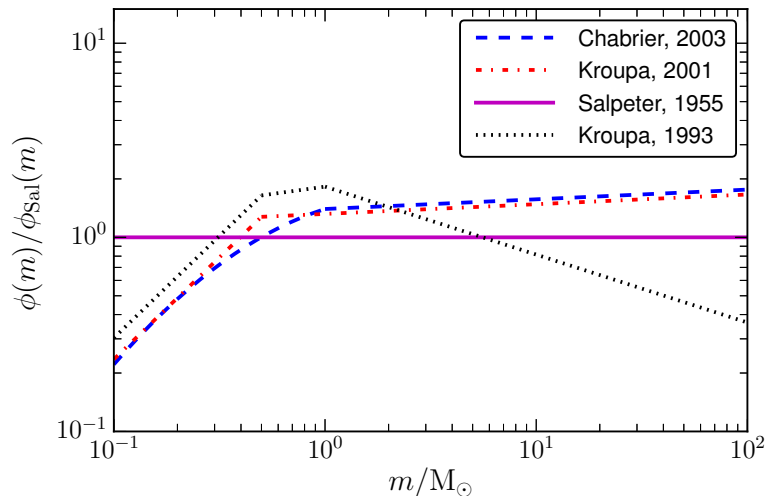


Figure 2.1: In this figure, we show the trend of the different IMFs studied in this work, as normalized with respect to the [Salpeter \(1955\)](#) IMF. The dotted line in black corresponds to the [Kroupa et al. \(1993\)](#) IMF; the dotted-dashed line in red to the [Kroupa \(2001\)](#) IMF; the dashed line in blue to the [Chabrier \(2003\)](#) IMF, and the solid line in purple corresponds to the [Salpeter \(1955\)](#) IMF.

stars of high metal content lose H, He, but also C, through radiatively line driven winds. Therefore, the C production is increased by mass loss whereas the oxygen production is decreased, since part of C which would have been transformed into O, is lost from the star ([Maeder, 1992](#)). Finally, the effect of rotation is to produce mixing and enhances mass loss, with the efficiency of the mixing process being larger at lower metallicities (see also [Chiappini et al. 2008](#), and references therein).

We remark on the fact that [Romano et al. \(2010\)](#) combine results of stellar models assuming only hydrostatic burning and rotation (Geneva group, for He, C, N, and O) with the results of models including explosive burning without rotation (Nomoto group, for heavier elements), giving rise to an inhomogeneous set of stellar yields, which can be physically incorrect. In the context of this study, the treatment of [Romano et al. \(2010\)](#) has a marginal effect, since the metallicity is dominated by the oxygen and carbon contributions. On the other hand, [Nomoto et al. \(2013\)](#) provide one of the most homogeneous set of stellar yields available at the present time, although it is still affected by the limitation of not including the effect of stellar rotation.

In [Figures 1.6 and 1.7](#), we show how the oxygen stellar yields of [Romano et al. \(2010\)](#) and [Nomoto et al. \(2013\)](#), respectively, vary as functions of the initial stellar mass and for different metallicities. The Geneva stellar yields are available only up to $60 M_{\odot}$ and we therefore assume in our standard case that the yields from 60 to $100 M_{\odot}$ are constant. On the other hand, the stellar yields of massive stars of [Kobayashi et al. \(2006\)](#), included in [Romano et al. 2010](#), for the elements heavier than oxygen) and [Nomoto et al. \(2013\)](#) are available only up to $40 M_{\odot}$ and thus we keep them constant for stars with larger initial mass. We remark on the fact that

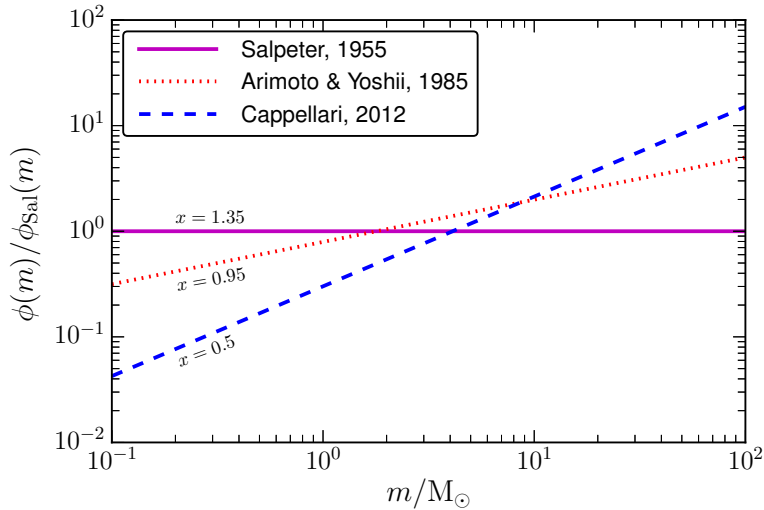


Figure 2.2: In this figure, we compare the Cappellari et al. (2012, blue dashed line) top-heavy IMF with the IMFs of Arimoto & Yoshii (1987, red dotted line) and Salpeter (1955, solid line in magenta). As in Fig. 2.1, all the IMFs are normalized with respect to the Salpeter (1955) IMF.

very massive stars are expected to leave a black hole as a remnant; therefore, a significant fraction of stellar nucleosynthetic products in the ejecta of very massive stars may eventually fall back onto the black hole. This process might cause a reduction of the stellar yields of very massive stars.

At solar metallicity, Romano et al. (2010) include stellar yields which have been computed by applying a stellar rotational velocity $v_{\text{rot}} = 300 \text{ km s}^{-1}$. From an observational point of view, Ramírez-Agudelo et al. (2013) found that almost 80 per cent of nearby stars rotate slower than $v_{\text{rot}} = 300 \text{ km s}^{-1}$, which thus can be considered as an approximate upper limit. To quantify the effect of stellar rotation in the stellar yields of oxygen from massive stars, in Table 7.1 we compare the predictions of models with and without stellar rotation, with the quantity $\langle P_{\text{O}} \rangle$ being defined as the IMF-averaged yield of oxygen in the mass range $M = 10\text{--}40 M_{\odot}$. The effect of stellar rotation in the Geneva stellar models is to increase the average oxygen stellar yield by a factor of ~ 1.5 for stars with initial mass below $40 M_{\odot}$ (see also Hirschi et al. 2005). Furthermore, at $Z = 4.0 \times 10^{-3}$, the IMF-averaged oxygen stellar yield of Nomoto et al. (2013) – which neglect the effect of stellar rotation – is larger than the value of the Geneva stellar models without stellar rotation, but rather similar to the corresponding value with rotation; conversely, at solar metallicity, the Geneva stellar models without rotation agree with Nomoto et al. (2013). IMFs containing a larger number of massive stars, such as the Chabrier (2003) and Kroupa (2001) ones, amplify the oxygen enrichment of the interstellar medium and give rise to larger values of $\langle P_{\text{O}} \rangle$, whatever be the set of stellar yields assumed.

In Vincenzo, Matteucci, Belfiore & Maiolino (2016), we study the effect of different initial mass functions: the Salpeter (1955), the Kroupa et al. (1993), the

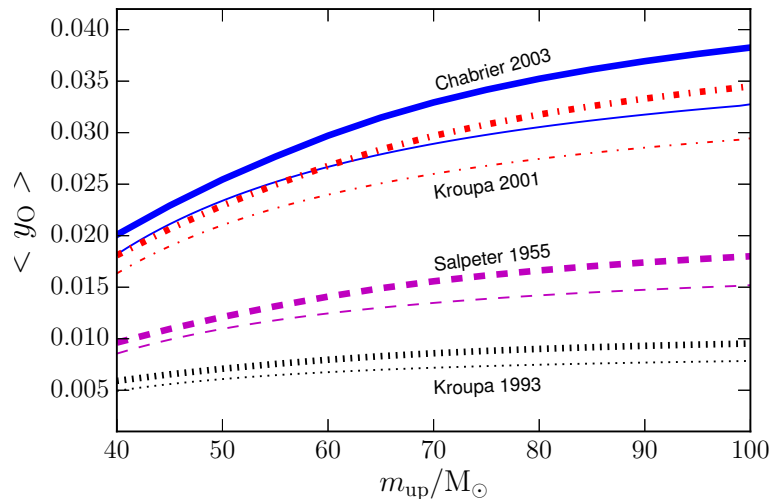


Figure 2.3: In this figure, we show how $\langle y_O \rangle$ is predicted to vary as a function of m_{up} , which is defined as the upper mass cutoff of the IMF. We have computed $\langle y_O \rangle$, by averaging the net yield of oxygen over the metallicity range $1.0 \times 10^{-3} \leq Z \leq 2.0 \times 10^{-2}$, within which y_O turns out to be nearly constant. Thick lines represent our results for the Romano et al. (2010) stellar yields, while thin lines represent the Nomoto et al. (2013) stellar yields. The various curves with different colours correspond to the same IMFs as in Fig. 2.1.

Kroupa (2001), and the Chabrier (2003) ones, which are shown in Fig. 2.1 as normalized with respect to the Salpeter (1955) IMF. We have chosen these IMFs since they have been the most widely used by various authors. Moreover, these IMFs give quite different weights to different stellar mass ranges, hence they will more clearly display differences in the final predicted net yields and return mass fractions. As one can notice from Fig. 2.1, the Kroupa et al. (1993) IMF predicts the largest fraction of intermediate mass stars, while having the lowest number of massive stars. On the other hand, the Chabrier (2003) and the Kroupa (2001) IMFs predict a higher number of both intermediate-mass stars and massive stars than the Salpeter (1955) one.

Finally, we also explore the effect of the top-heavy IMFs of Cappellari et al. (2012) and Arimoto & Yoshii (1987), which are shown in Fig. 2.2, as normalized with respect to the one by Salpeter (1955). These IMFs are defined as a single-slope power law: $\phi(m) \propto m^{-(1+x)}$, with the Cappellari et al. (2012) one having a slope $x = 0.5$ and the one by Arimoto & Yoshii (1987) assuming $x = 0.95$.

2.5.2 Results

In this Section, we present how the net nucleosynthetic yields of oxygen and metals and the return fractions vary when considering different IMFs and as functions of the stellar metallicity. We focus on the yield of oxygen, since it is the element most commonly measured and taken as representative of the bulk of the metallicity, and also because it is an element for which the instantaneous recycling approximation

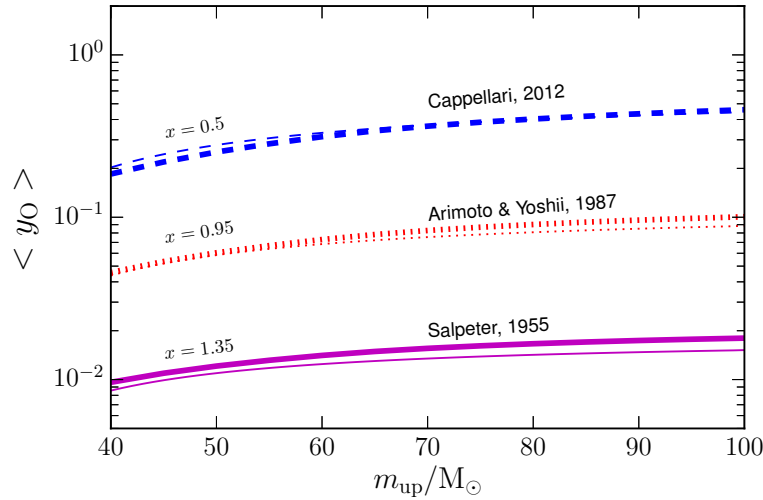


Figure 2.4: In this figure, we report how the average net yield of oxygen, $\langle y_O \rangle$, varies as a function of the upper cutoff of the IMF, when assuming the top-heavy IMF of Cappellari et al. (2012, blue dashed line) and the IMFs of Arimoto & Yoshii (1987, red dotted line) and Salpeter (1955, solid line in magenta). As in Fig. 2.3, $\langle y_O \rangle$ is computed by averaging y_O over the metallicity range $1.0 \times 10^{-3} \leq Z \leq 2.0 \times 10^{-2}$, and the various curves with different thickness correspond to the same stellar yields as in Fig. 2.3.

is appropriate. However, we provide a value also for the yield of the total mass of metals, although with some cautionary warnings.

In Table 2.2, we show how the net yield of oxygen per stellar generation varies as a function of the IMF and metallicity. In our “fiducial” case, reported in Table 2.2, we assume $m_{\text{up}} = 100 M_{\odot}$. Concerning the dependence on metallicity, the most interesting result is that the yield y_O is roughly constant down to very low metallicities. This result implies that the assumption of a time-independent net oxygen yield, as generally treated in analytical models, is a reasonable one. Interestingly, we find an enhancement of y_O for metal-free stellar populations (case with $Z = 1.0 \times 10^{-10}$ from Ekström et al. 2008). In fact, it is well established that, at very low Z , the mixing induced by rotation is particularly efficient (Chiappini et al., 2008); in this way, the nucleosynthetic products of the 3α reaction in the inner He-burning zone can diffuse to the outer stellar zones, so that radiative winds and mass loss (boosted by the high surface enrichment in heavy elements) are highly enriched with the CNO elements; this cannot be obtained by models of metal-free non-rotating massive stars (see, for example, Maeder 2009, for a detailed discussion).

We find that y_O is strongly dependent on the assumed IMF. The highest oxygen yield is obtained when adopting the IMF by Chabrier (2003), because it contains the largest number of massive stars compared to the other IMFs explored in this work (see Fig. 2.1). The IMF of Kroupa et al. (1993), instead, predicts the lowest y_O , since it contains the lowest fraction of high mass stars. In this context, it is important to distinguish the two IMFs suggested by Kroupa. In fact the Kroupa

2.5. Modern yields per stellar generation: the effect of the IMF and metallicity

Table 2.2: In this Table, we report the numerical values which we predict for the return mass fraction (R) and the yields of oxygen and metals per stellar generation (y_{O} and y_{Z} , respectively) as functions of the metallicity Z and for different initial mass functions. These values have been computed by assuming that the upper mass cutoff of the IMF $m_{\text{up}} = 100 M_{\odot}$. The stellar yields are the ones of [Romano et al. \(2010\)](#).

Z	Stellar yields: Romano et al. (2010)											
	R	y_{O}	y_{Z}	R	y_{O}	y_{Z}	R	y_{O}	y_{Z}	R	y_{O}	y_{Z}
	IMF: Salpeter (1955)			IMF: Chabrier (2003)			IMF: Kroupa et al. (1993)			IMF: Kroupa (2001)		
1.0×10^{-10}	0.285	0.028	0.042	0.436	0.059	0.088	0.284	0.015	0.026	0.411	0.053	0.079
1.0×10^{-5}	0.285	0.018	0.028	0.436	0.039	0.059	0.284	0.009	0.017	0.411	0.035	0.053
5.0×10^{-5}	0.285	0.018	0.028	0.436	0.039	0.059	0.284	0.009	0.017	0.411	0.035	0.053
1.0×10^{-4}	0.285	0.018	0.029	0.436	0.039	0.060	0.284	0.009	0.018	0.411	0.035	0.054
5.0×10^{-4}	0.286	0.018	0.029	0.437	0.039	0.060	0.285	0.009	0.018	0.412	0.035	0.054
1.0×10^{-3}	0.286	0.018	0.029	0.438	0.039	0.060	0.287	0.009	0.017	0.414	0.035	0.054
5.0×10^{-3}	0.292	0.018	0.027	0.447	0.038	0.057	0.295	0.009	0.016	0.422	0.034	0.051
1.0×10^{-2}	0.295	0.018	0.028	0.451	0.038	0.060	0.299	0.010	0.017	0.425	0.034	0.054
2.0×10^{-2}	0.298	0.018	0.031	0.455	0.037	0.065	0.302	0.010	0.018	0.430	0.034	0.059

(2001) is very similar to the [Chabrier \(2003\)](#) IMF and predicts a substantially higher yield than [Kroupa et al. \(1993\)](#). The [Salpeter \(1955\)](#) IMF predicts a net yield roughly halfway between the [Chabrier \(2003\)](#) and [Kroupa et al. \(1993\)](#) ones.

In Table 2.2, we show also how y_{Z} (where Z here is the sum of all metals) is predicted to vary as a function of different IMFs and metallicity. These values are shown here only for reference with previous works attempting to model the total metal content of galaxies, however we caution the reader against a blind application of analytical models assuming the instantaneous recycling approximation to the total metal content. Finally, in the same Table, we report the values of the returned fraction R , which is rather constant as a function of metallicity but shows some change for different initial mass functions. The approximate constancy of R as a function of the metallicity is due to the fact that this quantity is strongly dominated by the H and He contributions.

Our results for $y_{\text{O}}(Z)$, $y_{\text{Z}}(Z)$ and $R(Z)$, as obtained with the [Nomoto et al. \(2013\)](#) set of stellar yields, are reported in Table 2.3. On the one hand, the effect of the various IMFs is the same as discussed above for the stellar yields of [Romano et al. \(2010\)](#), see Table 2.2). On the other hand, by comparing the predicted net yields of metals and oxygen of [Romano et al. \(2010\)](#) with the ones of [Nomoto et al. \(2013\)](#), we can quantify the uncertainty introduced by different input stellar yields by a factor which is ~ 1.5 .

In Fig. 2.3, we explore how the choice of the upper cutoff of the IMF, m_{up} , affects the average net yield of oxygen, where $\langle y_{\text{O}} \rangle$ stands for the net yield of oxygen as averaged in the metallicity range $1.0 \times 10^{-3} \leq Z \leq 2.0 \times 10^{-2}$. Our results are shown for different IMFs (different colors) and different stellar yield compilations (thick and thin lines represent our results with [Romano et al. 2010](#) and [Nomoto et al. 2013](#), respectively). By looking at the figure, we see that the difference between the case with $m_{\text{up}} = 100 M_{\odot}$ and $m_{\text{up}} = 40 M_{\odot}$ is as much as a factor of about two. The difference is only ~ 50 per cent between $m_{\text{up}} = 100 M_{\odot}$ and $m_{\text{up}} = 60 M_{\odot}$. We find that, when assuming the [Chabrier \(2003\)](#) and [Kroupa et al. \(1993\)](#) IMFs, the

Table 2.3: In this Table, we report the numerical values which we predict for the return mass fraction (R) and the yields of oxygen and metals per stellar generation (y_{O} and y_{Z} , respectively) as functions of the metallicity Z and for different initial mass functions. These values have been computed by assuming that the upper mass cutoff of the IMF $m_{\text{up}} = 100 M_{\odot}$. The stellar yields are the ones of [Nomoto et al. \(2013\)](#).

Z	Stellar yields: Nomoto et al. (2013)											
	R	y_{O}	y_{Z}	R	y_{O}	y_{Z}	R	y_{O}	y_{Z}	R	y_{O}	y_{Z}
	IMF: Salpeter (1955)			IMF: Chabrier (2003)			IMF: Kroupa et al. (1993)			IMF: Kroupa (2001)		
0.0	0.261	0.021	0.043	0.403	0.044	0.087	0.244	0.011	0.024	0.380	0.040	0.079
1.0×10^{-3}	0.293	0.018	0.026	0.450	0.038	0.055	0.291	0.009	0.014	0.424	0.034	0.050
5.0×10^{-3}	0.300	0.016	0.025	0.459	0.034	0.052	0.300	0.008	0.013	0.433	0.030	0.047
1.0×10^{-2}	0.302	0.015	0.024	0.463	0.032	0.051	0.303	0.008	0.013	0.436	0.029	0.046
2.0×10^{-2}	0.305	0.014	0.023	0.466	0.030	0.049	0.307	0.007	0.012	0.439	0.027	0.044
5.0×10^{-2}	0.304	0.017	0.023	0.466	0.036	0.049	0.307	0.009	0.012	0.439	0.032	0.044

differences in $\langle y_{\text{O}} \rangle$ with different upper mass limits are almost doubled and halved, respectively, with respect to the case with the [Salpeter \(1955\)](#). Fig. 2.3 shows that the global variation of $\langle y_{\text{O}} \rangle$ spanned by all “classical” IMFs and the possible range of m_{up} is nearly a factor of ten.

By looking at Fig. 2.3, the curves corresponding to the [Romano et al. \(2010\)](#) stellar yields lie always above the curves with the [Nomoto et al. \(2013\)](#) stellar yields. This difference enlarges as m_{up} increases, because [Romano et al. \(2010\)](#) provide the oxygen stellar yields up to $60 M_{\odot}$, while [Nomoto et al. \(2013\)](#) only up to $40 M_{\odot}$ (see also Fig. 1.6), and we keep these stellar yields constant for stars with larger initial stellar mass. The latter assumption can introduce a systematic effect in the final values of y_{O} . We find that, by varying the upper limit of the integral at the numerator of equation 2.24 and by normalizing the IMF up to $m_{\text{up}} = 100 M_{\odot}$, the trend of the resulting $\langle y_{\text{O}} \rangle$ is similar to the trend of $\langle y_{\text{O}} \rangle$ as a function of the upper cutoff of the IMF (see Fig. 2.3).

Assuming a top-heavy IMF can cause an even larger increase of the yield of oxygen per stellar generation, being larger the number of massive stars which are present. We explore the effect of two top-heavy IMFs ([Cappellari et al., 2012](#); [Arimoto & Yoshii, 1987](#)), both defined as a single-slope power law. Our results for the $\langle y_{\text{O}} \rangle$ vs. m_{up} relations are shown in Fig. 2.4 for different IMFs and stellar yield assumptions. By looking at Fig. 2.4, as the slope is decreased from $x = 1.35$ ([Salpeter, 1955](#)) down to $x = 0.95$ ([Arimoto & Yoshii, 1987](#)) and $x = 0.5$ ([Cappellari et al., 2012](#)), the IMF becomes top-heavier and the value of y_{O} becomes larger and larger; furthermore, the standard deviation of $\langle y_{\text{O}} \rangle$ becomes larger as the slope x is decreased, indicating that $\langle y_{\text{O}} \rangle$ is slightly more influenced by the metallicity-dependence of the assumed set of stellar yields.

The predicted values of y_{O} for single-slope top-heavy IMF are very high and they may either imply that a “top-heavy” star formation mode has only lasted for a short interval of the galaxy lifetime and not relevant for the integrated metal production, or that a single power-law is not a proper representation of the “top-heavy initial mass function” and that a broken power-law is a more proper description.

There is increasing evidence in the literature that the IMF may vary among

2.6. Including the delayed production of iron by Type Ia Supernovae within analytical models: a novel method

different types of stellar systems, such as spheroids and disk galaxies, as well as faint dwarf galaxies (e.g. see Cappellari et al. 2012; Conroy & van Dokkum 2012; Weidner et al. 2013). Observationally, a Kroupa et al. (1993) IMF is favoured in describing the chemical evolution of the solar vicinity (see Romano et al. 2010), and the disk of spirals similar to the Milky Way, while the Kroupa (2001) and Chabrier (2003) IMFs are probably better for describing the evolution of spheroids such as bulges and ellipticals (see, for example, Chabrier et al. 2014). We have shown that the range of commonly adopted IMFs (even neglecting the extreme top-heavy ones) implies a large variation of net yield per stellar generation. This fact could add an extra systematic to studies attempting to model the observed abundances, which should be taken into account by properly using our compilation of yield for the different classes of galaxies. More specifically, if the IMF is not universal, we can expect a difference in net yield up to a factor larger than three for classical, widely-used IMFs, and even much larger for the top-heavy ones.

2.6 Including the delayed production of iron by Type Ia Supernovae within analytical models: a novel method

Analytical models of chemical evolution do not take into account the fact that the majority of the chemical elements in the ISM usually have more than one nucleosynthesis channel; to complicate further this scenario, each nucleosynthesis channel is also characterized by a distinctive distribution of typical time scales for the chemical enrichment, which differs from the other.

In this Section, we describe a novel method which we have developed for solving the problem of coupling different nucleosynthesis channels in analytical chemical evolution models; in particular, in Vincenzo, Matteucci & Spitoni (2016), we show how the nucleosynthetic products from core-collapse SNe can be coupled with the one by Type Ia SNe in a simplified but – at the same time – effective theoretical picture. We think that this method can be useful both for observers and theorists who wish to decouple the evolution of chemical elements like oxygen and iron, which do not trace each other and both are usually used as tracers of the galaxy metallicity.

Our new theoretical method assumes an instantaneous recycling approximation for chemical elements restored by massive stars and the Delay Time Distribution formalism for the delayed chemical enrichment by Type Ia Supernovae. The galaxy gas mass assembly history, together with the assumed stellar yields and initial mass function, represent the starting point of this method. Then, we derive a very simple and general equation which closely relates the Laplace transforms of the galaxy gas accretion and star formation history, which can be used to simplify the problem of retrieving these quantities in most of current galaxy evolution models. We find that – once the galaxy star formation history has been reconstructed from our assumptions – the differential equation for the evolution of the chemical element X can be suitably solved with classical methods.

In particular, we solve the following approximate differential equation for the evolution of the surface gas mass density of a generic chemical element X within the galaxy ISM, $\sigma_X(r, t)$:

$$\frac{d\sigma_X(r, t)}{dt} = -X(r, t) \psi(r, t) + \hat{\mathcal{E}}_X(r, t) + \hat{\mathcal{O}}_X(r, t) + \hat{\mathcal{R}}_{X,\text{Ia}}(r, t) \quad (2.26)$$

where we assume that the infall gas is of primordial chemical composition. The physical meaning of the various terms in the right-hand side of equation (2.26) can be summarized as follows.

- The first term represents the surface gas mass density of X which is removed per unit time and surface from the galaxy ISM because of the star formation activity. The quantity $X(r, t) = \sigma_X(r, t)/\sigma_{\text{gas}}(r, t)$ is the abundance by mass of the chemical element X .
- The second term, $\hat{\mathcal{E}}_X(r, t)$, takes into account both the stellar contributions to the enrichment of the newly formed chemical element X and the unprocessed quantity of X , returned per unit time and surface by dying stars without undergoing any nuclear processing in the stellar interiors. By assuming IRA, one can easily demonstrate that this term can be approximated as follows (Maeder, 1992):

$$\hat{\mathcal{E}}_X(r, t) = X(r, t) \psi(r, t) R + \langle y_X \rangle (1 - R) \psi(r, t), \quad (2.27)$$

where the quantity R represents the so-called “return mass fraction”, namely the total mass of gas returned into the ISM by a SSP, per unit mass of the SSP (see also Calura et al. 2014 for a more accurate approximation to compute the gas mass returned by multiple stellar populations), and $\langle y_X \rangle$ is the net yield of X per stellar generation (Tinsley, 1980).

- The third term in equation (2.26) removes the quantity of the chemical element X which is expelled out of the galaxy potential well because of galactic winds. We assume the galactic wind to be always active over the whole galaxy lifetime and its intensity is directly proportional to the galaxy SFR, namely

$$\hat{\mathcal{O}}_X(r, t) = \omega \psi(r, t), \quad (2.28)$$

with ω being the so-called “mass loading factor”, a free parameter in the models. We can also think at the galactic wind as a continuous feedback effect of the SFR, which warms up the galaxy ISM; as a consequence of this, the gas is removed from the cold phase of the ISM and hence it is not immediately available for further reprocessing by star formation.

- The fourth term represents the amount of X restored per unit time and surface by Type Ia SNe, where $\langle m_{X,\text{Ia}} \rangle$ is the average amount of X synthesized by each single Type Ia SN event. In particular,

$$\hat{\mathcal{R}}_{X,\text{Ia}}(r, t) = \langle m_{X,\text{Ia}} \rangle R_{\text{Ia}}(r, t), \quad (2.29)$$

2.6. Including the delayed production of iron by Type Ia Supernovae within analytical models: a novel method

with $R_{\text{Ia}}(r, t)$ being the Type Ia SN rate, as defined in equation (1.15).

In summary, by specifying all the various terms, we can rewrite equation (2.26) as follows:

$$\begin{aligned} \frac{d\sigma_X(r, t)}{dt} = & -\sigma_X(r, t) \frac{\psi(r, t)}{\sigma_{\text{gas}}(r, t)} (1 + \omega - R) + \\ & + \langle y_X \rangle (1 - R) \psi(r, t) + \langle m_{X, \text{Ia}} \rangle R_{\text{Ia}}(r, t). \end{aligned} \quad (2.30)$$

We remark on the fact that equation (2.30) can be numerically solved with classical methods (e.g., with the Runge-Kutta algorithm), once the star formation history (SFH) of the galaxy has been previously determined, either observationally or theoretically; in Section 2.6.1, we show how we derive this information. In this work, we solve equation (2.30) for oxygen, silicon and iron, by assuming $\langle y_{\text{O}} \rangle = 1.022 \times 10^{-2}$, $\langle y_{\text{Si}} \rangle = 8.5 \times 10^{-4}$, $\langle y_{\text{Fe}} \rangle = 5.6 \times 10^{-4}$ and $R = 0.285$, which can be obtained by assuming the Kroupa et al. (1993) IMF (see also Vincenzo, Matteucci, Belfiore & Maiolino 2016). We adopt the so-called 3/8-rule forth-order Runge-Kutta method to solve equation (2.30). Finally, we assume the stellar yields of Type Ia SNe from Iwamoto et al. (1999).

2.6.1 The galaxy star formation history

We test the effect of two distinct phenomenological laws for the star formation rate: i) a linear Schmidt-Kennicutt law, as assumed in the majority of analytical and numerical codes of chemical evolution, and ii) a nonlinear Schmidt-Kennicutt law. In the first case, the differential equation for the evolution of the galaxy surface gas mass density is linear and it can be easily solved with the Laplace transform method, for any assumed smooth gas mass assembly history, acting in the equation as a source term. In the second case, since the differential equation is nonlinear in the unknown, a numerical technique is adopted to solve the problem of retrieving the galaxy star formation history.

Linear Schmidt-Kennicutt law for the galaxy SFR

In the case of a linear Schmidt-Kennicutt law, the galaxy SFR is assumed to be directly proportional to the galaxy gas mass density, namely

$$\psi(r, t) = \nu_{\text{L}} \sigma_{\text{gas}}(r, t), \quad (2.31)$$

where ν_{L} is the so-called ‘‘star formation efficiency’’, a free parameter in the models, having the units of Gyr^{-1} . The galaxy SFH, namely the evolution of the galaxy SFR with time and radius, can be theoretically recovered under IRA, by solving the following approximate differential equation for the evolution of the galaxy surface gas mass density:

$$\frac{d\sigma_{\text{gas}}(r, t)}{dt} = -\psi(r, t) (1 + \omega - R) + \hat{\mathcal{I}}(r, t). \quad (2.32)$$

The last term in equation (2.32) corresponds to the assumed galaxy gas mass assembly history, namely $\hat{\mathcal{I}}(r, t) = (d\sigma_{\text{gas}}/dt)_{\text{inf}}$. Most of the chemical evolution models in the literature customarily assume a decaying exponential infall rate of gas with time. Historically, the first work in the literature suggesting such an infall law is the one by [Chiosi \(1980\)](#). Nevertheless, equation (2.32) can be numerically solved for any assumed galaxy gas accretion history with standard techniques (e.g., a Runge-Kutta algorithm).

If we compute the Laplace transform of equation (2.32), it is straightforward to verify that the following equation can be obtained:

$$\mathcal{L}(\hat{\mathcal{I}}(r, t))(s) = \frac{s + \alpha}{\nu_{\text{L}}} \mathcal{L}(\psi(r, t))(s) - \sigma_{\text{gas}}(r, 0), \quad (2.33)$$

where s is the frequency, with the units of Gyr^{-1} , and $\alpha = (1 + \omega - R)\nu$. Equation (2.33) is very general and closely relates the Laplace transform of the galaxy gas accretion history, $\mathcal{L}(\hat{\mathcal{I}}(r, t))(s)$, with the Laplace transform of the galaxy SFH, $\mathcal{L}(\psi(r, t))(s)$, provided the SFR follows a linear Schmidt-Kennicutt law. Equation (2.33) can be used both to retrieve the galaxy SFH from the assumed gas infall law and to solve the corresponding inverse problem, namely to reconstruct the galaxy gas mass assembly history from the observed SFH (one can assume a fitting function for the galaxy SFH to insert in equation 2.33).

By assuming in equation (2.33) the following law for the galaxy gas mass assembly history:

$$\hat{\mathcal{I}}(r, t) = \sum_j \hat{\mathcal{I}}_j(r, t) = \sum_j A_j(r) e^{-(t-t_j)/\tau_j} \Theta(t - t_j), \quad (2.34)$$

which corresponds to a summation of separated gas accretion episodes, each obeying a decaying exponential law with time scale τ_j and starting at the time t_j , then it is straightforward to verify that the solution for the galaxy SFH is the following:

$$\begin{aligned} \psi(r, t) = \sum_j \frac{\nu_{\text{L}} A_j(r)}{\alpha - \frac{1}{\tau_j}} \Theta(t - t_j) \left[e^{-(t-t_j)/\tau_j} - e^{-\alpha(t-t_j)} \right] + \\ + \nu_{\text{L}} \sigma_{\text{gas}}(r, 0) e^{-\alpha t} \Theta(t). \end{aligned} \quad (2.35)$$

We remind the reader that the function $\Theta(t)$ in the equations above is defined as the Heaviside step function. Finally, the parameter $A_j(r)$ is a normalization constant, which fixes the total gas mass accreted by the j th accretion episode.

For the sake of simplicity, in this work we assume the galaxy gas accretion history, as defined in equation (2.34), to be composed of a single episode, starting at $t = 0$. It can be shown that the functional form for galaxy SFH has the same expression as given in [Spitoni, Vincenzo & Matteucci \(2017\)](#).

It is worth remarking that a linear relation is inferred in galaxies only between the galaxy SFR and the molecular hydrogen surface mass density, σ_{H_2} ([Bigiel et al., 2008, 2011](#); [Schruba et al., 2011](#)), although the systematic uncertainties in this kind of studies might be still very large to draw firm conclusions. Nevertheless, [Kennicutt \(1998\)](#) noticed that the relation between the inferred SFR and the gas

2.6. Including the delayed production of iron by Type Ia Supernovae within analytical models: a novel method

mass density, $\sigma_{\text{gas}}(r, t)$, can be well fit with a linear law, such as equation (2.31), when the star formation efficiency is defined as the inverse of the typical dynamical time scale of the system, following the results of a previous theoretical study by Silk (1997).

Nonlinear Schmidt-Kennicutt law for the galaxy SFR

In this work, we also test the effect of assuming a nonlinear Schmidt-Kennicutt law for the evolution of the galaxy SFR, which has the following form:

$$\psi(r, t) = \text{SFR}_0 \left(\frac{\sigma_{\text{gas}}(r, t)}{\sigma_0} \right)^k, \quad (2.36)$$

where – following Kennicutt (1998) – we assume $\sigma_0 = \text{M}_\odot \text{pc}^{-2}$ and $k = 1.4$; finally, the quantity SFR_0 in equation (2.36) has the units of a star formation rate, namely $\text{M}_\odot \text{pc}^{-2} \text{Gyr}^{-1}$ (see also the discussion below). In our work, we treat the quantity SFR_0 as a free parameter, to reproduce the MW chemical abundance patterns.

In the case of a nonlinear Schmidt-Kennicutt law, the *global* star formation efficiency varies with time, according to the following equation:

$$\text{SFE}(r, t) = \frac{\psi(r, t)}{\sigma_{\text{gas}}(r, t)} = \frac{\text{SFR}_0}{\sigma_0} \left(\frac{\sigma_{\text{gas}}(r, t)}{\text{M}_\odot \text{pc}^{-2}} \right)^{k-1}. \quad (2.37)$$

We remark on the fact that, in the original work by Kennicutt (1998), $\text{SFR}_0 \approx 2.5 \times 10^{-1} \text{M}_\odot \text{pc}^{-2} \text{Gyr}^{-1}$, which represents an average quantity, derived by fitting the observed relation between the SFR and σ_{gas} in a sample of nearby star forming disc galaxies, which exhibit a large spread in the SFR- σ_{gas} diagram.

In the physical picture drawn by equation (2.36), we can argue that – as a consequence of a prolonged and continuous star formation activity, which warms up the galaxy ISM through stellar winds and Type II SNe – the galactic disc likely respond by regulating its dimensions (and hence its global thermodynamical quantities) to saturate towards a level of star formation, which is driven by the quantity SFR_0 . In summary, the slope and power law index in equation (2.36) might represent “*truly basic physical constants*”, as pointed out by Talbot & Arnett (1975) almost 40 years ago about the SFR law in the galaxy formation and evolution models.

We are aware that our considerations above are heuristic; in particular, there should be an underlying physical mechanism, common to almost all actively star forming stellar systems, which is not explained by our simple phenomenological recipes for star formation. A detailed physical theory must be developed, involving – for example – physical quantities in a statistical mechanics framework. In particular, one should be able to relate the astronomical quantity “star formation rate” with much more physical quantities, in order to gain a deeper knowledge about how a small scale phenomenon like the star formation can be regulated by large scale processes, and viceversa. An interesting attempt to develop a theory for the star formation activity in galaxies can be found in the work by Silk (1997).

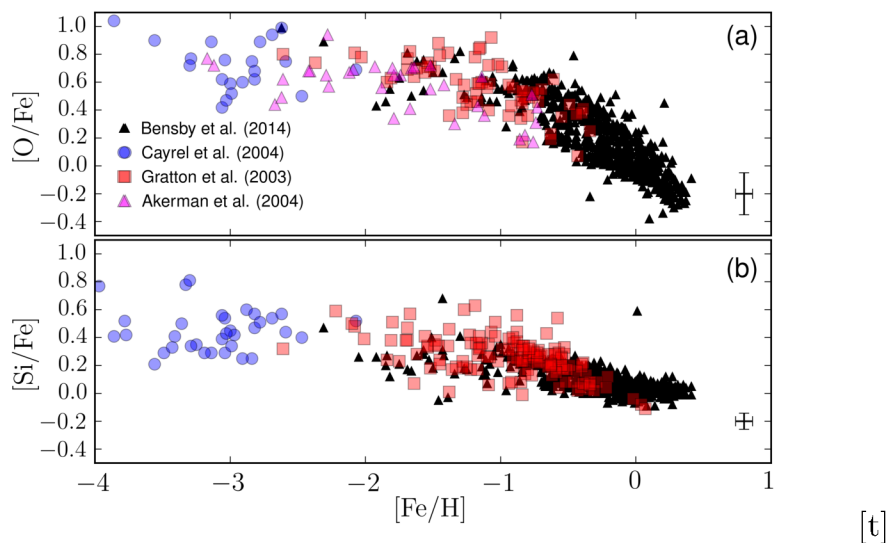


Figure 2.5: In this Figure, we show the observed data set for the $[O/Fe]$ (upper panel) and $[Si/Fe]$ (bottom panel) vs. $[Fe/H]$ chemical abundance patterns, that we assume in this work for the comparison with the predictions of our models. Data with different colors correspond to different works in the literature. In particular, our set of data include MW halo stars from Gratton et al. (2003, red squares), Cayrel et al. (2004, blue circles) and Akerman et al. (2004, magenta triangles), and halo, thin and thick disc stars from Bensby et al. (2014, black triangles).

When assuming a nonlinear Schmidt-Kennicutt law for the SF in galaxies, the differential equation for the evolution of $\sigma_{\text{gas}}(r, t)$ cannot be solved with standard mathematical techniques, such as the Laplace transform method, which can be easily applied to solve only linear ordinary differential equations. Therefore, we retrieve the run of the galaxy SFR with time by making use of a Runge-Kutta algorithm. It is worth noting that, if $k = 2$ in equation (2.36), then equation (2.32) for the evolution of σ_{gas} with time can be put in the form of a Riccati equation, which can also be solved analytically. Nevertheless, an index $k = 2$ seems to be ruled out by observations.

In summary, we firstly derive the evolution of σ_{gas} with time by solving equation (2.32) with a numerical algorithm; then, it is straightforward to recover the galaxy SFR by making use of equation (2.36).

Free parameters and methods

The free parameters of our model are given by i) the star formation efficiency, ν_L , when the linear Schmidt-Kennicutt law is assumed, or the quantity SFR_0 in the case of a nonlinear Schmidt-Kennicutt law; ii) the mass loading factor, ω , which determines the intensity of the galactic winds, and iii) the infall time scale, τ , which characterizes the intensity of the gas infall rate, assumed to be a decaying exponential law.

2.6. Including the delayed production of iron by Type Ia Supernovae within analytical models: a novel method

The assumed initial mass function and the set of stellar yields determine the return mass fraction, R , the net yield of the chemical element X per stellar generation, $\langle y_X \rangle$, and the yield of X from Type Ia SNe, $\langle m_{X,\text{Ia}} \rangle$. Other fundamental assumptions in the model are given by the DTD for the Type Ia SN rate and the prescription for the SFR law.

An observational constraint for the calibration of the gas infall history is given by the radial profile of the present day total surface mass density, $\sigma_{\text{tot}}(r, t_G)$. In this work, we apply our model to reproduce the observed chemical abundance patterns in the MW galaxy; hence we normalize the infall law, as given in equation (2.34), by requiring the following constraint:

$$\int_0^{t_G} dt \hat{\mathcal{I}}(t) = \sigma_{\text{tot}}(8 \text{ kpc}, t_G), \quad (2.38)$$

where we assume $t_G = 14 \text{ Gyr}$, a single infall episode, and $\sigma_{\text{tot}}(8 \text{ kpc}, t_G) = 54 \text{ M}_\odot \text{ pc}^{-2}$, which represents the present day total surface mass density at the solar neighborhood.

The best model is defined as the one capable of reproducing the observed trend of the $[\text{O}/\text{Fe}]$ vs. $[\text{Fe}/\text{H}]$ chemical abundance pattern, which represent the best observational constraint for chemical evolution models of the MW. Our best models is characterized by the following values for the free parameters:

1. $\nu_L = 2 \text{ Gyr}^{-1}$ and $\text{SFR}_0 = 2 \text{ M}_\odot \text{ pc}^{-2} \text{ Gyr}^{-1}$;
2. the infall time scale for the gas mass growth of the MW disc is $\tau = 7 \text{ Gyr}$;
3. the mass loading factor is $\omega = 0.4$.

Finally, the best models assume the single degenerate scenario for the Type Ia SN rate.

It is worth noting that the values of our best parameters are in agreement with previous recent studies (see, for example, [Minchev et al. 2013](#); [Nidever et al. 2014](#); [Spitoni 2015](#)). Furthermore, we remark on the fact that the predicted $[\text{Fe}/\text{H}]-[\text{O}/\text{Fe}]$ relation in the MW is fit by construction using fixed values for the key free parameters ν_L (or SFR_0), ω and τ .

Once the best set of free parameters is determined, we fix them and explore the effects of assuming different DTDs for the Type Ia SN rate and different prescriptions for the relation between the SFR and the surface gas mass density, $\sigma_{\text{gas}}(r, t)$. In this way, we can demonstrate the flexibility of our method for solving the chemical evolution of galaxies, by taking into account the major systematics in the theory.

2.6.2 The observed data set

The data set for the observed $[\text{Fe}/\text{H}]-[\text{O}/\text{Fe}]$ and $[\text{Fe}/\text{H}]-[\text{Si}/\text{Fe}]$ relations are shown in Fig.2.5a and Fig.2.5b, respectively, where the data from different works are drawn with different colors. Our set of data include both MW halo stars from

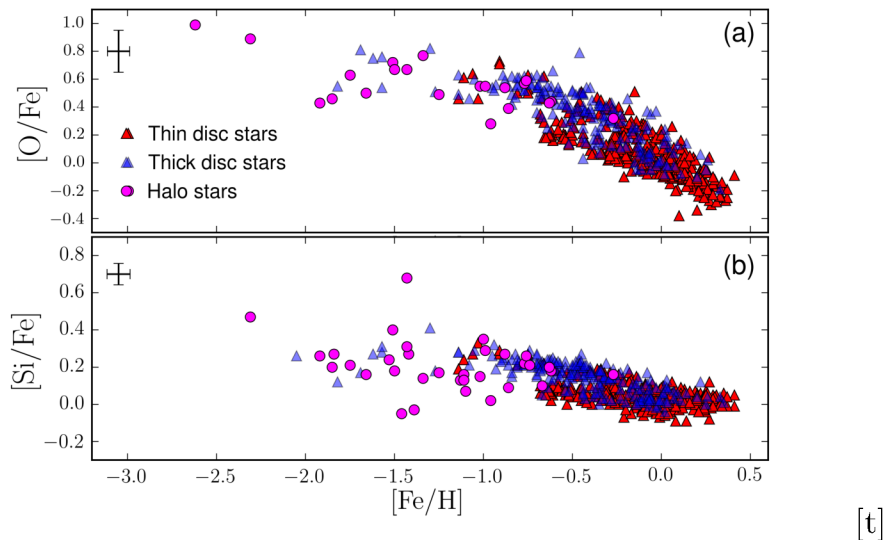


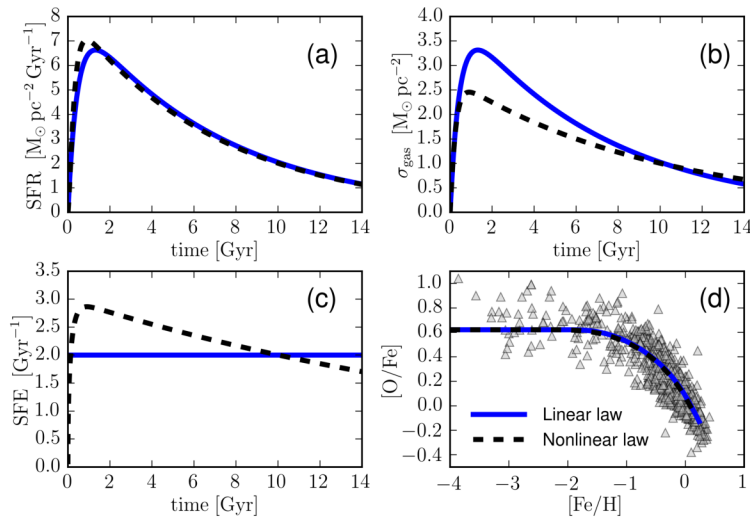
Figure 2.6: In this Figure, we show how the stars in the [Bensby et al. \(2014\)](#) sample are distributed among the various MW stellar components. Halo stars are drawn as magenta circles; thick disc stars as blue triangles; finally, thin disc stars are shown as red triangles. We remind the reader that [Bensby et al. \(2014\)](#) retrieve the membership of the stars in their sample with a kinematical criterion.

[Gratton et al. \(2003, red squares\)](#), [Akerman et al. \(2004, magenta triangles\)](#), and [Cayrel et al. \(2004, blue circles\)](#), and MW halo, thin and thick disc stars from [Bensby et al. \(2014, black triangles\)](#).

The data in [Fig.2.5](#) span a wide metallicity range, from $[\text{Fe}/\text{H}] \approx -4.0$ dex to $[\text{Fe}/\text{H}] \approx 0.5$ dex; they show a continuous trend in the $[\text{O}/\text{Fe}]$ and $[\text{Si}/\text{Fe}]$ abundance ratios as functions of the $[\text{Fe}/\text{H}]$ abundances, although highly scattered. There is an initial, slowly decreasing plateau, followed by steep decrease, which occurs at different $[\text{Fe}/\text{H}]$ abundances and with different slopes when halo and disc stars are considered separately. This is particularly evident when looking at the $[\text{Si}/\text{Fe}]$ ratios in [Fig.2.5b](#), where the data of the halo stars by [Gratton et al. \(2003, red squares\)](#) decrease with a different slope with respect to the disc data by [Bensby et al. \(2014, black triangles\)](#).

In [Fig.2.6](#), we focus on the data set by [Bensby et al. \(2014\)](#) and show how the stars of the halo (magenta circles), thick disc (blue triangles) and thin disc (red triangles) are distributed in the $[\text{Fe}/\text{H}]$ - $[\text{O}/\text{Fe}]$ (upper panel) and $[\text{Fe}/\text{H}]$ - $[\text{Si}/\text{Fe}]$ (bottom panel) diagrams. [Bensby et al. \(2014\)](#) were able to assign a membership to the majority of the stars in their sample, according to the MW stellar component they likely belong to; in particular, [Bensby et al. \(2014\)](#) adopted a conservative kinematical criterion to retrieve the membership of the stars in their sample (see their appendix A). The presence of two well separated sequences between thin and thick disc stars, as suggested by many recent works in the literature (see, for example, [Nidever et al. 2014](#); [Kordopatis et al. 2015](#)) is still not evident by looking at the data set in [Fig.2.6](#), since the data are still highly scattered.

2.6. Including the delayed production of iron by Type Ia Supernovae within analytical models: a novel method



[t]

Figure 2.7: In this Figure, we show the comparison between models with different prescriptions for the galaxy SFR. We examine a linear Schmidt-Kennicutt law (solid curves in blue; see equation 2.31) and a nonlinear Schmidt-Kennicutt law (dashed curves in black; see equation 2.36). In panel (a), we show the results for the evolution of the SFR as a function of time; in panel (b), we show how σ_{gas} is predicted to evolve with time; in panel (c), the temporal evolution of the star formation efficiency, defined as $\text{SFE} = \psi(r, t)/\sigma_{\text{gas}}(r, t)$, is drawn; finally, in panel (d), we show the evolutionary path of the models in the $[\text{Fe}/\text{H}]$ - $[\text{O}/\text{Fe}]$ diagram, with the grey triangles corresponding to the observed set of data for the MW (see Section 7.2). All the models assume a fixed value of the free parameters; in particular, $\nu_L = 2 \text{ Gyr}^{-1}$ (blue solid curves) and $\text{SFR}_0 = 2 M_{\odot} \text{ pc}^{-2} \text{ Gyr}^{-1}$ (black dashed curves); infall time scale $\tau = 7 \text{ Gyr}$; mass loading factor $\omega = 0.4$, and the single degenerate scenario for DTD of Type Ia SNe (see also Section 2.6.1 for the assumed set of free parameters).

2.6.3 Results: the Milky Way chemical evolution

In this Section, we present the results of our chemical evolution model, which is based on the methods and equations as described in Section 6.3. We study the MW chemical evolution, with the aim of reproducing the observed $[\text{O}/\text{Fe}]$ and $[\text{Si}/\text{Fe}]$ abundance ratios as functions of the $[\text{Fe}/\text{H}]$ abundance.

We firstly explore the effect of different prescriptions for the galaxy SFR. Successively, we investigate the effect of assuming different DTDs for Type Ia SNe.

Exploring the effect of different laws for the Galaxy SFR

In Fig. 2.7, we compare the predictions of our best model with the linear Schmidt-Kennicutt law (solid lines in blue) with a similar model assuming a nonlinear Schmidt-Kennicutt law. In particular, in Fig. 2.7a, we show the predicted evolution of the galaxy SFR as a function the galaxy lifetime; in Fig. 2.7b, the predicted evolution of σ_{gas} with time; in Fig. 2.7c, we show how the predicted star formation efficiency evolves as a function of time; finally, in Fig. 2.7d, we show our results for

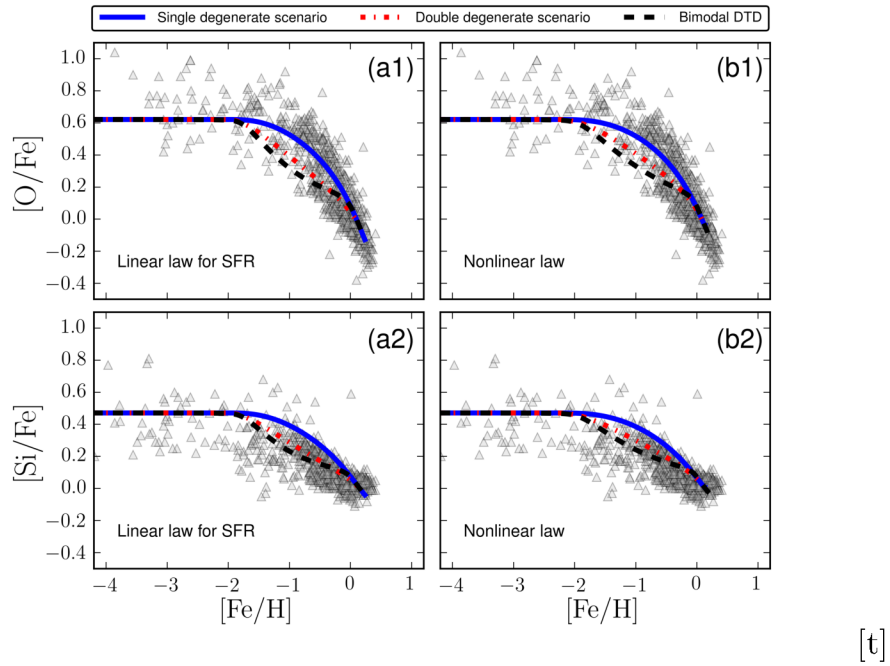


Figure 2.8: In this Figure, we show the main results of our work for the $[O/Fe]$ (upper panels) and $[Si/Fe]$ (bottom panels) vs. $[Fe/H]$ chemical abundance patterns. Curves with different colors correspond to different assumptions for the DTD of Type Ia SNe. In this work, we examine the single degenerate scenario (solid curves in blue), the double degenerate scenario (dashed-dotted red curves) and the bimodal DTD (dashed black curves). The panels (a1) and (a2) on the left show the predictions of the models with the linear Schmidt-Kennicutt law (see equation 2.31), while the panels (b1) and (b2) on the right show the models with the nonlinear Schmidt-Kennicutt law (see equation 2.36).

2.6. Including the delayed production of iron by Type Ia Supernovae within analytical models: a novel method

the [O/Fe] vs. [Fe/H] chemical abundance pattern.

By looking at Fig.2.7a, the predicted SFR is very similar when assuming the linear and the nonlinear Schmidt-Kennicutt law, with similar absolute values for ν_L and SFR_0 . The differences are always remarkable in the evolution of σ_{gas} with time (see Fig.2.7b), particularly in the earliest stages of the galaxy evolution; in fact, the model with the nonlinear Schmidt-Kennicutt law (dashed line in black) always predicts higher surface gas mass densities than the model with the linear Schmidt-Kennicutt law (solid blue line) for $t \lesssim 10$ Gyr. That can be explained by looking at Fig.2.7c, where we can appreciate that – for galaxy evolutionary times $t \lesssim 10$ Gyr – the model with the nonlinear law has always higher star formation efficiencies (see equation 2.37) than the model with the linear law, which has a fixed star formation efficiency $\nu = 2 \text{ Gyr}^{-1}$. Since the predicted evolution of the galaxy SFR is very similar when assuming a linear or nonlinear Schmidt-Kennicutt law, the differences in the predicted [O/Fe] vs. [Fe/H] relation are negligible (see Fig.2.7d).

The predicted evolutionary path of our models in the [Fe/H]-[O/Fe] diagram in Fig.2.7d can be explained as follows, by means of the so-called “time delay model” (Tinsley, 1979; Greggio & Renzini, 1983; Matteucci, 1986).

1. The plateau at very low [Fe/H] abundances stems from the chemical enrichment by massive stars, dying as core-collapse SNe, for which we assume IRA and hence a constant ratio between the net yields of oxygen and iron per stellar generation.
2. The initial plateau is then followed by a decrease, which is due to the delayed contribution of Type Ia SNe, injecting large amounts of iron into the galaxy ISM. The position of the knee in the [Fe/H]-[O/Fe] relation is determined by the galaxy star formation efficiency. In particular, decreasing the star formation efficiency determines a slower production of iron and α -elements by massive stars and hence the decrease of the [O/Fe] ratios occurs at low [Fe/H] abundances.

If we had assumed the original Kennicutt (1998) law, which prescribes $SFR_0 = 2.5 \times 10^{-1} M_{\odot} \text{ pc}^{-2} \text{ Gyr}^{-1}$, the star formation efficiencies would have been always roughly one order of magnitude lower than the findings of our best model, determining a decrease of the [O/Fe] ratios at very low [Fe/H] abundances, at variance with data.

Exploring the effect of different DTDs for Type Ia SNe

In Fig.2.8, we show the effect of varying simultaneously the assumed DTDs for Type Ia SNe (curves with different colors in all the panels) and the prescriptions for the SFR law (Fig.2.8a1 and Fig.2.8a2 show the results of the models with the linear Schmidt-Kennicutt law for [O/Fe] and [Si/Fe] vs. [Fe/H], respectively, while Fig.2.8b1 and Fig.2.8b2 show the results for the law by Kennicutt 1998).

By looking at Fig.2.8, we can appreciate that different distributions of delay times for Type Ia SNe determine different behaviors of the models. Whatever is the

assumed prescription for the galaxy SFR, the best agreement with the set of data for $[\text{O}/\text{Fe}]$ vs. $[\text{Fe}/\text{H}]$ is achieved by the model with the single degenerate scenario (blue solid lines), while the predicted trend of the $[\text{Si}/\text{Fe}]$ vs. $[\text{Fe}/\text{H}]$ with the single degenerate scenario is always above the data; such an offset for silicon is due to the still large uncertainty in the nucleosynthetic stellar yields of this chemical element.

The models with the bimodal DTD of [Mannucci et al. \(2006\)](#), (dashed curves in black) predict a remarkable change in the behavior of the declining trend of the $[\alpha/\text{Fe}]$ ratios, which is due to the assumed secondary population of Type Ia SNe, which contributes by 50 per cent to the global distribution of the delay times; this tardy component bolsters the iron pollution of the ISM at later times. Moreover, the $[\alpha/\text{Fe}]$ ratios with the bimodal DTD decline with the steepest slope among the assumed DTDs because of the too large number of prompt Type Ia SNe; this result is in agreement with the findings of [Matteucci et al. \(2006, 2009\)](#); [Yates et al. \(2013\)](#); all these studies agree that the average number of prompt Type Ia SNe can vary from ~ 15 per cent to a maximum of ~ 30 per cent with respect to the integrated number of Type Ia SNe, hence a percentage which should be lower than the 50 per cent assumed by [Mannucci et al. \(2006\)](#), although these authors concluded that for their data also a percentage of 30 per cent could be acceptable. Finally, the models with the double degenerate scenario (dashed-dotted red curves) predict a steeper declining trend of the $[\alpha/\text{Fe}]$ ratios than the single degenerate scenario as first Type Ia SNe explode.

2.6.4 Conclusions and discussion

In this Section, we have presented a new theoretical framework for following the chemical evolution of galaxies, by assuming IRA for chemical elements synthesized and restored by massive stars on short typical time-scales and the DTD formalism for the delayed chemical enrichment by Type Ia SNe. The main assumptions of our model are the galaxy gas mass assembly history, the stellar yields and the initial mass function. Finally, the SFR law represents also an other fundamental phenomenological assumption in the model.

We have derived a very simple and general formula (equation 2.33), relating the Laplace transform of the galaxy SFH with the Laplace transform of the galaxy gas mass assembly history, provided the galaxy SFR follows a linear Schmidt-Kennicutt law, namely $\psi(r, t) \propto \sigma_{\text{gas}}(r, t)$. This formula can be used both to derive the galaxy SFH from the assumed gas infall law and to solve the corresponding inverse problem (i.e., retrieving the galaxy gas accretion history from the observed SFH).

We remark on the fact that the Laplace transform method for solving ordinary differential equations can only be used when the latter are linear. For this reason, we have also considered the case of a nonlinear ordinary differential equation for the evolution of the galaxy surface gas mass density with time, which can be obtained when assuming $\psi(r, t) \propto \sigma_{\text{gas}}(r, t)^k$, with $k = 1.4$ (nonlinear Schmidt-Kennicutt law). In this work, we have retrieved the galaxy SFH with a nonlinear law for the galaxy SFR, by making use of standard numerical techniques.

We have shown that the differential equation for the evolution of a generic chemical element X can be solved with standard numerical methods (e.g., the

2.6. Including the delayed production of iron by Type Ia Supernovae within analytical models: a novel method

Runge-Kutta algorithm), once the galaxy SFH has been theoretically determined from our assumptions. We have applied our model to reproduce the $[\text{O}/\text{Fe}]$ and $[\text{Si}/\text{Fe}]$ vs. $[\text{Fe}/\text{H}]$ chemical abundance patterns as observed in the MW halo and disc stars, by exploring the effect of different DTDs for Type Ia SNe and different prescriptions for the SFR law. We have assumed the Galaxy disc to assemble by means of a single gas accretion episode, with typical time scale $\tau = 7$ Gyr. In any case, our method can be easily extended also for a two-infall model (Chiappini et al., 1997).

Our model with the single degenerate scenario for Type Ia SNe provides a very good agreement with the set of data of the MW. Since the nucleosynthetic stellar yields of the other α -elements still suffer of large uncertainty, the agreement between model and data for these chemical elements is still not good.

We are aware that a linear relation between the SFR and σ_{gas} seems not to be the best fit to data, unless the star formation efficiency is defined as the inverse of the typical dynamical time scale of the system. Nevertheless, we have shown that our models with a nonlinear Schmidt-Kennicutt law provide very similar results for the galaxy SFR and chemical abundance patterns as the model with the linear Schmidt-Kennicutt law.

We are aware that the assumption of a constant yield per stellar generation is a strong approximation, determining the predicted flat trend of the $[\alpha/\text{Fe}]$ ratios at low $[\text{Fe}/\text{H}]$ abundances, at variance with data showing a remarkable scatter. This scatter can be reproduced only by introducing an element of stochasticity in the model (for example, in the stellar yields, in the IMF or in the SFR). Moreover, the $[\alpha/\text{Fe}]$ ratios at very low $[\text{Fe}/\text{H}]$ abundances show a global trend, which can be reproduced only by relaxing IRA, and hence by including stellar lifetimes and variable nucleosynthetic stellar yields of massive stars, as in the detailed numerical codes of chemical evolution. As Type Ia SNe start exploding, the $[\alpha/\text{Fe}]$ ratios steeply decrease, in excellent agreement with data.

The theoretical method, as presented in this Section, differs from previous works in the literature, which similarly recover the galaxy chemical evolution from the assumed SFH (see, for example, Erb et al. 2006; Homma et al. 2015; Weinberg et al. 2016), because we initially start from the assumption of a galaxy gas mass assembly history. Then, the galaxy SFH has been retrieved by means of equation (2.33), which makes use of the Laplace transform to simplify the solution of the differential equation for the evolution of the galaxy gas mass. Our theoretical framework can be generalized for any choice of the galaxy gas infall law, as given – for example – by the analysis of cosmological hydrodynamical simulations (see, for example, Faucher-Giguère et al. 2011).

Our method for solving chemical evolution of galaxies can be easily included in other complementary stellar population synthesis models, by taking into account chemical elements – like iron – which are restored with a time delay from the star formation event. In this way, one can easily decouple the evolution of iron and oxygen, which contribute to the total metallicity of the galaxy ISM with different relative fractions as a function of the galaxy lifetime.

References

- Arimoto N., Yoshii Y., 1987, *A&A*, 173, 23
- Asplund M., Grevesse N., Sauval A. J., Scott P., 2009, *ARA&A*, 47, 481
- Akerman, C. J., Carigi, L., Nissen, P. E., Pettini, M., & Asplund, M. 2004, *A&A*, 414, 931
- Bell, E. F., McIntosh, D. H., Katz, N., & Weinberg, M. D. 2003, *ApJs*, 149, 289
- Bigiel, F., Leroy, A., Walter, F., et al. 2008, *AJ*, 136, 2846
- Bigiel, F., Leroy, A. K., Walter, F., et al. 2011, *ApJl*, 730, L13
- Bensby, T., Feltzing, S., & Oey, M. S. 2014, *A&A*, 562, A71
- Bouché, N., Dekel, A., Genzel, R., et al. 2010, *ApJ* 718, 1001
- Bower R. G., McCarthy I. G., Benson A. J., 2008, *MNRAS*, 390, 1399
- Cappellari M., McDermid R. M., Alatalo K., et al., 2012, *Nature*, 484, 485
- Cayrel, R., Depagne, E., Spite, M., et al. 2004, *A&A*, 416, 1117
- Chabrier G., 2003, *PASP*, 115, 763
- Chabrier G., Hennebelle P., Charlot S., 2014, *ApJ*, 796, 75
- Chiappini, C., Matteucci, F., & Gratton, R. 1997, *ApJ*, 477, 765
- Chiappini C., Ekström S., Meynet G., et al., 2008, *A&A*, 479, L9
- Chiosi, C. 1980, *A&A*, 83, 206
- Conroy C., van Dokkum P. G., 2012, *ApJ*, 760, 71
- Côté, B., Ritter, C., O’Shea, B. W., et al. 2015, arXiv:1509.06270
- Côté, B., O’Shea, B. W., Ritter, C., Herwig, F., & Venn, K. A. 2016, arXiv:1604.07824
- Croton D. J., Springel V., White S. D. M., et al., 2006, *MNRAS*, 365, 11
- De Lucia G., Kauffmann G., White S. D. M., 2004, *MNRAS*, 349, 1101
- Erb, D. K., Steidel, C. C., Shapley, A. E., et al. 2006, *ApJ*, 646, 107
- Ekström S., Meynet G., Chiappini C., Hirschi R., Maeder A., 2008, *A&A*, 489, 685
- Faucher-Giguère, C.-A., Kereš, D., & Ma, C.-P. 2011, *MNRAS*, 417, 2982
- Gibson B. K., 1997, *MNRAS*, 290, 471
- Gratton, R. G., Carretta, E., Claudi, R., Lucatello, S., & Barbieri, M. 2003, *A&A*, 404, 187
- Greggio L., Renzini A., 1983, *Mem. Soc. Astron. Ital.*, 54, 311
- Henry R. B. C., Edmunds M. G., Köppen J., 2000, *ApJ*, 541, 660
- Hirschi R., Meynet G., Maeder A., 2004, *A&A*, 425, 649
- Hirschi R., Meynet G., Maeder A., 2005, *A&A*, 433, 1013
- Hirschi R., 2007, *A&A*, 461, 571
- Ho I.-T., Kudritzki R.-P., Kewley L. J., et al., 2015, *MNRAS*, 448, 2030
- Homma, H., Murayama, T., Kobayashi, M. A. R., & Taniguchi, Y. 2015, *ApJ*, 799, 230
- Hunt, L., Dayal, P., Magrini, L., & Ferrara, A. 2016, *MNRAS*, 463, 2002
- Hunt, L., Dayal, P., Magrini, L., & Ferrara, A. 2016, *MNRAS*, 463, 2020
- Iwamoto, K., Brachwitz, F., Nomoto, K., et al. 1999, *ApJ*, 125, 439
- Karakas A. I., 2010, *MNRAS*, 403, 1413
- Kobayashi C., Umeda H., Nomoto K., Tominaga N., Ohkubo T., 2006, *ApJ*, 653, 1145
- Kobayashi C., Karakas A. I., Umeda H., 2011, *MNRAS*, 414, 3231
- Kordopatis, G., Wyse, R. F. G., Gilmore, G., et al. 2015, *A&A*, 582, A122
- Kroupa P., Tout C. A., Gilmore G., 1993, *MNRAS*, 262, 545
- Kroupa P., 2001, *MNRAS*, 322, 231
- Kudritzki, R.-P., Ho, I.-T., Schrubba, A., et al. 2015, *MNRAS*, 450, 342
- Kudritzki, R. P., Castro, N., Urbaneja, M. A., et al. 2016, *ApJ*, 829, 70
- Larson, R. B. 1976, *MNRAS*, 176, 31
- Lilly, S. J., Carollo, C. M., Pipino, A., Renzini, A., & Peng, Y. 2013, *ApJ*, 772, 119

- Maeder A., 1992, *A&A*, 264, 105
- Maeder A., Meynet G., Hirschi R., Ekström S., 2006, *Chemical Abundances and Mixing in Stars in the Milky Way and its Satellites*, 308
- Maeder A., 2009, *Physics, Formation and Evolution of Rotating Stars*, *Astronomy and Astrophysics Library*. ISBN 978-3-540-76948-4. Springer Berlin Heidelberg, 2009
- Matteucci, F., Chiosi, C., 1983, *A&A*, 123, 121
- Matteucci F., Greggio L., 1986, *A&A*, 154, 279
- Matteucci, F., & Francois, P. 1989, *MNRAS*, 239, 885
- Matteucci F., 2001, *Astrophysics and Space Science Library*, 253
- Matteucci, F., Panagia, N., Pipino, A., et al. 2006, *MNRAS*, 372, 265
- Matteucci, F., Spitoni, E., Recchi, S., & Valiante, R. 2009, *A&A*, 501, 531
- Matteucci F., 2012, *Chemical Evolution of Galaxies*. Springer-Verlag, Berlin
- Meynet G., Maeder A., 2002, *A&A*, 390, 561
- Meynet G., Hirschi R., Ekstrom S., et al., 2010, *IAU Symposium*, 265, 98
- Micali, A., Matteucci, F., & Romano, D. 2013, *MNRAS*, 436, 1648
- Nidever, D. L., Bovy, J., Bird, J. C., et al. 2014, *ApJ*, 796, 38
- Nomoto K., Tominaga N., Umeda H., Kobayashi C., & Maeda K., 2006, *Nuclear Physics A*, 777, 424
- Nomoto K., Kobayashi C., Tominaga N., 2013, *ARA&A*, 51, 457
- Padovani P., Matteucci F., 1993, *ApJ*, 416, 26
- Peeples M. S., Werk J. K., Tumlinson J., et al., 2014, *ApJ*, 786, 54
- Peng, Y.-j., & Maiolino, R. 2014, *MNRAS*, 443, 3643
- Ramírez-Agudelo O. H., Simón-Díaz S., Sana H., et al., 2013, *A&A*, 560, A29
- Recchi, S., Spitoni, E., Matteucci, F., Lanfranchi, G. A., 2008, *A&A*, 489, 55
- Recchi S., Kroupa P., 2015, *MNRAS*, 446, 4168
- Romano D., Karakas A. I., Tosi M., Matteucci F., 2010, *A&A*, 522, A32
- Salpeter E. E., 1955, *ApJ*, 121, 161
- Schruba, A., Leroy, A. K., Walter, F., et al. 2011, *AJ*, 142, 37
- Silk, J. 1997, *ApJ*, 481, 703
- Spitoni, E., Calura, F., Matteucci, F., & Recchi, S. 2010, *A&A*, 514, A73
- Spitoni, E. 2015, *MNRAS*, 451, 1090
- Spitoni, E., Vincenzo, F., & Matteucci, F., 2017, *A&A*, 599, A6
- Talbot R. J. Jr., Arnett W. D., 1973, *ApJ*, 186, 51
- Talbot, R. J., Jr., & Arnett, W. D., 1975, *ApJ*, 197, 551
- Tinsley B. M., 1979, *ApJ*, 229, 1046
- Tinsley B. M., 1980, *Fundamentals of Cosmic Physics*, 5, 287
- Vincenzo, F., Matteucci, F., Belfiore, F., Maiolino, R., 2016, *MNRAS*, 455, 4183
- Vincenzo, F., Matteucci, F., & Spitoni, E. 2016, *arXiv:1606.08469*
- Weidner C., Kroupa P., Pflamm-Altenburg J., Vazdekis A., 2013, *MNRAS*, 436, 3309
- Weinberg, D. H., Andrews, B. H., & Freudenburg, J. 2016, *arXiv:1604.07435*
- Yates, R. M., Henriques, B., Thomas, P. A., et al. 2013, *MNRAS*, 435, 3500
- Zahid H. J., Dima G. I., Kudritzki R. P., et al., 2014, *ApJ*, 791, 130

Part II

Chemical evolution of the Milky Way dwarf spheroidal galaxy satellites

3

Chemical evolution of classical and ultra-faint dwarf spheroidal galaxies

3.1 Introduction

Orbiting around the Milky Way, there is a large number of satellite galaxies, most of which have so low average surface brightnesses and small effective radii that their detection was very difficult in the past: from 1937 up to 1994, only nine of them were discovered and that number remained unchanged until 2005. They are the so-called *classical dwarf spheroidal galaxies* (dSphs), which are among the least luminous and most dark matter (DM) dominated galaxies which are observed today in the Universe. Dwarf spheroidal galaxies are classified as early-type since they are observed to possess very low gas mass at the present time and their stars are very iron-poor when compared to the Sun (see [Tolstoy et al. 2009](#) and [Koch 2009](#) for an exhaustive review).

Color-magnitude diagram (CMD) fitting analysis revealed star formation rate (SFR) in dSphs to have been either continuous for a long time or occurring in bursts. All dSph galaxies host an underlying very old stellar population with age $\gtrsim 10$ Gyr (e.g. [Grebel 1997](#)), and some of them are dominated by an intermediate-age stellar population with age in the range 4 – 8 Gyr ([Dall’Ora et al., 2003](#)). Very few dSphs have been observed to host younger stars, which populate the so-called “blue plume” in the CMD, sign of a relatively recent star formation activity, which occurred up to $\sim 2 - 3$ Gyr ago ([Monelli et al., 2003](#)).

All such features led cosmologists to hypothesize dSphs to be the evolved small progenitor systems which merged in the past to form the actual large structures in the Universe as the stellar halo of the Milky Way, in the framework of the Λ CDM standard cosmological model ([Helmi & White, 1999](#); [Bullock et al., 2001](#); [Harding](#)

et al., 2001; Bullock & Johnston, 2005). However, successive deeper investigations revealed them not to possess all the right properties to be the aforementioned hypothetical survived progenitors of the Galactic halo (see Helmi et al. 2006 and Catelan 2009 and references therein).

The Sloan Digital Sky Survey (SDSS) allowed in the past ten years (from 2005 up to the present time) to discover a large number of new dwarf galaxies orbiting around the Milky Way with physical properties very similar to dSph galaxies but average surface brightnesses and effective radii even much smaller (see, e.g., Belokurov et al. 2007, 2010): for such reasons, they have been named as *ultra-faint dwarf spheroidal galaxies* (UFDs). That is a mere naming convention, without any real physical motivation, since UFDs extend to fainter magnitudes and lower masses the same observed physical properties of dSphs. In fact UFD galaxies do not contain any gas at the present time and their stars are on average very iron-poor, with age $\gtrsim 10 - 12$ Gyr (Okamoto & Arimoto, 2012; Brown et al., 2013). So UFDs do not show any recent star formation activity. Such stellar systems soon aroused great interest in the scientific community, either for their extreme observed characteristics, or because such characteristics might shed light on the conditions of the Universe in the first billion years of its evolution (see Belokurov 2013 for a detailed discussion). The UFD environment constitutes the best candidate for verifying whether a first population of very massive and extremely metal-poor stars (the so-called Population III) might have existed or not. Such stars, at their death, should have enriched the interstellar medium (ISM) with some metals and therefore they might have left a chemical signature in the stars which were born immediately after, as some of the UFD stars (Ferrara 2012). As Salvadori & Ferrara (2012) had envisaged, this hypothesis might be supported by the observation of carbon-enhanced metal-poor (CEMP) stars in some UFD galaxies (Norris et al., 2010; Gilmore et al., 2013), which might be directly linked to the CEMP-Damped Ly- α systems observed in the spectra of quasars at high redshift (Cooke et al., 2011a,b). In this scenario, the latter might be the high-redshift unevolved counterparts of some of the UFD galaxies.

Aim of this Chapter is to study how dSph and UFD galaxies have evolved, by reconstructing - going back in time - the chemical enrichment history of their ISM, starting from the chemical abundances derived today in the atmospheres of their stars. We will adopt a detailed chemical evolution model which is able to follow the evolution of several chemical species (H, He, C, N, O, α -elements, Fe-peak elements, s- and r- process elements). This model is based on that presented by Lanfranchi & Matteucci (2004) and then used also in the works of Lanfranchi et al. (2006a), Lanfranchi et al. (2006b), Lanfranchi & Matteucci (2007), Lanfranchi et al. (2008), Cescutti et al. (2008), and Lanfranchi & Matteucci (2010).

Lanfranchi & Matteucci (2004) modeled the chemical evolution of six dSphs of the Local Group including Sextans, Sculptor, Sagittarius, Draco, Ursa Minor and Carina. Their main conclusions were that dSphs suffered from very low star formation efficiency, which caused the iron pollution from Type Ia SNe to become important when the $[\text{Fe}/\text{H}]$ of galaxy ISM was still very low. In this manner, and by assuming also intense galactic winds, they were able to explain the observed decrease in the trends of $[\alpha/\text{Fe}]$ vs. $[\text{Fe}/\text{H}]$. Galactic winds prevent the galaxy to

form stars soon after the onset of the outflow and this leads the stellar metallicity distribution function (MDF) in dSphs to be peaked towards low $[\text{Fe}/\text{H}]$ abundances, almost 1.5 dex below the one of Milky Way disc in the solar neighborhood, in agreement with observations.

As interesting papers appeared recently, [Romano & Starkenburg \(2013\)](#) modeled the chemical evolution of Sculptor by means of a new approach in a full cosmological framework, whereas [Koch et al. \(2012, 2013\)](#) present a first chemical evolution model of the Hercules UfD, based on the same numerical code we use in this work.

Here we focus on the chemical evolution of Sculptor and Carina, for which newer data are available, but especially we model the evolution of UfDs: Hercules and Boötes I. In Section 3.2 we describe the adopted chemical evolution model. In Section 3.3 the data sample is presented and in Section 3.4 the results are shown. Finally, in Section 3.5 some conclusions are drawn. All the results as presented in this Chapter have been published in [Vincenzo, Matteucci, Vattakunnel & Lanfranchi \(2014\)](#).

3.2 Assumptions of the model

We assume dSph and UfD galaxies to form by infall of primordial gas in a pre-existing DM halo. The infall rate obeys a decaying exponential law with very short typical time-scales, τ_{inf} , and the so-called *infall mass*, M_{inf} , represents the reservoir of the infalling gas from which the stars form. Hence the gas out of which dSph and UfD galaxies form is assumed to be of primordial chemical composition. In summary, in our models for the dSph and UfD galaxies, we assume the galaxy gas mass assembly history to follow a decaying exponential law with time, which is normalized with respect to the infall mass, M_{inf} .

We assume for dSphs an infall time-scale $\tau_{\text{dSph}} = 0.5$ Gyr, while for UfDs we adopt $\tau_{\text{UfD}} = 0.005$ Gyr, which is equivalent to assume that almost all the gas was present in the DM halo since the beginning. The reason for these choices will be clearer in the next sections and are dictated by fitting the observational constraints.

Thanks to the detailed treatment of the main physical processes involved in the chemical enrichment of the galaxy ISM, we are able to predict the trends of the chemical abundances of many elements relative to iron as a function of $[\text{Fe}/\text{H}]$, the MDF and the total stellar and gas masses at the present time. Other observational constraints are represented by i) the history of star formation (SFH), which may be characterized either by a single long episode or by several bursts of star formation, according to the CMD-fitting analysis; ii) the total mass of the DM halo and, finally, iii) the effective radius of the luminous baryonic component of the galaxy. We assume, when we do not have any information, a diffuse dark matter halo for these galaxies, with $S = \frac{r_{\text{L}}}{r_{\text{DM}}}$ between 0.2 and 0.4, where r_{DM} represents the core radius of each galaxy DM halo.

The main assumptions of the model, which is based on a similar numerical code as the one used in [Lanfranchi & Matteucci \(2004\)](#), are the following:

- each galaxy is modelled as a one zone with instantaneous and complete mixing of gas within it;
- stellar lifetimes are taken into account (no instantaneous recycling approximation);
- the nucleosynthesis prescriptions include the yields of [Iwamoto et al. \(1999\)](#) for Type Ia SNe, the yields of [Woosley & Weaver \(1995\)](#), with the corrections suggested by [François et al. 2004](#)) for massive stars, and the metallicity-dependent yields of [van den Hoek & Groenewegen \(1997\)](#) for low- and intermediate-mass stars.

The galaxy star formation rate is assumed to follow a linear Schmidt Kennicutt law, namely: $\psi(t) = \nu M_{\text{gas}}(t)$. Moreover, the galaxy can lose gas through galactic winds, which develop when the thermal energy of the gas $E_{\text{g}}^{\text{th}}(t)$ equals its binding energy to the galaxy potential well, $E_{\text{g}}^{\text{b}}(t)$. The latter quantity $E_{\text{g}}^{\text{b}}(t)$ is calculated by means of assumptions concerning the presence and the distribution of the DM which, for dSphs and UFDs, is usually represented as a diffuse halo (see [Bradamante et al. 1998](#)), whereas the thermal energy of gas $E_{\text{g}}^{\text{th}}(t)$ is primarily determined by the energy deposited by SN explosions into the ISM (see also for more details Section 1.3). The outflow rate is assumed to be directly proportional to the galaxy star formation rate, as follows:

$$\mathcal{O}(t) = \lambda \psi(t) = \omega M_{\text{gas}}(t), \quad (3.1)$$

where $\omega = \nu \lambda$ is defined as the product of the mass loading factor with the star formation efficiency and has the units of the inverse of a time. For dSph and UFD galaxies, we suppose the galactic wind to be *normal*, namely the ω parameter is equal for all the chemical elements, although we test also models with different kind of *differential* winds, following [Marconi et al. \(1994\)](#) and [Recchi et al. \(2001\)](#).

3.3 Data sample

In general, we have selected - when possible - only high-resolution data and we have scaled all of them to the same Solar abundances ([Asplund et al., 2009](#)). The reason for this was to homogenize the data as much as possible.

Sculptor dSph

Sculptor is a relatively faint ($M_V \approx -11.1$, from [Mateo 1998](#)) stellar system, located at a distance of 79 ± 4 kpc ([Koch, 2009](#)) away from us. Its features make it a fair representative of a typical dSph galaxy of the Local Group and it is also one of the most extensively investigated. It hosts the most iron-poor stars ever observed in a dSph, with $[\text{Fe}/\text{H}] = -3.96 \pm 0.06$ dex ([Tafelmeyer et al., 2010](#)).

We used the dataset of chemical abundances presented by [Shetrone et al. \(2003\)](#), [Tafelmeyer et al. \(2010\)](#), [Frebel \(2010\)](#) and [Kirby & Cohen \(2012\)](#). The data sample we used for the MDF is taken from [Romano & Starkenburg \(2013\)](#),

who combined the data samples of the DART project (Battaglia et al., 2008a; Starkeburg et al., 2010) and of Kirby et al. (2009, 2010).

Carina dSph

Carina is located at a distance of 94 ± 5 kpc and belongs to the faintest dSphs of the Local Group ($M_V \approx -9.3$, $\mu_V = 25.5 \pm 0.4$ mag arcsec⁻², from Mateo 1998). In the dSph realm, Carina is almost unique, since its CMD reveals a bursty SFH, which gave rise to the today observed multiple stellar populations (Hurley-Keller et al., 1998; Tolstoy et al., 2003).

The dataset of chemical abundances we used for the comparisons with the predictions of our models have been taken from the following works: Shetrone et al. (2003), Koch et al. (2008a), Lemasle et al. (2012) and Venn et al. (2012). The observed MDF has been taken from Koch et al. (2006).

Hercules UFD

The Hercules UFD was discovered by Belokurov et al. (2007) from the analysis of Sloan Digital Sky Survey (SDSS) data. The line of sight toward Hercules is heavily contaminated by Galactic foreground stars since it resides at a lower Galactic latitude than the other UFDs (de Jong et al., 2008). Furthermore, the mean radial velocity of Hercules stars is very similar to the mean radial velocity of thick disk stars.

Hercules appears clearly highly elongated, without any evidence of internal rotation ($\sigma_v \sim 3.72$ km s⁻¹, from Adén et al. 2009b). Such a large ellipticity with no rotational support might imply that Hercules is not in dynamical equilibrium and it is undergoing strong tidal distortions. Hercules lies at a distance of 132 ± 12 kpc from us, it has an absolute V-band magnitude $M_V = -6.6 \pm 0.3$ and a V-band surface brightness of only $\mu_V = 27.2 \pm 0.6$ mag arcsec⁻² (see Adén et al. 2009b and references therein).

The data sample we used for the chemical abundances in the Hercules UFD is taken from Adén et al. (2011), which provide the chemical abundances of calcium and iron, the only elements actually available for this galaxy.

Boötes I UFD

The Boötes I UFD was discovered by Belokurov et al. (2006), from the analysis of SDSS data. Siegel (2006) estimated the distance of Boötes I by using 15 RR Lyrae variable stars as standard candles; they found a distance: $D = 62 \pm 4$ kpc, very similar to that of the outermost halo globular clusters in our Galaxy. Finally, Belokurov et al. (2006) reported an absolute magnitude $M_V = -5.8$ and an half-light radius $r_h \sim 220$ pc.

The data samples of chemical abundances have been taken from the works of Norris et al. (2010) and Gilmore et al. (2013) (“NY” analysis, from Norris et al. 2010). The observed MDF has been worked out by Lai et al. (2011), by expanding their own sample to include non-overlapping stars from Norris et al. (2010) and

Chapter 3. Chemical evolution of classical and ultra-faint dwarf spheroidal galaxies

Sculptor: model parameters								
ν	ω	τ_{inf}	SFH	M_{inf}	M_{DM}	r_{L}	$S = \frac{r_{\text{L}}}{r_{\text{DM}}}$	IMF
[Gyr ⁻¹]	[Gyr ⁻¹]	[Gyr]	[Gyr]	M _⊙	M _⊙	[pc]		
0.01/0.05/0.1/0.2	5/10/15/20	0.5	0 – 7	1.0×10^8	3.4×10^8	260	0.260	Salpeter (1955)

Table 3.1: *Table:* we summarize here the specific characteristics of all the chemical evolution models performed for the Sculptor dSph. *Columns:* (1) star formation efficiency; (2) wind parameter; (3) infall time-scale; (4) period of major star formation activity (de Boer et al., 2012); (5) total infall gas mass; (6) mass of the dark matter halo (Battaglia et al., 2008b); (7) effective radius of the *luminous* (baryonic) matter (Walker et al., 2009); (8) ratio between the core radius of the dark matter halo and the effective radius of the *luminous* matter; (9) initial mass function.

Sculptor chemical evolution models					
Input parameters		Model predictions			
	ν	$M_{\star, \text{fin}}$	$M_{\text{gas, fin}}$	t_{wind}	[Fe/H] _{peak}
	[Gyr ⁻¹]	M _⊙	M _⊙	[Gyr]	dex
$\omega = 5 \text{ Gyr}^{-1}$	0.01	0.13×10^7	0.26×10^3	2.48	-1.91
	0.05	0.21×10^7	0.12×10^4	1.01	-1.73
	0.1	0.27×10^7	0.19×10^4	0.66	-1.62
	0.2	0.34×10^7	0.15×10^4	0.38	-1.42
$\omega = 10 \text{ Gyr}^{-1}$	0.01	0.12×10^7	0.14×10^3	2.48	-1.93
	0.05	0.18×10^7	0.67×10^3	1.01	-1.79
	0.1	0.21×10^7	0.69×10^3	0.66	-1.71
	0.2	0.24×10^7	0.29×10^3	0.38	-1.60
$\omega = 15 \text{ Gyr}^{-1}$	0.01	0.12×10^7	0.97×10^2	2.48	-1.94
	0.05	0.17×10^7	0.46×10^3	1.01	-1.81
	0.1	0.19×10^7	0.30×10^3	0.66	-1.74
	0.2	0.20×10^7	0.11×10^3	0.38	-1.67
$\omega = 20 \text{ Gyr}^{-1}$	0.01	0.12×10^7	0.75×10^2	2.48	-1.94
	0.05	0.17×10^7	0.35×10^3	1.01	-1.81
	0.1	0.17×10^7	0.12×10^3	0.66	-1.76
	0.2	0.18×10^7	0.58×10^2	0.38	-1.71

Table 3.2: *Table:* we reported for each model its main predictions. *Columns:* (1) wind parameter; (2) star formation efficiency; (3) predicted actual total stellar mass; (4) predicted actual total gas mass; (5) time of the onset of the galactic wind; (6) peak of the stellar MDF predicted by the models.

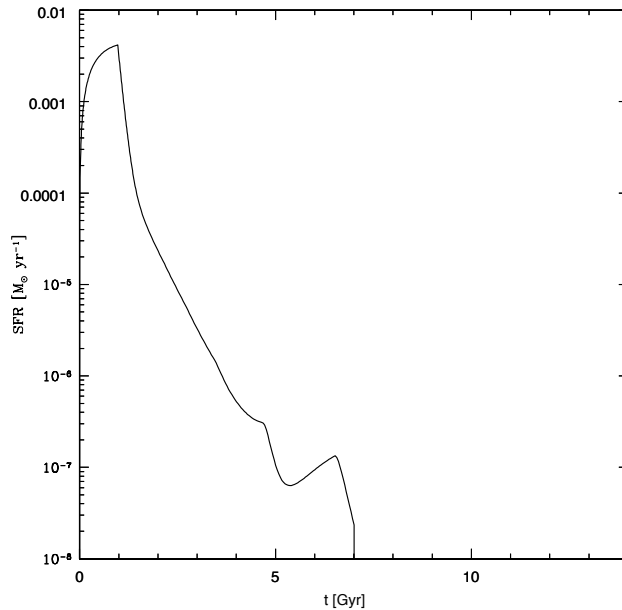


Figure 3.1: In this Figure we show the Sculptor SFR (in M_{\odot}/yr) as predicted by our model with $\nu = 0.05 \text{ Gyr}^{-1}$ and $\omega = 10$, which turned out to well reproduce at the same time the observed abundance ratio patterns and the MDF, as well as the other observed properties of the Sculptor dSph.

Feltzing et al. (2009). The data sample of Ishigaki et al. (2014), not considered in this work for its lower resolution than the other studies, shares three stars in common with Gilmore et al. (2013); in any case, the two data samples turn out to agree with each other in the final chemical abundances of the α -elements.

3.4 Results

3.4.1 Chemical evolution of the Sculptor dSph

We assume the galaxy to form from the accretion of $1.0 \times 10^8 M_{\odot}$ primordial gas, at an infall rate with a time-scale of 0.5 Gyr. According to what has been inferred observationally by means of the CMD-fitting analysis (de Boer et al., 2012), the SFH has been assumed to consist of only one long episode of star formation lasting 7 Gyr. Following the observations, the galaxy is characterized by a massive and extended dark matter halo, with a mass of $3.4 \times 10^8 M_{\odot}$ (Battaglia et al., 2008b); we assume a core radius $r_{DM} = 1 \text{ kpc}$. The effective radius of the *luminous* (baryonic) component of the galaxy has been set at the value of 260 pc (Walker et al., 2009). So the ratio between the core radius of the dark matter halo and the effective radius of the *luminous* matter is $S = \frac{r_L}{r_{DM}} = 0.260$. We need these quantities in order to compute the binding energy of the gas and hence the time at which the galaxy develops the galactic wind.

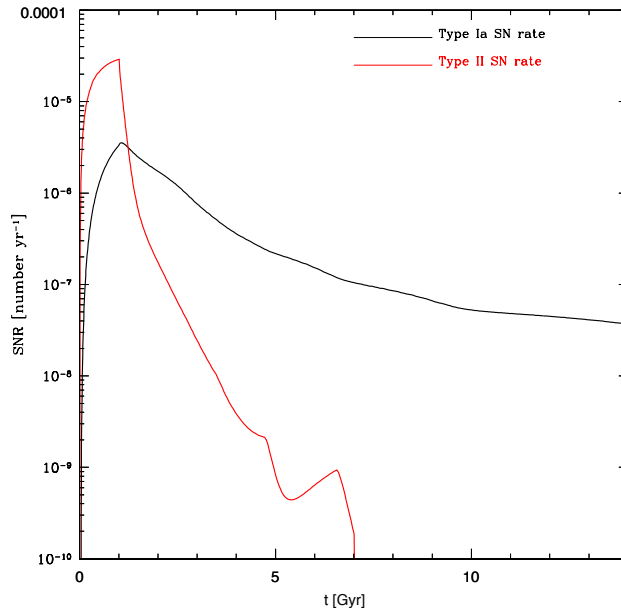


Figure 3.2: In this Figure we plot the Sculptor Type II and Type Ia supernova rates predicted by the same model as Fig. 3.1.

The complete set of the parameters characterizing the chemical evolution models performed for the Sculptor dSph is summarized in Table 3.1. We explore the parameter space by varying the values of ν (efficiency of star formation) and ω (wind parameter), in order to find a model able to reproduce the observed properties of the galaxy, such as the abundance ratios, the MDF and the present time gas and stellar masses. We run models with $\omega = 5, 10, 15$ and 20 ; then, for each value of ω , we vary the star formation efficiency ν , setting it at the following values: $\nu = 0.01, 0.05, 0.1$, and 0.2 Gyr^{-1} .

In Fig. 3.1 we show the trend of the predicted SFR as a function of time. By looking at this Figure, in the earliest stages of the galaxy evolution, the SFR increases very steeply because of the large amount of pristine gas accreted during the infall in a very short time-scale. In fact, we have assumed the SFR, $\psi(t)$, to be proportional to the gas mass. After the majority of the reservoir of gas M_{inf} has been accreted, the star formation begins to decrease in time, since both the SF activity and the galactic wind subtract gas from the galaxy ISM.

In Fig. 3.2 we compare the predicted Type II and Type Ia Supernova rates. While SNe Ia occur on a large range of time-scales (from ~ 35 Myr up to the age of the Universe), depending on the features of the progenitor system, the Type II SN rate traces very closely the trend of the SFR, because of the very short typical time-scales involved (from ~ 1 up to ~ 35 Myr). Thus, after the infall is substantially reduced, the Type II SN rate decreases much more steeply than the Type Ia SN rate. We predict a present time SNIa rate of $6.66 \times 10^{-4} \text{ SNum}$, where SNum represents the rate with units of one SN per 100 yr per $10^{10} M_{\odot}$ stellar mass (Li et al., 2011).

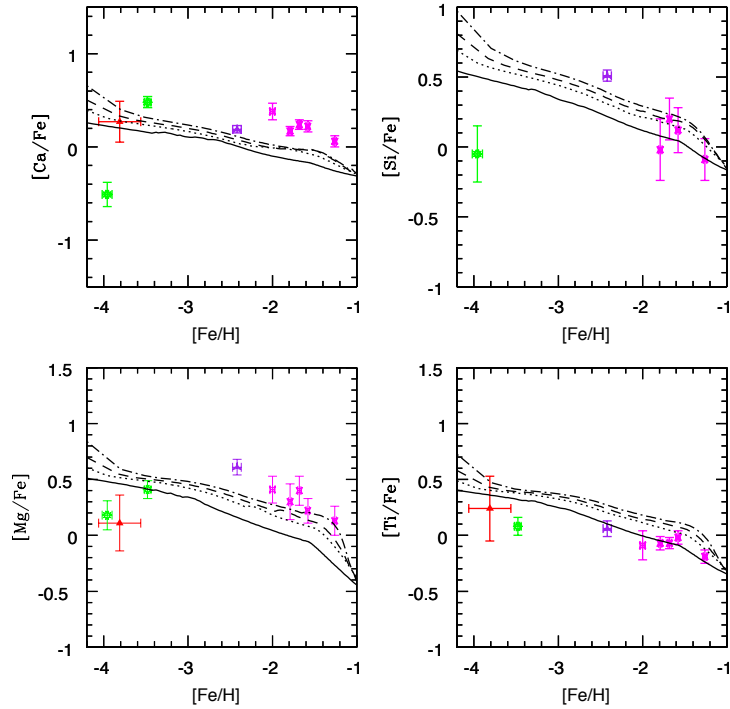


Figure 3.3: In this Figure, we compare the observed Sculptor $[\alpha/\text{Fe}]$ vs. $[\text{Fe}/\text{H}]$ abundance patterns for calcium, silicon, titanium and magnesium with the trends predicted by our $\omega = 10 \text{ Gyr}^{-1}$ models. Data are from Shetrone et al. (2003, in magenta), Tafelmeyer et al. (2010, in green), Frebel (2010, in red) and Kirby & Cohen (2012, in purple). The solid line corresponds to the model with $\nu = 0.01 \text{ Gyr}^{-1}$, the dotted line to the model with $\nu = 0.05 \text{ Gyr}^{-1}$, the long dashed line to the model with $\nu = 0.1 \text{ Gyr}^{-1}$ and the dot-dashed line to the model with $\nu = 0.2 \text{ Gyr}^{-1}$. Low star formation efficiencies ν cause to be small the amount of iron coming from Type II SNe. So, when Type Ia SNe start to pollute the ISM with large amounts of iron, the $[\text{Fe}/\text{H}]$ of the ISM is very low. This gives rise to the decrease of $[\alpha/\text{Fe}]$ as $[\text{Fe}/\text{H}]$ increases. Furthermore, the onset of the galactic wind causes a steepening in the decrease of $[\alpha/\text{Fe}]$ as a function of $[\text{Fe}/\text{H}]$

For each of the models we have calculated, Table 3.2 reports its main predictions regarding the stellar and gas masses at the present time, the time of onset of the galactic wind, and the $[\text{Fe}/\text{H}]$ -peak of the stellar MDF. In the first two columns, Table 3.2 shows again the input parameters (ν and ω) characterizing each model.

By looking at Table 3.2, for a fixed value of the wind parameter ω , models with increasing star formation efficiencies predict slightly larger final total stellar masses and, at the same time, slightly lower final total gas masses. This happens both because star formation is more efficient, and because the galactic wind is predicted to start earlier and earlier, being larger the number of SN events triggering the wind.

The wind parameter ω - which roughly represents the efficiency with which the chemical elements are carried out of the galaxy - characterizes the intensity

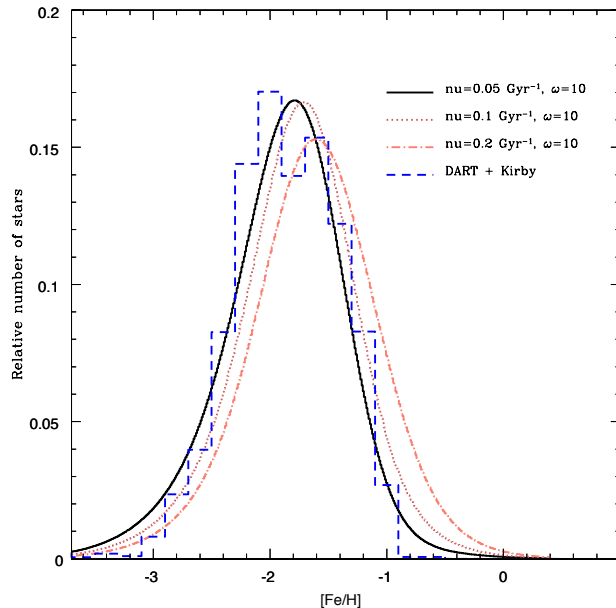


Figure 3.4: The Figure shows the comparison between the observed stellar MDF of the Sculptor dSph and the predictions of our $\omega = 10 \text{ Gyr}^{-1}$ models. The observed dataset comes from Romano & Starkenburg (2013), who combined the data samples of the DART project (Battaglia et al., 2008a; Starkenburg et al., 2010) and of Kirby et al. (2009, 2010). By enhancing the star formation efficiency, the peak of the MDF shift towards higher $[\text{Fe}/\text{H}]$ abundance ratios, because of the shorter time-scales involved in the chemical enrichment of the ISM. At the same time, the height of the peak diminishes, because of the stronger outflow rates ($\propto \psi(t)$), which clean up the galaxy of the gas; that is more evident by passing from $\nu = 0.1 \text{ Gyr}^{-1}$ up to $\nu = 0.2 \text{ Gyr}^{-1}$. The best agreement is obtained with the $\nu = 0.05 \text{ Gyr}^{-1}$ and $\omega = 10 \text{ Gyr}^{-1}$ model.

of the outflow rate. By increasing the wind parameter ω , our models predict the final total gas mass to be lower, since the galactic wind removes the interstellar gas from the galaxy potential well more efficiently. Moreover, as one would expect, the final total stellar mass slightly decreases if the efficiency of the galactic wind is strengthened.

All the models at Table 3.2 predict final stellar masses which are of the same order of magnitude as the observed one $M_{*,obs} = (1.2 \pm 0.6) \times 10^6 M_{\odot}$, which has been derived by de Boer et al. (2012) by integrating the SFR up to the present time; however, this mass is still quite uncertain, since it strongly depends not only on the IMF adopted, but also on the overall CMD-fitting technique. Moreover, all the models predict very low final gas masses ($\sim 10^2 - 10^3 M_{\odot}$), which are lower than $M_{\text{HI}} \approx 1.0 \times 10^4 M_{\odot}$ estimated by Mateo (1998) and very much lower than the most recent estimate of Grcevich & Putman (2009), which inferred for Sculptor an upper limit in the HI mass of $M_{\text{HI}} < 2.34 \times 10^5 M_{\odot}$, although affected by a very large uncertainty.

Finally, from Table 3.2, it is possible to appreciate the net effect of changing

the star formation efficiency ν and the wind parameter ω on the MDF-peak. The lowest $[\text{Fe}/\text{H}]$ at which the MDF has its peak is obtained by the models with the lowest ν and the highest ω .

Sculptor dSph: abundance ratios and interpretation

As already mentioned, the α -elements are mainly produced by Type II SNe, on short time-scales, whereas the bulk of iron and iron-peak elements ($\sim 2/3$ of the total) are produced by Type Ia SNe on a very large range of typical time-scales. The residual quantities of iron and iron-peak elements ($\sim 1/3$ of the total) are synthesized by Type II SNe.

Different typical star formation time-scales can affect the $[\alpha/\text{Fe}]$ vs. $[\text{Fe}/\text{H}]$ diagram with a typical signature (Matteucci & Brocato, 1990; Matteucci, 2001). In fact, low star formation efficiencies cause the amount of iron from Type II SNe to grow very slowly within the ISM. As the first Type Ia SNe start to explode, they deposit a large quantity of iron into the ISM and the $[\alpha/\text{Fe}]$ ratio is expected to steeply decrease at still very low $[\text{Fe}/\text{H}]$. Conversely, high star formation efficiencies give rise to large fractions of iron produced by Type II SNe. In this case, a plateau in the $[\alpha/\text{Fe}]$ vs. $[\text{Fe}/\text{H}]$ diagram is predicted and the decrease occurs at relatively high $[\text{Fe}/\text{H}]$ abundances (see Matteucci 2001). Therefore, the abundance ratios in dSph reflect their low SFR (Lanfranchi & Matteucci, 2004). In Fig. 3.3 we show the effect of different ν values on the predicted $[\alpha/\text{Fe}]$ vs. $[\text{Fe}/\text{H}]$ relations. To lower further the SFR and thus steepening even more the decrease in the $[\alpha/\text{Fe}]$ vs. $[\text{Fe}/\text{H}]$, one can adopt higher values of the wind parameter ω . In fact, the galactic wind subtracts gas to the SF and makes it to decrease. In the models of Fig. 3.3, we assume the outflow to remove all the chemical elements with the same efficiency, i.e. with same ω parameter.

We note that in Fig. 3.3 the data relative to Mg lie below our model predictions. The reason for this can be uncertainties in the data or more likely uncertainties in the Mg yields. These anomalous low-Mg stars have been often associated with inhomogeneous enrichment on small scales from, e.g., single or at least few SNe (Koch et al., 2008a,b; Simon et al., 2010; Frebel & Bromm, 2012; Keller et al., 2014). However, in small systems we should expect that different regions of the ISM mix on small typical timescales and, if the star formation timescales are large enough (and this is the case for dSphs and UFDs), the ISM should have had enough time to mix before new star formation occurs. So we should expect that the enrichment in low-mass and small-scale systems, with very low star formation efficiencies, is more homogeneous rather than more inhomogeneous. In fact, the cooling time for these small systems could be quite low (see Recchi et al. 2002). Furthermore, dSphs seem to be supported by the random motions of stars rather than by regular motions. So, we expect that the thermalisation processes have been efficient and that the one-zone assumption is reasonable. Finally, small systems do not show evident abundance gradients and this is another indicator of a well mixed ISM.

Carina: model parameters								
ν	ω	τ_{inf}	SFH	M_{inf}	M_{DM}	r_{L}	$S = \frac{r_{\text{L}}}{r_{\text{DM}}}$	IMF
[Gyr ⁻¹]	[Gyr ⁻¹]	[Gyr]	[Gyr]	M_{\odot}	M_{\odot}	[pc]		
0.05/0.1/0.2	5/10/20	0.5	0 – 2; 2 – 4; 7 – 9; 9 – 11	1.0×10^8	4.0×10^7	290	0.3625	Salpeter (1955)

Table 3.3: *Table:* we summarize here the specific characteristics of all the chemical evolution models performed for the Carina dSph. *Columns:* (1) star formation efficiency; (2) wind parameter; (3) infall time-scale; (4) period of major star formation activity (Rizzi et al., 2003); (5) total infall gas mass; (6) mass of the dark matter halo (Gilmore et al., 2007); (7) effective radius of the *luminous* (baryonic) matter (Gilmore et al., 2007); (8) ratio between the core radius of the dark matter halo (Gilmore et al., 2007) and the effective radius of the *luminous* matter; (9) initial mass function.

Sculptor dSph: MDF and interpretation

An other important constraint to verify the goodness of a chemical evolution model is to check whether it is able to reproduce the observed stellar MDF. In Fig. 3.4, we show the comparison between the observed stellar MDF and our $\omega = 10 \text{ Gyr}^{-1}$ models. As shown in this Figure, by increasing the star formation efficiency, the predicted stellar MDF peaks towards higher [Fe/H] abundances, since shorter time-scales are involved in the galactic chemical enrichment produced by successive generations of stars. At the same time, by increasing the ν parameter (especially from $\nu = 0.1 \text{ Gyr}^{-1}$ to $\nu = 0.2 \text{ Gyr}^{-1}$), the height of the MDF peak diminishes because of the stronger outflow rate ($\propto \psi(t)$) which leaves, on average, less gas available for star formation. The model which best reproduces the MDF shape of Sculptor is characterized by a star formation efficiency $\nu = 0.05 \text{ Gyr}^{-1}$.

Sculptor dSph: previous models

One of the first detailed chemical evolution models of Sculptor was presented by Lanfranchi & Matteucci (2004). Here we adopt the same theoretical prescriptions and the same numerical code used in that first work

Lanfranchi & Matteucci (2004) did not possess yet an observed MDF dataset for the comparison with the models, since very precise determinations of the Sculptor SFH and physical characteristics have been obtained only recently.

However, although Lanfranchi & Matteucci (2004) had to work with very poorer dataset of chemical abundances, their predictions were similar to the results of this work. The main differences between the models calculated by this work and the ones of Lanfranchi & Matteucci (2004) are the following ones:

- The galactic wind in Lanfranchi & Matteucci (2004) is *differential*, i.e. some elements - in particular the products of SNe Ia - are lost more efficiently than others from the galaxy, following Recchi et al. (2001).
- The models of Lanfranchi & Matteucci (2004) assume a more extended and massive dark matter halo ($M_{\text{DM}} = 5.0 \times 10^9 M_{\odot}$ and $S = \frac{r_{\text{L}}}{r_{\text{DM}}} = 0.1$) than our models.

Carina chemical evolution models					
Input parameters		Model predictions			
	ν	$M_{\star,\text{fin}}$	$M_{\text{gas,fin}}$	t_{wind}	$[\text{Fe}/\text{H}]_{\text{peak}}$
	[Gyr $^{-1}$]	M_{\odot}	M_{\odot}	[Gyr]	dex
$\omega = 5 \text{ Gyr}^{-1}$	0.05	0.16×10^7	0.12×10^4	0.77	-1.87
	0.1	0.20×10^7	0.96×10^3	0.45	-1.71
	0.2	0.28×10^7	0.12×10^4	0.24	-1.50
$\omega = 10 \text{ Gyr}^{-1}$	0.05	0.13×10^7	0.65×10^3	0.77	-1.90
	0.1	0.14×10^7	0.18×10^3	0.45	-1.88
	0.2	0.17×10^7	0.24×10^3	0.24	-1.55
$\omega = 20 \text{ Gyr}^{-1}$	0.05	0.12×10^7	0.31×10^3	0.77	-1.91
	0.1	0.11×10^7	0.30×10^2	0.45	-1.90
	0.2	0.11×10^7	0.51×10^2	0.24	-1.87

Table 3.4: *Table:* we reported for each model its main predictions. *Columns:* (1) wind parameter; (2) star formation efficiency; (3) predicted actual total stellar mass; (4) predicted actual total gas mass; (5) time of the onset of the galactic wind; (6) peak of the stellar MDF predicted by the models.

- The infall gas mass in [Lanfranchi & Matteucci \(2004\)](#) is slightly higher than ours. In fact it is: $M_{\text{inf}} = 5.0 \times 10^8 M_{\odot}$.

[Lanfranchi & Matteucci \(2004\)](#) suggested as best model for Sculptor the one with $\nu = 0.2 \text{ Gyr}^{-1}$ and $\omega_i = 13 \text{ Gyr}^{-1}$.

3.4.2 Chemical evolution of the Carina dSph

The most important difference between Sculptor and Carina resides in their SFH. While the Sculptor SFH is characterized by only one episode, with the SFR continuous for 7 Gyr, the Carina dSph has been observed, from the analysis of its CMD, to have undergone a bursty SFH. So, following [Rizzi et al. \(2003\)](#) and the suggestions of [Lanfranchi et al. \(2006b\)](#), we adopt for the Carina dSph a SFH characterized by 4 episodes, all lasting 2 Gyr, with the first two occurring from 0 to 4 Gyr and the second two occurring from 7 to 11 Gyr.

The galaxy DM halo is characterized by a total mass $M_{\text{DM}} = 4.0 \times 10^7 M_{\odot}$, and a core radius $r_{\text{DM}} = 0.8 \text{ kpc}$ ([Gilmore et al., 2007](#)). The effective radius of the *luminous* (baryonic) matter has been set at the value $r_{\text{L}} = 290 \text{ pc}$ ([Gilmore et al., 2007](#)). So, the ratio between the core radius of the DM halo and the effective radius of the baryonic matter is $S = \frac{r_{\text{C}}}{r_{\text{L}}} = 0.3625$.

According to our model of chemical evolution, the galaxy assembled from the accretion of an *infall mass* $M_{\text{inf}} = 1.0 \times 10^8 M_{\odot}$, made up of primordial gas, with the infall time-scale being assumed to be 0.5 Gyr.

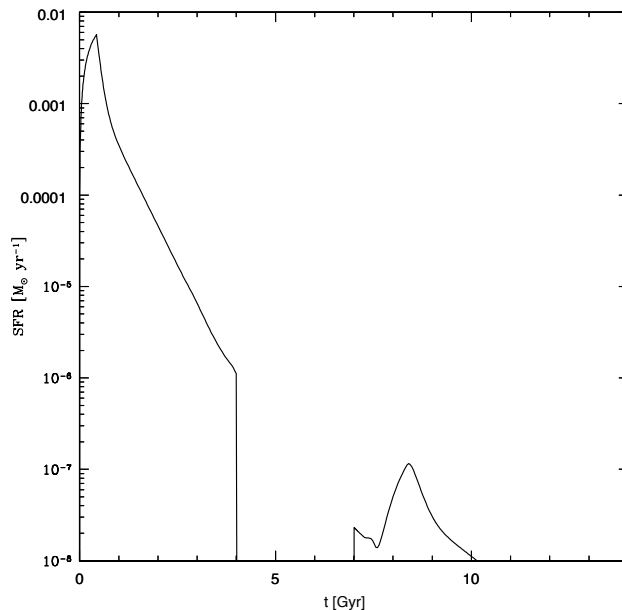


Figure 3.5: In this Figure we show the Carina SFR (in M_{\odot}/yr) as predicted by our model with $\nu = 0.2 \text{ Gyr}^{-1}$ and $\omega = 10 \text{ Gyr}^{-1}$.

In Table 3.3, we summarize all the chemical evolution models we have computed for the Carina dSph. Following the procedure used for the Sculptor dSph, we vary again only the ν and the ω parameters, namely the star formation efficiency and the wind parameter, respectively.

In Fig. 3.5, we show the predicted SFR of the Carina dSph. By looking at that Figure, we can see that there is almost a continuous transition between the first (0 – 2 Gyr) and the second burst (2 – 4 Gyr), as well as from the third (7 – 9 Gyr) and the fourth burst (9 – 11 Gyr). This is due to the fact that the time interval between those episodes is so short that neither the galactic wind nor the gas restored by dying stars might have highly affected the gas mass and therefore the intensity of the SFR. In fact, the SFR has been assumed to be proportional to the gas mass in the galaxy. The discontinuity is clear only between the second (2 – 4 Gyr) and the third (7 – 9 Gyr) burst: during the temporary break (4 – 7 Gyr) of star formation, the gas mass in the galaxy decreases because of the strong outflow rate. So, at the epoch of the third burst (at 7 Gyr), the intensity of the SFR is much lower than the intensity of the SFR at the end of the second burst (at 4 Gyr), when there was much more gas. Here we did not consider external effects on the SFH (see for this Pasetto et al. 2011).

Fig. 3.6 shows the SN rates predicted by the best model. We predict a present time SNIa rate of $7.16 \times 10^{-4} \text{ SNUM}$

In Table 3.4, we report the main predictions of all the chemical evolution models which we have performed for the Carina dSph. In the first two columns, we list the input parameters (ν and ω) characterizing each model. Briefly, by looking at the Table, the reader can note again that enhancing the star formation efficiency ν ,

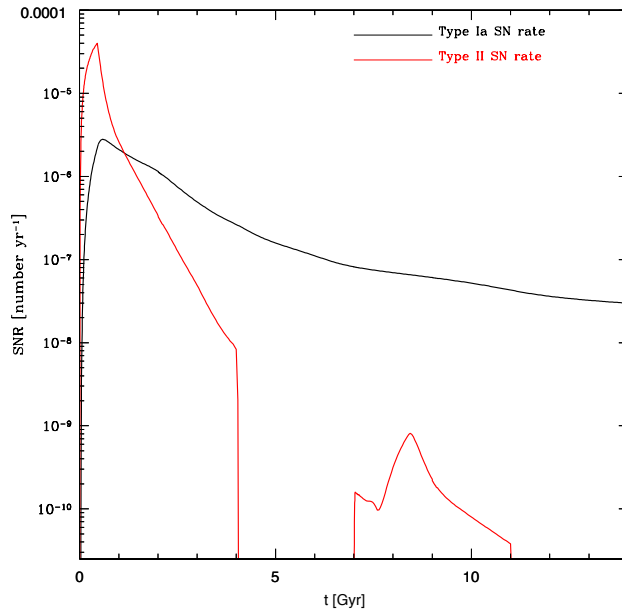


Figure 3.6: In this Figure we plot the Carina Type II and Type Ia supernova rates predicted by the same model as Fig. 3.5.

for a fixed value of the wind parameter ω , will cause the peak of the MDF to shift towards higher values of $[\text{Fe}/\text{H}]$, the galactic wind to begin at earlier times, and the total stellar mass at the present time to be larger. Conversely, for a fixed value of the star formation efficiency ν , models with higher values of the wind parameter ω predict the MDF to shift towards lower $[\text{Fe}/\text{H}]$, and both the stellar and gas masses to be lower at the present time. In order to explain such trends, the same arguments expressed in section 3.4.1 regarding the Sculptor dSph are also valid here, and we will not repeat them again.

From Table 3.4, all the chemical evolution models we calculated predict both final gas and stellar masses at the present time which are in agreement with the observations ($M_{\text{gas,obs}} < 2.1 \times 10^2 M_{\odot}$ from [Grcevich & Putman 2009](#), and $M_{\star,\text{obs}} \approx 1.0 \times 10^6 M_{\odot}$ from [Dekel & Silk 1986](#)).

Carina dSph: abundance ratios and interpretation

Since we adopt low star formation efficiencies, the $[\alpha/\text{Fe}]$ ratio is predicted to decrease at very low $[\text{Fe}/\text{H}]$, and such a decrease steepens even more once the galactic wind starts (see also section 3.4.1). These trends are illustrated in Fig. 3.7 for the pattern of the $[\text{O}/\text{Fe}]$ vs. $[\text{Fe}/\text{H}]$ abundance ratios and in Fig. 3.8 for the calcium, silicon, magnesium and titanium abundance ratios. Especially for the oxygen, there is quite a good agreement between the predictions of our models and the observations.

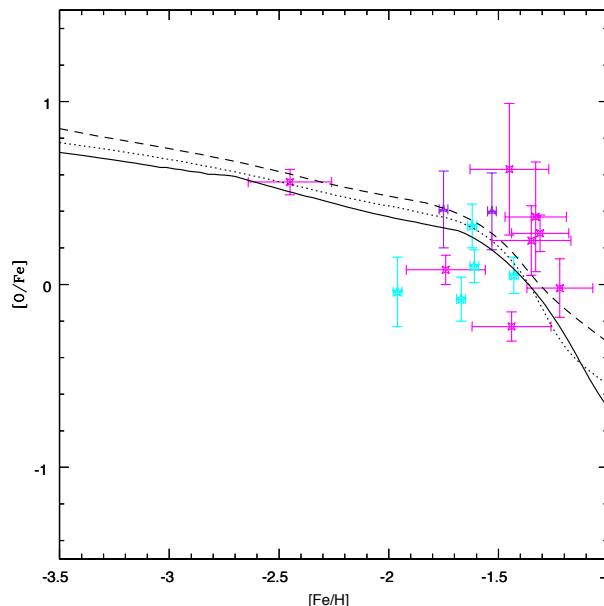


Figure 3.7: In this Figure, we compare the observed $[O/Fe]$ vs. $[Fe/H]$ abundance ratios of the Carina dSph member stars with the trends predicted by our $\omega = 10 \text{ Gyr}^{-1}$ models. The dataset consists of the data samples of Shetrone et al. (2003, in cyan), Koch et al. (2008a, in magenta) and Venn et al. (2012, in purple). The solid line corresponds to the model with $\nu = 0.05 \text{ Gyr}^{-1}$, the dotted line to the model with $\nu = 0.1 \text{ Gyr}^{-1}$ and the dashed line to the model with $\nu = 0.2 \text{ Gyr}^{-1}$.

Carina dSph: MDF and interpretation

In Fig. 3.9, we compare the observed stellar MDF with the one predicted by our $\omega = 10 \text{ Gyr}^{-1}$ models. The best matching is given by the model with $\nu = 0.2 \text{ Gyr}^{-1}$ and $\omega = 10 \text{ Gyr}^{-1}$. Therefore, star formation in Carina was bursty and characterized by a higher efficiency - and so by lower typical time-scales - than in Sculptor. The most evident effect caused by their different typical star formation time-scales resides in the $[Fe/H]$ of their MDF-peak, which is predicted by the best model for Sculptor ($\nu = 0.05 \text{ Gyr}^{-1}$) to be at $[Fe/H] = -1.79$ dex, whereas the Carina best model predicts it at $[Fe/H] = -1.55$ dex.

Carina dSph: previous models

The first detailed chemical evolution model calculated for the Carina dSph was presented in Lanfranchi & Matteucci (2004) and its main basic differences from our models have been already summarized in section 3.4.1. We recall here that they assumed all dSphs to be characterized by the same infall mass and the same mass of DM halo. Conversely, they were able to vary the SFH from galaxy to galaxy, as it was given by the CMD-fitting analysis. They adopted for the Carina dSph a SFH taken from Hernandez et al. (2000), which was not confirmed by later and more accurate observations (Rizzi et al., 2003). In a subsequent paper,

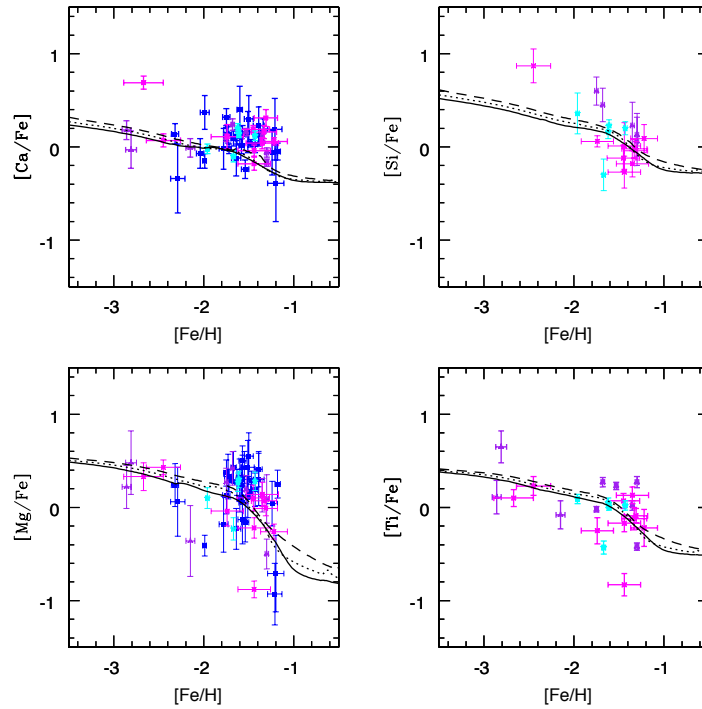


Figure 3.8: In this Figure, we compare the $[\alpha/\text{Fe}]$ vs. $[\text{Fe}/\text{H}]$ abundance ratios for calcium, silicon, titanium and magnesium as observed in the Carina dSph member stars with the trends predicted by our $\omega = 10 \text{ Gyr}^{-1}$ models. The dataset consists of the data samples of [Shetrone et al. \(2003, in cyan\)](#), [Koch et al. \(2008a, in magenta\)](#), [Lemasle et al. \(2012, blue\)](#) and [Venn et al. \(2012, in purple\)](#). The solid line corresponds to the model with $\nu = 0.05 \text{ Gyr}^{-1}$, the dotted line to the model with $\nu = 0.1 \text{ Gyr}^{-1}$ and the dashed line to the model with $\nu = 0.2 \text{ Gyr}^{-1}$.

[Lanfranchi et al. \(2006b\)](#) adopted the SFH from [Rizzi et al. \(2003\)](#) and were able to reproduce the observed stellar MDF.

The final results of both chemical evolution models ([Lanfranchi & Matteucci \(2004\)](#) vs. [Lanfranchi et al. \(2006b\)](#)) are very similar to the ones found by this work, although they adopted a *differential* galactic wind ([Recchi et al., 2001](#)). The best model of [Lanfranchi et al. \(2006b\)](#) has $\nu = 0.14 \text{ Gyr}^{-1}$ and $\omega_i = 5 \text{ Gyr}^{-1}$.

3.4.3 Chemical evolution of the Hercules UfD

The chemical evolution models we have run for the Hercules UfD adopt the same theoretical prescriptions - and so the same numerical code - as the ones adopted for the dSph galaxies. The mass of the DM halo M_{DM} , the effective radius of the *luminous* (baryonic) component of the galaxy, as well as the SFH of the galaxy have been taken from the observations and kept fixed for all the models. The main difference resides in the fact that UfDs suffered an even slower SFR than dSphs (see also [Salvadori & Ferrara 2009](#)).

Hercules: parameters of the models								
ν	ω	τ_{inf}	SFH	M_{inf}	M_{DM}	r_{L}	$S = \frac{r_{\text{L}}}{r_{\text{DM}}}$	IMF
[Gyr $^{-1}$]	[Gyr $^{-1}$]	[Gyr]	[Gyr]	M_{\odot}	M_{\odot}	[pc]		
0.002/0.003/0.005/0.008	10	0.005	0 – 1	1.0/2.5/5.0 $\times 10^7$	1.9 $\times 10^6$	330	0.3	Salpeter (1955)

Table 3.5: *Table:* we summarize here the specific characteristics of all the chemical evolution models performed for the Boötes I UFD. *Columns:* (1) star formation efficiency; (2) wind parameter; (3) infall time-scale; (4) period of major star formation activity (de Jong et al., 2008; Sand et al., 2009); (5) total infall gas mass; (6) mass of the dark matter halo (Adén et al., 2009a); (7) effective radius of the *luminous* (baryonic) matter (Martin et al., 2008); (8) ratio between the core radius of the dark matter halo and the effective radius of the *luminous* matter; (7) initial mass function.

Hercules chemical evolution models						
Input parameters	Model predictions					
	ν	ω	$M_{\star, \text{fin}}$	$M_{\text{gas, fin}}$	t_{wind}	$[\text{Fe}/\text{H}]_{\text{peak}}$
	[Gyr $^{-1}$]	[Gyr $^{-1}$]	M_{\odot}	M_{\odot}	[Gyr]	dex
$M_{\text{inf}} = 1.0 \times 10^7 M_{\odot}$	0.002	10	0.11×10^5	0.35×10^1	0.97	−3.06
	0.003	10	0.14×10^5	0.49×10^1	0.76	−3.03
	0.005	10	0.17×10^5	0.18×10^1	0.56	−2.99
	0.008	10	0.21×10^5	0.82×10^0	0.41	−2.94
$M_{\text{inf}} = 2.5 \times 10^7 M_{\odot}$	0.002	10	0.28×10^5	0.88×10^1	2.41	−3.05
	0.003	10	0.42×10^5	0.13×10^2	1.36	−2.87
	0.005	10	0.66×10^5	0.22×10^2	0.92	−2.67
	0.008	10	0.85×10^5	0.22×10^2	0.71	−2.62
$M_{\text{inf}} = 5.0 \times 10^7 M_{\odot}$	0.002	10	0.55×10^5	0.48×10^8	no wind	−3.05
	0.003	10	0.85×10^5	0.26×10^2	6.76	−2.87
	0.005	10	0.14×10^6	0.44×10^2	1.68	−2.65
	0.008	10	0.22×10^6	0.71×10^2	1.07	−2.43

Table 3.6: *Table:* we reported for each model with *normal wind* its main predictions. *Columns:* (1) Infall mass; (2) star formation efficiency; (3) wind parameter; (4) predicted actual total stellar mass; (5) predicted actual total gas mass; (6) time of the onset of the galactic wind; (7) peak of the stellar MDF predicted by the models.

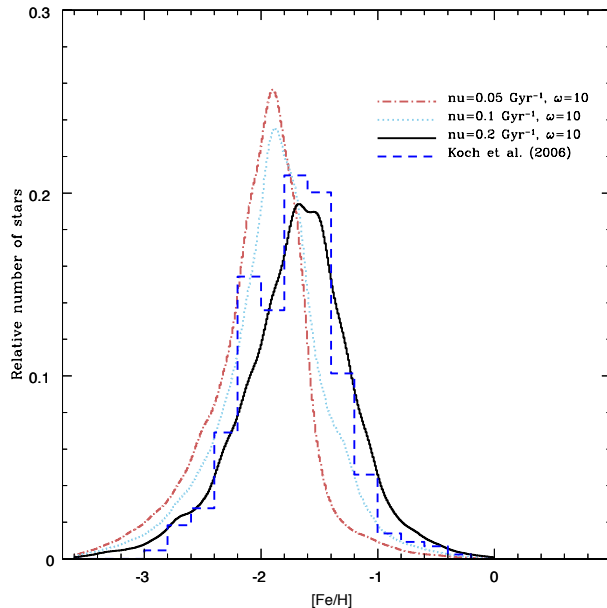


Figure 3.9: The Figure shows the comparison between the observed stellar MDF in the Carina dSph (data from Koch et al. 2006) and the stellar MDFs predicted by our $\omega = 10 \text{ Gyr}^{-1}$ models. The model which best reproduces the observed MDF is characterized by $\nu = 0.2 \text{ Gyr}^{-1}$ and $\omega = 10 \text{ Gyr}^{-1}$.

We assume for the Hercules UFD a DM halo with mass $M_{\text{DM}} = 1.9 \times 10^6 M_{\odot}$ (Adén et al., 2009a). The fraction between the core radius of the DM halo and the effective radius of the baryonic component of the galaxy has been set at $S = \frac{r_{\text{L}}}{r_{\text{DM}}} = 0.3$, where the effective radius of the *luminous* (baryonic) component of the galaxy has been assumed to be $r_{\text{L}} = 330 \text{ pc}$ (Martin et al., 2008).

Since the CMD-fitting analysis derived a SFH concentrated in the very early epochs of the galaxy evolution (de Jong et al., 2008; Sand et al., 2009), we assumed the galaxy to have formed stars in the first Gyr of its evolution (see Table 3.5). This is the only SFH which allowed us to reproduce all the observed features of the galaxy.

Table 3.5 summarizes the parameters of the most relevant models we calculated for the chemical evolution of the Hercules UFD. We test models with three different infall masses: $M_{\text{inf}} = 1.0, 2.5, \text{ and } 5.0 \times 10^7 M_{\odot}$, which have been accreted inside the potential well of the dark matter halo in a very short infall time-scale: $\tau_{\text{inf}} = 0.005 \text{ Gyr}$. This is equivalent to assume that the gas mass is all present since the beginning. The chemical composition of the infalling gas has been assumed to be primordial.

Three different implementations of the galactic wind were tested:

- *normal wind*: all the chemical elements are characterized by the same wind parameter ω . This means that the galactic wind expels all the elements with same efficiency.

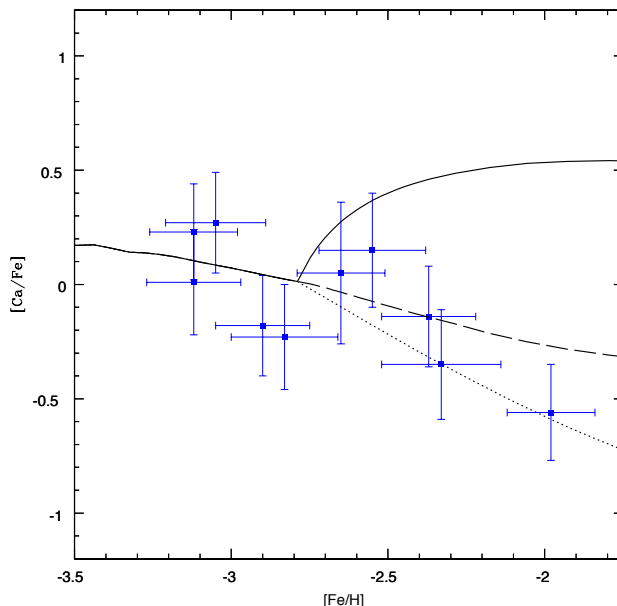


Figure 3.10: In this Figure, we compare the $[Ca/Fe]$ vs. $[Fe/H]$ trends in Hercules predicted by models with different implementations of the galactic wind. The dataset has been taken from Adén et al. (2011). The curve in solid line corresponds to the model with iron-enhanced differential wind (Recchi et al., 2001); the dotted line corresponds to the prediction of the model with α -enhanced differential wind (Marconi et al., 1994), whereas the dashed line represents the prediction of the model with normal wind. The observed dataset (blue squares with errorbars) are from Adén et al. (2011).

- *α -enhanced differential wind* (Marconi et al., 1994): the α -elements are expelled by galactic winds with more efficiency than the iron. This means that $\omega_\alpha > \omega_{Fe}$. We implemented this galactic wind by adopting: $\omega_\alpha = \omega$ and $\omega_{Fe} = 0.3 \times \omega$. This can be explained if we assume that massive stars explode in clusters and therefore they transfer more efficiently their energy into the ISM than isolated SNe such as Type Ia ones.
- *Iron-enhanced differential wind* (Recchi et al., 2001): the iron is expelled by galactic winds more efficiently than the α -elements. This means that $\omega_{Fe} > \omega_\alpha$. This assumption is based on the fact that SNe Ia explode in a medium already heated and diluted by the previous activity of SNe II, as suggested by Recchi et al. (2001). However, Recchi et al. (2004) have later shown that this conclusion is valid only for an isolated starburst.

In Table 3.6, we report the predictions of our models; the first two columns specify each model in terms of its input parameters M_{inf} , ν , and ω . All the models predict a very small total gas mass at the present time, in agreement with the observations ($M_{gas,obs} < 466 M_\odot$, from Greivich & Putman 2009). The actual total stellar mass of the galaxy ($M_{*,obs} = 7.2^{+1.2}_{-1.1} \times 10^4 M_\odot$, from Martin et al. 2008) is quite well reproduced by our models. However, we have to stress that such

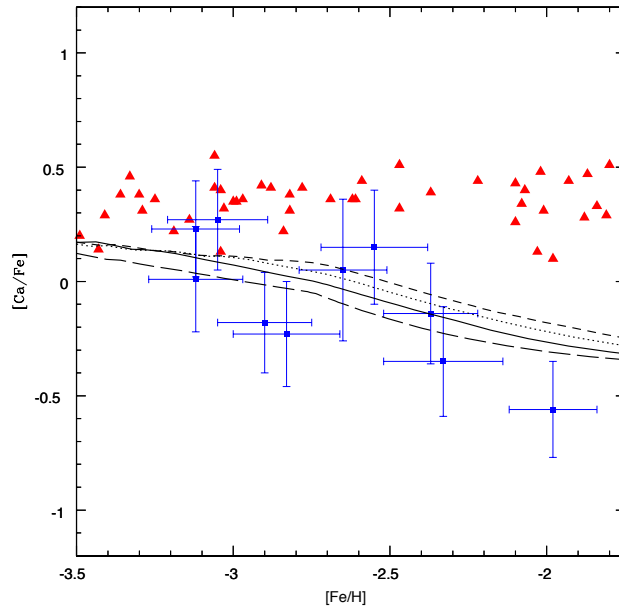


Figure 3.11: In this Figure, we compare the $[\text{Ca}/\text{Fe}]$ vs. $[\text{Fe}/\text{H}]$ abundance pattern as observed in the Hercules UFD member stars (data from Adén et al. 2011) with the predictions of our models with $\omega = 10 \text{ Gyr}^{-1}$ (normal wind) and $M_{\text{inf}} = 1.0 \times 10^7 M_{\odot}$. We show also the abundance pattern of $[\text{Ca}/\text{Fe}]$ vs. $[\text{Fe}/\text{H}]$ as observed in Galactic halo stars (red triangles, data from Gratton et al. 2003; Reddy et al. 2003; Cayrel et al. 2004; Reddy et al. 2006). The prediction of the model with $\nu = 0.002 \text{ Gyr}^{-1}$ is in long dashed line; the model with $\nu = 0.003 \text{ Gyr}^{-1}$ is in solid line; the model with $\nu = 0.005 \text{ Gyr}^{-1}$ is illustrated in dotted line, whereas the model with $\nu = 0.008 \text{ Gyr}^{-1}$ is represented by the dashed line. By looking at this Figure, it is clear that Hercules UFD member stars suggest different trend of $[\text{Ca}/\text{Fe}]$ as a function of $[\text{Fe}/\text{H}]$.

observed quantities remain still rather uncertain at the present time.

All our models predict the MDF to peak at extremely low $[\text{Fe}/\text{H}]$ abundances. This is an effect both of the very low star formation efficiencies and of the very shallow potential well, which allows the galactic wind to develop earlier and, therefore, to diminish further the SFR in the subsequent evolution of the galaxy. Although we varied the ν parameter within a small range (from $\nu = 0.002 \text{ Gyr}^{-1}$ up to $\nu = 0.008 \text{ Gyr}^{-1}$), we obtain significant variations in the final predicted features of the galaxy.

As one can see in Table 3.6, diminishing the infall mass M_{inf} will cause the MDF to peak at smaller $[\text{Fe}/\text{H}]$ values, once the other parameters are fixed. That is because the SFR has been assumed to be proportional to the gas mass inside the galaxy. In fact, the larger the gas mass available, the higher will be the star formation activity; so the chemical enrichment of the ISM will proceed at higher rates, shifting the MDF towards higher $[\text{Fe}/\text{H}]$.

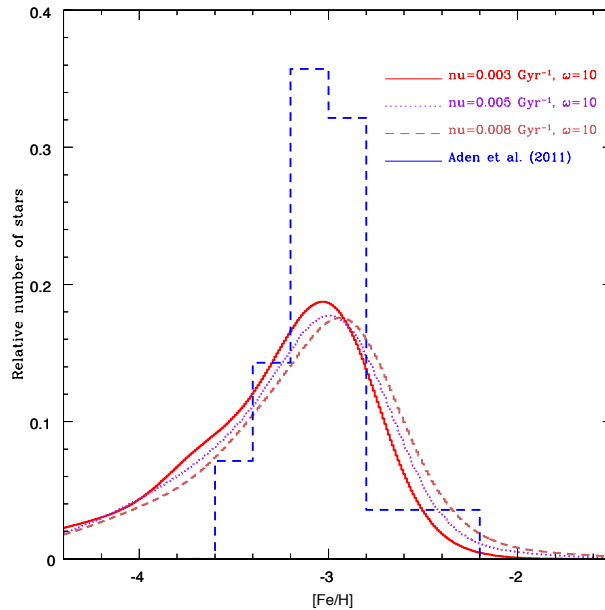


Figure 3.12: In this Figure, we show the comparison between the observed stellar MDF of the Hercules UfD (data from Adén et al. 2011) and the predictions of our models with $\omega = 10 \text{ Gyr}^{-1}$ (normal wind) and $M_{\text{inf}} = 1.0 \times 10^7 M_{\odot}$. The dataset is built up on a sample of only 28 RGB stars, with $[\text{Fe}/\text{H}]$ values in a very tight range, between $[\text{Fe}/\text{H}] = -3.1$ dex and $[\text{Fe}/\text{H}] = -2.9$ dex and very low relative numbers of stars in the other bins towards both lower and higher $[\text{Fe}/\text{H}]$ abundances. The MDF predicted by our models are based on a large number of artificial stars, according to the SFH and to the IMF assumed. We are not able to reproduce the height of the observed-MDF peak. Our choice of the best model is oriented towards the model which reproduces the $[\text{Fe}/\text{H}]_{\text{peak}}$ abundance of the observed MDF, which turns out to have $\nu = 0.003 \text{ Gyr}^{-1}$ and $\omega = 10 \text{ Gyr}^{-1}$.

Hercules UfD: abundance ratios and interpretation

At extremely low $[\text{Fe}/\text{H}]$, it turns out that $[\text{Ca}/\text{Fe}]$ in the Hercules UfD steeply decreases from abundances above the solar values ($[\text{Ca}/\text{Fe}] = +0.32 \pm 0.22$ dex at $[\text{Fe}/\text{H}] = -3.10 \pm 0.16$ dex) down to $[\text{Ca}/\text{Fe}] = -0.51 \pm 0.21$ dex at $[\text{Fe}/\text{H}] = -2.03 \pm 0.14$ dex (Adén et al., 2011). In order to reproduce such a trend, confirmed also by successive observational spectroscopic studies of UfD stars (Gilmore et al., 2013; Vargas et al., 2013), we test a formation scenario characterized by a very short infall time-scale ($\tau_{\text{infall}} = 0.005 \text{ Gyr}$) and very low star formation efficiencies ($0.003 \text{ Gyr}^{-1} \leq \nu \leq 0.008 \text{ Gyr}^{-1}$), even lower than for dSphs and in agreement with previous studies (Salvadori & Ferrara, 2009). The short infall time-scale gives rise to an enhanced SFR in the earliest stages of galaxy evolution, during which large amounts of α -elements were likely to be ejected by Type II SN explosions into the ISM, whereas the extremely low star formation efficiency produces a very slow growth of the $[\text{Fe}/\text{H}]$ abundance; so when SNe Ia occur, the $[\text{Fe}/\text{H}]$ is still very low and the $[\text{Ca}/\text{Fe}]$ steeply decreases.

In Fig. 3.10, we show the effect of the various wind implementations on the

Boötes I: parameters of the models								
ν	ω	τ_{inf}	SFH	M_{inf}	M_{DM}	r_{L}	$S = \frac{r_{\text{L}}}{r_{\text{DM}}}$	IMF
[Gyr ⁻¹]	[Gyr ⁻¹]	[Gyr]	[Gyr]	M_{\odot}	M_{\odot}	[pc]		
0.002/0.005/0.01/0.05	10/15	0.005	0 – 4	1.0/2.5/5.0 × 10 ⁷	0.30 × 10 ⁷	242	0.2	Salpeter (1955)

Table 3.7: *Table:* we summarize here the specific characteristics of all the chemical evolution models performed for the Boötes I UFD. *Columns:* (1) star formation efficiency; (2) wind parameter; (3) infall time-scale; (4) period of major star formation activity (de Jong et al., 2008); (5) total infall gas mass; (6) mass of the dark matter halo (Collins et al., 2013); (7) effective radius of the *luminous* (baryonic) matter (Martin et al., 2008); (8) ratio between the core radius of the dark matter halo and the effective radius of the *luminous* matter; (9) initial mass function.

[Ca/Fe] vs. [Fe/H] diagram. An iron-enhanced *differential wind* is not able to reproduce the observed steep decrease in [Ca/Fe] vs. [Fe/H]. Conversely, models with normal and α -enhanced differential wind agree with the observations. By looking at this Figure, the three models predict the galactic wind to start at the same time. In fact, by fixing the τ_{inf} and M_{inf} parameters, the time of the galactic wind onset depends only upon the features of the galaxy potential well (which affects the binding energy of the gas) and upon the SFH of the galaxy (which affects the computation of the thermal energy of the ISM). Therefore, the only parameter affecting the time of onset of the galactic wind is the ν parameter, whereas the ω parameter, as well as its particular implementation, comes into play only after the wind has started. An iron-enhanced differential wind predicts the [Ca/Fe] to increase as [Fe/H] grows, soon after the wind onset, at variance with observations. In fact, while SNe Ia enrich the ISM with large amounts of iron, causing the [Fe/H] in the ISM to grow with time, the iron is also expelled by the galactic wind with higher efficiency than the α -elements as the calcium.

Since we do not still have evidences of galactic outflows enriched in α -elements, we preferred as best models those with normal galactic wind.

In Fig. 3.11, we show the effect of changing the ν parameter on the [Ca/Fe] vs. [Fe/H] diagram, with $\omega = 10 \text{ Gyr}^{-1}$ (normal wind) and $M_{\text{inf}} = 1.0 \times 10^7 M_{\odot}$. The model which best reproduces the overall trend suggested by the dataset is characterized by $\nu = 0.003 \text{ Gyr}^{-1}$ and $\omega = 10 \text{ Gyr}^{-1}$. In this Figure, we report also the observed [Ca/Fe] vs. [Fe/H] abundance pattern of Galactic halo stars. Although more data are necessary, Hercules UFD stars and Galactic halo stars display different trends of [Ca/Fe] vs. [Fe/H]. In particular, halo stars do not share the fast decline in [α /Fe] exhibited by the stars in Hercules. This fact seems to rule out the hypothesis that UFDs would have been the building blocks of the stellar halo of the Milky Way. In fact, models (e.g. Brusadin et al. 2013) suggest that the Galactic halo have formed on a time-scale of $\approx 0.2 \text{ Gyr}$ with a SF efficiency $\nu = 0.2 \text{ Gyr}^{-1}$ and wind parameter $\simeq 14$.

Boötes I chemical evolution models						
Input parameters			Model predictions			
	ν	ω	$M_{*,\text{fin}}$	$M_{\text{gas,fin}}$	t_{wind}	$[\text{Fe}/\text{H}]_{\text{peak}}$
	$[\text{Gyr}^{-1}]$	$[\text{Gyr}^{-1}]$	M_{\odot}	M_{\odot}	$[\text{Gyr}]$	dex
$M_{\text{inf}} = 1.0 \times 10^7 M_{\odot}$	0.002	10	0.14×10^5	0.35×10^1	1.17	-2.99
	0.005	10	0.21×10^5	0.50×10^1	0.68	-2.91
	0.01	10	0.29×10^5	0.14×10^1	0.45	-2.81
	0.05	10	0.68×10^5	0.68×10^0	0.16	-2.55
$M_{\text{inf}} = 2.5 \times 10^7 M_{\odot}$	0.002	10	0.58×10^5	0.90×10^1	2.01	-2.68
	0.005	10	0.75×10^5	0.57×10^2	2.65	-2.69
	0.01	10	0.11×10^6	0.39×10^2	0.76	-2.51
	0.05	10	0.25×10^6	0.55×10^1	0.29	-2.31
$M_{\text{inf}} = 5.0 \times 10^7 M_{\odot}$	0.002	10	0.19×10^6	0.19×10^2	3.21	-2.39
	0.005	10	0.25×10^6	0.45×10^2	1.72	-2.34
	0.01	10	0.33×10^6	0.89×10^2	1.12	-2.28
	0.05	10	0.70×10^6	0.35×10^2	0.44	-2.06

Table 3.8: *Table:* we reported for each model its main predictions. *Columns:* (1) wind parameter; (2) star formation efficiency; (3) predicted actual total stellar mass; (4) predicted actual total gas mass; (5) time of the onset of the galactic wind; (6) peak of the stellar MDF predicted by the models.

Hercules UFD: MDF and interpretation

The observed stellar MDF (Adén et al., 2011) is built up on a very poor statistical sample, which consists of only 28 RGB stars - the most luminous ones - previously identified and studied by Adén et al. (2009b). It turns out that most of the stars in the Adén et al. (2011) sample resides in a very tight metallicity range, between $[\text{Fe}/\text{H}] = -3.1$ dex and $[\text{Fe}/\text{H}] = -2.9$ dex, with very low relative numbers of stars in the other bins towards both lower and higher $[\text{Fe}/\text{H}]$ abundances. Conversely, our predicted stellar MDF is based upon a very large number of *artificial* stars determined from the assumed SFR and IMF. So, when we normalize the number of stars counted in a specific $[\text{Fe}/\text{H}]$ -bin to the total number of stars, the height of the peak in the observed stellar MDF turns always out much higher than the more “populated” and dispersed MDF of our models.

In Fig. 3.12, we have reported the comparisons between the observed MDF and our models with $M_{\text{inf}} = 1.0 \times 10^7 M_{\odot}$. By looking at the Figure, the only model matching the observations is characterized by a star formation efficiency $\nu = 0.003 \text{ Gyr}^{-1}$; it is able to reproduce the $[\text{Fe}/\text{H}]$ -position of the peak, as well as the width of the observed MDF, although it predicts a rather large relative number of stars in the extremely low $[\text{Fe}/\text{H}]$ -wing, which spectroscopic observations have not yet been able to cover, because of the extremely low flux coming from those UFD member stars and the still relative low signal-to-noise ratio affecting the observations. By supposing that at extremely low $[\text{Fe}/\text{H}]$ abundances a hypothetical

previous very massive population of stars might have enriched the medium with metals, the predicted relative number of stars with very low $[\text{Fe}/\text{H}]$ could be diminished, as it was similarly suggested in the past for solving the so-called *G-dwarf problem* in the solar neighborhood. Here we only envisage this hypothesis but we did not test its validity. Finally, by supposing that the chemical composition of the initial infall gas mass is not primordial but rather pre-enriched with metals by a previous population of stars, the observed enhanced α -element abundances at extremely low $[\text{Fe}/\text{H}]$ might be explained. In fact, this might increase the initial metal content within the ISM and allow to build up that “common *metallicity floor*” to all the various different galaxy types, as suggested by Ferrara (2012).

Our best model for Hercules requires $\nu = 0.003 \text{ Gyr}^{-1}$, $\omega = 10 \text{ Gyr}^{-1}$ and $M_{\text{inf}} = 1.0 \times 10^7 M_{\odot}$.

3.4.4 Chemical evolution of the Boötes I UfD

We assume for the Boötes I UfD a dark matter halo with mass $M_{\text{DM}} = 0.30 \times 10^7 M_{\odot}$ (Collins et al., 2013). The ratio between the core radius of the DM halo and the effective radius of the galaxy baryonic component has been assumed to be $S = \frac{r_{\text{L}}}{r_{\text{DM}}} = 0.2$, where the effective radius of the baryonic (*luminous*) component of the galaxy is $r_{\text{L}} = 242 \text{ pc}$ (Martin et al., 2008). The SFH has been assumed to be made of only one episode lasting 4 Gyr, from 0 up to 4 Gyr (de Jong et al., 2008).

The infall mass of primordial gas from which the galaxy formed by accretion has been varied; we tested models with $M_{\text{inf}} = 1.0, 2.5$ and $5.0 \times 10^7 M_{\odot}$. The infall time-scale of such initial reservoir of gas has been assumed to be very short, $\tau_{\text{inf}} = 0.005 \text{ Gyr}$. In Table 3.7, we reported the parameters of our Boötes I chemical evolution models. All the models are characterized by a *normal* galactic wind.

In Table 3.8, we report the main predictions of our chemical evolution models. In the first two columns, we listed the input parameters: M_{inf} and ν . From the Table, the lower the star formation efficiency ν - as well as the lower the infall mass M_{inf} - the lower will be the $[\text{Fe}/\text{H}]$ at which the stellar MDF has its peak. Our models predict extremely low total gas content at the present time, as well as much lower total stellar mass than in dSph galaxies. This is again an effect both of the low initial infall gas mass and of the very low star formation efficiencies. The predicted final total gas masses are in agreement with the observed values ($M_{\text{gas,obs}} < 86 M_{\odot}$, from Grcevich & Putman 2009), as well as the predicted final total stellar masses agree quite well with the observed value $M_{\star,\text{obs}} = (6.7 \pm 0.6) \times 10^4 M_{\odot}$, from Martin et al. (2008), which is however very uncertain since it was inferred from a poor number of hypothetical stars belonging to the galaxy: $N_{\star} = 324_{-23}^{+28}$, derived by means of a maximum likelihood algorithm applied to SDSS data. Furthermore, the observed total stellar mass strongly depends also on the IMF adopted and here we report the quantity derived by Martin et al. (2008) when using the Salpeter (1955) IMF.

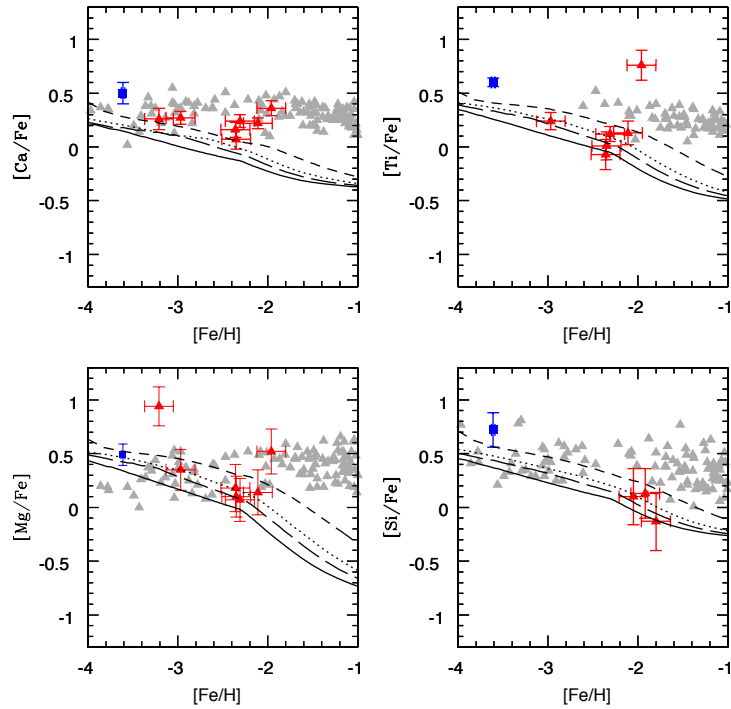


Figure 3.13: In this Figure, we compare the $[\alpha/\text{Fe}]$ vs. $[\text{Fe}/\text{H}]$ abundance ratios for calcium, silicon, titanium and magnesium as observed in the Boötes I UFD member stars with the trends predicted by our models with $\omega = 10 \text{ Gyr}^{-1}$ (normal wind) and $M_{\text{inf}} = 2.5 \times 10^7 M_{\odot}$. The dataset consists of the data samples of Norris et al. (2010, blue squares) and Gilmore et al. (2013, red triangles) (“NY” analysis, from Norris et al. 2010). The model with $\nu = 0.002 \text{ Gyr}^{-1}$ is given by the solid line; the model with $\nu = 0.005 \text{ Gyr}^{-1}$ is given by the long dashed line, whereas the model with $\nu = 0.01 \text{ Gyr}^{-1}$ is represented by the dotted line. Eventually, the model with $\nu = 0.05 \text{ Gyr}^{-1}$ is represented by the dashed line. We show also the abundance patterns of $[\alpha/\text{Fe}]$ vs. $[\text{Fe}/\text{H}]$ as observed in Galactic halo stars (grey triangles, data from Gratton et al. 2003; Reddy et al. 2003; Cayrel et al. 2004; Reddy et al. 2006).

Boötes I UFD: abundance ratios and interpretation

In order to reproduce the $[\alpha/\text{Fe}]$ vs. $[\text{Fe}/\text{H}]$ observed trends (Gilmore et al., 2013; Norris et al., 2010), which are indeed rather uncertain, we adopted a very short infall time-scale - which enhances the SFR in the earliest stages of the galaxy evolution, giving rise to high $[\alpha/\text{Fe}]$ abundances at extremely low $[\text{Fe}/\text{H}]$ - coupled with very low star formation efficiencies - which cause the decrease in the α -element abundances to start at very low $[\text{Fe}/\text{H}]$. We show our results in Fig. (3.13), where we compare our theoretical curves with the observed dataset of the $[\alpha/\text{Fe}]$ vs. $[\text{Fe}/\text{H}]$ abundance patterns for calcium, silicon, titanium and magnesium. In this Figure, we compare also the chemical abundances of Boötes I UFD member stars with those of Galactic halo stars.

The best agreement with the observed dataset is obtained by the model with $\nu = 0.01 \text{ Gyr}^{-1}$, $\omega = 10 \text{ Gyr}^{-1}$ and $M_{\text{inf}} = 2.5 \times 10^7 M_{\odot}$. At extremely low

[Fe/H], the stars of Boötes I display enhanced [Ca/Fe] abundance ratios. Although our theoretical curves are able to reproduce the titanium, magnesium and silicon abundance patterns, there is still a discrepancy with calcium. That is probably due to the large uncertainty in the calcium yields from massive stars.

Boötes I UFD: MDF and interpretation

The observed stellar MDF has been taken from [Lai et al. \(2011\)](#). Originally, their data sample was constituted by low-resolution spectra of 25 stars, which then was extended to 41 stars by adding non-overlapping stars from [Norris et al. \(2010\)](#) and [Feltzing et al. \(2009\)](#). This gave rise to an inhomogeneous collection of datasets, which is also a rather poor statistical sample.

As in the case of the Hercules stellar MDF (see section 3.4.3), also here we are not able to reproduce the height of the observed MDF-peak. This is clearly illustrated in Fig. 3.14, where we also show that the only model able to reproduce the peak and the width of the observed MDF is characterized by $\nu = 0.01 \text{ Gyr}^{-1}$, $\omega = 10 \text{ Gyr}^{-1}$ and $M_{\text{inf}} = 2.5 \times 10^7 M_{\odot}$.

3.5 Conclusions

Summary on dSph chemical evolution

We have assumed that dSph galaxies form by accretion of an *infall mass* of $M_{\text{inf}} = 1.0 \times 10^8 M_{\odot}$ with primordial chemical composition. The infall rate obeys to a decaying exponential law with an *infall time-scale* $\tau_{\text{inf}} = 0.5 \text{ Gyr}$. The mass content and the core radius of the DM halo have been taken from the observations. In particular, here we modeled Sculptor and Carina and our results can be summarized as follows.

- Only by assuming low star formation efficiencies ($\nu = 0.05 - 0.5 \text{ Gyr}^{-1}$) relative to the Milky Way ($\nu \sim 1 \text{ Gyr}^{-1}$ in the solar vicinity, [Chiappini et al. 1997](#)), we have been able to explain the decline in the $[\alpha/\text{Fe}]$ abundance ratios observed at very low [Fe/H]. In fact, the lower the ν parameter, the lower is the amount of iron produced by Type II SNe; this causes the [Fe/H] of the ISM, at which Type Ia SNe become predominant in the iron pollution, to be lower. This precisely determines the decrease in the $[\alpha/\text{Fe}]$ at very low [Fe/H]. This is due to the fact that most of α -elements originates in Type II SNe whereas most of Fe originates in Type Ia SNe exploding on a large range of times (time-delay model).
- Low star formation efficiencies increase the star formation time-scales, giving rise to stellar MDFs peaked towards very low [Fe/H], in very good agreement with the observations indicating that dSphs are very metal-poor stellar systems.
- Galactic winds - driven by SN explosions - play a relevant role in the dSph chemical evolution. We adopted for dSphs a *normal* wind, i.e. a wind with

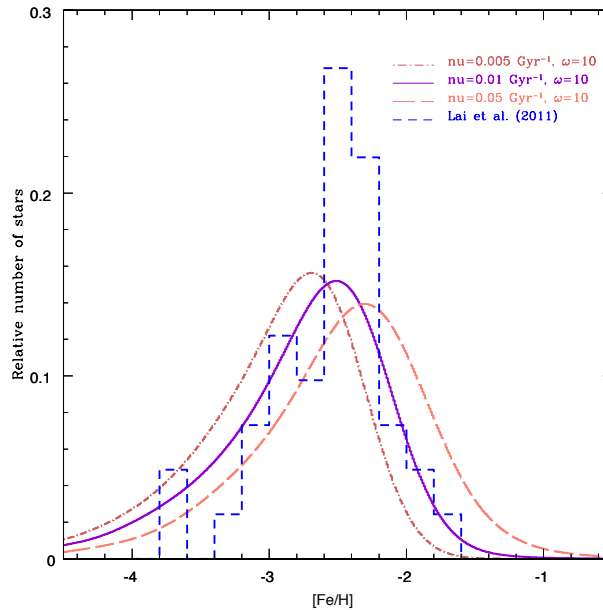


Figure 3.14: In this Figure, we show the comparison between the observed stellar MDF of the Boötes I UfD (data from [Lai et al. 2011](#)) and the predictions of our models with $\omega = 10 \text{ Gyr}^{-1}$ (normal wind) and $M_{\text{inf}} = 2.5 \times 10^7 M_{\odot}$. Again, as in the case of the Hercules UfD, the dataset is built up on a sample of only 41 stars, highly concentrated in a very tight $[\text{Fe}/\text{H}]$ range. We are not able to reproduce the height of the observed-MDF peak. The model which best reproduces the $[\text{Fe}/\text{H}]_{\text{peak}}$ abundance of the observed MDF turns out to have $\nu = 0.01 \text{ Gyr}^{-1}$ and $\omega = 10 \text{ Gyr}^{-1}$.

an efficiency equal for all the chemical elements. The net effect of the galactic wind is to diminish further the SFR and cause the $[\alpha/\text{Fe}]$ to follow a steeper decline as $[\text{Fe}/\text{H}]$ increases. Thanks to the strong outflow rates, our models predict very low final total gas masses, according to observations.

- Only by adopting star formation episodes occurring far beyond the reionization epoch, our models were able to build up final total stellar masses of the same order of magnitude as the observed ones ($M_{\star, \text{obs}} \sim 10^6 M_{\odot}$), and they could also reproduce the other observed features of dSph galaxies. Our assumptions were based on the results of the CMD-fitting analysis, which have been able, in the past few years, to derive the SFH of many dwarf galaxies of the Local Group.
- We adopted the [Salpeter \(1955\)](#) IMF for all the models. In a recent paper, [McWilliam et al. \(2013\)](#) suggested that to explain the abundance data in Sagittarius an IMF with a lower fraction of massive stars than a Salpeter-like IMF should be preferred (see the next Chapter).
- Our best models are in good agreement with the previous works ([Lanfranchi & Matteucci, 2004](#); [Lanfranchi et al., 2006b](#)) and confirm their goodness. Our

best model for Sculptor requires $\nu = 0.05 \text{ Gyr}^{-1}$ and $\omega = 10 \text{ Gyr}^{-1}$, whereas our best model for Carina requires $\nu = 0.2 \text{ Gyr}^{-1}$ and $\omega = 10 \text{ Gyr}^{-1}$.

Summary on UfD chemical evolution

We have modeled Hercules and Boötes I, by adopting the same numerical code of dSphs but with different characteristic input parameters. In what follows, we summarize the main features of our UfD chemical evolution models:

- Since UfDs are known today to be the faintest and most DM dominated galaxies, we adopted *infall masses* $M_{\text{inf}} = (1.0 - 5.0) \times 10^7 M_{\odot}$, which are lower than the ones assumed for dSphs and supported by observations. Such initial reservoir of gas, with primordial chemical composition, was accreted in the galaxy DM halo on a very short typical time-scale ($\tau_{\text{inf}} = 0.005 \text{ Gyr}$).
- Our best model for Hercules requires $\nu = 0.003 \text{ Gyr}^{-1}$, $\omega = 10 \text{ Gyr}^{-1}$, $M_{\text{inf}} = 1.0 \times 10^7 M_{\odot}$ and $\tau_{\text{inf}} = 0.005 \text{ Gyr}$, whereas our best model for Boötes I requires $\nu = 0.01 \text{ Gyr}^{-1}$, $\omega = 10 \text{ Gyr}^{-1}$, $M_{\text{inf}} = 2.5 \times 10^7 M_{\odot}$ and $\tau_{\text{inf}} = 0.005 \text{ Gyr}$.
- The $[\alpha/\text{Fe}]$ abundance ratios are observed to steeply decrease at very low $[\text{Fe}/\text{H}]$. This is clearly a signature of very low star formation efficiencies ($\nu = 0.001 - 0.01 \text{ Gyr}^{-1}$), even lower than for the dSph ones ($\nu \approx 0.05 - 0.5 \text{ Gyr}^{-1}$). In fact, Type Ia SNe start to dominate in the iron pollution of the ISM when the $[\text{Fe}/\text{H}]$ of the ISM is still very low. This result is in agreement with the previous studies of UfD galaxies, such as [Salvadori & Ferrara \(2009\)](#)
- The very low adopted star formation efficiencies cause the stellar MDFs to be peaked at very low $[\text{Fe}/\text{H}]$, in very good agreement with observations.
- From the CMD-fitting analysis, as well as from the study of the pulsation and metallicity properties of their variable stars, UfDs host very old stellar populations, with ages $> 10 - 12 \text{ Gyr}$. So, we have assumed them to have undergone star formation only in the first billion years of their chemical evolution history. This fact, coupled with the very low star formation efficiencies, causes the building up of very low final total stellar masses $M_{\star, \text{fin}} \sim 10^4 - 10^5 M_{\odot}$, which are much lower than in the observed dSph ones, and in agreement with observational values.
- The actual total gas masses in UfDs are negligible or even undetected. This is a clear evidence of intense galactic winds, which are efficient in the gas removal from the galaxy potential well and started very soon in the galaxy evolution. We tested models with *normal wind*, α -enhanced *differential wind*, and iron-enhanced *differential wind*. All such models agree in predicting negligible final total gas masses but each of them has a different effect in the $[\alpha/\text{Fe}]$ vs. $[\text{Fe}/\text{H}]$ diagram.
- Both *normal* and α -enhanced galactic winds predict a trend of the $[\alpha/\text{Fe}]$ vs. $[\text{Fe}/\text{H}]$ diagram which well agrees with observations. On the other hand,

an iron-enhanced *differential wind* predicts the $[\alpha/\text{Fe}]$ to increase as $[\text{Fe}/\text{H}]$ grows once the galactic wind has started, at variance with observations. We suggest the galactic wind to be normal with an efficiency $\omega = 10 \text{ Gyr}^{-1}$, which is the same value adopted here for reproducing the main properties of dSph galaxies.

- Our chemical evolution models have been able to reproduce, at the same time and reasonably well, all the observed features of the two UFD galaxies studied, such as the abundance ratio patterns of the α -elements, the stellar MDF, and the total stellar and gas masses at the present time. From the main characteristics of our chemical evolution models and from the observed trend of the UFD chemical abundances, we suggest that the hypothesis that UFDs would have been the survived “building blocks” of the Milky Way halo is unlikely, since the two seem to have undergone very different galactic chemical enrichment histories. In particular, the Galactic halo abundance pattern suggests more vigorous star formation and galactic wind, together with a longer time-scale of gas accretion (see Brusadin et al. 2013). However, more data on UFDs are necessary before drawing firm conclusions.

References

- Adén D., Wilkinson M. I., Read J. I., et al., 2009a, ApJ, 706, L150
Adén D., Feltzing S., Koch A., et al., 2009b, A&A, 506, 1147
Adén D., Eriksson K., Feltzing S., et al., 2011, A&A, 525, A153
Asplund M., Grevesse N., Sauval A. J., Scott P., 2009, ARA&A, 47, 481
Battaglia G., Irwin M., Tolstoy E., et al., 2008a, MNRAS, 383, 183
Battaglia G., Helmi A., Tolstoy E., et al., 2008b, ApJ, 681, L13
Belokurov V., Zucker D. B., Evans N. W., et al., 2006, ApJ, 647, L111
Belokurov V., Zucker D. B., Evans N. W., et al., 2007, ApJ, 654, 897
Belokurov V., Walker M. G., Evans N. W., et al., 2010, ApJ, 712, L103
Belokurov V., 2013, NAR, 57, 100
Bradamante F., Matteucci F., D’Ercole A., 1998, ApJ, 337, 338
Brown T. M., Tumlinson J., Geha M., et al., 2013, arXiv:1310.0824
Brusadin G., Matteucci F., Romano D., 2013, A&A, 554, A135
Bullock J. S., Kravtsov A. V., Weinberg D. H., 2001, ApJ, 548, 33
Bullock J. S., Johnston K. V., 2005, ApJ, 635, 931
Cannon R. D., Hawarden T. G., Tritton S. B., 1977, MNRAS, 180, 81P
Catelan M., 2009, ApSS, 320, 261
Cayrel R., Depagne E., Spite M., et al., 2004, A&A, 416, 1117
Cescutti G., François P., Matteucci F., Cayrel R., Spite M., 2006, A&A, 448, 557
Cescutti G., Matteucci F., Lanfranchi G. A., McWilliam A., 2008, A&A, 491, 401
Chabrier G., 2003, PASP, 115, 763
Chiappini C., Matteucci F., Gratton R., 1997, ApJ, 477, 765
Chieffi A., Limongi M., 2013, ApJ, 764, 21
Collins M. L. M., Chapman S. C., Rich R. M., et al., 2013, arXiv:1309.3053
Cooke R., Pettini M., Steidel C. C., Rudie G. C., Jorgenson R. A., 2011, MNRAS, 412, 1047
Cooke R., Pettini M., Steidel C. C., Rudie G. C., Nissen P. E., 2011, MNRAS, 417, 1534

- Dall’Ora M., Ripepi V., Caputo F., et al., 2003, *AJ*, 126, 197
- de Boer T. J. L., Tolstoy E., Hill V., et al., 2012, *A&A*, 539, A103
- de Jong J. T. A., Rix H. W., Martin N. F., et al., 2008, *AJ*, 135, 1361
- Dekel A., Silk J., 1986, *ApJ*, 303, 39
- Feltzing S., Eriksson K., Kleyana J., Wilkinson M. I., 2009, *A&A*, 508, L1
- Ferrara A., 2012, *American Institute of Physics Conference Series*, 1480, 317
- François P., Matteucci F., Cayrel R., et al., 2004, *ApJ*, 421, 613
- Frebel A., Kirby E. N., Simon J. D., 2010, *Nature*, 464, 72
- Frebel A., Bromm V., 2012, *ApJ*, 759, 115
- Gilmore G., Wilkinson M. I., Wyse R. F. G., et al., 2007, *ApJ*, 663, 948
- Gilmore G., Norris J. E., Monaco L., et al., 2013, *ApJ*, 763, 61
- Gratton R. G., Carretta E., Claudi R., Lucatello S., Barbieri M., 2003, *A&A*, 404, 187
- Grcevich J., Putman M. E., 2009, *ApJ*, 696, 385
- Grebel E. K., 1997, *Reviews in Modern Astronomy*, 10, 29
- Harding P., Morrison H. L., Olszewski E. W., et al., 2001, *AJ*, 122, 1397
- Helmi A., White S. D. M., 1999, *MNRAS*, 307, 495
- Helmi A., Irwin M. J., Tolstoy E., et al., 2006, *ApJ*, 651, L121
- Hernandez X., Gilmore G., Valls-Gabaud D., 2000, *MNRAS*, 317, 831
- Hurley-Keller D., Mateo M., Nemeč J., 1998, *AJ*, 115, 1840
- Ishigaki M. N., Aoki W., Arimoto N., Okamoto S., 2014, *arXiv:1401.1265*
- Iwamoto K., Brachwitz F., Nomoto K., et al., 1999, *ApJ*, 125, 439
- Keller S. C., Bessell M. S., Frebel A., et al., 2014, *Nature*, 506, 463
- Kirby E. N., Guhathakurta P., Bolte M., Sneden C., Geha M. C., 2009, *ApJ*, 705, 328
- Kirby E. N., Guhathakurta P., Simon J. D., et al., 2010, *ApJS*, 191, 352
- Kirby E. N., Cohen J. G., 2012, *AJ*, 144, 168
- Koch A., Grebel E. K., Wyse R. F. G., et al., 2006, *ApJ*, 131, 895
- Koch A., Grebel E. K., Gilmore G. F., et al., 2008, *ApJ*, 135, 1580
- Koch A., McWilliam A., Grebel E. K., Zucker D. B., Belokurov V., 2008, *ApJL*, 688, L13
- Koch A., 2009, *Astronomische Nachrichten*, 330, 675
- Koch A., Feltzing S., Adén D., Matteucci F., 2013, *A&A*, 554, A5
- Koch A., Matteucci F., Feltzing S., 2012, *American Institute of Physics Conference Series*, 1480, 190
- Lai D. K., Lee Y. S., Bolte M., et al., 2011, *ApJ*, 738, 51
- Lanfranchi G. A., Matteucci F., 2004, *MNRAS*, 351, 1338
- Lanfranchi G. A., Matteucci F., Cescutti G., 2006a, *MNRAS*, 365, 477
- Lanfranchi G. A., Matteucci F., Cescutti G., 2006b, *A&A*, 453, 67
- Lanfranchi G. A., Matteucci F., 2007, *A&A*, 468, 927
- Lanfranchi G. A., Matteucci F., Cescutti G., 2008, *A&A*, 481, 635
- Lanfranchi G. A., Matteucci F., 2010, *A&A*, 512, A85
- Lemasle B., Hill V., Tolstoy E., et al., 2012, *A&A*, 538, A100
- Li W., Chornock R., Leaman J., et al., 2011, *MNRAS*, 412, 1473
- Marconi G., Matteucci F., Tosi M., 1994, *MNRAS*, 270, 35
- Martin N. F., de Jong J. T. A., Rix H.-W., 2008, *ApJ*, 684, 1075
- Mateo M. L., 1998, *ARA&A*, 36, 435
- Matteucci F., Brocato E., 1990, *ApJ*, 365, 539
- Matteucci F., 2001, *Astrophysics and Space Science Library*, 253
- Matteucci F., Recchi S., 2001, *ApJ*, 558, 351
- McWilliam A., Wallerstein G., Mottini M., 2013, *ApJ*, 778, 149
- Monelli M., Pulone L., Corsi C. E., et al., 2003, *AJ*, 126, 218
- Norris J. E., Yong D., Gilmore G., Wyse R. F. G., 2010, *ApJ*, 711, 350

Chapter 3. Chemical evolution of classical and ultra-faint dwarf spheroidal galaxies

- Norris J. E., Wyse R. F. G., Gilmore G., et al., 2010, *ApJ*, 723, 1632
Okamoto S., Arimoto N., 2012, *Galactic Archaeology: Near-Field Cosmology and the Formation of the Milky Way*, 458, 283
Pasetto S., Grebel E. K., Berczik P., Chiosi C., Spurzem R., 2011, *A&A*, 525, A99
Recchi S., Matteucci F., D’Ercole A., 2001, *MNRAS*, 322, 800
Recchi S., Matteucci F., D’Ercole A., Tosi M., 2002, *A&A*, 384, 799
Recchi S., Matteucci F., D’Ercole A., Tosi, M., 2004, *A&A*, 426, 37
Reddy B. E., Tomkin J., Lambert D. L., Allende Prieto C., 2003, *MNRAS*, 340, 304
Reddy B. E., Lambert D. L., Allende Prieto C., 2006, *MNRAS*, 367, 1329
Rizzi L., Held E. V., Bertelli G., Saviane I., 2003, *ApJ*, 589, L85
Romano D., Starkenburg E. 2013, *MNRAS*, 434, 471
Salpeter E. E., 1955, *ApJ*, 121, 161
Salvadori S., Ferrara A., 2009, *MNRAS*, 395, L6
Salvadori S., Ferrara A., 2012, *MNRAS*, 421, L29
Sand D. J., Olszewski E. W., Willman B., et al., 2009, *ApJ*, 704, 898
Shapley H., 1938, *Harvard College Observatory Bulletin*, 908, 1
Schmidt, 1959, *ApJ*, 129, 243
Shetrone M., Venn K. A., Tolstoy E., et al., 2003, *ApJ*, 125, 684
Siegel M. H., 2006, *ApJ*, 649, L83
Simon J. D., Frebel A., McWilliam A., Kirby E. N., Thompson I. B., 2010, *ApJ*, 716, 446
Starkenburg E., Hill V., Tolstoy E., et al., 2010, *A&A*, 513, A34
Starkenburg E., Hill V., Tolstoy E., et al., 2013, *A&A*, 549, A88
Tafelmeyer M., Jablonka P., Hill V., et al., 2010, *A&A*, 524, A58
Tolstoy E., Venn K. A., Shetrone M., et al., 2003, *AJ*, 125, 707
Tolstoy E., Hill V., Tosi M., 2009, *ARA&A*, 47, 371
van den Hoek L. B., Groenewegen M. A. T., 1997, *A&AS*, 123, 305
Vargas L. C., Geha M., Kirby E. N., Simon J. D., 2013, *ApJ*, 767, 134
Venn K. A., Shetrone M. D., Irwin M. J., et al., 2012, *ApJ*, 751, 102
Vincenzo, F., Matteucci, F., Vattakunnel, S., & Lanfranchi, G. A. 2014, *MNRAS*, 441, 2815
Walker M. G., Mateo M., Olszewski E. W., et al., 2009, *ApJ*, 704, 1274
Wolf J., Martinez G. D., Bullock J. S., et al., 2010, *MNRAS*, 406, 1220
Woolsey S. E., Weaver T. A., 1995, *ApJS*, 101, 181
Yin J., Matteucci F., Vladilo G., 2011, *ApJ*, 531, A136

4

The integrated galactic initial mass function and neutron star mergers in the Sagittarius dwarf spheroidal galaxy

4.1 Introduction

The Sagittarius (Sgr) dwarf galaxy was the last classical dwarf spheroidal (dSph) discovered before the advent of the Sloan Digital Sky Survey. Its discovery was made by [Ibata et al. \(1994\)](#) and it was identified while performing a spectroscopic radial velocity survey of the Galactic bulge stars ([Ibata et al., 1997](#)). Its heliocentric distance ($D_{\odot} = 26 \pm 2$ kpc, from [Simon et al. 2011](#)) makes it the second closest known satellite galaxy of the Milky Way (MW) and, because of the strong tidal interaction suffered by the Sgr dSph during its orbit, it has left behind a well-known stellar stream ([Ibata et al., 2001](#); [Majewski et al., 2003](#); [Belokurov et al., 2006](#)), whose chemical characteristics have been recently studied and compared with the ones of the Sgr main body and other dSph galaxies by [de Boer et al. \(2014\)](#). The Sgr dwarf galaxy has been classified as a dSph because of its very low central surface brightness ($\mu_V = 25.2 \pm 0.3$ mag arcsec⁻², from [Majewski et al. 2003](#)), its very small total amount of gas ($M_{\text{HI,obs}} \sim 10^4 M_{\odot}$, from [McConnachie 2012](#)) and because of the age and metallicity of its main stellar population, which dates back to the age of the Universe and it is on average very iron poor. Chemical abundances in Sgr have been measured by many authors up to now (see [Lanfranchi et al. 2006](#) and references therein). Most of these studies have shown that the abundance patterns in Sgr are different than those in the MW.

In this Chapter, we present the results of the work by [Vincenzo, Matteucci,](#)

Recchi, Calura, McWilliam & Lanfranchi (2015); in particular, we aim at testing the suggestions of McWilliam et al. (2013), which claimed that the α -element deficiencies observed in the Sgr dSph galaxy cannot be explained only by means of the time-delay model (Tinsley, 1979; Greggio & Renzini, 1983; Matteucci, 1986) but they rather result from an initial mass function (IMF) deficient in the highest mass stars. On the other hand, Lanfranchi & Matteucci (2003, 2004) suggested that the low values of the $[\alpha/\text{Fe}]$ ratios, as observed in dSphs, can be interpreted as due to the time-delay model (α -elements produced on short time-scales by core-collapse SNe and Fe by SNe Ia with a time delay) coupled with a low star formation rate (SFR), assuming a Salpeter (1955) IMF.

McWilliam et al. (2013) also suggested that the Eu abundances in the Sgr galaxy might be explained by core-collapse SNe, whose progenitors are stars less massive than the main oxygen producers, as previously envisaged also by Wanajo et al. (2003). Since many studies of nucleosynthesis have pointed out the difficulty of producing r-process elements during SN explosions (Arcones et al., 2007), in Vincenzo, Matteucci, Vattakunnel & Lanfranchi (2014), we test different scenarios for the Eu production, both the one in which Eu is produced by core-collapse SNe and the most recent one, where the Eu is synthesized in neutron star mergers (NSMs, Korobkin et al. 2012; Tsujimoto & Shigeyama 2014; Shen et al. 2014; van de Voort et al. 2015). The latter scenario was explored in the context of a detailed chemical evolution model by Matteucci et al. (2014), where they were able to well match the $[\text{Eu}/\text{Fe}]$ abundance ratios observed in the MW stars.

Here, we study the detailed chemical evolution of Sgr by comparing the effect of the integrated galactic initial mass function (IGIMF, in the formulation of Recchi et al. 2014, hereafter R14) with the predictions of the canonical Salpeter (1955) and Chabrier (2003) IMFs. The main effect of the metallicity-dependent IGIMF of R14 is a dependence of the maximum possible stellar mass, that can be formed within a stellar cluster, on the $[\text{Fe}/\text{H}]$ abundance and on the SFR, especially if the latter is very low. Since the dSphs turn out to have been characterized by very low SFRs, the effect of the IGIMF on their evolution is expected to be important. In this way, we will be able to test if the hypothesis of McWilliam et al. (2013) is correct.

In the past, the effect of the IGIMF in the chemical evolution of elliptical galaxies has been studied by Recchi et al. (2009), while Calura et al. (2010) modelled the chemical evolution of the solar neighbourhood when assuming the IGIMF. The originality of this work resides in the fact that we test the effect of a metallicity-dependent IMF, a study never done before in the framework of a detailed chemical evolution model. As a further element of originality, we include for the first time the Eu from NSMs in a chemical evolution model of a dSph galaxy.

This Chapter is organized as follows. In Section 4.2, we describe the metallicity-dependent IGIMF formalism that we include in our models. In Section 4.3, the data sample is presented. In Section 4.4, we describe the chemical evolution model adopted for the Sgr dSph and in Section 4.5 we show and discuss the results of our study. Finally, in Section 4.6, we summarize the main conclusions of our work.

4.2 The integrated galactic initial mass function

Following [Kroupa & Weidner \(2003\)](#) and [Weidner & Kroupa \(2005\)](#), the IGIMF is defined by weighting the classical IMF, $\phi(m)$, with the mass distribution function of the stellar clusters, $\xi_{\text{ecl}}(M_{\text{ecl}})$, within which the star formation process is assumed to take place:

$$\begin{aligned} \xi_{\text{IGIMF}}(m, \psi(t), [\text{Fe}/\text{H}]) &= \\ &= \int_{M_{\text{ecl},\text{min}}}^{M_{\text{ecl},\text{max}}(\psi(t))} dM_{\text{ecl}} \xi_{\text{ecl}}(M_{\text{ecl}}) \phi(m \leq m_{\text{max}}, [\text{Fe}/\text{H}]). \end{aligned} \quad (4.1)$$

The IGIMF is normalized in mass, such that

$$\int_{m_{\text{min}}}^{m_{\text{max}}} dm m \xi_{\text{IGIMF}}(m, \psi(t), [\text{Fe}/\text{H}]) = 1.$$

The functional form of the IGIMF that we test in this work depends both on the SFR and on the $[\text{Fe}/\text{H}]$ abundance of the parent galaxy, following the *mild model* of R14. The IGIMF is based on the following assumptions, based on observations.

- The mass spectrum of the embedded stellar clusters is assumed to be a power law, $\xi_{\text{ecl}} \propto M_{\text{ecl}}^{-\beta}$, with a slope $\beta = 2$ ([Zhang & Fall, 1999](#); [Recchi et al., 2009](#)). In accordance with the mass of the smallest star-forming stellar cluster known (the Tauris—Auriga aggregate), we assumed $M_{\text{ecl},\text{min}} = 5 M_{\odot}$, whereas the upper mass limit of the embedded cluster is a function of the SFR ([Weidner & Kroupa, 2004](#)):

$$\log M_{\text{ecl},\text{max}} = A + B \log \frac{\psi(t)}{M_{\odot} \text{yr}^{-1}}, \quad (4.2)$$

with $A = 4.83$ and $B = 0.75$.

- Within each embedded stellar cluster of a given mass M_{ecl} and $[\text{Fe}/\text{H}]$ abundance, the IMF is assumed to be invariant. In our study, we assume an IMF which is defined as a two-slope power law:

$$\phi(m) = \begin{cases} A m^{-\alpha_1} & \text{for } 0.08 M_{\odot} \leq m < 0.5 M_{\odot} \\ B m^{-\alpha_2} & \text{for } 0.5 M_{\odot} \leq m < m_{\text{max}}, \end{cases} \quad (4.3)$$

where $\alpha_1 = 1.30$ and $\alpha_2 = 2.35$ as in the original work of [Weidner & Kroupa \(2005\)](#), and $\alpha_2 = 2.3 + 0.0572 \cdot [\text{Fe}/\text{H}]$ in the mild formulation of R14. The latter relation was adapted by R14 from the original work of [Marks et al. \(2012\)](#). It turns out from equation (4.3) that the overall $[\text{Fe}/\text{H}]$ dependence entirely resides in the slope of the IMF in the high-mass range. The maximum stellar mass m_{max} that can occur in the cluster and up to which the IMF is sampled, is calculated according to the mass of the embedded cluster, M_{ecl} ; furthermore, m_{max} must be in any case smaller than the empirical limit, which here has been assumed to be $150 M_{\odot}$ (see, for more details, [Weidner](#)

& Kroupa 2004). The m_{\max} — M_{ecl} relation is simply due to the fact that, in the case of very low SFRs, the small clusters may not have enough mass to give rise to very massive stars; on the other hand, in the case of large SFRs, the maximum possible mass of the embedded clusters may be very large and so very massive stars are able to originate (see R14). So m_{\max} depends both on the SFR and, to a lesser extent, on the [Fe/H] abundance of the parent galaxy.

It is worth remarking that recent studies (Weidner et al., 2011; Kroupa et al., 2013; Weidner et al., 2013) suggest that the star cluster IMFs can become top-heavy at SFRs larger than $\sim 10 M_{\odot} \text{ yr}^{-1}$. This range of SFRs is clearly out of reach for Sgr, therefore we have neglected this modification of the IGIMF theory in our study.

In Fig. 4.1, we show what is the effect of the dependence of the IGIMF upon the SFR. For very low SFRs ($\leq 1 M_{\odot} \text{ yr}^{-1}$), the IGIMF turns out to be very much truncated and the maximum mass that can be formed strongly depends on the SFR itself. This is due to the fact that, in galaxies with a low SFR, the mass distribution function of the embedded clusters is truncated at low values of M_{ecl} (see equation 4.2) and small embedded clusters cannot produce very massive stars.

In Fig. 4.2, we illustrate how m_{\max} is determined both by the SFR and by the [Fe/H] abundance. The effect of the [Fe/H]-dependence is clearly opposite to that of the SFR-dependence. As time passes by, one would expect that the iron content within the galaxy interstellar medium (ISM) increases; so, in this formulation, if the SFR is constant, the maximum stellar mass that can be formed within each embedded cluster is expected to decrease in time. In any case, it is worth noting that the dependence of m_{\max} upon the SFR is much stronger than the dependence upon [Fe/H] when the SFRs under play are extremely low.

4.3 Data sample

We use the data set of chemical abundances from the works of Bonifacio et al. (2000, 2004), Sbordone et al. (2007) and McWilliam et al. (2013). Bonifacio et al. (2000) derived the abundances of many chemical elements for two giant stars in Sgr, observed with the high-resolution Ultraviolet and Visual Echelle Spectrograph (UVES) at the Kueyen-Very Large Telescope (VLT). Bonifacio et al. (2004) did a similar work as Bonifacio et al. (2000), including the two stars previously analysed. From the former work we took the abundances of Eu, while from the latter one we took the abundances of Mg and O. Sbordone et al. (2007) presented the chemical abundances of 12 red giant stars belonging to the Sgr main body and the chemical abundances of five red giant stars belonging to the Sgr globular cluster Terzan 7, acquired with the UVES at the European Southern Observatory (ESO) VLT. McWilliam et al. (2013) derived the abundances of several chemical elements from high-resolution spectra of three stars lying on the faint red giant branch of M54, which is considered the most populous globular cluster of Sgr, lying in the densest regions of the galaxy. McWilliam et al. (2013) acquired the spectra using the Magellan Echelle spectrograph (MIKE) and their three stars were confirmed from their kinematics to belong to the Sgr galaxy by Bellazzini et al. (2008). McWilliam

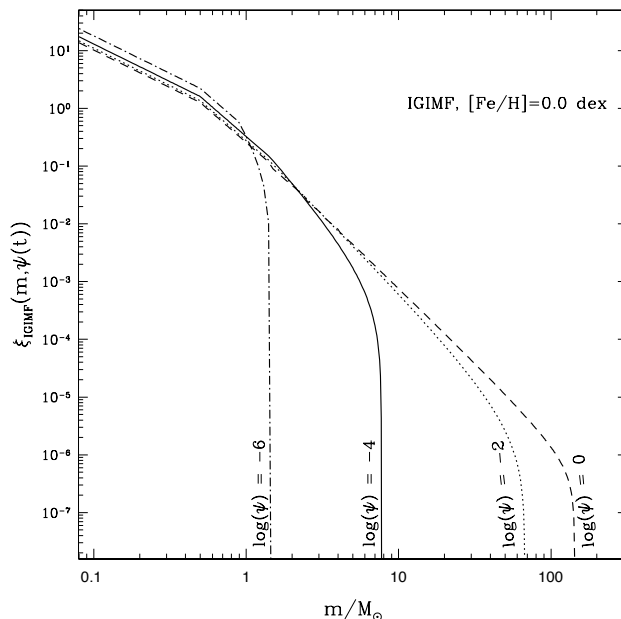


Figure 4.1: In this figure, we show the predicted IGIMF, ξ_{IGIMF} , as a function of the stellar mass m in the case of solar iron abundance and for various SFRs: from $\psi(t) = 10^{-6} M_{\odot} \text{yr}^{-1}$ up to $\psi(t) = 1 M_{\odot} \text{yr}^{-1}$. The net effect of lowering the SFR is to truncate the IGIMF towards lower stellar masses.

et al. (2013) found their chemical abundances of Eu and Mg consistent with those of Bonifacio et al. (2000, 2004).

4.4 The chemical evolution model

4.4.1 The general model for dSphs

The Sgr dSph is assumed to assemble from infall of primordial gas into a pre-existing dark matter (DM) halo, in a relatively short typical time-scale. The infall gas mass has been set to $M_{\text{inf}} = 5.0 \times 10^8 M_{\odot}$ and the infall time-scale has been set to $\tau_{\text{inf}} = 0.5$ Gyr, following the results of Lanfranchi et al. (2006). We assume Sgr to have a massive and diffuse DM halo, with a mass $M_{\text{DM}} = 1.2 \times 10^8 M_{\odot}$ (Walker et al., 2009) and $S \equiv r_{\text{L}}/r_{\text{DM}} = 0.1$, where $r_{\text{L}} = 1550$ pc (Walker et al., 2009) represents the effective radius of the baryonic matter and r_{DM} is the core radius of the DM halo. We remind the reader that we need the latter quantities in order to compute the potential well of the gas and the time of the onset of the galactic wind, which is triggered by the energy released into the ISM by the stellar winds and by the core-collapse (Type II, Type Ib, Type Ic) and Type Ia SNe (see, for more details, Bradamante et al. 1998 and Yin et al. 2011). Once the wind has

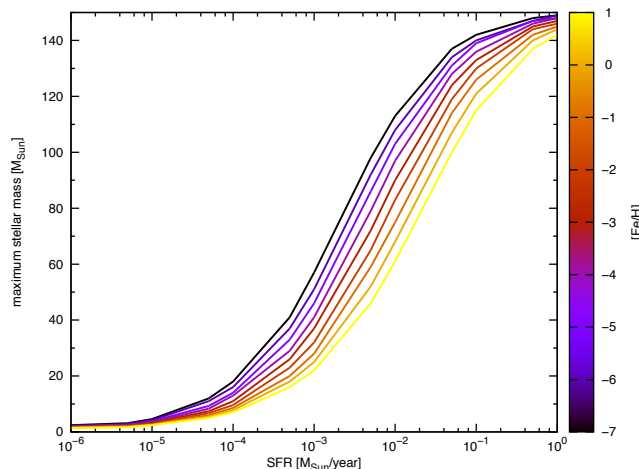


Figure 4.2: This figure shows how the maximum stellar mass (on the y -axis) varies as a function of the SFR (on the x -axis) and as a function of the $[\text{Fe}/\text{H}]$ abundance (colour-coding: from -7 dex up to 1 dex). Increasing the $[\text{Fe}/\text{H}]$ abundance has an opposite effect on m_{max} with respect to the increasing of the SFR.

started^{*}, the intensity of the outflow rate is directly proportional to the SFR.

The galaxy is modelled as a one-zone within which the mixing of the gas is instantaneous and complete and the stellar lifetimes are taken into account. We include the metallicity-dependent stellar yields of [Karakas \(2010\)](#) for the low- and intermediate-mass stars. For massive stars, we assume the He, C, N and O stellar yields at the various metallicities of [Meynet & Maeder \(2002\)](#), [Hirschi et al. \(2005\)](#), [Hirschi \(2007\)](#) and [Ekström et al. \(2008\)](#) and, for heavier elements, the yields of [Kobayashi et al. \(2006\)](#). Finally, we include the yields of [Iwamoto et al. \(1999\)](#) for the Type Ia SNe. We assume the same stellar yields as [Matteucci et al. \(2014\)](#), see also [Romano et al. 2010](#) for a detailed description, and Chapter 2.5 of this Thesis). It is worth noting that the yields of [Romano et al. \(2010\)](#) have been selected because they are, at the present time, the best in order to reproduce the abundance patterns in the solar vicinity.

We test in our model, separately, three different Eu nucleosynthetic yields:

- the yields of [Cescutti et al. \(2006, model 1, table 2\)](#), in which the Eu is produced by core-collapse SNe, whose progenitors are massive stars with mass in the range $M = 12\text{-}30 M_{\odot}$;
- the yields of [Ishimaru et al. \(2004\)](#), which can be found tabled in [Cescutti et al. \(2006, model 4, table 2\)](#), where the Eu is produced by massive stars with mass in the range $M = 8\text{-}10 M_{\odot}$, exploding as core-collapse SNe;
- the yield prescriptions of [Matteucci et al. \(2014\)](#), where we address the reader

^{*}In our model, the galactic wind develops when the thermal energy of the gas exceeds its binding energy to the galaxy.

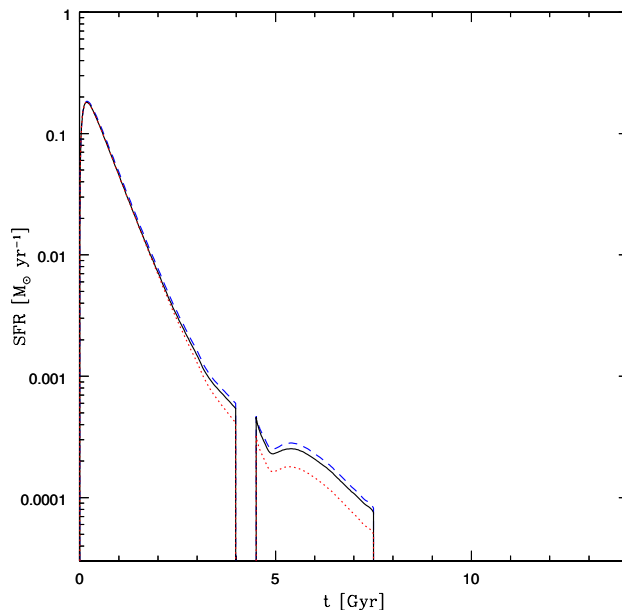


Figure 4.3: In this figure, we compare the temporal evolution of the SFR as predicted by assuming the metallicity-dependent IGIMF of R14 (black solid line) with the same quantity predicted by assuming the [Salpeter \(1955, dotted line in red\)](#) and [Chabrier \(2003, blue dashed line\)](#) IMFs. The trend of the SFR traces that of the gas mass content within the galaxy. In all the cases considered here, the SFR is always much lower than $1 M_{\odot} \text{yr}^{-1}$. Notice that the various curves almost overlap. This is due to the fact that the IMF has little effect on the global mass budget.

for details, for the Eu produced by NSMs. [†] The first case we test is the model Mod3NS' (see fig. 6 of [Matteucci et al. 2014](#)), where we assume that the Eu mass per NSM event is $M_{\text{Eu,NSM}} = 3.0 \times 10^{-6} M_{\odot}$; the progenitors of neutron stars lie in the range $9\text{-}50 M_{\odot}$; the fraction of binary systems in this mass range becoming NSMs is $\alpha_{\text{NSM}} = 0.02$, and the time delay for NS coalescence is $\Delta t_{\text{NSM}} = 1 \text{ Myr}$ (we check also 100 Myr as shown in Section 4.5.1). Moreover, we test also a model with $M_{\text{Eu,NSM}} = 10^{-5} M_{\odot}$ per merger event, and the other parameters being the same as Mod3NS'. This value of the Eu yield is in agreement with the results of recent calculations ([Bauswein et al., 2014](#); [Just et al., 2015](#); [Wanajo et al., 2014](#)).

The prescriptions for the galaxy star formation rate and galactic winds are the same as explained in Chapter 3 for the chemical evolution of the classical and ultra-faint dwarf spheroidal galaxies. In particular, we assume the galaxy star formation rate to be directly proportional to the global gas mass within the interstellar medium; finally, the galactic wind is assumed to be *normal*, namely all the chemical elements are carried out of the galaxy potential well with the same

[†]Note that because of a typo mistake, the correct yield of Eu in [Matteucci et al. \(2014\)](#) was $3.0 \times 10^{-6} M_{\odot}$ instead of $3.0 \times 10^{-7} M_{\odot}$ (see [Matteucci et al. 2015](#)).

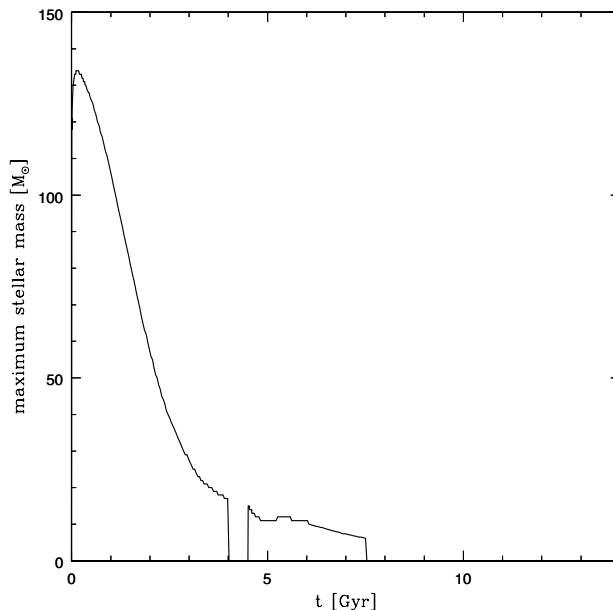


Figure 4.4: Given the temporal evolution of the SFR and of the $[\text{Fe}/\text{H}]$ abundance predicted by our chemical evolution model, this figure reports how the maximum stellar mass that can be formed at every time t evolves as a function of the time itself, when assuming the metallicity-dependent IGMF of R14. It is clear how much the truncation becomes important when the IGMF is adopted in a detailed chemical evolution model of a galaxy with very low SFRs.

efficiency ω (in units of Gyr^{-1}).

4.4.2 The model for Sagittarius

In this study we follow the results of [Lanfranchi et al. \(2006\)](#), which provide an estimate of the parameters of the chemical evolution model for Sgr able to reproduce the observational data. They found that Sgr should have been characterized by intermediate values of the star formation efficiencies ν , included between 1 and 5 Gyr^{-1} , and by intense galactic winds, with efficiencies ω varying between 9 and 13 Gyr^{-1} . We remark on the fact that [Lanfranchi et al. \(2006\)](#) assumed a constant [Salpeter \(1955\)](#) IMF.

In accordance to the observations, we assume that Sgr is composed of two distinct stellar populations, one of old age ≥ 10 Gyr (the blue horizontal branch population discovered by [Monaco et al. 2003](#)) and one of intermediate age, which dates back to 8.0 ± 1.5 Gyr (the so-called Population A, studied by [Bellazzini et al. 2006](#)). So we adopt for the galaxy a star formation history with two separate episodes, the first one occurring between 0 and 4 Gyr since the beginning of the galaxy evolution, the second one between 4.5 and 7.5 Gyr. Thus, according to these observational evidences, the star formation is set to zero outside those time intervals. During the star formation episodes, the SFR follows the classical linear Schmidt-Kennicutt law.

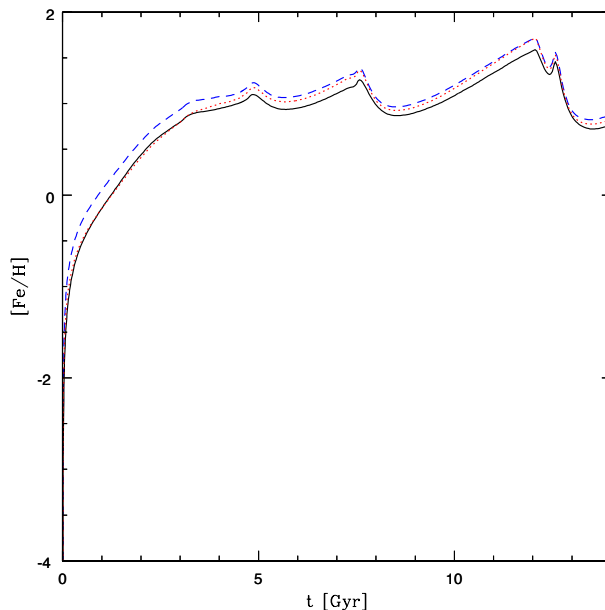


Figure 4.5: In this figure, the predicted age–metallicity relation is shown. The y -axis reports the $[\text{Fe}/\text{H}]$ abundance of the galaxy ISM as predicted by our chemical evolution models, while the x -axis reports the time in Gyr since the beginning of the galaxy evolution. The iron content within the ISM increases very steeply in the first billion years, then its trend flattens. The different IMFs considered in this work predict very similar age–metallicity relations. We remark on the fact that the $[\text{Fe}/\text{H}]$ abundance in this figure refers to the abundance in the ISM; if one wants to see how many stars formed at a given time and therefore at a given $[\text{Fe}/\text{H}]$ of the ISM, one should look at the stellar MDF (see Section 4.5). The lines correspond to the same IMFs as in Fig. 4.3.

In order to test what is the effect of the IGIMF in the framework of a detailed chemical evolution model, we fix the following values for the parameters of the model: $\nu = 3 \text{ Gyr}^{-1}$ and $\omega = 9 \text{ Gyr}^{-1}$, which are the best parameters found by Lanfranchi et al. (2006). We then compare the results obtained by assuming the IGIMF with the ones obtained by assuming the canonical Salpeter (1955) and Chabrier (2003) IMFs.

As a reminder for the reader, the Salpeter (1955) IMF is a single-slope power law, which has the following form:

$$\phi(m) \propto m^{-2.35}, \text{ for } 0.1 \leq \frac{m}{M_{\odot}} < 100, \quad (4.4)$$

whereas the Chabrier (2003) has a log-normal distribution function for low-mass stars:

$$\phi(m) \propto \begin{cases} \frac{1}{m} \exp\left(-\frac{(\log(m) - \log(0.079))^2}{2 \cdot 0.69^2}\right), & \text{for } 0.1 \leq \frac{m}{M_{\odot}} < 1 \\ m^{-2.3}, & \text{for } 1 \leq \frac{m}{M_{\odot}} < 100. \end{cases} \quad (4.5)$$

In our chemical evolution model the minimum possible stellar mass is $M_{\text{low}} =$

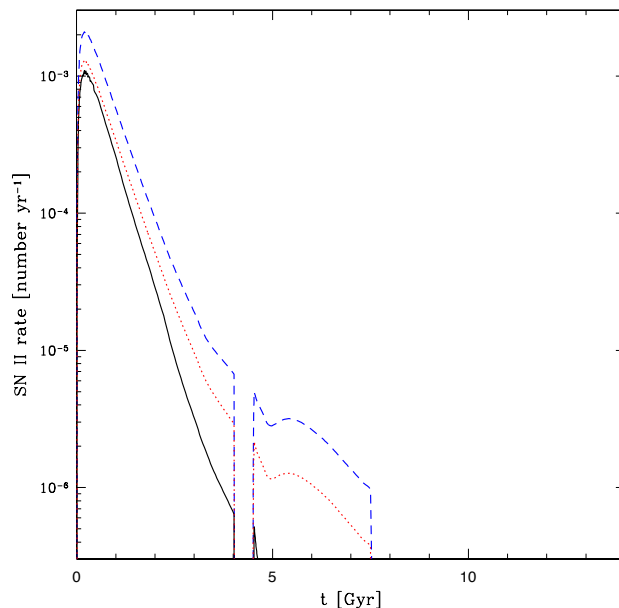


Figure 4.6: This figure reports the core-collapse SN rate predicted as a function of the time. Because of the truncation of the IGIMF, the core-collapse SN rate predicted by the IGIMF is always lower than the one predicted by the classical IMFs. The lines correspond to the same IMFs as in Fig. 4.3.

$0.1 M_{\odot}$, whereas the maximum possible stellar mass is $M_{\text{up}} = 100 M_{\odot}$; so, if the maximum stellar mass of the IGIMF turns out to be larger than M_{up} , we set it at the maximum possible value of $100 M_{\odot}$. The reason for that resides in the fact that stars more massive than $100 M_{\odot}$ have a negligible effect in any IMF and it is difficult to find yields for them in the literature.

4.5 Results

This work is based on the chemical evolution model described in Section 4.4 and our aim is to investigate the effect of three different IMFs: the canonical [Salpeter \(1955\)](#), the [Chabrier \(2003\)](#) IMF and the metallicity-dependent IGIMF of R14.

The galaxy is always predicted to possess at the present time a very small total amount of gas. In particular, the total HI mass results $M_{\text{HI}} \approx 1.8 \times 10^4 M_{\odot}$ with the [Chabrier \(2003\)](#) IMF, $M_{\text{HI}} \approx 1.3 \times 10^4 M_{\odot}$ with the [Salpeter \(1955\)](#) IMF and $M_{\text{HI}} \approx 1.8 \times 10^4 M_{\odot}$ with the IGIMF. All the latter quantities are almost in agreement with the upper limit of the total HI mass derived by [Koribalski et al. \(1994\)](#), which is $M_{\text{HI,obs}} \sim 10^4 M_{\odot}$.

The model with the IGIMF predicts the largest final total stellar mass for the galaxy, which is $M_{\star,\text{fin}} \approx 1.1 \times 10^8 M_{\odot}$. In fact, the model with the [Salpeter \(1955\)](#) and [Chabrier \(2003\)](#) IMFs predict $M_{\star,\text{fin}} \approx 7.9 \times 10^7 M_{\odot}$ and $M_{\star,\text{fin}} \approx 5.2 \times 10^7 M_{\odot}$, respectively, which have the same order of magnitude of the observed total stellar

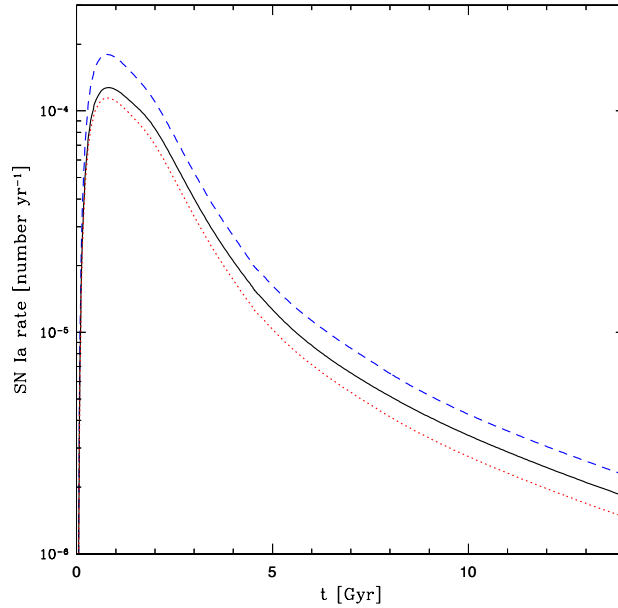


Figure 4.7: In this figure, we compare the Type Ia SN rate as a function of the time. The integrated number of SNe Ia predicted with the [Chabrier \(2003\)](#) IMF turns out to be the largest one. The lines correspond to the same IMFs as in Fig. 4.3.

mass $M_{\star} \sim 2.1 \times 10^7 M_{\odot}$ (see [McConnachie 2012](#) and references therein). In this study, we have neglected the fact that Sgr has lost many stars after its SF ceased; this may explain why the actual stellar mass predicted by our chemical evolution models is larger than the present-day observed mass.

The model with the IGIMF predicts the galactic wind to develop for the first time at $t_{\text{GW}} = 30$ Myr while the model with the [Salpeter \(1955\)](#) and the [Chabrier \(2003\)](#) IMFs predict the onset of the galactic wind at $t_{\text{GW}} = 25$ and 20 Myr, respectively. Since we assume the SFR to proceed since the beginning, the retarded onset of the galactic wind with the IGIMF is likely due to the strong truncation of IGIMF itself, which inhibits the formation of very massive stars, the ones having the shortest typical lifetimes and exploding as core-collapse Supernovae. This can be confirmed by the intensity of the SFRs under play; if they are $\leq 1 M_{\odot}\text{yr}^{-1}$, then the truncation is important. By looking at Fig. 4.3, where the predicted trend of the SFR is plotted as a function of time, it turns out that the predicted SFRs in Sgr are always much lower than $1 M_{\odot}\text{yr}^{-1}$. The temporal evolution of the maximum stellar mass that can be formed during the star formation activity, in the case of the IGIMF, is shown in Fig. 4.4. The steep increasing trend of m_{max} at the beginning is due to the rapid increase of the SFR during the initial infall event. Then, m_{max} decreases because of the declining SFR. The $[\text{Fe}/\text{H}]$ dependence is crucial during the initial infall event, when the $[\text{Fe}/\text{H}]$ abundance rapidly increases, counterbalancing the SFR dependence and preventing the IGIMF to reach masses very close to the empirical limit of $150 M_{\odot}$. In fact, the bulk of chemical enrichment in this galaxy occurs in the first Gyr of its evolution; then, the age–metallicity relation becomes

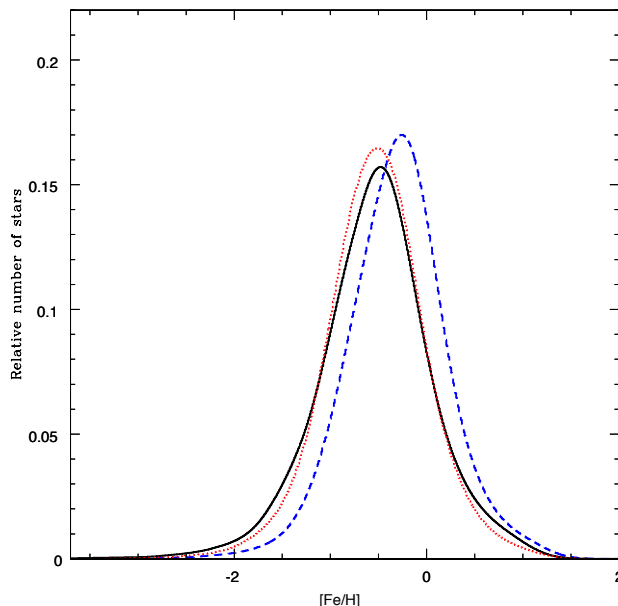


Figure 4.8: In this figure, we compare the stellar MDF as predicted by the various models. The theoretical MDFs have been smoothed with a Gaussian function having $\sigma = 0.2$. The IGIMF and the [Salpeter \(1955\)](#) IMF predict the MDF to peak at $[\text{Fe}/\text{H}] = -0.48$ dex and $[\text{Fe}/\text{H}] = -0.51$ dex, respectively, in agreement with the mean value $\langle [\text{Fe}/\text{H}] \rangle = -0.5 \pm 0.2$ dex, measured by [Cole \(2001\)](#). The [Chabrier \(2003\)](#) predicts the peak to occur at $[\text{Fe}/\text{H}] = -0.26$ dex. The lines correspond to the same IMFs as in Fig. 4.3.

much more shallow and the main role is played by the SFR, which decreases very steeply. In Fig. 4.5, we report the age–metallicity relations predicted by assuming the different IMFs. The small fluctuations visible in Fig. 4.5 are due to the bursting mode of star formation and the

The core-collapse SN rate as a function of time is shown in Fig. 4.6. The progenitors of core-collapse SNe are assumed to be massive stars with mass $M > 8 M_{\odot}$, which have very short typical lifetimes since star formation, in the range $1 \text{ Myr} < \tau_M < 30 \text{ Myr}$. As one can see from the figure, the IGIMF predicts numbers of core-collapse SNe per unit time which are always lower than the ones predicted by the classical IMFs. Among the IMFs here considered, the highest number of stars over the entire high-mass range originate when assuming the [Chabrier \(2003\)](#) IMF (see also [Romano et al. 2005](#)). In fact, the [Chabrier \(2003\)](#) IMF for $M \geq 1 M_{\odot}$ has a slope $\alpha_{\text{Chab.}} = -2.3$ (see equation 4.5), which is flatter than the [Salpeter \(1955\)](#) one ($\alpha_{\text{Sal.}} = -2.35$, see equation 4.4). For this reason, the core-collapse SN rate with the [Chabrier \(2003\)](#) exceeds the other.

In Fig. 4.7, we report the predicted Type Ia SN rate as a function of time. We assume Type Ia SNe to originate from white dwarfs in binary systems exploding by C-deflagration. We adopt the *single-degenerate model*, with the same prescriptions as in [Matteucci \(2001\)](#), see also Chapter 1 of this Thesis). According to this particular progenitor model, a degenerate C–O white dwarf (the primary, initially more

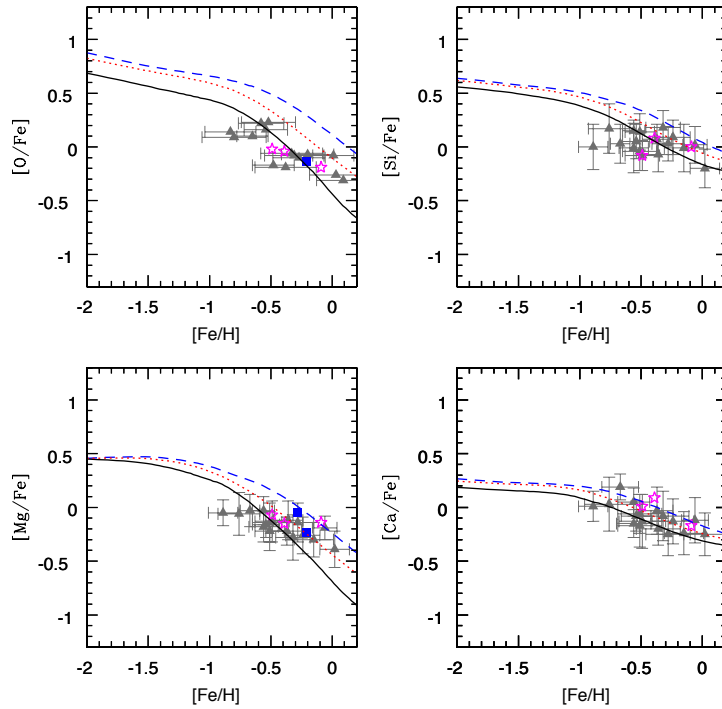


Figure 4.9: In this figure, we report the $[\alpha/\text{Fe}]$ versus $[\text{Fe}/\text{H}]$ abundance ratio patterns as predicted by the IGIMF of R14 (black solid line) and by the Salpeter (1955, dashed line in red) and Chabrier (2003, blue dashed line) IMFs. The data are from Bonifacio et al. (2000, 2004, blue squares), Sbordone et al. (2007, grey triangles) and McWilliam et al. (2013, magenta stars). The trend can be easily explained by means of the time-delay model (Matteucci & Brocato, 1990; Matteucci, 2001; Lanfranchi & Matteucci, 2004) and by looking at the core-collapse and Type Ia SN rates in Fig. 4.6 and 4.7, respectively. The lines correspond to the same IMFs as in Fig. 4.3.

massive, star) accretes material from a red giant or main-sequence companion (the secondary, initially less massive, star); in summary, when the white dwarf reaches the Chandrasekhar mass, the C-deflagration occurs and the white dwarf explodes as a Type Ia Supernova (for more details, see Matteucci 2001). Depending primarily on the mass of the secondary star, which is the clock for the explosion, Type Ia SNe can explode over a very large interval of time-scales since the star formation, which can vary between 30 Myr and the age of the Universe. By looking at Fig. 4.7, the Type Ia SN rate with the Chabrier (2003) IMF dominates over the other two; in fact, the Chabrier (2003) IMF predicts also a higher number of low- and intermediate-mass stars with $M > 1 M_{\odot}$ (Romano et al., 2005).

4.5.1 MDF and chemical abundances

The stellar metallicity distribution function (MDF) predicted by the model with the IGIMF has the peak at $[\text{Fe}/\text{H}] = -0.48$ dex, close to the position of the peak

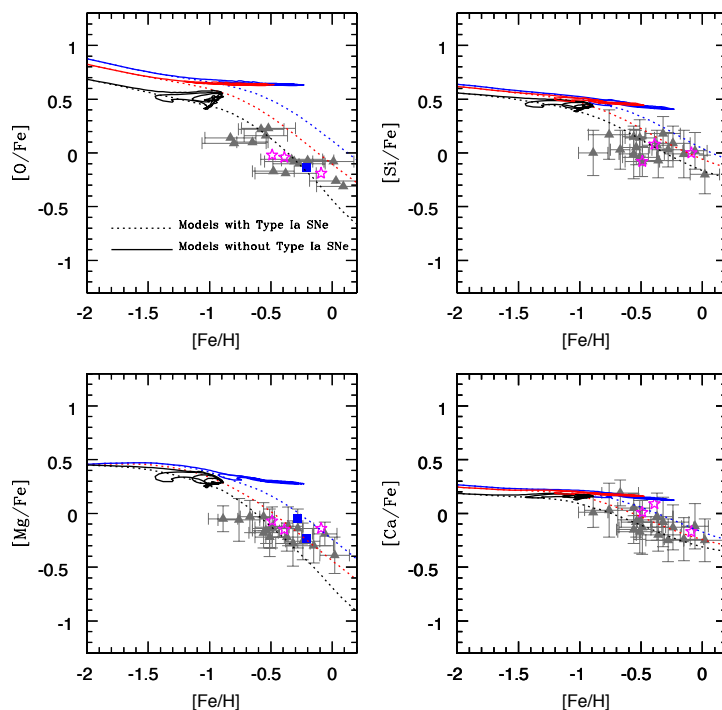


Figure 4.10: In this figure, we study the effect on the predicted $[\alpha/\text{Fe}]$ versus $[\text{Fe}/\text{H}]$ abundance pattern of suppressing Type Ia SNe. The dotted lines correspond to the model with the inclusion of Type Ia SNe, while the solid lines represent the model when the contribution of Type Ia SNe has been suppressed. The dotted lines correspond to the same IMFs as in Fig. 4.9.

predicted by the model with the [Salpeter \(1955\)](#) IMF, which is at $[\text{Fe}/\text{H}] = -0.51$ dex. Conversely, the $[\text{Fe}/\text{H}]$ peak of the MDF with the [Chabrier \(2003\)](#) IMF occurs at $[\text{Fe}/\text{H}] = -0.26$ dex, which is much higher than the other two values. This can be seen in Fig. 4.8 and it is due to the fact that the integrated number of Type Ia and core-collapse SNe with the [Chabrier \(2003\)](#) IMF is much higher than that predicted when assuming the IGIMF or the [Salpeter \(1955\)](#) IMF (see Figs 4.6 and 4.7). So, on average, fixing all the other parameters of the model, a quite enhanced iron pollution from SNe is expected when adopting the [Chabrier \(2003\)](#) IMF. Finally, the IGIMF and the [Salpeter \(1955\)](#) IMF predict a $[\text{Fe}/\text{H}]$ abundance for the peak of the stellar MDF which is in agreement with the mean value $\langle [\text{Fe}/\text{H}] \rangle = -0.5 \pm 0.2$ dex, measured by [Cole \(2001\)](#) for the Sgr main stellar population.

In Fig. 4.9, we compare the predicted $[\alpha/\text{Fe}]$ abundance ratios as a function of the $[\text{Fe}/\text{H}]$ abundances with the observational data of [Bonifacio et al. \(2000, 2004\)](#), [Sbordone et al. \(2007\)](#) and [McWilliam et al. \(2013\)](#). We remind the reader that Type Ia SNe enrich the ISM mainly with iron (almost 2/3 of the total content) and iron-peak elements, whereas the α -elements are mainly produced by core-collapse SNe, which also provide some iron, typically $\sim 1/3$ of the total. However, some α -elements, such as the calcium and the silicon, are also synthesized by Type Ia

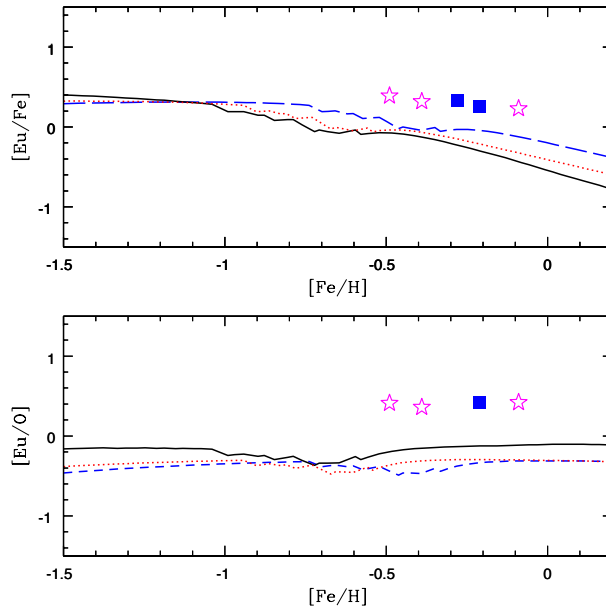


Figure 4.11: In these figures, we compare the predictions of our models with different IMFs for the $[\text{Eu}/\text{Fe}]$ and $[\text{Eu}/\text{O}]$ versus $[\text{Fe}/\text{H}]$ abundance patterns, when the yield of [Cescutti et al. \(2006\)](#) are included. The latter assume the Eu to be produced by massive stars with mass in the range $M = 12\text{--}30 M_{\odot}$, which explode as core-collapse SNe. None of the models with these yields is able to reproduce both the $[\text{Eu}/\text{Fe}]$ and $[\text{Eu}/\text{O}]$ abundance ratio patterns at the same time. The various lines correspond to the same IMFs as in [Fig. 4.3](#).

SNe, although in smaller quantities than those coming from core-collapse SNe. We have also to remark the fact that the fraction of the total iron content coming from Type II and Type Ia SNe depends on the assumed IMF and the aforementioned proportions have been calculated by assuming Salpeter-like IMFs (see for more details, [Matteucci 2014](#)).

By looking at [Fig. 4.9](#), the overall trend predicted by assuming the three different IMFs is quite similar and it can be easily explained by the *time-delay model* ([Matteucci & Brocato, 1990](#); [Matteucci, 2001](#); [Lanfranchi & Matteucci, 2004](#)), which can be resumed as follows: the decrease of $[\alpha/\text{Fe}]$ at very low $[\text{Fe}/\text{H}]$ is due to the very low SFRs under play, which cause Type Ia SNe to be important in the iron pollution when the ISM was not yet heavily enriched with iron by core-collapse SNe; then, the further steepening of $[\alpha/\text{Fe}]$ is due to the strong outflow rate. The fundamental role played by the so-called time-delay model in shaping the trend of the $[\alpha/\text{Fe}]$ ratios, as a function of $[\text{Fe}/\text{H}]$, is shown in [Fig. 4.10](#), where we study the effect of suppressing Type Ia SNe in the chemical enrichment process. As one can see from the figure, if there are no Type Ia SNe, which are the most important Fe producers in galaxies, a truncated IMF such as the IGIMF would never be able to reproduce the data by itself. Furthermore, only by means of Type Ia SNe the galaxy can reach the observed $[\text{Fe}/\text{H}]$ abundances. In fact, the predicted trend reflects only the contribution of core-collapse SNe to Fe. It is only

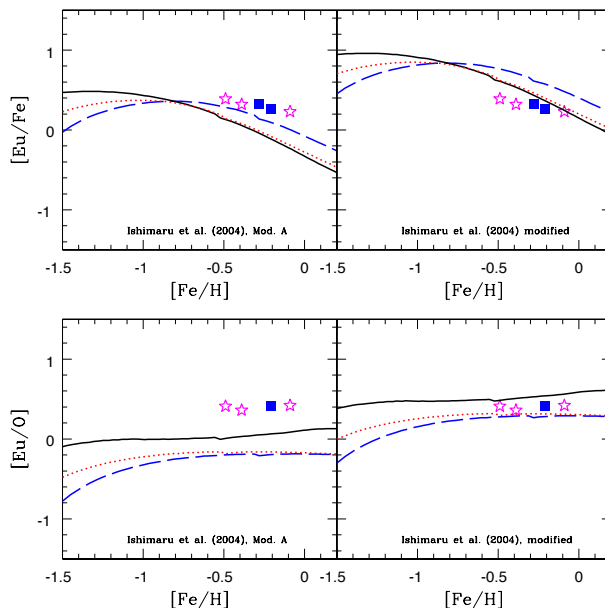


Figure 4.12: In the top- and bottom-left figures, we compare the predictions of our models with different IMFs for the $[\text{Eu}/\text{Fe}]$ and $[\text{Eu}/\text{O}]$ versus $[\text{Fe}/\text{H}]$ abundance patterns, when the yield of [Ishimaru et al. \(2004\)](#) are included. The latter assume the Eu to be produced by stars with mass in the range $M = 8\text{-}10 M_{\odot}$, which explode as core-collapse SNe. None of the models with these yields is able to reproduce both the $[\text{Eu}/\text{Fe}]$ and $[\text{Eu}/\text{O}]$ abundance ratio patterns at the same time. In the top- and bottom-right figures, we show the predictions of our models when the Eu yields of [Ishimaru et al. \(2004\)](#) are multiplied by a factor of 3; in this case, we can obtain a better results both for the $[\text{Eu}/\text{Fe}]$ and the $[\text{Eu}/\text{O}]$ abundance ratios, which can be reproduced by the model the IGIMF. The various lines correspond to the same IMFs as in [Fig. 4.3](#).

the contribution of Type Ia SNe that can explain the decrease of $[\alpha/\text{Fe}]$ ratios and produce the right amount of Fe.

The position of the knee in the $[\alpha/\text{Fe}]$ ratios as a function of $[\text{Fe}/\text{H}]$ varies from galaxy to galaxy and it primarily depends upon the total mass of the galaxy, where the dSphs with larger mass exhibit the knee preferentially at higher $[\text{Fe}/\text{H}]$. We explain this fact by assuming higher efficiency of SF for dwarf galaxies of larger total mass, with the low mass ultrafaint dwarf spheroidals needing the lowest SF efficiencies ([Salvadori & Ferrara, 2009](#); [Vincenzo, Matteucci, Vattakunnel & Lanfranchi, 2014](#)).

By looking at [Fig. 4.9](#), for a given value of $[\text{Fe}/\text{H}]$, the model with the IGIMF predicts the lowest $[\alpha/\text{Fe}]$ abundances while the highest $[\alpha/\text{Fe}]$ ratios are reached when assuming the [Chabrier \(2003\)](#) IMF. In order to obtain the same high values of $[\alpha/\text{Fe}]$ in a model with the IGIMF, one should slightly increase the star formation efficiency. This can be also explained by looking at [Fig. 4.6](#), from which one can conclude that the [Chabrier \(2003\)](#) IMF predicts the highest core-collapse SN rates, whereas the IGIMF the lowest ones, over the entire galaxy lifetime. So in

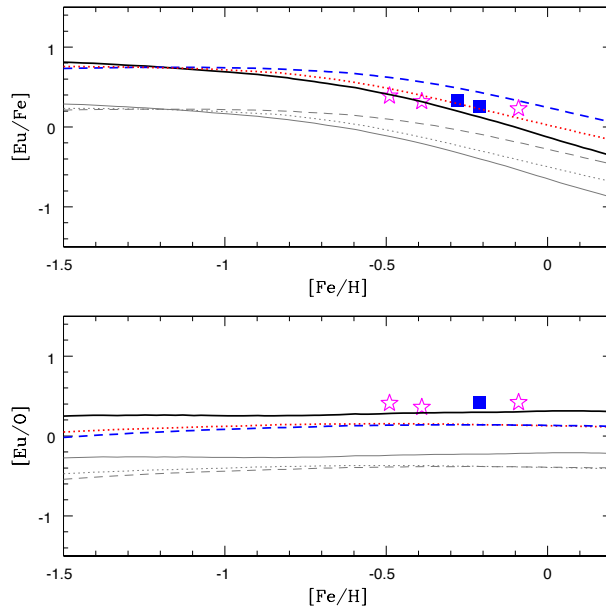


Figure 4.13: In this figure, we compare the $[\text{Eu}/\text{Fe}]$ and $[\text{Eu}/\text{O}]$ as functions of $[\text{Fe}/\text{H}]$ as predicted by the IGIMF and by the classical [Salpeter \(1955\)](#) and [Chabrier \(2003\)](#) IMFs. The models which assume an Eu mass per NSM event $M_{\text{Eu,NSM}} = 1.0 \times 10^{-5} M_{\odot}$ correspond to the thick coloured lines, whereas the models with $M_{\text{Eu,NSM}} = 3.0 \times 10^{-6} M_{\odot}$ to the thin grey lines. The line crossing in the top figure around $[\text{Fe}/\text{H}] = -1.1$ is due to SNe Ia, which in the case of the IGIMF and Salpeter IMF start to explode when the $[\text{Fe}/\text{H}]$ abundance of the ISM is lower than in the case with the Chabrier IMF. The various lines within each set correspond to the same IMFs as in Fig. 4.3.

conclusion, given a particular value of the galaxy gas mass fraction $\mu = M_{\text{gas}}/M_{\text{tot}}$, the [Chabrier \(2003\)](#) IMF predicts the highest metal content in the galaxy while the IGIMF predicts the lowest one.

In Fig. 4.11, we show the predictions of our models with the Eu yields of [Cescutti et al. \(2006\)](#) for the $[\text{Eu}/\text{Fe}]$ versus $[\text{Fe}/\text{H}]$ abundance ratio patterns. We remind the reader that in this case the Eu is assumed to be produced by core-collapse SNe in the range $M = 12\text{-}30 M_{\odot}$ and the stellar yields were determined ad hoc to reproduce the observational trend observed in the MW stars. We find that neither the IGIMF nor the classical IMFs are able to reproduce the observed data set when adopting those yields.

[Wanajo et al. \(2003\)](#) and [McWilliam et al. \(2013\)](#) proposed that Eu could be produced by core-collapse SNe whose progenitors are less massive than the stars more important in oxygen production, which have masses $\gtrsim 30 M_{\odot}$. We tested this scenario in our chemical evolution model of the Sgr dwarf. Therefore, we have included in our models the Eu yields by [Ishimaru et al. \(2004\)](#) from core-collapse SNe in the range $8\text{-}10 M_{\odot}$. According to these yields, the Eu is produced as an r-process element, with $X_{\text{Eu}}^{\text{new}} = 3.1 \times 10^{-7} M_{\odot}/M_{\star}$ being the fraction of Eu ejected by a star of mass M_{\star} . The results which we obtain by assuming the yields of

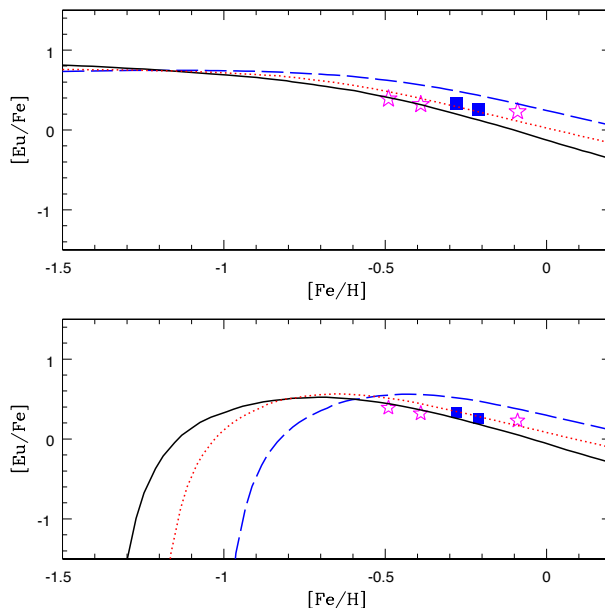


Figure 4.14: In this figure, we show the effect on the $[\text{Eu}/\text{Fe}]$ versus $[\text{Fe}/\text{H}]$ relations of varying the delay time for the coalescence of the NS close binary system from $\Delta t_{\text{NSM}} = 1$ Myr (top figure) to 100 Myr (bottom figure). The various lines correspond to the same IMFs as in Fig. 4.3 and all the models assume a mass of Eu per NSM event $M_{\text{Eu,NSM}} = 1.0 \times 10^{-5} M_{\odot}$.

Ishimaru et al. (2004) can be seen in Fig. 4.12, where we show the $[\text{Fe}/\text{H}]$ - $[\text{Eu}/\text{Fe}]$ relation, as predicted by our models with different IMFs. In that figure, we show also the results of our models with the Ishimaru et al. (2004) yields artificially increased by a factor of 3.

We find that the models with the original Ishimaru et al. (2004) yields are not able to reproduce $[\text{Eu}/\text{Fe}]$ and $[\text{Eu}/\text{O}]$ at the same time. In fact, while the $[\text{Eu}/\text{Fe}]$ ratios can be better explained by the models with the Chabrier (2003) IMF, because of the higher weight of the 8-10 M_{\odot} stars in this IMF, the high $[\text{Eu}/\text{O}]$ ratios cannot be reproduced even by the model with the IGIMF, which predicts a lack of O. By increasing the Ishimaru et al. (2004) yields, we obtain a better result and, in principle, we could explain in this way the observed Eu abundances in this galaxy.

Since the r-process nucleosynthesis is still debated in the literature, we also tested the case in which NSM events are the main responsible for the production of Eu in galaxies, a hypothesis which has received a large interest recently (e.g. Mennekens & Vanbeveren 2014; Matteucci et al. 2014; van de Voort et al. 2015; Wehmeyer et al. 2015). In Fig. 4.13, the $[\text{Eu}/\text{Fe}]$ and $[\text{Eu}/\text{O}]$ ratios as predicted by our models with $M_{\text{Eu,NSM}} = 1.0 \times 10^{-5} M_{\odot}$ (thick lines) are compared with the ones predicted by our models assuming $M_{\text{Eu,NSM}} = 3.0 \times 10^{-6} M_{\odot}$ (thin lines), as in Matteucci et al. (2014). In both cases, the truncation of the IGIMF strongly affects the predicted $[\text{Eu}/\text{O}]$ ratios, which are always higher than the $[\text{Eu}/\text{O}]$ ratios predicted with the standard IMFs.

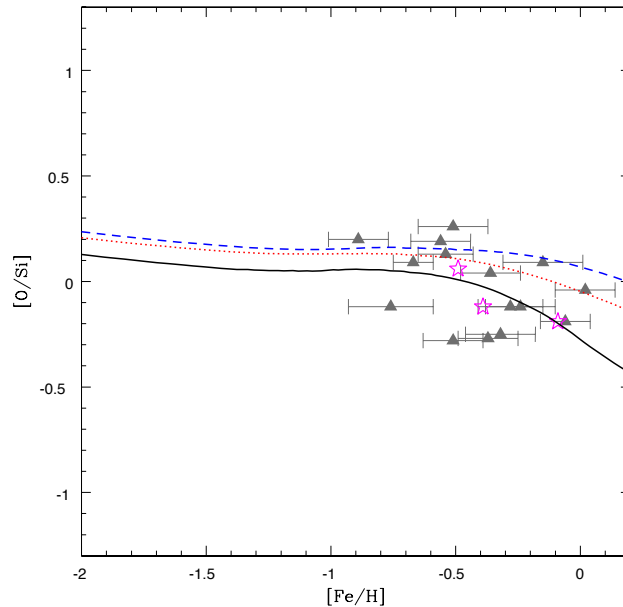


Figure 4.15: In this figure, we report the predictions of our models for the $[O/Si]$ ratios (hydrostatic over explosive α -element ratios) as functions of $[Fe/H]$, in order to ascertain if the data suggest a truncated IMF. The various lines correspond to the same IMFs as in Fig. 4.3.

Our models with $M_{Eu,NSM} = 3.0 \times 10^{-6} M_{\odot}$ are still not able to reproduce the abundance ratios in the Sgr dwarf. The choice of the $M_{Eu,NSM} = 3.0 \times 10^{-6} M_{\odot}$ derives from the best value quoted by Matteucci et al. (2014) to reproduce Eu in the solar vicinity: however, the yields of Eu per event can be as high as $M_{Eu,NSM} = 1.0 \times 10^{-5} M_{\odot}$, in agreement with the upper limit of Korobkin et al. (2012) and with current calculations adopting more recent nuclear data (e.g., Wanajo et al. 2014). With this value we can clearly better reproduce both the $[Eu/Fe]$ and the $[Eu/O]$ abundance ratios observed in this galaxy. Because of the mentioned still existing nucleosynthesis uncertainties and the small number of observations available for dSph galaxies and Sgr galaxy in particular, our results can only safely demonstrate that the idea of McWilliam et al. (2013) is correct and that the $[Eu/O]$ ratio can be a possible diagnostic in future observations and studies of chemical evolution.

In this context, we do not wish to explore all the possible combinations for Eu production sites, as in Matteucci et al. (2014) where models including both core-collapse and NSMs were considered. The paucity of data for Sgr, in fact, prevents us from drawing any conclusions on Eu produced in stars with mass as large as $50 M_{\odot}$, leaving their chemical signature at low metallicities. For the same reason, we cannot safely conclude anything about the time delay for the coalescence of neutron stars. To illustrate that, in Fig. 4.14, we show what is the effect on the predicted $[Eu/Fe]$ versus $[Fe/H]$ relations of varying the delay time for coalescence from $\Delta t_{NSM} = 1$ Myr (top figure) to $\Delta t_{NSM} = 100$ Myr (bottom figure). We remark on the fact that these are extreme cases, given the uncertainty still present

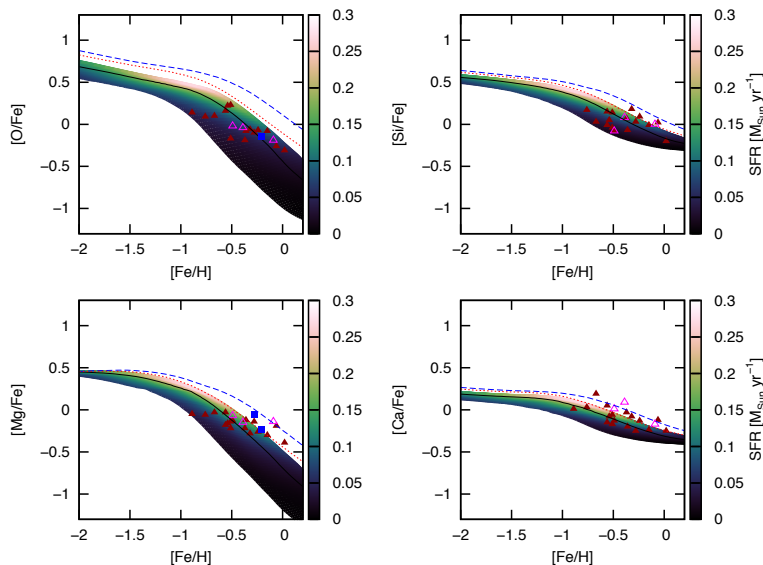


Figure 4.16: In this figure, we show what is the effect of varying the ν parameter in the $[\alpha/\text{Fe}]$ versus $[\text{Fe}/\text{H}]$ abundance pattern when the IGIMF is assumed. The colour-coded curves have been obtained by varying the SF efficiencies in the range $\nu = 1 - 5 \text{ Gyr}^{-1}$, with the wind parameter fixed at the value $\omega = 9 \text{ Gyr}^{-1}$. The colour-coding represents the SFR expressed in units of $M_{\odot} \text{ yr}^{-1}$ and the model with the lowest SF efficiency ($\nu = 1 \text{ Gyr}^{-1}$) corresponds to the lowest edge of the plot, while the model with the highest SF efficiency ($\nu = 5 \text{ Gyr}^{-1}$) corresponds to the highest edge. The black solid line, the dotted line in red and the dashed line in blue correspond to the reference models with $\nu = 3 \text{ Gyr}^{-1}$ and $\omega = 9 \text{ Gyr}^{-1}$ with the IGIMF, the [Salpeter \(1955\)](#) and the [Chabrier \(2003\)](#) IMFs, respectively, as shown in Fig. 4.9; also the data are the same as in Fig. 4.9.

in the delay time for NSMs (see [Dominik et al. 2012](#); [van de Voort et al. 2015](#)).

In Fig. 4.15, we show also the abundance patterns of $[\text{O}/\text{Si}]$. Following the suggestions of [McWilliam et al. \(2013\)](#), the truncation of the IMF can leave a signature in the hydrostatic over explosive α -element abundance ratios. The Si is an explosive α -elements and its stellar yields are not affected by the truncation as much as those of oxygen. By looking at the Figure, the [McWilliam et al. \(2013\)](#) data for $[\text{O}/\text{Si}]$ are well reproduced with the IGIMF, supporting the idea that a truncated IMF should be preferred in this galaxy. However, the data are still uncertain and prevent us from drawing firm conclusions.

It is interesting to note that the dispersion in the $[\text{r-process}/\text{Fe}]$ abundance ratios observed in the extreme metal-poor halo stars suggests that the frequency of r-process producers, per SN event, must be ~ 5 per cent ([McWilliam et al., 1995](#); [Fields et al., 2002](#)). This could be considered as a support to the idea of NSMs as Eu producers, since NSM binaries are a small fraction of the number of core-collapse SN events (we assume $\alpha_{\text{NSM}} = 0.02$, as in [Matteucci et al. 2014](#)).

Table 4.1: We report the differences produced in the averaged abundance ratios by adopting different sets of stellar yields and different IMFs. ‘Romano’ stands for the yields adopted in [Romano et al. \(2010\)](#); ‘CL’ stands for the yields of Chieffi and Limongi (private communication); ‘WW95’ stands for the set of yields with [Woosley & Weaver \(1995\)](#), as described in the text.

	$\Delta[\text{Si}/\text{Fe}] \pm \sigma$	$\Delta[\text{O}/\text{Fe}] \pm \sigma$	$\Delta[\text{Mg}/\text{Fe}] \pm \sigma$	$\Delta[\text{Ca}/\text{Fe}] \pm \sigma$
IMF: Salpeter				
Romano/CL	0.033 ± 0.007	0.03 ± 0.02	0.22 ± 0.03	0.23 ± 0.09
WW95/CL	0.18 ± 0.06	0.12 ± 0.04	0.20 ± 0.06	0.33 ± 0.13
Romano/WW95	0.15 ± 0.06	0.13 ± 0.02	0.08 ± 0.04	0.10 ± 0.05
IMF: Chabrier				
Romano/CL	0.047 ± 0.006	0.05 ± 0.03	0.20 ± 0.03	0.25 ± 0.10
WW95/CL	0.18 ± 0.06	0.11 ± 0.05	0.18 ± 0.06	0.34 ± 0.13
Romano/WW95	0.13 ± 0.06	0.12 ± 0.03	0.07 ± 0.04	0.09 ± 0.06
IGIMF				
Romano/CL	0.10 ± 0.07	0.28 ± 0.24	0.48 ± 0.17	0.11 ± 0.07
WW95/CL	0.13 ± 0.05	0.24 ± 0.21	0.48 ± 0.30	0.17 ± 0.11
Romano/WW95	0.14 ± 0.08	0.12 ± 0.04	0.12 ± 0.07	0.09 ± 0.06

4.5.2 Exploring the parameter space

In Fig. 4.16, we explore the effect of changing the model parameter ν in the $[\alpha/\text{Fe}]$ versus $[\text{Fe}/\text{H}]$ abundance ratio patterns, when the metallicity-dependent IGIMF of R14 is assumed. The third dimension (colour-coding) in the figure corresponds to the SFRs under play and the parameter space that we explore is the one provided by [Lanfranchi et al. \(2006\)](#), with the SF efficiencies continuously varying in the range $\nu = 1\text{-}5 \text{ Gyr}^{-1}$. We remark on the fact that [Lanfranchi et al. \(2006\)](#) assumed a [Salpeter \(1955\)](#) IMF.

By looking at Fig. 4.16, by increasing the SF efficiency, it allows us to reach higher $[\alpha/\text{Fe}]$ ratios as well as higher SFRs at a fixed $[\text{Fe}/\text{H}]$ abundance. Furthermore, the models with $\nu = 3 \text{ Gyr}^{-1}$ and $\omega = 9 \text{ Gyr}^{-1}$ with the [Salpeter \(1955\)](#) and [Chabrier \(2003\)](#) IMFs predict always higher $[\alpha/\text{Fe}]$ abundances than the models calculated with the IGIMF. This is due to the extremely low efficiency of formation of massive stars when the IGIMF is assumed for galaxies with very low SFRs.

The effect of changing the wind parameter ω is much lower than varying the SF efficiency ν . For a fixed value of the SF efficiency, the time of the onset of the galactic wind as well as the $[\text{Fe}/\text{H}]$ ratio of the ISM at that epoch are always the same. So different values of the ω parameter affect the chemical evolution only after the onset of the galactic wind. Once the wind has started, both the $[\alpha/\text{Fe}]$ abundance ratios and the SFR decrease further.

We have computed chemical evolution models of the Sgr dwarf with different stellar yield prescriptions, in order to provide a first estimate of the uncertainties due to the stellar yields. Our results are reported in Table 4.1. We have tested dif-

ferent sets of stellar yields besides those of [Romano et al. \(2010\)](#), which we consider as the best in reproducing the solar vicinity abundance pattern. In particular, in addition to them, we have tested also:

- the yields of [Woosley & Weaver \(1995\)](#), with the corrections suggested by [François et al. 2004](#)) for massive stars, and the yields of [van den Hoek & Groenewegen \(1997\)](#) for low- and intermediate-mass stars (this set of stellar yields is the one assumed in the models of Chapter 3);
- the most recent yields from massive stars of the Chieffi and Limongi group (private communication), and the yields of [Karakas \(2010\)](#) from low- and intermediate-mass stars.

We find that the models with the [Romano et al. \(2010\)](#) set of stellar yields agree very well in the predicted [O/Fe] and [Si/Fe] abundance ratios with the models which include the recent yields of the Chieffi and Limongi group. On the other hand, there is still quite a large uncertainty in the stellar yields of Mg and Ca, which affect the results of our models for these two chemical elements; in particular, the final results for [Mg/Fe] and [Ca/Fe] as a function of [Fe/H] may differ by almost 0.2 dex.

In Table 4.1, we explored also the combined effect of different IMF and stellar yield assumptions. We find that the effect of assuming different stellar yields is almost similar for [O/Fe] and [Si/Fe], if we assume the [Salpeter \(1955\)](#) or the [Chabrier \(2003\)](#) IMFs. On the other hand, when assuming the IGIMF, we find that our models become on average more influenced by the assumed stellar yields.

4.6 Conclusions

In this Chapter, we present the results of models testing the effects of different IMFs on the chemical evolution of Sgr dwarf galaxy. In particular, we have considered the IGIMF of R14, which depends on the metallicity and SFR, and the invariant [Salpeter \(1955\)](#) and [Chabrier \(2003\)](#) IMFs. We have run several models by studying the effect of the various parameters, such as the efficiency of SF and the wind parameter.

We have compared different scenarios for the production of Eu. In particular, we have considered the recent NSM scenario of [Matteucci et al. \(2014\)](#) and the canonical scenario in which Eu is produced by core-collapse SNe.

Finally, we have studied the effect of different stellar yield assumptions on the predicted abundance ratio patterns in this galaxy and we have explored also the combined effect of varying both the IMF and the stellar yield assumptions.

In what follows, we summarize the main conclusions of our work.

- The IGIMF tends to predict lower $[\alpha/\text{Fe}]$ and $[\text{Eu}/\text{Fe}]$ ratios in objects with low SFR than the classical [Salpeter \(1955\)](#) and [Chabrier \(2003\)](#) IMFs. In fact, in the case of the IGIMF, there is a deficiency in the formation of massive stars, which are the main contributors of the α -elements. The dependence of the IGIMF on the SFR is much stronger than that on the metallicity, which

in fact could be neglected. Our results support the conclusion that the time-delay model is necessary to explain the trend of the $[\alpha/\text{Fe}]$ and $[\text{Eu}/\text{Fe}]$ ratios as a function of $[\text{Fe}/\text{H}]$; furthermore, the assumption of a truncated IMF such as the IGIMF provides a better qualitative agreement with the abundance ratio patterns observed in the Sgr galaxy, although both the data and the stellar yields that we assume in our models are still too uncertain to draw firm conclusions. It is worth recalling that the effect of changing the IMF consists mainly in shifting the $[X/\text{Fe}]$ (with X the abundance of a generic element) curves up or down along the Y -axis, whereas the shape of the $[X/\text{Fe}]$ versus $[\text{Fe}/\text{H}]$ curves is mainly determined by the lifetimes of the stellar producers of X and Fe and by the star formation history (time-delay model).

- The oxygen is the hydrostatic α -element which is most sensitive to the cut-off in mass of the IMF, while the explosive α -elements such as the silicon and the calcium are much less sensitive. So the hydrostatic over explosive α -element abundance ratios can retain a well-defined signature of a truncated IMF, as suggested by [McWilliam et al. \(2013\)](#). The O and Si are among the chemical elements which are less affected by uncertainties relative to their stellar yields; the results of our models, in particular the comparison of the $[\text{O}/\text{Si}]$ versus $[\text{Fe}/\text{H}]$ relations predicted by our models with the [McWilliam et al. \(2013\)](#) data, might support the idea that the IMF in the Sgr galaxy is truncated, with the IGIMF being the favourite among the different IMFs here explored. However, again, the data are still too uncertain to draw firm conclusions.
- All our models with Eu coming from core-collapse SNe are not able to reproduce the $[\text{Eu}/\text{Fe}]$ and $[\text{Eu}/\text{O}]$ abundance ratios at the same time, unless the yields from stars in the range $8\text{-}10 M_{\odot}$ are artificially increased by a factor of ~ 3 . When including the Eu produced by NSMs as the only source of this element, we are also able to well match the data, by assuming yields as suggested by recent calculations ([Bauswein et al., 2014](#); [Wanaajo et al., 2014](#); [Just et al., 2015](#)).
- Since NSMs, which are nowadays considered as more promising sites for Eu production, arise from stars which have an initial mass in a lower range than that of the most important oxygen producers, the hypothesis of [McWilliam et al. \(2013\)](#) remains true. Furthermore, we confirm that in Sgr the truncation of the IMF might have played a relevant role in the $[\text{Eu}/\text{O}]$ versus $[\text{Fe}/\text{H}]$ relations, while the $[\text{Eu}/\text{Fe}]$ versus $[\text{Fe}/\text{H}]$ is due mainly to the time-delay model.
- By exploring the parameter space, and in particular by studying the effect of the star formation and galactic wind efficiencies, we found that the major role in determining the final abundance pattern in Sgr galaxy is played by the star formation efficiency, while the wind parameter has only a small effect.
- The IMFs considered here are all able to reproduce the present time observed total HI mass. On the other hand, the model with the IGIMF predicts final

total stellar masses which are slightly larger than the ones predicted by the models with the classical IMFs. This is probably due to the delayed onset of the galactic wind in IGIMF models, because of the reduced energetic feedback from massive stars. The galaxy forms stars for a longer period and thus a large mass in long-living, low-mass stars can accumulate.

- The present results can be useful to study also other dSphs, since the history of these galaxies is characterized by a low SFR, which implies a truncated IMF in the formalism of the IGIMF theory.

Our last comment is that combining the chemical evolution models with the spectro-photometric ones might greatly help to better constrain the role and the effect of the IGIMF in the evolution of galaxies.

References

- Arcones A., Janka H. T., Scheck L., 2007, *A&A*, 467, 1227
Asplund M., Grevesse N., Sauval A. J., Scott P., 2009, *ARA&A*, 47, 481
Bauswein A., Ardevol Pulpillo R., Janka H. T., Goriely S., 2014, *ApJ*, 795, LL9
Bradamante F., Matteucci F., D’Ercole A., 1998, *ApJ*, 337, 338
Bellazzini M., Correnti M., Ferraro F. R., Monaco L., Montegriffo P., 2006, *A&A*, 446, L1
Bellazzini M. et al., 2008, *AJ*, 136, 1147
Belokurov V. et al., 2006, *ApJ*, 642, L137
Bonifacio P., Hill V., Molaro P., Pasquini L., Di Marcantonio P., Santin P., 2000, *A&A*, 359, 663
Bonifacio P., Sbordone L., Marconi G., Pasquini L., Hill V., 2004, *A&A*, 414, 503
Calura F., Recchi S., Matteucci F., Kroupa P., 2010, *MNRAS*, 406, 1985
Cescutti G., François P., Matteucci F., Cayrel R., Spite M., 2006, *A&A*, 448, 557
Chabrier G., 2003, *PASP*, 115, 763
Cole A. A., 2001, *ApJ*, 559, L17
de Boer T. J. L., Belokurov V., Beers T. C., Lee Y. S., 2014, *MNRAS*, 443, 658
Dominik M., Belczynski K., Fryer C., Holz D. E., Berti E., Bulik T., Mandel I., O’Shaughnessy R., 2012, *ApJ*, 759, 52
Ekström S., Meynet G., Chiappini C., Hirschi R., Maeder A., 2008, *A&A*, 489, 685
Fields B. D., Truran J. W., Cowan, J. J., 2002, *ApJ*, 575, 845
François P., Matteucci, F., Cayrel R., Spite M., Spite F., Chiappini C., 2004, *ApJ*, 421, 613
Greggio L., Renzini A., 1983, *Mem. Soc. Astron. Ital.*, 54, 311
Hirschi R., Meynet G., Maeder A., 2005, *A&A*, 433, 1013
Hirschi R., 2007, *A&A*, 461, 571
Ibata R. A., Gilmore G., Irwin M. J., 1994, *Nature*, 370, 194
Ibata R. A., Wyse R. F. G., Gilmore G., Irwin M. J., Suntzeff N. B., 1997, *AJ*, 113, 634
Ibata R., Irwin M., Lewis G. F., Stolte A., 2001, *ApJ*, 547, L133
Ishimaru Y., Wanajo S., Aoki W., Ryan S. G., 2004, *ApJ*, 600, L47
Iwamoto K., Brachwitz F., Nomoto K., Kishimoto N., Umeda H., Hix W. R., Thielemann F. K., 1999, *ApJ*, 125, 439
Just O., Bauswein A., Pulpillo R. A., Goriely S., Janka H.-T., 2015, *MNRAS*, 448, 541
Karakas A. I., 2010, *MNRAS*, 403, 1413

- Kobayashi C., Umeda H., Nomoto K., Tominaga N., Ohkubo T., 2006, *ApJ*, 653, 1145
- Koribalski B., Johnston S., Otrupcek R., 1994, *MNRAS*, 270, L43
- Korobkin O., Rosswog S., Arcones A., Winteler C., 2012, *MNRAS*, 426, 1940
- Kroupa P., Weidner C., 2003, *ApJ*, 598, 1076
- Kroupa, P., Weidner, C., Pflamm-Altenburg, J., Thies I., Dabringhausen J., Marks M., Maschberger T., 2013, *Planets, Stars and Stellar Systems. Volume 5: Galactic Structure and Stellar Populations*, Springer, Dordrecht, 115
- Lanfranchi G. A., Matteucci F., 2003, *MNRAS*, 345, 71
- Lanfranchi G. A., Matteucci F., 2004, *MNRAS*, 351, 1338
- Lanfranchi G. A., Matteucci F., Cescutti G., 2006, *A&A*, 453, 67
- McConnachie A. W., 2012, *AJ*, 144, 4
- McWilliam A., Preston G. W., Sneden C., Searle L., 1995, *AJ*, 109, 2757
- McWilliam A., Wallerstein G., Mottini M., 2013, *ApJ*, 778, 149
- Majewski S. R., Skrutskie M. F., Weinberg M. D., Ostheimer J. C., 2003, *ApJ*, 599, 1082
- Marks M., Kroupa P., Dabringhausen J., Pawlowski M. S., 2012, *MNRAS*, 422, 2246
- Matteucci F., Brocato E., 1990, *ApJ*, 365, 539
- Matteucci F., Greggio L., 1986, *A&A*, 154, 279
- Matteucci F., 2001, *Astrophysics and Space Science Library*, 253
- Matteucci F., Recchi S., 2001, *ApJ*, 558, 351
- Matteucci F., 2014, *The Origin of the Galaxy and Local Group*, Saas-Fee Advanced Course. Springer-Verlag, Berlin, 2014, p. 145
- Matteucci F., Romano D., Arcones A., Korobkin O., Rosswog S., 2014, *MNRAS*, 438, 2177
- Matteucci F., Romano D., Arcones A., Korobkin O., Rosswog S., 2015, *MNRAS*, 447, 326
- Mennekens N., Vanbeveren D., 2014, *A&A*, 564, AA134
- Meynet G., Maeder A., 2002, *A&A*, 390, 561
- Monaco L., Bellazzini M., Ferraro F. R., Pancino E., 2003, *ApJ*, 597, L25
- Recchi S., Calura F., Kroupa P., 2009, *A&A*, 499, 711
- Recchi S., Calura F., Gibson B. K., Kroupa P., 2014, *MNRAS*, 437, 994 (R14)
- Romano D., Chiappini C., Matteucci F., Tosi M., 2005, *A&A*, 430, 491
- Romano D., Karakas A. I., Tosi M., Matteucci F., 2010, *A&A*, 522, A32
- Salpeter E. E., 1955, *ApJ*, 121, 161
- Salvadori S., Ferrara A., 2009, *MNRAS*, 395, L6
- Sbordone L., Bonifacio P., Buonanno R., Marconi G., Monaco L., Zaggia S., 2007, *A&A*, 465, 815
- Shen S., Cooke R., Ramirez-Ruiz E., Madau P., Mayer L., Guedes J., 2014, preprint (arXiv:1407.3796)
- Schmidt M., 1959, *ApJ*, 129, 243
- Simon J. D., et al., 2011, *ApJ*, 733, 46
- Tinsley B. M., 1979, *ApJ*, 229, 1046
- Tsujimoto T., Shigeyama T., 2014, *A&A*, 565, L5
- van den Hoek L. B., Groenewegen M. A. T., 1997, *A&AS*, 123, 305
- van de Voort F., Quataert E., Hopkins P. F., Kereš D., Faucher-Giguère C. A., 2015, *MNRAS*, 447, 140
- Vincenzo F., Matteucci F., Vattakunnel S., Lanfranchi G. A., 2014, *MNRAS*, 441, 2815
- Vincenzo, F., Matteucci, F., Recchi, S., et al. 2015, *MNRAS*, 449, 1327
- Walker M. G., Mateo M., Olszewski E. W., Peñarrubia J., Wyn Evans N., Gilmore G., 2009, *ApJ*, 704, 1274
- Wanajo S., Tamamura M., Itoh N., Nomoto K., Ishimaru Y., Beers T. C., Nozawa S., 2003, *ApJ*, 593, 968

Chapter 4. The integrated galactic initial mass function and neutron star mergers in the Sagittarius dwarf spheroidal galaxy

- Wanajo S., Sekiguchi Y., Nishimura N., Kiuchi K., Kyutoku K., Shibata M., 2014, *Apj*, 789, LL39
- Wehmeyer B., Pignatari M., Thielemann F. K., 2015, preprint (arXiv:1501.07749)
- Weidner C., Kroupa P., 2004, *MNRAS*, 348, 187
- Weidner C., Kroupa P., 2005, *ApJ*, 625, 754
- Weidner, C., Kroupa, P., & Pflamm-Altenburg, J. 2011, *MNRAS*, 412, 979
- Weidner C., Ferreras I., Vazdekis A., La Barbera F., 2013, *MNRAS*, 435, 2274
- Woolsey S. E., Weaver T. A., 1995, *ApJS*, 101, 181
- Yin J., Matteucci F., Vladilo G., 2011, *ApJ*, 531, A136
- Zhang Q., Fall S. M., 1999, *ApJ*, 527, L81

5

Are ancient dwarf satellites the building blocks of the Galactic halo?

5.1 Introduction

The current cosmological Λ cold dark matter (Λ CDM) paradigm predicts large-scale structures in the Universe to assemble from the coalescence of small-scale ones, via cooling and condensation of gas in always larger dark matter halos (Press & Schechter, 1974; White & Rees, 1978; Springel et al., 2006). According to this paradigm, galaxies like the Milky Way (MW) formed through cosmic epochs by accreting a large number of small satellite systems which, even today, might be still in the process of merging.

Dwarf spheroidal galaxies (dSphs) were proposed in the past as the best candidates of such small progenitor systems, merging through the past cosmic time to form the actual stellar halo of the Galaxy (e.g. Grebel 2005). In fact, from an observational point of view, the MW dSph satellites have been for many years in the past the faintest and most dark matter dominated stellar systems ever observed. Nevertheless, the role played by dSphs in shaping the halo of the MW has always remained controversial. Major issues were the relatively small number of discovered dSph satellites (the so-called *missing satellite problem*, e.g. Bullock et al. 2010; Klypin et al. 1999; Moore et al. 1999) and the different chemical abundance patterns of the halo and dSph stars (Shetrone et al., 2001; Venn et al., 2004; Vincenzo, Matteucci, Vattakunnel & Lanfranchi, 2014).

In order to test the capability of the hierarchical galaxy formation scenario to explain the MW halo metallicity distribution function (MDF), Prantzos (2008) developed an analytical chemical evolution model, where the Galaxy halo grows through successive merger events of small sub-halos, which were assumed to have

similar physical properties as current dSphs. Although the treatment of the chemical evolution of the interstellar medium (ISM) was approximate, Prantzos (2008) was able to reproduce the Galaxy halo MDF, only by relying on the stellar mass distribution function of the merging sub-halo population, which the current hierarchical galaxy formation paradigm can predict with very high accuracy. Nevertheless, Prantzos (2008) did not discuss any implication on the $[\alpha/\text{Fe}]$ versus $[\text{Fe}/\text{H}]$ abundance pattern, which is one of the main issues which hierarchical picture has to deal with, since the abundance patterns of surviving Local Group galaxies do not match those of the stars in the stellar halo.

In the past literature, interesting works are the ones by Unavane et al. (1996); Jofré & Weiss (2011), which used the age distributions of the stars in the halo and dSphs to test the origin of the halo stars. Furthermore, by including a chemical evolution model within a full cosmological framework, Font et al. (2006) concluded that the observed discrepancy in the $[\alpha/\text{Fe}]$ ratios can be solved if the majority of the MW halo formed by accreting sub-halos with mass in the range 10^5 - $10^8 M_{\odot}$, which were likely disrupted very early (> 8 - 9 Gyr ago). Finally, by using RR Lyrae stars as tracers of the Galactic halo ancient stellar populations, Fiorentino et al. (2015) showed that dSphs do not appear to be the major building-blocks of the halo, suggesting an extreme upper limit of 50 per cent to their contribution.

In recent years, Willman et al. (2005); Belokurov et al. (2006a,b, 2007) – by using the Sloan Digital Sky Survey (SDSS, York et al. 2000) – were able to discover an entirely new population of hitherto unknown stellar systems: the so-called ultra faint dwarf spheroidal galaxies (UFDs), which are characterized by extremely low luminosities, high dark matter content, and very old and iron-poor stellar populations (Belokurov et al., 2006a; Norris et al., 2008, 2010; Brown et al., 2012). Furthermore, UFD systems are observed to be completely gas-free at the present time. The number of UFDs has increased constantly in the last decade and completeness estimates suggest that many more of these faint satellites are still to be discovered in the Local Group (Tollerud et al., 2008).

In the last years, the Dark Energy Survey, PanSTARRS, ATLAS, and MagLiteS surveys almost doubled the total number of discovered UFD MW satellites, going towards always lower luminosities and effective radii (see, for example, the works by Bechtol et al. 2015, Drlica-Wagner et al. 2015, Kim et al. 2015, Kim & Jerjen 2015, Koposov et al. 2015, Laevens et al. 2015, Martin et al. 2015, Luque et al. 2016, Torrealba et al. 2016, and Drlica-Wagner et al. 2016). These recent discoveries might place the new UFDs as the survived building blocks of the Galaxy stellar halo, dramatically lacking in the past.

The main aims of this Chapter can be summarized as follows.

- We test the hypothesis that dSph and UFD galaxies have been the building blocks of the Galactic halo, by assuming that the halo formed by accretion of stars belonging to these galaxies.
- We explore the scenario, in which the Galactic halo formed by accretion of chemically enriched gas originating from dSph and UFD galaxies.

All the results of this Chapter have been published in Spitoni, Vincenzo, Matteucci & Romano (2016).

This Chapter is organized as follows: in Section 5.2 we present our chemical evolution models for the Galaxy, dSph and UfD galaxies, in Section 5.3 we describe the way in which we implement the enriched gas infall on the chemical evolution of the Galactic halo. The results are presented in Section 5.4. Finally, our conclusions are summarized in Section 5.5.

5.2 The assumed chemical evolution models

The Galactic halo is assumed to assemble by accreting enriched material, with chemical abundances identical to those of the gas outflowing/stripped from dSph and UfD galaxies. In this Section we will give some details about the reference chemical evolution models for the MW, dSph, and UfD galaxies.

On the one hand, all the MW models assume the following prescription for the star formation rate (SFR), which resembles a [Kennicutt \(1998\)](#) law:

$$\psi(t) \propto \nu \sigma_g^k, \quad (5.1)$$

where ν is the star formation efficiency, σ_g is the surface gas density, and $k = 1.5$ is the gas surface exponent. On the other hand, the SFR of dSph and UfD galaxies is assumed to be proportional to the volume gas density ρ_g , with an exponent $k = 1$:

$$\psi(t) \propto \nu \rho_g^k. \quad (5.2)$$

In [Romano et al. \(2015\)](#), it is recalled that – for star-forming regions with roughly constant scale heights – the index $k = 1.5$ for the surface gas mass density can be turned into an index $k = 1$ for volume gas mass densities; therefore, equation (5.1) for the MW is consistent with equation (5.2) for the dSph and UfD galaxies.

5.2.1 The Milky Way

We consider the following two reference chemical evolution models for the MW galaxy: the so-called *two infall model* and *two infall plus outflow model*, as developed and described in [Brusadin et al. \(2013\)](#). In what follows, we summarize their main characteristics.

Two infall model for the Milky Way

The two-infall model (2IM) as presented by [Brusadin et al. \(2013\)](#) is an updated version of the model by [Chiappini et al. \(1997\)](#). The Galaxy is assumed to form by means of two main infall episodes: the first was responsible for the halo and the thick disc formation, while the second assembled the thin disc. Both infall episodes are assumed to obey a decaying exponential law with time. In particular, the accretion rate of a given element i , at the time t and Galactocentric distance r , is defined as follows:

$$A(r, t, i) = X_{A_i} \left(a(r) e^{-t/\tau_H(r)} + b(r) e^{-(t-t_{\max})/\tau_D(r)} \right), \quad (5.3)$$

Chapter 5. Are ancient dwarf satellites the building blocks of the Galactic halo?

Table 5.1: Parameters of the chemical evolution models for the Milky Way ([Brusadin et al. \(2013\)](#)) in the solar neighborhood.

The Milky Way: the solar neighborhood model parameters

Models	Infall type	τ_{H} [Gyr]	τ_{D} [Gyr]	Threshold [$M_{\odot}\text{pc}^{-2}$]	k	ν [Gyr^{-1}]	IMF	ω [Gyr^{-1}]
2IM	2 infall	0.8	7	4 (halo-thick disc)	1.5	2 (halo-thick disc)	Scalo (1986)	/
				7 (thin disc)		1 (thin disc)		
2IMW	2 infall	0.2	7	4 (halo-thick disc)	1.5	2 (halo-thick disc)	Scalo (1986)	14
				7 (thin disc)		1 (thin disc)		

Table 5.2: Parameters of the chemical evolution model for a general dSph galaxy.

dSphs: parameters of the model

ν [Gyr^{-1}]	k	ω	τ_{inf} [Gyr]	SFH (99% of stars) [Gyr]	M_{inf} [M_{\odot}]	M_{DM} [M_{\odot}]	r_{L} [pc]	$S = \frac{r_{\text{L}}}{r_{\text{DM}}}$	IMF	t_{gw} [Gyr]	[Fe/H] _{peak} [dex]
0.1	1	10	0.5	0-2.43	10^7	$3.4 \cdot 10^8$	260	0.52	Salpeter (1955)	0.013	-2.10

Table 5.3: Parameters of the chemical evolution model for a general UFD galaxy.

UFDs: parameters of the model

ν [Gyr^{-1}]	k	ω	τ_{inf} [Gyr]	SFH (99% of stars) [Gyr]	M_{inf} [M_{\odot}]	M_{DM} [M_{\odot}]	r_{L} [pc]	$S = \frac{r_{\text{L}}}{r_{\text{DM}}}$	IMF	t_{gw} [Gyr]	[Fe/H] _{peak} [dex]
0.01	1	10	0.001	0-0.49	10^5	10^6	35	0.1	Salpeter (1955)	0.088	-3.30

where the quantity $X_{A_i} = \sigma_i(t)/\sigma_{\text{gas}}(t)$ is the abundance by mass of the element i in the infalling material; $t_{\text{max}} = 1$ Gyr is the time for the maximum infall on the thin disc; $\tau_{\text{H}} = 0.8$ Gyr is the time scale for the formation of the halo and thick-disc; finally, $\tau_{\text{D}}(r)$ is the timescale for the formation of the thin disc and it is a function of the galactocentric distance (inside-out formation; [Matteucci & François 1989](#); [Chiappini et al. 2001](#)). In the original 2IM model, the abundances X_{A_i} have primordial gas compositions and are constant in time.

The coefficients $a(r)$ and $b(r)$ in equation (5.3) are obtained by normalizing the infall law with respect to the present day total surface mass densities of the halo and thin disc, respectively; for instance, we assume the following radial profile for the thin disc total surface mass density at the present time:

$$\sigma(r) = \sigma_0 e^{-r/r_{\text{D}}}, \quad (5.4)$$

where $\sigma_0 = 531 \text{ M}_{\odot} \text{ pc}^{-2}$ is the central total surface mass density and $r_{\text{D}} = 3.5 \text{ kpc}$ represents the scale length (see also ([Matteucci, 2001](#))).

The halo total surface mass density at solar position is quite uncertain; we assume it to be $17 \text{ M}_{\odot} \text{ pc}^{-2}$. In fact, the total surface mass density in the solar vicinity roughly corresponds to $\sim 71 \text{ M}_{\odot} \text{ pc}^{-2}$ ([Kuijken & Gilmore, 1991](#)), including both the halo and the disc contributions, with $\sim 54 \text{ M}_{\odot} \text{ pc}^{-2}$ corresponding to the disc contribution.

Two infall plus outflow model for the Milky Way

In the two-infall plus outflow model of [Brusadin et al. \(2013\)](#) (we will indicate it as the 2IMW model), a gas outflow is assumed to occur during the halo phase. Following [Hartwick \(1976\)](#), the outflow rate has the following expression:

$$\left(\frac{d\sigma_{\text{g}}}{dt}\right)_{\text{out}} = -\omega \psi(t), \quad (5.5)$$

where ω is the outflow efficiency.

Summary of the free parameters and data

In Table 5.1, we summarize the main characteristics of the two chemical evolution models that we assume for the MW. We only focus on the study of the halo phase, with the aim of investigating the effects of a pre-enriched infall of gas.

We assume that the halo phase spans a range of [Fe/H] abundances, which is defined up to -1 dex.

In our model, we do not modify the gas infall laws of the [Brusadin et al. \(2013\)](#) model, i.e. the way in which the Galaxy assembles remains the same. *We only consider a time dependent enriched infall, i.e. $X_{A_i} = X_{A_i}(t)$, with the same chemical abundances of the outflowing gas from dSph and UFD galaxies.*

Concerning the observational data for α -elements and iron, as done in [Micali et al. \(2013\)](#), we employ only data in which NLTE corrections are considered. In particular, the data we use for Galactic halo stars are from [Gratton et al. \(2003\)](#);

Cayrel et al. (2004); Akerman et al. (2004); Mashonkina et al. (2007); Shi et al. (2009). For barium, we use the data by Frebel (2010), as selected and binned by Cescutti et al. (2013).

5.2.2 The dSph and UfD galaxies

To model the chemical evolution of dSph and UfD galaxies, we refer to the work by Vincenzo, Matteucci, Vattakunnel & Lanfranchi (2014), as presented in Chapter 3 of this Thesis. In Tables 5.2 and 5.3, the main parameters of the generic models for “classical” dSph and UfD galaxies are reported, respectively. We assume that UfD objects are characterized by a very small star formation efficiency (0.01 Gyr^{-1}) and by an extremely short time scale of formation (0.001 Gyr). Hence UfD objects started to form stars as most of their infall mass, $M_{\text{inf}} = 10^5 M_{\odot}$, was accumulated in their DM potential well ($\tau_{\text{inf}} = 0.001 \text{ Gyr}$) and the star formation efficiency is very low ($\nu = 0.01 \text{ Gyr}^{-1}$). Our chemical evolution model for a typical dSph galaxy assumes an infall mass $M_{\text{inf}} = 10^7 M_{\odot}$, an infall timescale $\tau_{\text{inf}} = 0.5 \text{ Gyr}$, and a star formation efficiency $\nu = 0.1 \text{ Gyr}^{-1}$. *Although the star formation history (SFH) is assumed to be extended over the entire galaxy lifetime* both for the dSph and the UfD galaxy, it is strongly concentrated in the earliest stages of the galaxy evolution; in fact, as most of the infall mass has been accumulated and the galactic wind has started, the intensity of the SFR becomes negligible. We acknowledge that this kind of SFR history is not representative of the more luminous dSph galaxies (e.g. Weisz et al. 2014). We point out that, in modeling the dSphs and UfDs, we did not consider any threshold in the gas density for star formation, as in Vincenzo, Matteucci, Vattakunnel & Lanfranchi (2014).

For the dSph model, the galactic wind is predicted to occur at 0.013 Gyr after the galaxy formation, whereas for UfDs at 0.088 Gyr . As expected, the UfD galaxies develop a wind at later times because of the smaller adopted star formation efficiency (SFE), which causes the thermal energy of the galaxy ISM – as deposited by Type II and Type Ia SNe and stellar winds – to increase more slowly. Moreover, because of the shorter typical formation time-scale, the G-dwarf metallicity distribution function (MDF) of UfD galaxies peaks at lower $[\text{Fe}/\text{H}]$ values than the dSph galaxies.

5.2.3 Nucleosynthesis prescriptions

In this work, we adopt the nucleosynthesis prescriptions of Romano et al. (2010, their model 15), which provide a compilation of stellar yields able to reproduce the abundance patterns of several chemical elements in the solar neighborhood. We remind the reader that Romano et al. (2010) include the following sets of stellar yields (see also Chapter 2.5.1 and Chapter 4.4.1):

1. For low- and intermediate-mass stars ($0.8\text{--}8 M_{\odot}$), they include the metallicity-dependent stellar yields of Karakas (2010). For SNe Ia, the adopted nucleosynthesis prescriptions are from Iwamoto et al. (1999).
2. For massive stars ($M > 8 M_{\odot}$), which are the progenitors of either SNe II or HNe, depending on the explosion energy, they assume the metallicity-

dependent He, C, N and O stellar yields, as computed with the Geneva stellar evolutionary code, which takes into account the combined effect of mass loss and rotation [Meynet & Maeder \(2002\)](#); [Hirschi et al. \(2005\)](#); [Hirschi \(2007\)](#); [Ekström et al. \(2008\)](#); for all the elements heavier than oxygen, they assume the up-to-date stellar evolution calculations by [Kobayashi et al. \(2006\)](#).

For barium, we assume the stellar yields of [Cescutti et al. \(2006, their model 1, in table 4\)](#). In particular, [Cescutti et al. \(2006\)](#) include the metallicity-dependent stellar yields of Ba as computed by [Busso et al. \(2001\)](#), in which barium is produced by low-mass AGB stars, with mass in the range $1.0 \leq M \leq 3.0 M_{\odot}$, as an s-process neutron capture element. A second channel for the Ba-production was included by [Cescutti et al. \(2006\)](#), by assuming that massive stars in their final explosive stage are capable of synthesizing Ba as a primary r-process element. Such r-process Ba producers have mass in the range $12 \leq M \leq 30 M_{\odot}$.

We remark on the fact that the contribution to barium from massive stars was empirically computed by [Cescutti et al. \(2006\)](#), by matching the [Ba/Fe] versus [Fe/H] abundance pattern as observed in the Galactic halo stars. They assumed for massive stars the iron stellar yields of [Woosley & Weaver \(1995\)](#), as corrected by [François et al. \(2004\)](#).

5.3 Milky Way models with an enriched infall of gas

We take into account – in a self-consistent way – time-dependent chemical abundances for the infall material in the halo phase; in particular, we assume $X_{A_i} = X_{A_i}(t)$ in equation (5.3), with the values of $X_{A_i}(t)$ corresponding to the chemical abundances of the ejected material by dSph and UFD galaxies through their galactic winds. This is the novelty of our work. Actually, it may well be that the gas heated by SN explosions is stored in a hot gaseous halo surrounding the satellites, from which it is stripped owing to the interaction with our Galaxy. In what follows, we will only mention galactic winds for the sake of simplicity, but this alternate option (stripping) would work equally well. The gas infall law is the same as in the 2IM or 2IMW models and we only consider a time dependent chemical composition of the infall gas mass.

We assume the following two models:

- **Model i):** The chemical abundance of the infalling gas during the halo phase is primordial before the onset of the galactic winds in the dSph (or UFD) galaxies. Successively, namely after the onset of the galactic wind, the infalling gas has the same chemical abundances as in the galactic wind. In all our Galactic models, the gas infall laws are identical to the reference model of [Brusadin et al. \(2013\)](#); the only thing that we modify is the chemical composition of the infalling gas. In all the successive figures and in the text, we refer to this kind of models with the label “Name of the reference model for the MW + dSph” or “Name of the reference model for the MW + UFD”.
- **Model ii):** we explore the case of a diluted infall of gas during the MW halo phase. In particular, after the galactic wind develops in the dSph (or

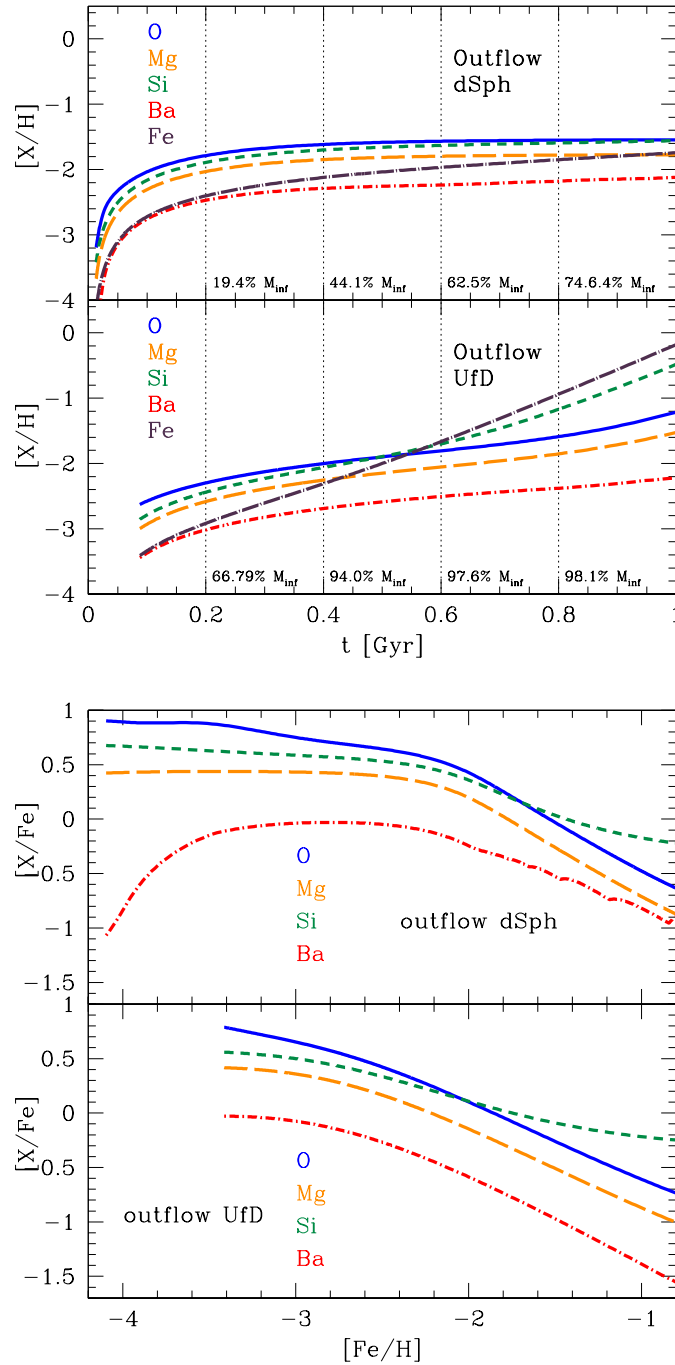


Figure 5.1: *Upper panels:* The evolution in time of the chemical abundances for O, Mg, Si, Ba, Fe in the gas ejected as galactic wind from dSphs and UfDs. As shown in Tables 2 and 3 in UfDs the onset of the wind happens at later times compared with dSph objects: $t_{gw}(dSph) < t_{gw}(UfD)$. We also indicate the cumulative ejected gas mass by outflows at 0.2, 0.4, 0.6, and 0.8 Gyr in terms of percentage of the infall mass M_{inf} . *Lower panels:* The abundance ratio $[X/Fe]$ as a function of $[Fe/H]$ for the following chemical elements: O, Mg, Si, and Ba of the outflowing gas ejected by a dSph galaxy, and by a UfD galaxy.

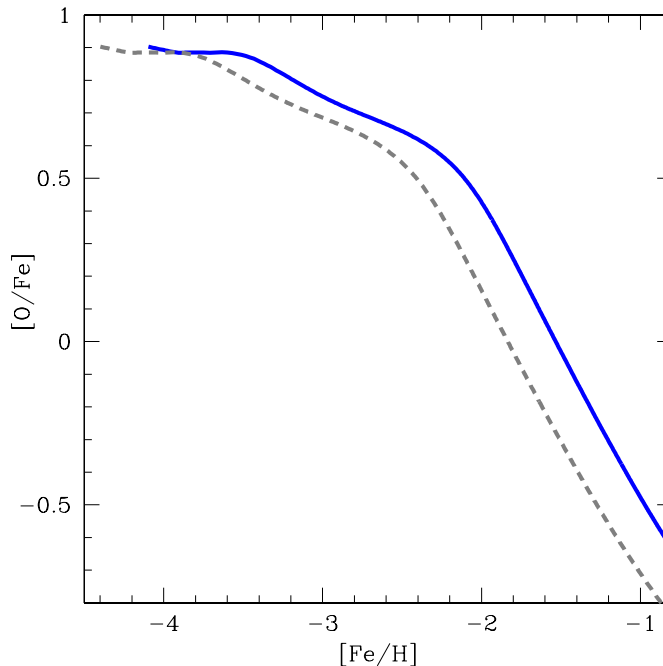


Figure 5.2: The abundance ratio $[O/Fe]$ as a function of $[Fe/H]$ of the outflowing gas ejected by the dSph galaxy (blue solid line) compared with the “mixed” infall model (dashed gray line).

UfD) galaxies, the infalling gas has a chemical composition which, by 50 per cent, is contributed by the dSph (or UfD) outflows; the remaining 50 per cent is contributed by primordial gas of a different extra-galactic origin (in agreement with the work of [Fiorentino et al. 2015](#)). As stated above, the infall law follows the same law as assumed in the 2IM or 2IMW models presented in [Brusadin et al. \(2013\)](#). In all the successive figures and in the text, we refer to these models with the labels “Name of the MW model + dSph (or UfD) MIX”.

In the two upper panels of Fig. 5.1, we show the evolution in time of the chemical composition of the outflowing gas from the dSph and the UfD galaxy for O, Mg, Si, Ba and Fe (curves with different colors). It is worth noting that, in the outflows from UfD galaxies, the Fe and Si abundances are larger than in the outflows from dSphs.

We recall that Fe is mostly produced by Type Ia SNe and Si is also produced in a non negligible amount by the same SNe. Since in our models the ratio between the infall time scales of UfDs and dSphs is extremely low, at later times the pollution from Type Ia SNe is more evident in the UfD outflow. As shown in Tables 5.2 and 5.3, the onset of the galactic wind in UfDs occurs at later times than in dSphs.

In the two lower panels of Fig. 5.1, we present the $[X/Fe]$ versus $[Fe/H]$ abundance patterns, where X corresponds to O, Mg, Si, and Ba (curves with different colors).

Finally, in Fig. 5.2, we show how the [O/Fe] ratio is predicted to vary as a function of [Fe/H] in the galactic wind of a classical dSph galaxy (see Table 5.2); we compare this pattern with the “MIX” case, where the abundances of the infalling gas from dSph galaxies are diluted by 50 per cent with gas of primordial chemical composition.

5.4 Results

In this Section, we present the results of our chemical evolution models for the Galactic halo, by assuming that either

- all the stars of the Galactic halo were born in situ in dSph galaxies;

or

- the Galactic halo formed by accretion of pre-enriched material, originating in dSphs and UfdS (Models i in Section 5.3). We explore also the case in which the infalling enriched material is diluted by pristine gas of different extra-galactic origin (Models ii in Section 5.3).

The results are divided into two separate subsections, according to the MW chemical evolution model which is assumed, namely the 2IM (two-infall) or the 2IMW (two infall plus outflow) model.

5.4.1 Results: the Galactic halo in the model 2IM

In Fig. 5.3, the [O/Fe] vs. [Fe/H] chemical abundance patterns, as predicted by all our 2IM-based models, are compared with the observed data in the Galactic halo stars. In order to test the hypothesis that Galactic halo stars have been stripped from dSph or Ufd systems, we show also the predictions of our chemical evolution models for dSphs and UfdS (long dashed lines in grey and black, respectively); by looking at the figure, the two models cannot explain the observed $[\alpha/\text{Fe}]$ ratios for $[\text{Fe}/\text{H}] \gtrsim -2.0$ dex. In fact, halo stars have always larger [O/Fe] ratios than dSph and Ufd stars.

In Fig. 5.3 we show also the predictions of our models assuming the halo to form by accreting enriched material from the galactic winds of dSph and Ufd galaxies. In particular, we compare the reference 2IM model (which assumes primordial infall) with the “2IM+dSph” and “2IM+Ufd” models (where the infall gas is enriched according to Model i and ii, respectively; see also Section 5.3); finally, we show also the “2IM+dSph MIX” and “2IM+Ufd MIX” models, where the chemical abundances of the outflowing gas from dSphs and UfdS is diluted with primordial gas by 50 per cent.

Firstly, we can appreciate that – for the oxygen data of halo stars – a better agreement is obtained when assuming an enriched infall for the halo phase. We recall that a key ingredient of the 2IM model is the presence of a threshold in the surface gas mass density during the halo-thick disc phase, $\sigma_{\text{g,th}} = 4 M_{\odot} \text{pc}^{-2}$, below which the star formation is assumed to be suppressed. During the halo phase such

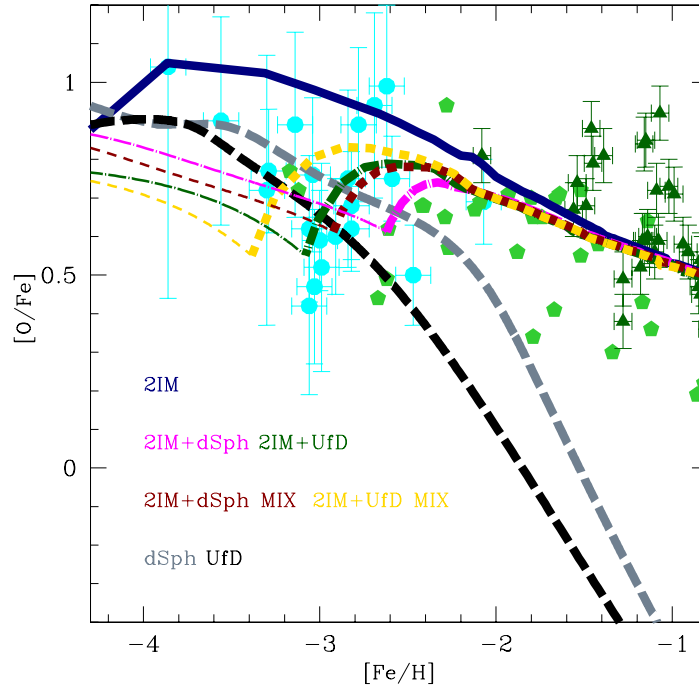


Figure 5.3: The abundance ratio $[O/Fe]$ as a function of $[Fe/H]$ in the solar neighborhood for the reference model 2IM is drawn with the solid blue line. *Models of the Galactic Halo with the enriched infall from dSph:* the magenta dashed dotted line and the red short dashed line represent the models 2IM+dSph and 2IM+dSph MIX, respectively. *Models of the Galactic Halo with the enriched infall from UfDs:* the green dashed dotted line and the yellow short dashed line represent the models 2IM+UfD and 2IM+UfD MIX, respectively. Thinner lines indicate the ISM chemical evolution phases in which the SFR did not start yet in the Galactic halo, and during which stars are no created. *Models of the dSph and UfD galaxies:* The long dashed gray line represents the abundance ratios for the dSph galaxies, whereas long dashed black line for the UfD galaxies. *Observational data of the Galactic Halo:* Cayrel et al. (2004) (cyan circles), Akerman et al. (2004) (light green pentagons), Gratton et al. (2003) (dark green triangles).

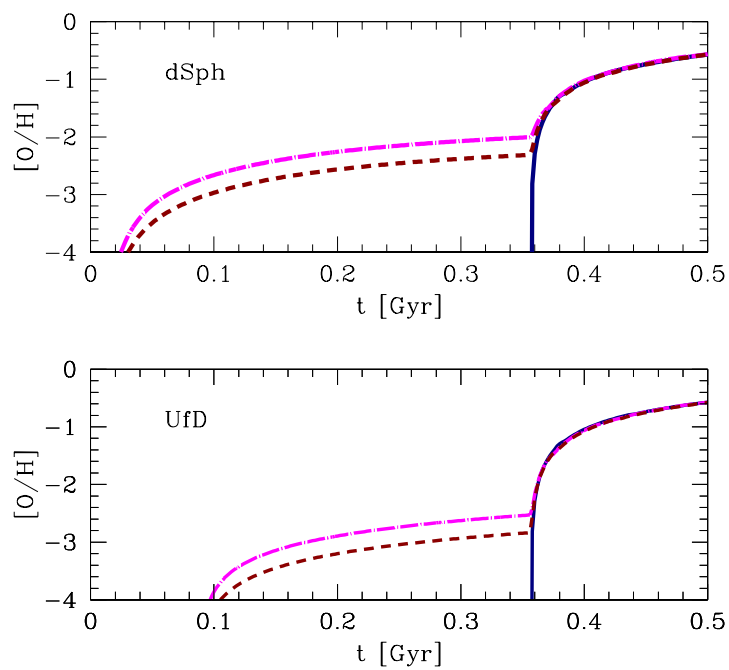


Figure 5.4: *Upper panel:* The abundance ratio $[O/H]$ as a function of Galactic time in the solar neighborhood. We compared the 2IM model (blue solid line) with the model where we have taken into account the enriched infall from dSph galaxies (model 2IM+dSph with dashed dotted magenta line). With the short dashed red line we represent the model 2IM+dSph MIX. *Lower panel:* As in the upper panel but considering the enriched gas from UfD galaxies.

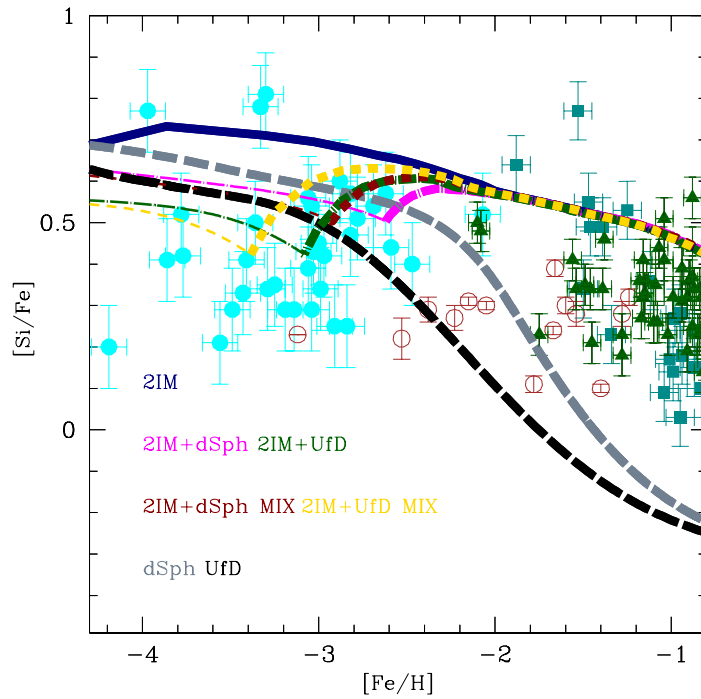


Figure 5.5: The abundance ratio $[\text{Si}/\text{Fe}]$ as a function of $[\text{Fe}/\text{H}]$ in the solar neighborhood. *Models of the Galactic Halo with the enriched infall from dSph:* the magenta dashed dotted line and the red short dashed line represent the models 2IM+dSph and 2IM+dSph MIX, respectively. *Models of the Galactic Halo with the enriched infall from UfDs:* the green dashed dotted line and the yellow short dashed line represent the models 2IM+UfD and 2IM+UfD MIX, respectively. *Models of the dSph and UfD galaxies:* The long dashed gray line represents the abundance ratios for the dSph galaxies, whereas long dashed black line for the UfD galaxies. *Observational data of the Galactic Halo:* Cayrel et al. (2004) (cyan circles), Shi et al. (2009) (open brown circles), Reddy et al. (2006) (filled blue squares), Gratton et al. (2003) (dark green triangles).

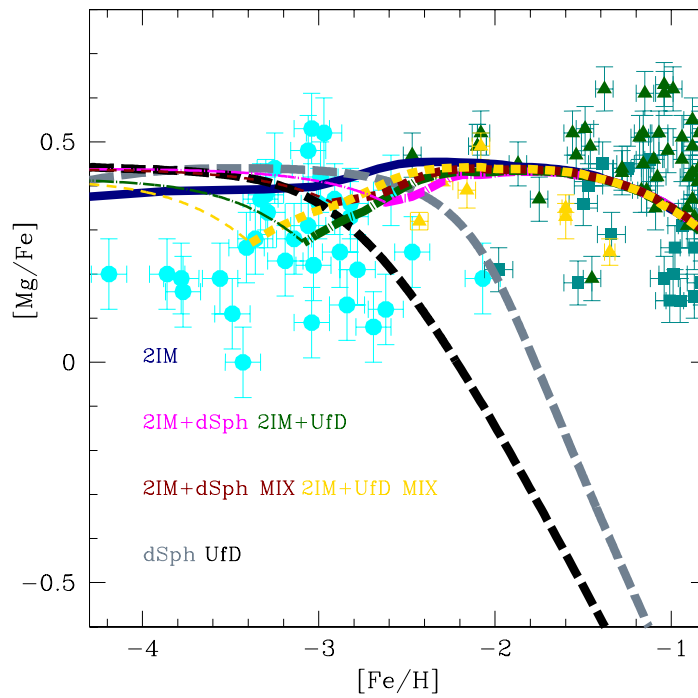


Figure 5.6: The abundance ratio $[Mg/Fe]$ as a function of $[Fe/H]$ in the solar neighborhood. *Models of the Galactic Halo with the enriched infall from dSph:* the magenta dashed dotted line and the red short dashed line represent the models 2IM+dSph and 2IM+dSph MIX, respectively. *Models of the Galactic Halo with the enriched infall from UfDs:* the green dashed dotted line and the yellow short dashed line represent the models 2IM+UfD and 2IM+UfD MIX, respectively. *Models of the dSph and UfD galaxies:* The long dashed gray line represents the abundance ratios for the dSph galaxies, whereas long dashed black line for the UfD galaxies. *Observational data of the Galactic Halo:* Cayrel et al. (2004) (cyan circles), Moshonkina et al. (2007) (yellow triangles), Reddy et al. (2006) (filled blue squares), Gratton et al. (2003) (dark green triangles).

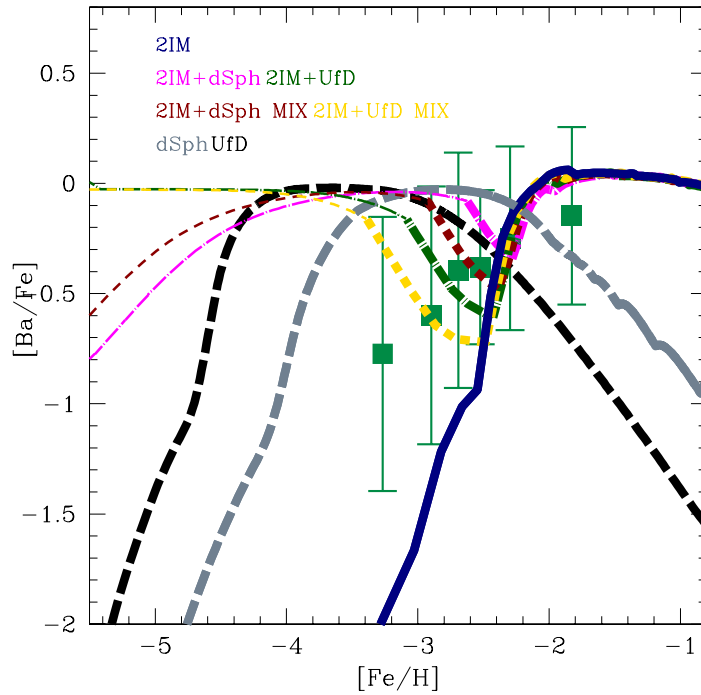


Figure 5.7: The abundance ratio $[\text{Ba}/\text{Fe}]$ as a function of $[\text{Fe}/\text{H}]$ in the solar neighborhood. *Models of the Galactic Halo with the enriched infall from dSph:* the magenta dashed dotted line and the red short dashed line represent the models 2IM+dSph and 2IM+dSph MIX, respectively. *Models of the Galactic Halo with the enriched infall from UfDs:* the green dashed dotted line and the yellow short dashed line represent the models 2IM+UfD and 2IM+UfD MIX, respectively. *Models of the dSph and UfD galaxies:* The long dashed gray line represents the abundance ratios for the dSph galaxies, whereas long dashed black line for the UfD galaxies. *Observational data of the Galactic Halo:* Frebel (2010).

a critical threshold is reached only at $t = 0.356$ Gyr from the Galaxy formation; therefore, the Galaxy turns out to form stars only for $t > 0.356$ Gyr. Nevertheless, we have to consider also the time of the onset of the galactic wind, which – in the dSph model – occurs at $t_{\text{gw}} = 0.013$ Gyr, before the star formation threshold is reached.

In summary, the behavior of the different curves with enriched infall in Fig. 5.3 can be explained as follows: *during the first 0.356 Gyr, both the “2IM+dSph” and “2IM+dSph MIX” models do not predict any star formation activity, and the chemical evolution is solely determined by the “exponential” gas mass growth with time-dependent chemical abundances (see equation 5.3).*

In Fig. 5.3 and in all the successive figures, the thin lines in the $[\text{X}/\text{Fe}]$ vs. $[\text{Fe}/\text{H}]$ diagram indicate the evolutionary times when the gas mass density is below the threshold for star formation; hence thin lines indicate that no stars have been created at those epochs of the Galaxy evolution.

To summarize, we distinguish three different phases in the halo chemical evolution, as predicted by the “2IM+dSph” model:

- **Phase 1):** 0-0.013 Gyr, the infall is primordial, the wind in dSphs has not started yet, and there is no SF;
- **Phase 2):** 0.013-0.356 Gyr, the infall is enriched by dSphs and the SFR is zero;
- **Phase 3):** 0.356-1 Gyr; the infall is enriched by dSphs and the SFR is different from zero.

During **phase 3)**, the SF takes over, determining a sudden increase of the $[\text{O}/\text{Fe}]$ ratios; this is due to the pollution from massive stars, which occurs on short typical time-scales.

We note that the entire spread of the data cannot be explained by assuming a time-dependent enriched infall, as in the “2IM+dSph” or the “2IM+dSph MIX” model, even though the agreement with the halo data is better than the 2IM model with primordial infall.

It is important to underline that, until the SF is non-zero, no stars are created and the ISM chemical evolution is only due to the time-dependent enriched infall from the galactic winds of dSph galaxies. This means that the first stars in the “2IM+dSph” model have $[\text{Fe}/\text{H}] > -2.4$ dex. In this case, to explain all the data with $[\text{Fe}/\text{H}] \leq -2.4$ dex, we need stars formed in dSph systems and then stripped.

Concerning our results with the enriched infall from the UfD outflow, we recall that the reference UfD model predicts the galactic wind to start at 0.08 Gyr. We find that the “2IM+UfD” and “2IM+UfD MIX” models for the halo still reproduce the data but with the same caveat aforementioned.

In Fig. 5.4, we show the time evolution of the oxygen abundance for the 2IM (primordial infall), “2IM+dSph”, “2IM+dSph MIX”, “2IM+UfD”, and “2IM+UfD MIX” models. We notice that the reference 2IM model, as explained before, shows an ISM chemical evolution only for $t > 0.356$ Gyr, while the models with an enriched infall from dSphs predict the fastest chemical enrichment, since the galactic wind occurs earlier than in UfD systems.

In Figs. 5.5 and 5.6, we show the results of all our chemical evolution models with the 2IM scenario for the $[\text{Si}/\text{Fe}]$ and $[\text{Mg}/\text{Fe}]$ vs. $[\text{Fe}/\text{H}]$ chemical abundance patterns, respectively. The various curves with different colors represent the same chemical evolution models as in Fig. 5.3. As concluded for the $[\text{O}/\text{Fe}]$ versus $[\text{Fe}/\text{H}]$ abundance diagram, our reference chemical evolution models for dSph and UFD galaxies cannot explain the observed Galactic halo data over the entire range of $[\text{Fe}/\text{H}]$ abundances. This rules out the hypothesis that all Galactic halo stars were stripped or accreted in the past from dSphs or UFDs. This result is in agreement with previous works in the literature as the ones of Unavane et al. (1996); Venn et al. (2004). On the other hand, as stated above, if we assume that the Galactic halo formed by accreting enriched gas from dSphs or UFDs, we also need a stellar contribution from dSphs and UFDs to explain the stars at very low $[\text{Fe}/\text{H}]$ that currently reside in the halo.

It is worth noting that, for the α -elements studied in this work, all the models with an enriched infall tend to reach the $[\alpha/\text{Fe}]$ ratios of the 2IM reference model as the $[\text{Fe}/\text{H}]$ abundance in the halo phase increases. This is due to the fact that – when the SF becomes active – the pollution from dying stars overcomes effect of an enriched infall.

We note that a different star formation threshold in the MW model would modify the duration of **phase 2**). As shown in Mott et al. (2013), if we do not take into account radial gas flows (see also Portinari & Chiosi 2000; Spitoni & Matteucci 2011; Cavichia et al. 2014), a threshold in the gas density is required to explain the abundance gradients along the Galactic disk; in particular, typical values of $4 M_{\odot} \text{pc}^{-2}$ in the halo phase and $7 M_{\odot} \text{pc}^{-2}$ in the thin disk phase provide the best agreement with data.

In Fig. 5.7, we show the results for the $[\text{Ba}/\text{Fe}]$ vs. $[\text{Fe}/\text{H}]$ abundance diagram. The observational data are from Frebel (2010), as selected and binned by Cescutti et al. (2013). By looking at the figure, the 2IM model does not provide a good agreement with the observed data set for $[\text{Fe}/\text{H}] < -2.5$ dex. The initial increasing trend of the $[\text{Ba}/\text{Fe}]$ ratios in the 2IM model is due to the contribution of the first Ba-producers, which are massive stars with mass in the range $12\text{-}30 M_{\odot}$.

By looking at Fig. 5.7, one can also appreciate that our chemical evolution models for dSphs and UFDs fail in reproducing the observed data, since they predict the $[\text{Ba}/\text{Fe}]$ ratios to increase at much lower $[\text{Fe}/\text{H}]$ abundances than the observed data. Concerning the chemical evolution of barium for dSphs, our predictions are in agreement with Lanfranchi et al. (2008), where they compared the evolution of the s - and r - process elements in our Galaxy with the one in dSph galaxies.

The trend in Fig. 5.7 for dSph and UFD galaxies is due to the very low SFEs assumed in these objects, which cause the first Ba-polluters to enrich the ISM at extremely low $[\text{Fe}/\text{H}]$ abundances. The subsequent decrease of the $[\text{Ba}/\text{Fe}]$ ratios is due to the large iron content deposited by Type Ia SNe in the ISM, which happens at still very low $[\text{Fe}/\text{H}]$ abundances in dSphs and UFDs. Hence, in the range $-3.5 \lesssim [\text{Fe}/\text{H}] \lesssim -2.5$ dex, while Galactic halo stars exhibit an increasing trend of the $[\text{Ba}/\text{Fe}]$ vs. $[\text{Fe}/\text{H}]$ abundance ratio pattern, UFD stars show a decreasing trend (see also Koch et al. 2013).

In Fig. 5.7, all our models involving an enriched infall from dSphs and UFDs de-

viate substantially from the observed trend of the $[\text{Ba}/\text{Fe}]$ versus $[\text{Fe}/\text{H}]$ abundance pattern in Galactic halo stars. Such a discrepancy enlarges for $[\text{Fe}/\text{H}] < -2.4$ dex, where those models predict always larger $[\text{Ba}/\text{Fe}]$ ratios than the 2IM model.

5.4.2 Results: the Galactic halo in the model 2IMW

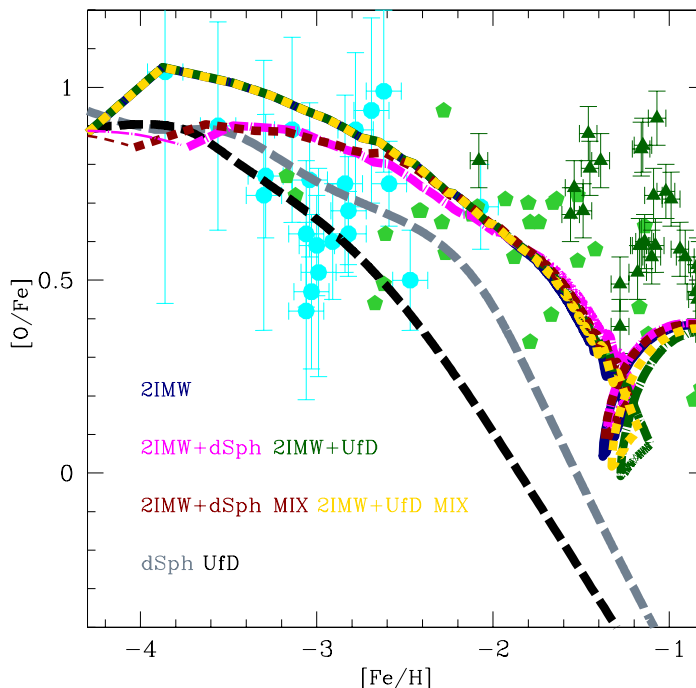


Figure 5.8: The abundance ratio $[\text{O}/\text{Fe}]$ as a function of $[\text{Fe}/\text{H}]$ in the solar neighborhood as in Fig. 5.3 but for the 2IMW model.

In this subsection, we show our results, when the time-dependent enriched infall from dSph and UfD galaxies is applied to the reference 2IMW model for the MW halo. In Fig. 5.8, we show the results of our models for the $[\text{Fe}/\text{H}]$ - $[\text{O}/\text{Fe}]$ diagram in the solar neighborhood.

As mentioned in Section 5.2, the reference 2IMW model is characterized in the halo phase by an outflow of gas with a rate proportional to the SFR. Moreover, the halo formation timescale, τ_{H} , in the 2IMW model is smaller than in the 2IM model (see Table 5.1); a shorter formation time-scale leads to a faster chemical evolution at early times. In fact, as shown by Brusadin et al. (2013, see their figure 2), the SFR in the 2IMW model starts at ~ 0.05 Gyr, since the critical threshold in the surface gas mass density is reached earlier than in the 2IM model.

For the “2IMW+dSph” model, we distinguish three different phases in the halo phase:

- **Phase 1):** 0-0.013 Gyr, during which the infall is primordial, the wind in dSphs has not started yet and there is no star formation;

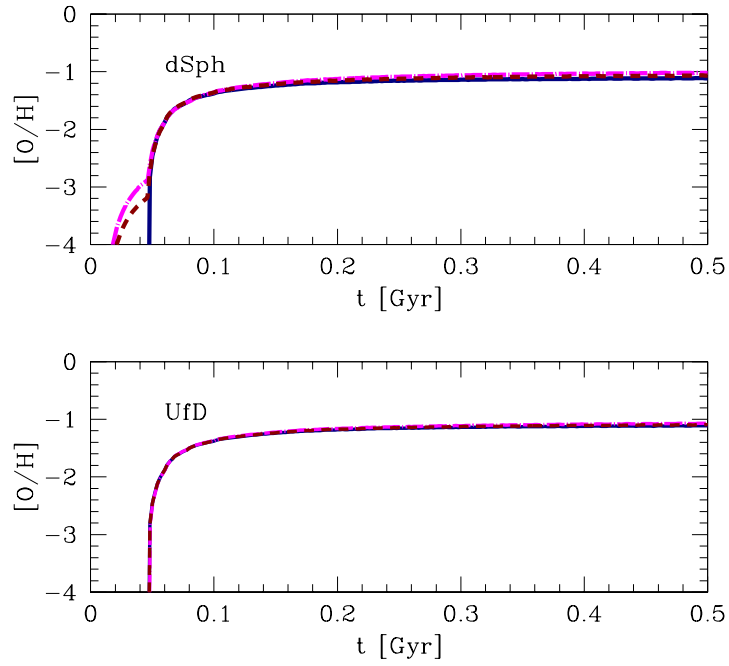


Figure 5.9: As in Fig. 5.4 the evolution in time for oxygen but for the 2IMW model.

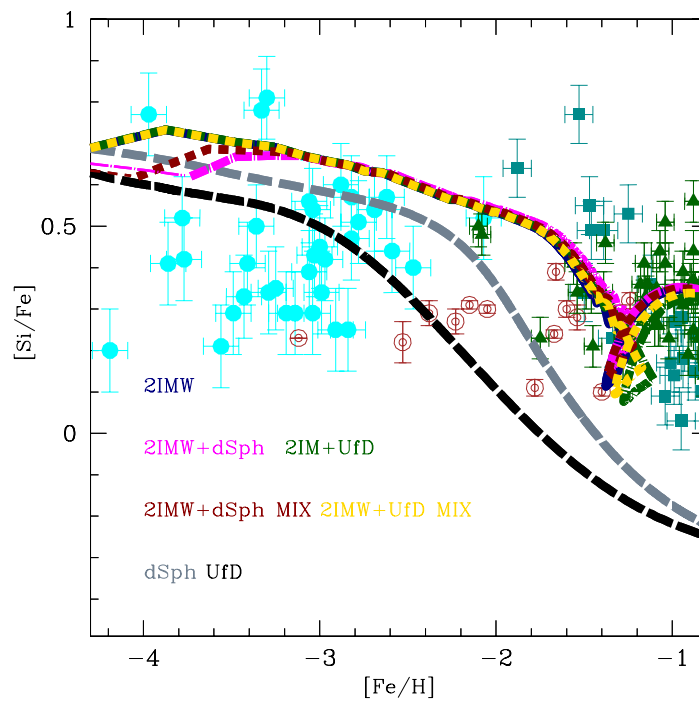


Figure 5.10: The abundance ratio $[\text{Si}/\text{Fe}]$ as a function of $[\text{Fe}/\text{H}]$ in the solar neighborhood. As in Fig. 5.5 but for the 2IMW model.

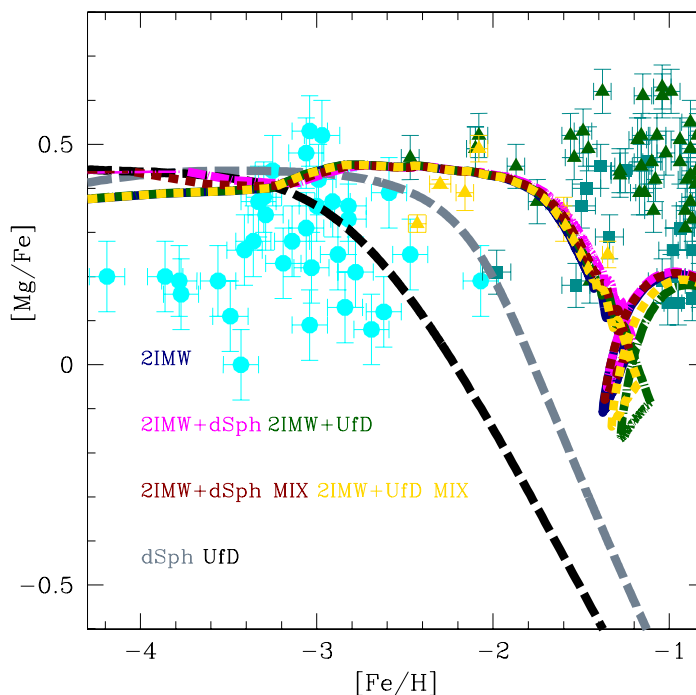


Figure 5.11: The abundance ratio $[Mg/Fe]$ as a function of $[Fe/H]$ in the solar neighborhood. As in Fig. 5.6 but for the 2IMW model.

- **Phase 2):** 0.013-0.05 Gyr, during which the infall is enriched by dSphs and the SFR is zero;
- **Phase 3):** 0.05-1 Gyr, during which the infall is enriched by dSphs and the SFR is different from zero.

On one hand, when comparing the “2IMW+dSph” model in Fig. 5.8 with the “2IM+dSph” model in Fig. 5.3, we can see that the former predicts **phase 2)** (infall enriched with no SF activity) to be shorter.

On the other hand, when comparing the “2IMW+UfD” model with the reference 2IMW model in Fig. 5.8, we can see that the two models overlap over almost the entire range of $[Fe/H]$ abundances, at variance with the predictions of all the 2IM-based models (see Fig. 5.3). In fact – since the UfD model predicts the galactic wind onset at 0.088 Gyr, as the SF is already active in the 2IMW model (the SF activity begins at 0.05 Gyr) – the **phase 2)** evolution (namely, chemical evolution without SF) is not present in the 2IMW+UfD model. Therefore, in the “2IMW+UfD”, we cannot distinguish between the effect of an enriched infall from UfDs and the chemical feedback by Type II SNe born in-situ, namely in the Galactic halo itself, because the effect of an enriched infall from UfD on the MW halo chemical evolution becomes negligible.

This can also be appreciated by looking at Fig. 5.9, where we show the predicted time evolution of the oxygen abundance of all the 2IMW-based models.

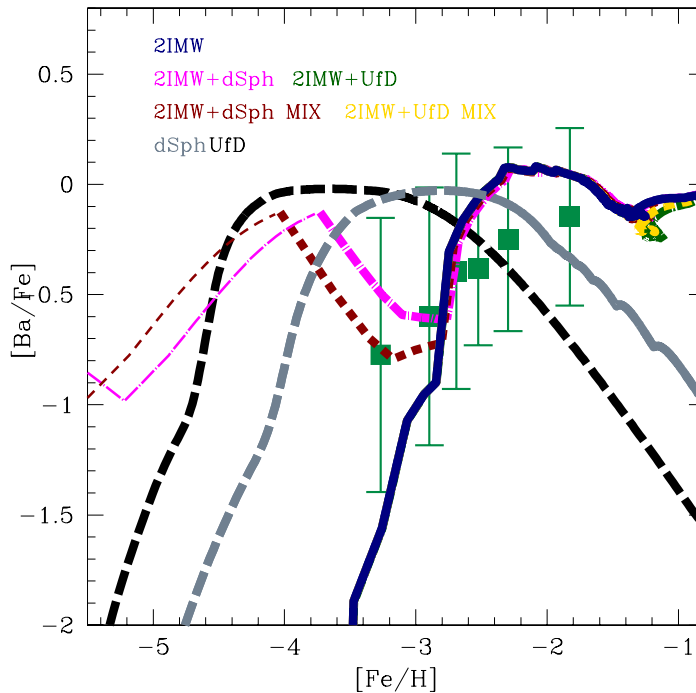


Figure 5.12: The abundance ratio $[\text{Ba}/\text{Fe}]$ as a function of $[\text{Fe}/\text{H}]$ in the solar neighborhood. As in Fig. 5.7 but for the 2IMW model.

We can see that – for the UfD case – the model with an enriched infall is almost identical to the reference 2IMW model.

In Figs. 5.10 and 5.11, we present the results of our models for the $[\text{Si}/\text{Fe}]$ and $[\text{Mg}/\text{Fe}]$ vs. $[\text{Fe}/\text{H}]$ diagrams in the solar neighborhood, respectively. As for oxygen in Fig. 5.8, the effect of an enriched infall from UfD galaxies is almost negligible compared to the pollution of chemical elements produced by dying halo stars.

Concerning the $[\text{Ba}/\text{Fe}]$ vs. $[\text{Fe}/\text{H}]$ abundance pattern, in Fig. 5.12 we compare the predictions of our models with the Galactic halo data. We notice that the 2IMW model provides now a better agreement with the observed data than the 2IM model, although the predicted $[\text{Ba}/\text{Fe}]$ ratios at $[\text{Fe}/\text{H}] < -3$ dex still lie below the observed data. By assuming an enriched infall from dSph or UfD galaxies, the predicted $[\text{Ba}/\text{Fe}]$ ratios agree with the observed data also at $[\text{Fe}/\text{H}] < -3$ dex. In conclusion, in order to reproduce the observed $[\text{Ba}/\text{Fe}]$ ratios over the entire range of $[\text{Fe}/\text{H}]$ abundances, a time-dependent enriched infall in the Galactic halo phase is required. We are aware that for barium more detailed data are needed, therefore at this stage we cannot draw firm conclusions.

We note that, in general, the $[\alpha/\text{Fe}]$ ratios in dSphs and UfDs overlap with the ones of halo stars as we move towards lower and lower $[\text{Fe}/\text{H}]$ abundances, where the chemical enrichment is dominated – in all galaxies – by the nucleosynthesis of core collapse SNe. This makes difficult to test whether some stars from dwarf satellites have indeed been accreted by the halo. Rather, it is likely that a fraction

as high as 50 per cent of the gas out of which the halo formed has been shed by the MW galaxy satellites, whose relics we see (in part) nowadays, devoid of their gas. This is only valid for satellite systems with a very short duration of star formation, as modeled in this work.

We have identified in the [Ba/Fe] ratios a better discriminant of the origin of halo stars. The differences predicted for the dwarf galaxies relative to the halo suggest that it is unlikely that the dSphs and UFDs have been the building blocks of the halo.

In Fig. 5.13 we show the predicted G-dwarf MDF for the same models as shown in Figs. 5.3 and 5.8. Our models have been convolved with a Gaussian function with $\sigma = 0.2$ dex. As pointed out also by Brusadin et al. (2013), the reference 2IM model is not able to reproduce the peak of the distribution. Only by assuming a shorter formation time-scale, coupled with a gas outflow event in the MW halo chemical evolution (model 2IMW), we are able to properly fit the observed distribution. Anyway, in both cases the enriched infall of gas from dSph and UFD objects does not affect the predicted distributions. In Fig. 5.14, we show the G-dwarf distribution of the [O/Fe] ratios; here, both 2IM- and 2IMW-based models, show a peak at [O/Fe] ≈ 0.5 dex.

5.5 Conclusions

We have firstly explored the hypothesis that dSph and UFD galaxies are the survived building blocks of the Galactic halo, by assuming that the halo formed by accretion (and stripping) of stars belonging to these galaxies.

Then, we have presented a different scenario in which the Galactic halo formed by accretion of enriched gas with the same chemical composition as the outflowing gas from dSphs and UFDs. Finally, we have tested the effect of diluting the infalling material from dSphs and UFDs with primordial gas of different extra-galactic origin.

Our main conclusions can be summarized as follows:

- We find that the predicted $[\alpha/\text{Fe}]$ versus $[\text{Fe}/\text{H}]$ abundance patterns, as predicted by UFD and dSph chemical evolution models, deviate substantially from the observed data of the Galactic halo stars, for $[\text{Fe}/\text{H}] \gtrsim -2$ dex; this means that – at those metallicities – the chemical evolution of the Galactic halo was different than in the satellite galaxies. We notice that for barium the chemical evolution models of dSphs and UFDs fail to reproduce the observational data of the Galactic halo stars over the whole range of $[\text{Fe}/\text{H}]$ abundances.
- We can safely rule out the hypothesis that the stellar halo of the MW entirely formed from the merging of galaxies which were the ancestors of the current dSphs and UFDs. Our results are in agreement with the previous suggestions of Unavane et al. (1996); Venn et al. (2004). We cannot rule out, however, the hypothesis that a substantial contribution to the formation of the Galaxy stellar halo was provided by a population of dwarf galaxies

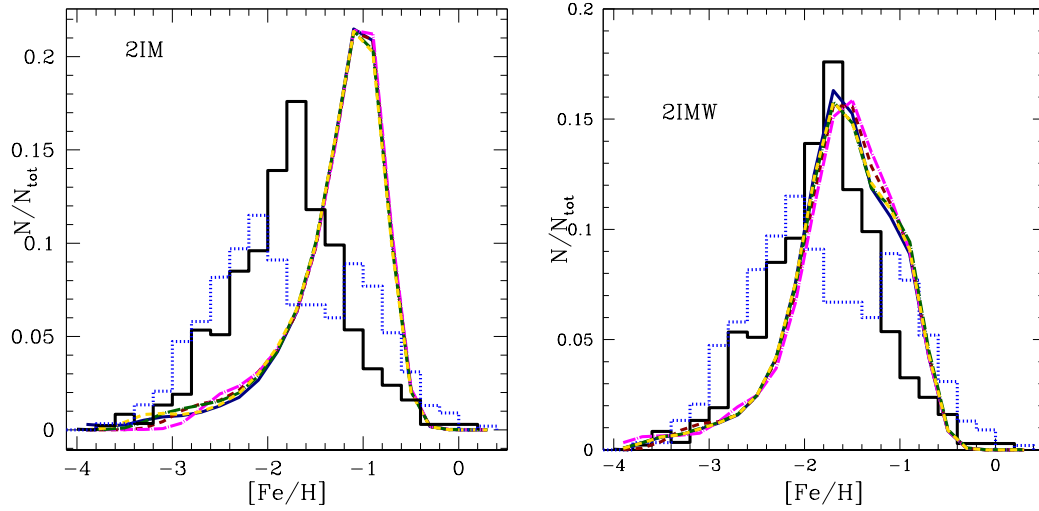


Figure 5.13: The G-dwarf metallicity distributions ($[\text{Fe}/\text{H}]$) predicted by models with enriched infall of gas based on the reference 2IM model (*left panel*) and the ones based on the 2IMW model (*right panel*), are compared to the observed distributions by Ryan & Norris (1991, dotted blue histogram) and Schörck et al. (2009; solid black histogram). Concerning the *left panel*, model color lines are the same as in Fig. 5.3, on the other hand in the *right panel* color lines are the same as in Fig. 5.8. Our predictions have been convolved with a Gaussian with an error of 0.2 dex.

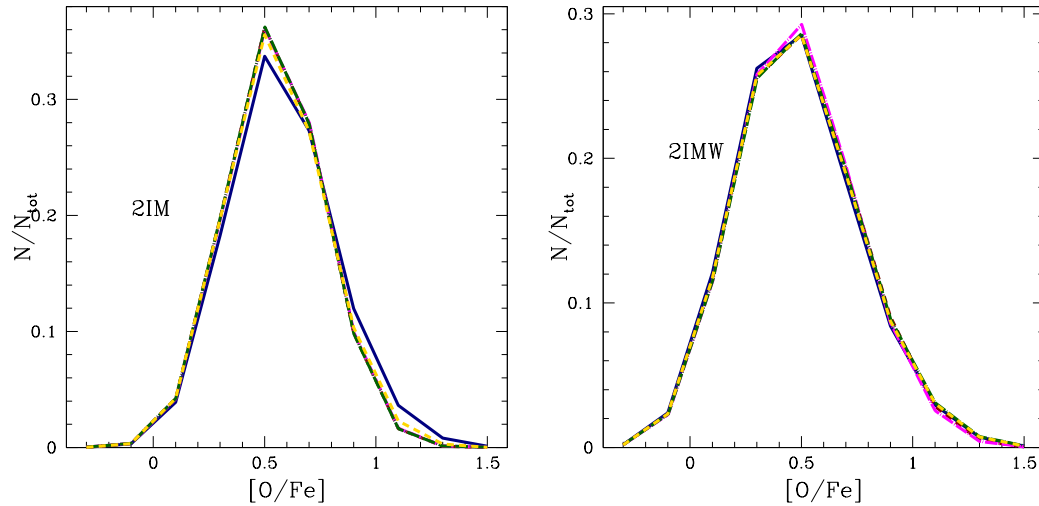


Figure 5.14: The G-dwarf distributions in terms of $[\text{O}/\text{Fe}]$ predicted by models with enriched infall of gas based on the reference 2IM model (*left panel*) and the ones based on the 2IMW model (*right panel*). Concerning the *left panel*, model color lines are the same as in Fig. 5.3, on the other hand in the *right panel* color lines are the same as in Fig. 5.8. Our predictions have been convolved with a Gaussian with an error of 0.2 dex.

which were more massive and more evolved from the point of view of the ISM chemical evolution than the current dSphs and UFDs.

- Concerning the chemical evolution models for the MW in the presence of an enriched gas infall we obtain that: **i)** the effects on the $[\alpha/\text{Fe}]$ vs. $[\text{Fe}/\text{H}]$ plots depend on the infall time scale for the formation of the halo; **ii)** the presence of a gas threshold in the star formation highly affect the predictions of the models at low $[\text{Fe}/\text{H}]$ abundances. In fact, the most evident effects can be appreciated in the 2IM model (two-infall model), which is characterized by the longest time scale of formation ($\tau_{\text{H}} = 0.8$ Gyr) and the longest period without star formation activity among all the models presented here.
- In general, the enriched infall is not capable by itself to explain the observational spread in the halo data of the $[\alpha/\text{Fe}]$ ratios at low $[\text{Fe}/\text{H}]$ abundances. Moreover, also if we assume an enriched infall, we need stars produced in situ in dSph or UFD objects and later accreted to the Galactic halo, to explain the data at the lowest $[\text{Fe}/\text{H}]$ values.
- The optimal element to test different theories of halo formation is barium which is (relatively) easily measured in low-metallicity stars. In fact, we have shown that the predicted $[\text{Ba}/\text{Fe}]$ vs. $[\text{Fe}/\text{H}]$ relation in dSphs and UFDs is quite different than in the Galactic halo. Moreover, the $[\text{Ba}/\text{Fe}]$ ratio can be substantially influenced by the assumption of an enriched infall. In particular, the two infall plus outflow model can better reproduce the data in the whole range of $[\text{Fe}/\text{H}]$ abundances, and this is especially true if also time-dependent enriched infall during the halo phase is assumed.

References

- Akerman, C. J., Carigi, L., Nissen, P. E., Pettini, M., Asplund, M., 2004, *A&A*, 414, 93
Bechtol, K., Drlica-Wagner, A., Balbinot, E., et al., 2015, *ApJ*, 807, 50
Belokurov, V., 2013, *NAR*, 57, 100
Belokurov, V., Zucker, D. B., Evans, N. W., et al., 2006a, *ApJ*, 647, L111
Belokurov, V., Zucker, D. B., Evans, N. W., et al. 2006b, *ApJ*, 642, L137
Belokurov, V., Zucker, D. B., Evans, N. W., et al., 2007, *ApJ*, 654, 897
Brown, T. M., Tumlinson, J., Geha, M., et al., 2012, *ApJ*, 753, L21
Brusadin, G., Matteucci, F., Romano, D., 2013, *A&A*, 554, A135
Bullock, J.S., 2010, arXiv:1009.4505
Busso, M., Gallino, R., Lambert, D. L., Travaglio, C., Smith, V. V. 2001, *ApJ*, 557, 802
Cayrel, R., Depagne, E., Spite, M., et al., 2004, *A&A*, 416, 1117
Cescutti, G., François, P., Matteucci, F., Cayrel, R., Spite, M., 2006, *A&A*, 448, 557
Cavichia, O., Molla, M., Costa, R. D. D., Maciel, W. J. 2014, *MNRAS*, 437, 3688
Cescutti, G., Chiappini, C., Hirschi, R., Meynet, G., Frischknecht, U. 2013, *A&A*, 553, A51
Chiappini, C., Matteucci, F., Gratton, R., 1997, *ApJ*, 477, 765
Chiappini, C., Matteucci, F., Romano, D., 2001, *ApJ*, 554, 1044
Drlica-Wagner, A., Bechtol, K., Rykoff, E. S., et al. 2015, *ApJ*, 813, 109
Drlica-Wagner, A., Bechtol, K., Allam, S., et al., 2016, arXiv:1609.02148
Ekström, S., Meynet, G., Chiappini, C., Hirschi, R., Maeder, A. 2008, *A&A*, 489, 685

- Fiorentino, G., Bono, G., Monelli, M., et al., 2015, *ApJ*, 798, L12
- Font, A.S., Johnston, K. V., Bullock, J. S., Robertson, B. E., 2006, *ApJ*, 638, 585
- François, P., Matteucci, F., Cayrel, R., et al. 2004, *A&A*, 421, 613
- Frebel, A. 2010, *Astron. Nachr.*, 331, 474
- Freeman, K. C. 2010, *Galaxies and their Masks*, 319
- Gilmore, G., Randich, S., Asplund, M., et al., 2012, *The Messenger*, 147, 25
- Grebel, E. K., 2005, *IAU Colloq. 198: Near-fields cosmology with dwarf elliptical galaxies*, 1
- Gratton, R. G., Carretta, E., Desidera, S., Lucatello, S., Mazzei, P., Barbieri, M., 2003, *A&A*, 406, 131
- Hartwick, F., 1976, *ApJ*, 209, 418
- Hirschi, R. 2005, in *From Lithium to Uranium: Elemental Tracers of Early Cosmic Evolution*, ed. V. Hill, P. François, F. Primas, *IAU Symp.*, 228, 331
- Hirschi, R. 2007, *A&A*, 461, 571
- Iwamoto, K., Brachwitz, F., Nomoto, K., Kishimoto, N., Umeda, H., Hix, W. R., Thielemann, F.K., 1999, *ApJS*, 125, 439
- Jofré, P., Weiss, A. 2011, *A&A*, 533, A59
- Karakas, A. I. 2010, *MNRAS*, 403, 1413
- Kennicutt, R. C., Jr, 1998, *ApJ*, 498, 541
- Kim, D., Jerjen, H., Mackey, D., Da Costa, G. S., & Milone, A. P. 2015, *ApJ*, 804, L44
- Kim, D., & Jerjen, H. 2015, *ApJ*, 808, L39
- Klypin, A., Gottlöber, S., Kravtsov, A. V., Khokhlov, A. M., 1999, *ApJ*, 516, 530
- Kobayashi, C., Umeda, H., Nomoto, K., Tominaga, N., Ohkubo, T., 2006, *ApJ*, 653, 1145
- Koch, A., Feltzing, S., Adén, D., Matteucci, F. 2013, *A&A*, 554, A5
- Koposov, S. E., Belokurov, V., Torrealba, G., & Evans, N. W. 2015, *ApJ*, 805, 130
- Kuijken, K., Gilmore, G., 1991, *ApJ*, 367, L9
- Lanfranchi, G. A., Matteucci, F., Cescutti, G., 2008, *A&A*, 481, 635
- Laevens, B. P. M., Martin, N. F., Bernard, E. J., et al. 2015, *ApJ*, 813, 44
- Luque, E., Pieres, A., Santiago, B., et al., 2016, *arXiv:1608.04033*
- Martin, N. F., Nidever, D. L., Besla, G., et al. 2015, *ApJ*, 804, L5
- Mashonkina, L., Korn, A. J., Przybilla, N., 2007, *A&A*, 461, 261
- Majewski, S. R., Wilson, J. C., Hearty, F., et al. 2010, in K. Cunha, M. Spite, B. Barbuy (eds.), *IAU Symposium*, Vol. 265 of *IAU Symposium*, pp 480–481
- Matteucci, F. 2001, *The Chemical Evolution Of The Galaxy* (Kluwer Academic Publishers)
- Matteucci, F., François, P. 1989, *MNRAS*, 239, 885
- Meynet, G., Maeder, A. 2002, *A&A*, 390, 561
- Micali, A., Matteucci, F., Romano, D., 2013, *MNRAS*, 436, 1648
- Moore, B., Ghigna, S., Governato, F., Lake, G., Quinn, T., Stadel, J., Tozzi, P., 1999, *ApJ*, 524, L19
- Mott, A., Spitoni, E., Matteucci, F. 2013, *MNRAS*, 435, 2918
- Norris, J. E., Gilmore, G., Wyse, R. F. G., et al., 2008, *ApJ*, 689, L113
- Norris J. E., Yong D., Frebel A., Wilkinson M. I., Belokurov V., Zucker D. B., 2010, *ApJ*, 723, 1632
- Portinari, L., Chiosi, C. 2000, *A&A*, 355, 929
- Prantzos, N. 2008, *A&A*, 489, 525
- Press, W. H., Schechter, P., 1974, *ApJ*, 187, 425
- Recchi S., Spitoni E., Matteucci F., Lanfranchi G. A., 2008, *A&A*, 489, 555
- Reddy B. E., Lambert D. L., Allende Prieto C., 2006, *MNRAS*, 367, 1329
- Romano, D., Karakas, A. I., Tosi, M., Matteucci F., 2010, *A&A*, 522, A32

Chapter 5. Are ancient dwarf satellites the building blocks of the Galactic halo?

- Romano, D., Bellazzini, M., Starkenburg, E., Leaman, R. 2015, MNRAS, 446, 4220
Ryan, S., Norris, J. 1991, AJ, 101, 1865
Salpeter, E. E., 1955, ApJ, 121, 161
Scalo, J. M. 1986, FCPH, 11, 1
Schörck, T., Christlieb, N., Cohen, J. G., et al. 2009, A&A, 507, 817
Schmidt, M., 1959, ApJ, 129, 243
Shetrone, M. D., Côté, P., Sargent, W. L. W., 2001, ApJ, 548, 592
Shi, J. R., Gehren, T., Mashonkina, L., Zhao, G., 2009, A&A, 503, 533
Spitoni, E., Calura, F., Matteucci, F., Recchi, S., 2010, A&A, 514, A73
Spitoni, E., Matteucci, F. 2011, A&A, 531, A72
Spitoni, E., 2015, MNRAS, 451, 1090
Spitoni, E., Vincenzo, F., Matteucci, F., & Romano, D., 2016, MNRAS, 458, 2541
Springel, V., Frenk, C. S., White, S. D. M., 2006, Nature, 440, 1137
Steinmetz, M., Zwitter, T., Siebert, et al. 2006, AJ, 132, 1645
Tollerud, E. J., Bullock, J. S., Strigari, L. E., Willman, B., 2008, ApJ, 688, 277
Torrealba, G., Koposov, S. E., Belokurov, V., et al. 2016, MNRAS, 463, 712
Unavane, M., Wyse, R. F. G., Gilmore, G., 1996, MNRAS, 278, 727
Venn, K. A., Irwin, M., Shetrone, M. D., et al., 2004, AJ, 128, 1177
Vincenzo, F., Matteucci, F., Vattakunnel, S., Lanfranchi, G. A., 2014, MNRAS, 441, 2815
Weisz, D. R., Johnson, B. D., Conroy, C., 2014, ApJ, 794, L3
White, S. D. M., Springel, V., 2000, The First Stars, 327
White, S. D. M., Rees M. J., 1978, MNRAS, 183, 341
Willman, B., Blanton, M.R., West, A. A., et al., 2005, AJ, 129, 2692
Woolsey, S.E., Weaver, T.A. 1995, ApJS, 101, 181
Yanny, B., Rockosi, C., N. H. J. et al., 2009, AJ, 137, 4377
York, D.G., Adelmann, J., Anderson, J.E., Jr., et al., 2000, AJ, 120, 1579

6

Lighting up stars in chemical evolution models: the CMD of Sculptor

6.1 Introduction

In this Chapter, we present a novel approach to obtain a synthetic color-magnitude diagram (CMD) of galaxies, starting from predictions of chemical evolution models. Our new *photo-chemical model* ‘lights up’ the stars of chemical evolution models, according to their initial mass, metallicity and age; in this way, we can obtain a new set of observational constraints for chemical evolution models beyond the usual photospheric chemical abundances. The method presented in this work can provide – in principle – a deeper insight in the interpretation of current observations, since we can understand how our hypothesis about galaxy formation and evolution can affect the final configuration of the CMD. All the results of this Chapter have been published in [Vincenzo, Matteucci, de Boer, Cignoni & Tosi \(2016\)](#).

By solving a set of physically-motivated differential equations, which take into account the main physical processes taking place and influencing the evolution of the galaxy interstellar medium (ISM), numerical codes of chemical evolution are able to provide the galaxy star formation history (SFH) and age-metallicity relation; the evolution of the galaxy stellar and gas mass, and the run of the ISM chemical abundances with time. Building up a photo-chemical code consists then in coupling the output of chemical evolution models with a database of stellar isochrones, currently available and computed with very high accuracy.

Most of the previous works in the literature recover the SFH of galaxies from the observed CMD by adopting sophisticated fitting techniques (e.g. [Harris & Zaritsky 2001](#); [Dolphin 2002](#); [Aparicio & Gallart 2004](#); [Tolstoy et al. 2009](#); [Cignoni & Tosi 2010](#); [Monelli et al. 2010](#); [Hidalgo et al. 2011](#)); in particular, they search for

the suitable linear combination of simple stellar populations (SSPs) with different age and metallicity, which provides the best agreement with the observed photometric properties of the galaxy composite stellar population. As a byproduct, this ‘classical’ procedure can also predict an average galaxy age-metallicity relation. Nevertheless, no underlying approximate physical model is assumed in these works for the galaxy formation and evolution.

In this work, we focus on reproducing the CMD of the Sculptor dwarf spheroidal galaxy (dSph). In particular, we investigate whether the best chemical evolution model for Sculptor – reproducing the galaxy stellar metallicity distribution function (MDF) – is able to predict a synthetic CMD which agrees with the observed one.

This Chapter is organized as follows: in Section 6.2 we summarize the main properties of the Sculptor dSph and describe the observed set of data used in this work for the comparison with our models; in Section 6.3 we present the main characteristics of our photo-chemical model and the methods we employ to fairly compare the synthetic with the observed CMD; in Section 6.4 we show our results, and in Section 6.5 we draw some conclusions.

6.2 The observed dataset

The Sculptor dwarf galaxy was discovered by [Shapley \(1938\)](#). Although it might appear simple at first glance, from the study of the kinematical, chemical and spatial distribution of its stellar populations, [Tolstoy et al. \(2004\)](#) were able to disentangle in this galaxy an inner, kinematically ‘cold’, metal-rich stellar population from an outer ‘hot’ metal-poor one, later on confirmed by [Battaglia et al. \(2008\)](#) and [Walker & Peñarrubia \(2011\)](#). Other studies based on photometric datasets also were able to identify (or confirm) the existence of stellar populations distinct in metallicity ([Majewski et al., 1999](#)), age and spatial distribution ([de Boer et al., 2011, 2012](#)).

[McConnachie \(2012\)](#) reported for Sculptor an average V-band surface brightness $\mu_V = 23.5 \pm 0.5 \text{ mag arcsec}^{-2}$, an half-light radius $r_h = 283 \pm 45 \text{ pc}$, and an absolute V-band magnitude $M_V = -11.1 \pm 0.5 \text{ mag}$. We make use of the distance modulus $\mu = 19.62 \pm 0.04 \text{ mag}$ derived by [Martínez-Vázquez et al. \(2015\)](#).

The observed CMD is taken from [de Boer et al. \(2011, see Fig. 6.1\)](#), which were able to resolve stars down to the oldest main sequence turn-off (MSTO) of the Sculptor dSph, by taking advantage of the deep wide-field photometry of CTIO/MOSAIC. In order to avoid a non-negligible contamination of foreground MW disc field stars, we consider only stars along the line-of-sight to the Sculptor dSph with elliptical radius $r_{\text{ell}} \leq 0.6 \text{ deg}$ and corresponding to clean isolated detections; the percentage of stars with these characteristics in the [de Boer et al. \(2011\)](#) catalog is about 92 per cent of the entire sample. We find that, for $r_{\text{ell}} > 0.6 \text{ deg}$, the noisy pattern introduced by foreground stars becomes larger than the “signal” of the Sculptor CMD one wants to recover (see also figure 5 in [de Boer et al. 2011](#)).

The observed stellar MDF is taken from [Romano & Starkeburg \(2013\)](#), which combined the [Kirby et al. \(2009, 2010\)](#) spectroscopic sample (with Sculptor stars belonging to the inner 0.2 deg of elliptical radius) with the dataset provided by

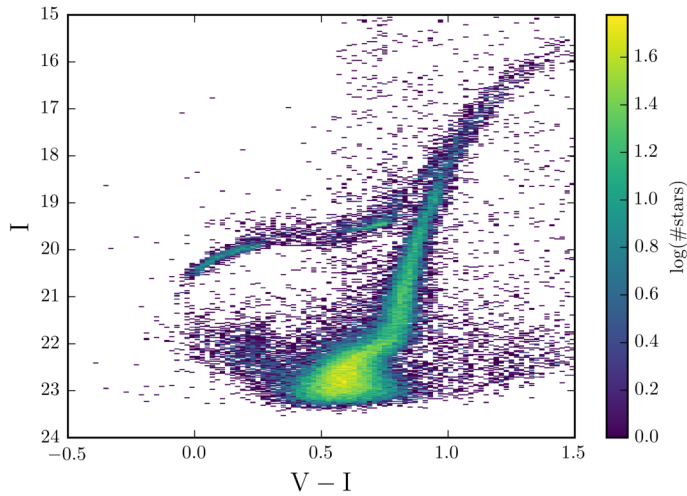


Figure 6.1: In this Figure, we show the observed CMD of the Sculptor dSph (de Boer et al., 2011). The dataset is shown as 2-D histogram, with the bin size in both the x - and y -dimensions being 0.02 dex; the color coding in the figure corresponds to the number of stars within each grid element. We consider in our analysis only clean isolated stellar detections and the Sculptor member stars with an elliptical radius $r_{\text{ell}} \leq 0.6$ deg.

the Dwarf galaxies Abundances and Radial velocities Team (DART, covering a much larger radial extent and making use of the calcium triplet equivalent width to infer the Fe abundances; see Battaglia et al. 2008; Starkenburg et al. 2010), in order to have an MDF which were representative of the global Sculptor stellar populations. By looking at Romano & Starkenburg (2013, their figure A1), the low-metallicity portion of their MDF is almost solely determined by the DART sample, with the Kirby et al. (2009, 2010) MDF mainly contributing towards larger $[\text{Fe}/\text{H}]$ abundances.

6.3 Model, assumptions and methods

6.3.1 Database of stellar isochrones and stellar lifetimes

We make use of the PARSEC stellar isochrones (Bressan et al., 2012; Tang et al., 2014; Chen et al., 2015), as computed for the following grid of stellar ages and metallicities, by assuming a Reimers mass loss with efficiency $\eta = 0.2$.

- The step in metallicity in our isochrone database is $\Delta Z = 1.0 \times 10^{-4}$, from a minimum metallicity $Z_{\text{min}} = 1.0 \times 10^{-4}$ to a maximum metallicity $Z_{\text{max}} = 3.0 \times 10^{-2}$.
- The step in age between two adjacent isochrones is $\Delta \log(t/\text{yr}) = 0.01$, from a minimum age $\log(t_{\text{min}}/\text{yr}) = 6.5$ to a maximum age $\log(t_{\text{max}}/\text{yr}) = 10.12$.

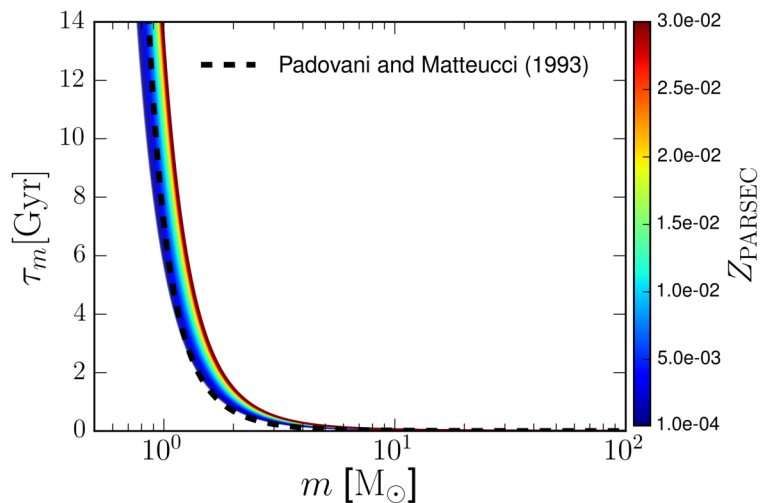


Figure 6.2: In this figure, we show how the stellar lifetimes we have derived from the PARSEC stellar evolutionary tracks vary as functions of the stellar mass and metallicity. The dashed black curve corresponds to the stellar lifetimes of [Padovani & Matteucci \(1993\)](#).

For self-consistency, we assume in our model the same stellar lifetimes as the ones which can be derived from the PARSEC database; in particular, we fit the stellar lifetimes with the following function:

$$\tau_m(Z) = A(Z) \times \exp \left[B(Z) m^{-C(Z)} \right], \quad (6.1)$$

where $A(Z)$, $B(Z)$ and $C(Z)$ are the fitting parameters, provided with the corresponding $1-\sigma$ errors in the supplementary material, as functions of the metallicity Z . In Fig. 6.2 we compare our derived stellar lifetimes with the ones of [Padovani & Matteucci \(1993\)](#), which do not depend on metallicity and are extensively used in chemical evolution models.

6.3.2 Modelling the chemical evolution of Sculptor

The numerical code of chemical evolution is the same as the one adopted in [Vincenzo, Matteucci, Vattakunnel & Lanfranchi \(2014\)](#); [Vincenzo et al. \(2016\)](#) – where we address the reader for details – for the study of the classical and ultra-faint dSph galaxies. We make use of an updated version, by assuming the stellar yield compilation of [Romano et al. \(2010, their model 15; see also Chapter ??\)](#) and the stellar lifetimes derived from the PARSEC isochrones.

We assume the galaxy to assemble by accreting pristine gas from an external reservoir, until an infall mass – given by M_{inf} – is accumulated at $t_G = 14$ Gyr. The infall rate is assumed to follow a decaying exponential law, with typical time-scale τ_{inf} . We assume for the star formation rate the Schmidt-Kennicutt law, namely $\text{SFR}(t) = \nu M_{\text{gas}}(t)$, where ν is the so-called star formation efficiency (SFE) and M_{gas} is the galaxy gas mass. The run of the intensity of the SFR with time is

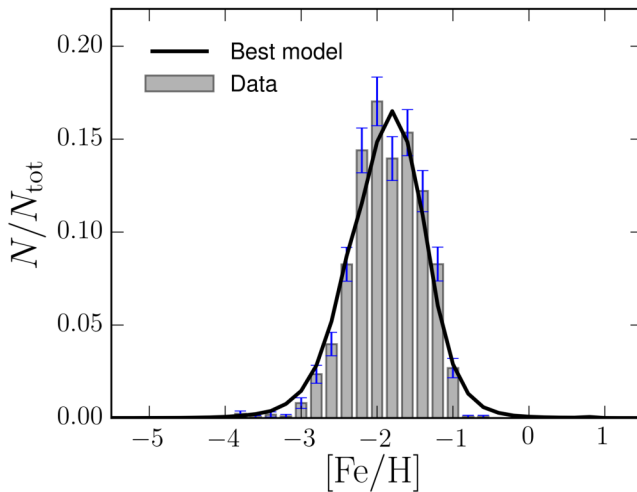


Figure 6.3: In this figure, we compare the observed Sculptor stellar MDF (Romano & Starkenburg, 2013, grey histogram with blue error bars) with the predictions of our best Sculptor chemical evolution model, having star formation efficiency $\nu = 0.04 \text{ Gyr}^{-1}$, wind efficiency $\lambda_{\text{wind}} = 3.0 \text{ Gyr}^{-1}$, infall mass $M_{\text{inf}} = 2.31 \times 10^8 M_{\odot}$, and infall time-scale $\tau_{\text{inf}} = 0.3 \text{ Gyr}$. The predicted MDF is convolved with a Gaussian function with $\sigma = 0.2$.

crucially regulated by the various physical processes acting on M_{gas} , namely inflows and outflows of gas, returned matter from dying stars and supernovae, astration due to the star formation activity itself.

A fundamental role in the evolution of dSphs is played by the galactic outflows, which are predicted to occur very soon in these galaxies because of their shallow potential well; the intensity of the outflow rate is assumed to be directly proportional to the SFR. On the one hand, if the efficiency for the gas removal is high (typically $\lambda_{\text{wind}} \approx 10 \text{ Gyr}^{-1}$), then the galaxy gas mass suddenly decreases and hence the SFR rapidly drops to zero; on the other hand, if the galactic wind has a relatively lower efficiency (typically $\lambda_{\text{wind}} \approx 1 \text{ Gyr}^{-1}$), then the decrease in the SFR is smoother and it drops to zero on longer typical time-scales.

The assumed best model

We have explored the parameter space, by running a large number of chemical evolution models. The best parameters for Sculptor are found by minimizing the χ^2 figure of merit, with the best model being the one reproducing the shape of the observed stellar MDF, which represents the most reliable observational constraint to any slight variation of the free parameters. We vary the SFE in the range $\nu = 0.03\text{-}0.2 \text{ Gyr}^{-1}$, the wind efficiency in the range $\lambda_{\text{wind}} = 2.0\text{-}10 \text{ Gyr}^{-1}$, and the infall time-scale in the range $\tau_{\text{inf}} = 0.1\text{-}0.5 \text{ Gyr}$. In order to allow our photochemical model to be more flexible when comparing its predictions with data, we make the further approximation of assuming the galactic wind to be always active over the whole galaxy lifetime; since all the galaxy physical properties in

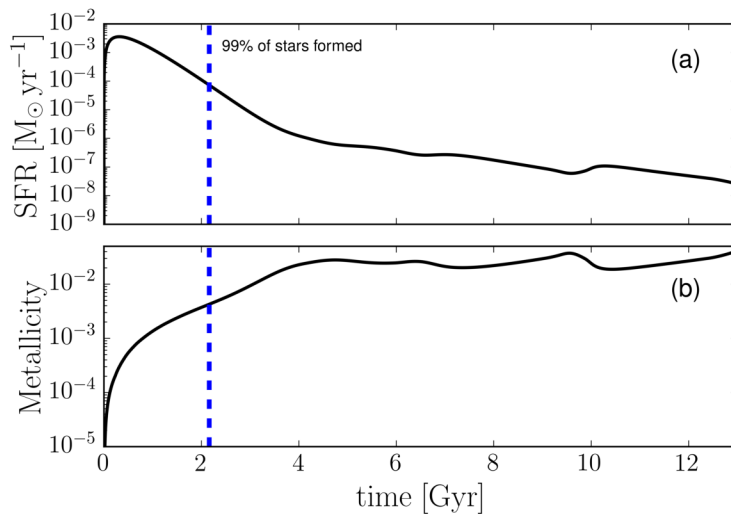


Figure 6.4: In this figure, we show the predicted SFH (top panel) and age-metallicity relation (bottom panel) as predicted by our best chemical evolution model for Sculptor. Our best model for Sculptor predicts that ~ 99 per cent of the stars observable at the present time are formed within the first 2.16 Gyr of the galaxy evolution; this time corresponds to the vertical dashed blue line in the figures. Furthermore, the number of stars with initial metallicity $Z < 1.0 \times 10^{-4}$ is roughly ~ 5.72 per cent of the total number of stars alive at the present time.

our chemical evolution model are normalized with respect to the infall mass, this assumption causes the predicted stellar MDF not to be influenced by the variation of the infall mass. In this simplified formulation of the galactic wind, all the galaxy physical properties (such as the SFR, stellar mass, gas mass, and so on) simply scale with the infall mass and our results can be easily readjusted for a different assumption of the cutoff in the elliptical radius of Sculptor stars (here we consider only stars with $r_{\text{ell}} \leq 0.6$ deg). We find that the best chemical evolution model is characterized by the following parameters:

- star formation efficiency $\nu = 0.04 \text{ Gyr}^{-1}$;
- wind efficiency $\lambda_{\text{wind}} = 3.0 \text{ Gyr}^{-1}$;
- infall time-scale $\tau_{\text{infall}} = 0.3 \text{ Gyr}$.

We assume at the beginning a reference infall mass $M_{\text{infall,ref}} = 1.0 \times 10^8 M_{\odot}$, as in [Vincenzo, Matteucci, Vattakunnel & Lanfranchi \(2014\)](#), for which we predict a present-day total stellar mass $M_{\star,\text{ref}} = 8.27 \times 10^5 M_{\odot}$. The infall mass of the best model is then obtained by rescaling our results for the reference model so as to have the same number of stars in the synthetic and observed CMD. We find for our best model an infall mass $M_{\text{infall,best}} = 2.31 \times 10^8 M_{\odot}$, giving rise to a present-day total stellar mass $M_{\star,\text{best}} = 1.91 \times 10^6 M_{\odot}$, larger than the value $M_{\star} = (1.2 \pm 0.6) \times 10^6 M_{\odot}$ estimated by [de Boer et al. \(2012\)](#), but of the same order of magnitude.

According to the fitting formula of [Faucher-Giguère et al. \(2011\)](#), which is assumed in many recent works to mimic a cosmologically motivated infall in galaxy

formation and evolution models, dwarf galaxies with $M_{\text{halo}} = 10^8 M_{\odot}$ must have accreted almost 63 per cent of their cumulative infall mass (which turns out to be $M_{\text{inf}} \approx 1.4 \times 10^8 M_{\odot}$) in the first ~ 1.5 Gyr of their evolution, namely from redshift $z = 6$ to redshift $z \sim 4$, a larger timescale than the one found by our best model ($\tau_{\text{inf}} = 0.3$ Gyr). Nevertheless, we remark on the fact that the [Faucher-Giguère et al. \(2011\)](#) fitting formula is strictly valid only in the redshift range $0 < z < 6$, namely only after the reionization epoch; therefore, a comparison with the gas mass assembly history of our model is not straightforward.

In Fig. 6.3 the predicted stellar MDF of the best model (convolved with a Gaussian function with $\sigma = 0.2$ dex) is compared with the observed one ([Romano & Starkenburg, 2013](#)). The assumed very low SFE causes the MDF to be peaked at low $[\text{Fe}/\text{H}]$ abundances. The width of the MDF is mostly determined by the wind efficiency; in particular, the lower the λ_{wind} parameter, the wider is the bulk of the galaxy star formation activity and hence also the MDF.

In Figure 6.4a) we show the predicted SFH of our best model, while in Figure 6.4b) we show the corresponding age-metallicity relation. In summary, the length of the bulk of the galaxy star formation activity can be regulated in our model by suitably varying the main parameters determining the star formation and outflow intensity and the galaxy gas accretion rate; these parameters are the SFE, which determines the intensity of the SFR and the rate of thermal energy injection by supernovae, the wind efficiency, which determines the slope with which the SFR drops to zero, and the infall time-scale, which crucially determines the evolution with time of the galaxy potential well.

6.3.3 The photo-chemical model

The stepwise structure of the photo-chemical model is the following.

- We sample the galaxy SFH, as predicted by our best chemical evolution model for Sculptor, to randomly extract an age for the formation of a given star.
- We sample the assumed initial mass function (IMF) to randomly assign a mass to the star. In this work we assume the [Salpeter \(1955\)](#) IMF for simplicity.
- We use the age-metallicity relation of our best Sculptor chemical evolution model to find the initial metallicity of the star.
- Given the age, mass and metallicity of the star, we check whether the star is alive or not at the present time, by assuming the metallicity dependent stellar lifetimes we have derived from the PARSEC stellar evolutionary tracks (see Section 6.3.1).
- If the star can be observed at the present time, we store the photometric properties of the synthetic star, to later draw it in the synthetic CMD.

On the one hand, the strength of our method resides in the very fine grid of the assumed isochrone database; moreover, in our approach, we start from the

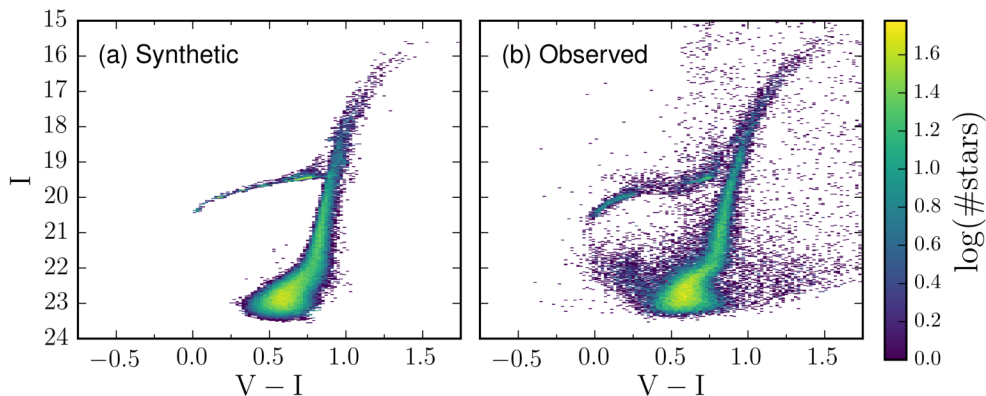


Figure 6.5: In the left panel of this figure, we show the prediction of our photo-chemical model for the CMD of the Sculptor dSph, whereas on the right panel we show for comparison the observed CMD. The synthetic and the observed CMDs are shown as 2-D histograms, with the bin size in both the x - and y -dimensions being 0.02 dex and the color-coding representing the number of stars, on a logarithmic scale, residing within each grid element.

predictions of chemical evolution models, assuming *ab initio* an underlying galaxy formation and evolution scenario, which is physically-motivated. On the other hand, the main shortcoming of our model is due to the fact that the lowest available metallicity in the PARSEC database is $Z_{\min} = 1.0 \times 10^{-4}$. We assume that all the stars with $Z < Z_{\min}$ have the same photometric properties as the stars with $Z = Z_{\min}$. This fact can introduce a systematic error. By looking at Figs. 6.4a) and b), according to our best model, the galaxy spends its first 122 Myr at metallicity $Z < 1.0 \times 10^{-4}$; the number of stars with initial metallicity $Z < 1.0 \times 10^{-4}$ is roughly ~ 5.72 per cent of the total number of stars alive at the present time.

Methods

To get a fair comparison with the observed CMD, we convolve the synthetic CMD with the distribution of the observed photometric errors, by assuming that the latter are Gaussian. In particular, we first divide the observed CMD in a uniform grid and, for each grid element ij , we compute the average V- and I-band observed photometric errors, $\bar{\sigma}_{ij}(V, I)$, which we adopt as the standard deviations of the photometric noise in the ij -th grid element. Hence, for any given k -th synthetic star residing in the ij -th grid element, we add the following noise to its predicted V- and I-band magnitudes: $\bar{\sigma}_k(V, I) = r_k \times \bar{\sigma}_{ij}(V, I)$, where r_k is a random number, drawn according to the standard normal distribution. In this way, the model ‘spreads out’ according to the errors in the data and we can fairly compare the synthetic with the observed CMD.

The synthetic CMD corrected for the photometric noise is then convolved with the results of the artificial star test performed by de Boer et al. (2011). In particular, by following a standard procedure, de Boer et al. (2011) inserted in the observed images a large catalog of artificial stars; after reducing and analyzing the

altered images, they could compute the fraction of artificial stars recovered in the data as a function of their input magnitude and color. We use the results of their test to compute the recovered fraction in each grid element, so as to throw out from the synthetic CMD the remaining lost fraction. By means of this type of analysis, one can apply to the synthetic CMD the same completeness profile as is present in the data. After correcting the synthetic CMD for the incompleteness, the number of synthetic stars strongly reduces, becoming $N_{\text{tot, syn}} \approx 40636$.

6.4 Results

In this Section, we present the results of our photo-chemical model for the CMD of the Sculptor dSph. The main result of our work is shown in Fig. 6.5, where the synthetic CMD of Sculptor (left diagram) is compared with the observed one (right diagram). In order to better understand where the discrepancies between the observed and the synthetic CMD reside, in Fig. 6.6 we plot the residuals, which correspond to the color-coding in the figure. In particular, to better visualize the differences, we define the residual in the ij -th grid element as:

$$R_{ij} = \frac{n_{ij,\text{obs}} - n_{ij,\text{syn}}}{\sqrt{n_{ij,\text{syn}}}}, \quad (6.2)$$

with $n_{ij,\text{obs}}$ and $n_{ij,\text{syn}}$ being the number of stars in the observed and synthetic CMD, respectively. The regions of the observed Sculptor CMD without any synthetic star are shown in Fig. 6.6 as a greyscale density plot.

On the one hand, by a visual inspection of Figs. 6.5 and 6.6, we can obtain a quite good agreement for the red giant branch (RGB), the horizontal branch (HB) and the asymptotic giant branch (AGB) of the observed CMD. On the other hand, at fainter magnitudes, particularly in the sub-giant branch (SGB) and at the MSTO, the observed CMD extends towards slightly bluer colors than the synthetic one. Moreover, our model cannot reproduce the observed population of blue straggler stars which extend the Main Sequence towards blue colors and could be – in principle – reproduced by including the effect of merging binary stellar systems. We do not include blue straggler stars in our photo-chemical model.

We remark on the fact that it is not obvious that a model reproducing the chemical evolution of Sculptor can also capture the main features of the observed galaxy CMD. In fact, the final configuration of the synthetic CMD turns out to be highly affected by the variation of the free parameters of chemical evolution models. In particular, by increasing the SFE, the stellar metallicities accordingly increase at any fixed galactic time, causing the entire synthetic CMD to shift towards redder colors. The IMF acts in a similar way as the SFE, with the additional effect of filling up the various stellar evolutionary phases in the CMD with different relative fractions. Finally, the wind parameter and the infall time-scale crucially affect the spread of the predicted CMD, since they determine the length of the bulk of the galaxy star formation activity.

In Fig. 6.7a), we compare the predicted stellar ($V - I$)-color distribution (black solid line) with the observed one (blue histogram); this quantity turns out to be

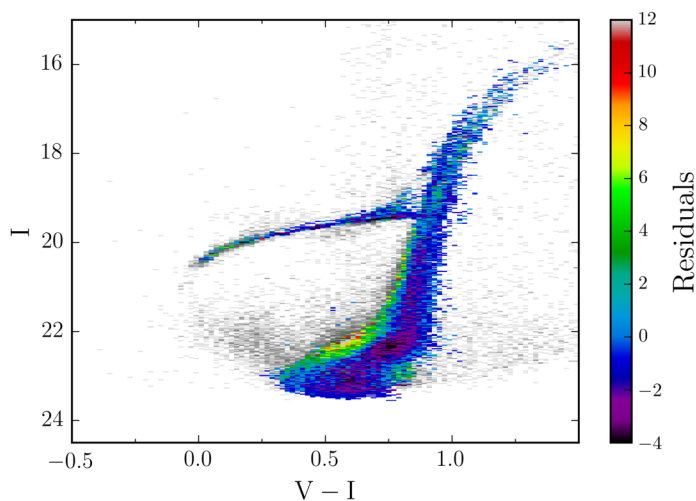


Figure 6.6: In this Figure, we show the residuals (see eq. 6.2) for the comparison between the observed and the synthetic CMD. The greyscale density plot represents the regions of the observed Sculptor CMD where no synthetic stars are predicted. We find a good agreement for the RGB, HB and AGB stars, whereas the MSTO and the SGB of the observed CMD extend towards bluer colors than the synthetic CMD. We cannot reproduce the population of blue straggler stars in the observed CMD, since we do not include them in our model.

particularly sensitive to metallicity variations among the galaxy stellar populations. In Fig. 6.7b), the predicted stellar luminosity function in the I -band (black solid line) is compared with the observed one (blue line with error bars, which are shown as a shaded blue area); the trend of this second quantity is more affected by the galaxy SFH and stellar lifetimes. An age indicator for the galaxy is given by the fraction of stars on the HB relative to the one on the RGB; we predict $N_{\text{HB}}/N_{\text{RGB}} \approx 0.17$.

At a first glance, our photo-chemical model is able to predict and qualitatively reproduce the main features of the observed $(V-I)$ -color distribution; in particular, the first peak in Fig. 6.7a) (the one at bluer colors) is determined by the MSTO and SGB stars, whereas the second peak (the one at redder colors) is the signature left by the ascending RGB and HB stars.

Concerning the blue portion of the color distribution, from a visual inspection of Fig. 6.7a), we cannot reproduce the observed population of blue straggler stars, which – as aforementioned – are not included in our photo-chemical model. Furthermore, a remarkable discrepancy resides in the decaying trend of the blue wing of the predicted color distribution, which contains a lower number of stars than the data, and in the predicted ‘saddle’, which turns out to be higher than the observed one. This can be also appreciated by looking at the residual plot in Fig 6.6, where the observed CMD clearly contains a larger number of MSTO and SGB stars with blue colors than the synthetic CMD. This discrepancy seems likely the signature of metal-poor stellar populations in the Sculptor dSph, which our one-zone chemical evolution model has not been able to capture. Nevertheless, in principle, it could

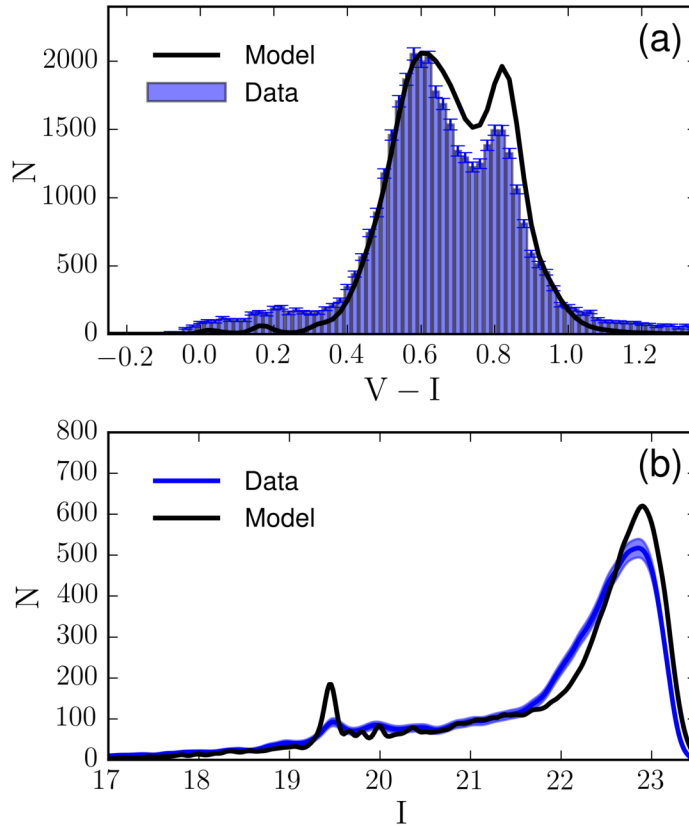


Figure 6.7: In the top panel of this figure, we compare the predicted stellar ($V - I$)-color distribution (black solid line) with the observed one (blue histogram with errorbars). In the bottom panel, we compare the predicted stellar luminosity function in the I -band (back solid line) with the observed one (blue line, with the shaded blue area representing the $1-\sigma$ errors). MSTO stars are predicted to reside in the synthetic CMD at $m_I \gtrsim 23.0$ mag, whereas SGB stars at $22.0 \lesssim m_I \lesssim 23.0$ mag. The peak in the I -band stellar luminosity function at $m_I \approx 19.5$ mag is caused by HB stars.

also indicate a predicted age-metallicity relation which is steeper than what seems to be required by observations; in fact, one would obtain a similar discrepancy if also the synthetic metal-rich stars are older than the observed ones.

Interestingly, by looking at Fig. 6.3, the observed stellar MDF suggests the presence of two distinct peaks, corresponding to two separated main stellar populations in the galaxy. The latter feature cannot be resolved by our best chemical evolution model, which indeed predicts the stellar MDF to have a single peak, lying between the two of the observed distribution. We remark on the fact that this feature is peculiar to the Romano & Starkenburg (2013) MDF, which combines the DART sample – determining the low metallicity portion of the observed MDF – with the one by Kirby et al. (2009, 2010), concentrated towards slightly higher metallicity. The regions where the observed CMD contains a larger number of blue (metal-poor) stars than the synthetic one likely correspond to the low-metallicity

peak in the observed MDF, which is also the most pronounced one. Accordingly, the higher ‘saddle’ in the predicted color distribution (see the top panel in Fig. 6.7) confirms that the model predicts galaxy stellar populations which are intermediate between the observed metal-poor and metal-rich ones.

The observed stellar MDF, as derived by Romano & Starkeburg (2013), includes stars with $r_{\text{ell}} \geq 0.6$ deg, namely beyond the radial cutoff we assume for the observed CMD. As one moves towards the outer zones of the galaxy, the Sculptor stellar populations are observed to become increasingly old and metal-poor, determining the observed stellar MDF at low metallicity. Nevertheless, the relative number of stars also increasingly diminishes when moving outwards, with almost 50 per cent of the Romano & Starkeburg (2013) sample being contributed by stars with $r_{\text{ell}} \leq 0.2$ dex. Furthermore, the shape of the observed stellar MDF in the inner radial bins does not significantly vary at low metallicity with respect to the MDF in the outer bins (see figure 14 of de Boer et al. 2012). Therefore, if we had applied a radial cutoff at $r_{\text{ell}} = 0.6$ deg also to the observed MDF, our analysis would not have been significantly altered.

A viable solution to reduce the discrepancy between the observed and the synthetic CMD would be, for example, to disentangle the two different stellar populations in the observed MDF, by assuming two underlying separated distributions, peaked at slightly lower and higher $[\text{Fe}/\text{H}]$ abundances than the predicted MDF of the best model. In this way, the metal-poor stellar population could be reproduced by assuming a lower SFE than the metal-rich one. After superimposing the two stellar populations in the synthetic CMD with appropriate weights, one would extend the synthetic CMD towards slightly bluer color, hence obtaining a better agreement with the observed CMD. Finally, we cannot exclude that the lack of binary stars in our photo-chemical model might also contribute to the discrepancy between the observed and the synthetic CMD, since their inclusion would cause a broadening of the MS and therefore a redistribution of the colors of the synthetic stars in Fig. 6.7a).

In Fig. 6.7b), the observed stellar I -band luminosity function is compared with the predicted one. For the RGB and AGB stars, there is a good agreement between the model and data. Furthermore, the model predicts a peak at $m_I \approx 19.5$ mag, which represents the effect of HB stars; the presence of this peak is not visible in the observed I -band stellar luminosity function because of the large foreground contamination in the redder part of the observed CMD, both at fainter and at brighter I -band magnitudes than the ones of the observed HB. If we had considered only Sculptor stars in the innermost regions of the galaxy (e.g. with $r_{\text{ell}} \leq 0.2$ deg), we would have obtained a well agreement between model and data also for the HB stars. At fainter magnitudes, the model in Fig. 6.7b) contains a larger number of MSTO and a lower number of SGB stars than the data; this discrepancy might be partly due to the inherent uncertainty in the assumed completeness profile, which is particularly important for these evolutionary stages, as well as it could also indicate the need for an IMF with a lower number of low-mass stars than the Salpeter (1955) IMF assumed in this work.

6.5 Conclusions and discussion

In this Chapter, we have presented a new approach to draw the synthetic CMD of galaxies. In particular, we have developed *ab-initio* a new photo-chemical model, which we have applied to reproduce the observed CMD of Sculptor dSph. Our numerical code starts from the predictions of chemical evolution models about the galaxy SFH and age-metallicity relation. Then, by assuming the PARSEC stellar evolutionary tracks, we can ‘light up’ the stars with different age, mass and metallicity of chemical evolution models, in order to draw a synthetic CMD. We have defined the best chemical evolution model for Sculptor as the one reproducing the observed galaxy stellar MDF.

Several improvements could be done in our photo-chemical model, by considering for example an underlying cosmological framework, whose primary effect would be to influence the evolution of the galaxy gas mass assembly with time. Interestingly, a very first attempt to draw the CMD of a dSph galaxy within a full cosmological framework by making use of a semi-analytical model for the galaxy formation and evolution is represented by the work of [Salvadori et al. \(2008\)](#), which adopted the freely available IAC-STAR code ([Aparicio & Gallart, 2004](#)), however, they did not provide a detailed discussion of their findings about the predicted galaxy CMD. A further improvement in our photo-chemical model would be to include the effects of unresolved binary stars and foreground contamination in the synthetic CMD.

The strength of our approach resides in the statistical sampling of the galaxy predicted SFH and assumed IMF, as well as in the assumption of a very fine grid of stellar isochrones, both in metallicity and in age. The main shortcoming is related to the PARSEC stellar isochrones, which are computed only for $Z \geq 10^{-4}$.

The SFH can be regulated in our models for dSphs by suitably varying the main parameters triggering the onset of the galactic wind and determining its intensity. In fact, once the galactic wind has started, the SFR rapidly drops to zero, since most of the infall mass has been accumulated fast within short typical time-scales. Our best model for Sculptor predicts that ~ 99 per cent of the stars observable at the present time are formed within the first 2.16 Gyr of the galaxy evolution. We predict at the present time a total stellar mass $M_{\star, \text{best}} = 1.91 \times 10^6 M_{\odot}$, which is of the same order of magnitude as other estimates like $M_{\star} = (1.2 \pm 0.6) \times 10^6 M_{\odot}$ by [de Boer et al. \(2012\)](#). Also the predicted evolution of the SFR as a function of time is in agreement with the findings of [de Boer et al. \(2012\)](#).

Stellar systems or interstellar regions with low gas density, such as low-mass dwarf galaxies or the outer parts of spiral galaxies, likely follow a star formation law which deviates from the usually assumed Schmidt-Kennicutt law, $\text{SFR}(t) = \nu M_{\text{gas}}(t)$; for this reason, we have done some numerical experiments by assuming the same expression for the star formation rate as in the original work of [Kennicutt \(1998\)](#) (see also [Gatto et al. 2015](#) for a detailed study in the context of hydrodynamical simulations). By assuming the [Kennicutt \(1998\)](#) law, we predict the SFH to be more concentrated in the earliest epoch of the galaxy evolution and the metallicity Z to initially evolve more rapidly than our best-fitting model; then, at later times, Z remains quite constant when the [Kennicutt \(1998\)](#) law is assumed,

while it increases in our best-fitting model. Finally, we find that the final total gas and stellar mass are almost the same when the two different expressions for the star formation rate are assumed.

We have shown that our photo-chemical model is able to capture the main features of the observed CMD of the Sculptor dSph, with the best agreement being obtained for the RGB, HB and AGB stars. The discrepancy has been found at fainter luminosity in the MSTO and SGB, where the observed CMD extends towards bluer colors than the synthetic one. That may be caused by underlying metal-poor stellar populations which our photo-chemical model has not been able to capture as well as to the lack of binary stars in our model, which would also broaden the synthetic CMD at faint magnitudes. In fact, the predicted stellar MDF is characterized by a single peak, whereas the observed one suggests the presence of two peaks, residing at slightly lower and higher [Fe/H] abundances than the model peak. In particular, the more pronounced peak in the observed MDF corresponds to the one at lower [Fe/H] abundances. Therefore, our photo-chemical model contains stellar populations which are intermediate between the metal-poor and the metal-rich ones in the observed stellar MDF.

In order to reduce the discrepancy, one could superimpose the results of multiple one-zone chemical evolution models and find the linear combination which provides the best agreement with the observed stellar MDF. This will be the subject of a future work, in which we will also show the effect of varying the free parameters of chemical evolution models on the synthetic CMD.

Although the uncertainties in the assumed completeness profile can be important at the MSTO and SGB, the discrepancy between model and data in the I -band stellar luminosity function for $m_I \gtrsim 21.0$ mag might be alleviated by assuming an IMF which contains a lower number of low-mass stars than the [Salpeter \(1955\)](#) IMF assumed in this work and by including the effect of binary stars.

References

- Aparicio A., Gallart C., 2004, *AJ*, 128, 1465
Battaglia G., Helmi A., Tolstoy E., et al., 2008, *ApJL*, 681, L13
Bressan A., Marigo P., Girardi L., et al., 2012, *MNRAS*, 427, 127
Chabrier G., 2003, *PASP*, 115, 763
Chen Y., Bressan A., Girardi L., et al., 2015, *MNRAS*, 452, 1068
Cignoni M., Tosi M., 2010, *Advances in Astronomy*, 2010, 158568
de Boer T. J. L., Tolstoy E., Saha A., et al., 2011, *A&A*, 528, A119
de Boer T. J. L., Tolstoy E., Hill V., et al., 2012, *A&A*, 544, A73
Dolphin A. E., 2002, *MNRAS*, 332, 91
Faucher-Giguère C.-A., Kereš D., Ma C.-P., 2011, *MNRAS*, 417, 2982
Gatto A., Walch S., Low M.-M. M., et al., 2015, *MNRAS*, 449, 1057
Harris J., Zaritsky D., 2001, *ApJS*, 136, 25
Hidalgo S. L., Aparicio A., Skillman E., et al., 2011, *ApJ*, 730, 14
Irwin M., Hatzidimitriou D., 1995, *MNRAS*, 277, 1354
Kennicutt R. C., Jr., 1998, *ApJ*, 498, 541
Kirby E. N., Guhathakurta P., Bolte M., Sneden C., Geha M. C., 2009, *ApJ*, 705, 328
Kirby E. N., Guhathakurta P., Simon J. D., et al., 2010, *ApJ*, 191, 352

-
- Kroupa P., 2001, MNRAS, 322, 231
Martínez-Vázquez C. E., Monelli M., Bono G., et al., 2015, MNRAS, 454, 1509
Majewski S. R., Siegel M. H., Patterson R. J., Rood, R. T., 1999, ApJL, 520, L33
Matteucci F., 2012, Chemical Evolution of Galaxies, Springer-Verlag Berlin Heidelberg
McConnachie A. W., 2012, AJ, 144, 4
Monelli M., Hidalgo S. L., Stetson P. B., et al., 2010, ApJ, 720, 1225
Padovani P., Matteucci F., 1993, ApJ, 416, 26
Romano D., Karakas A. I., Tosi M., Matteucci F., 2010, A&A, 522, A32
Romano D., Starkenburg E., 2013, MNRAS, 434, 471
Salpeter E. E., 1955, ApJ, 121, 161
Salvadori S., Ferrara A., Schneider R., 2008, MNRAS, 386, 348
Shapley H., 1938, Nature, 142, 715
Starkenburg E., Hill V., Tolstoy E., et al., 2010, A&A, 513, A34
Tang J., Bressan A., Rosenfield P., et al., 2014, MNRAS, 445, 4287
Tolstoy E., Irwin M. J., Helmi A., et al., 2004, ApJL, 617, L119
Tolstoy E., Hill V., Tosi M., 2009, ARA&A, 47, 371
Vincenzo F., Matteucci F., Vattakunnel S., Lanfranchi G. A., 2014, MNRAS, 441, 2815
Vincenzo F., Matteucci F., Recchi S., et al., 2015, MNRAS, 449, 1327
Vincenzo, F., Matteucci, F., de Boer, T. J. L., Cignoni, M., & Tosi, M. 2016, MNRAS, 460, 2238
Walker M. G., Peñarrubia J., 2011, ApJ, 742, 20

Part III

Chemical evolution of galaxies in the Local Universe

7

Nitrogen and oxygen abundances in the Local Universe

7.1 Introduction

The self-regulation of star formation in galaxies by gas accretion and galactic outflows is a fundamental ingredient in the modern framework of galaxy evolution. Both the analysis of large galaxy surveys and the direct observation of high-velocity clouds (e.g. Fraternali et al. 2002; Oosterloo et al. 2007; Heald et al. 2011; Gentile et al. 2013), as well as hydrodynamical simulations (Prochaska & Wolfe, 2009; Faucher-Giguère et al., 2011; van de Voort et al., 2011; Dekel et al., 2013; Fraternali et al., 2015) point towards the need for continuous accretion of pristine gas onto galaxies (see also Fraternali & Binney 2008; Putman et al. 2012). Moreover, historically, the so-called ‘G-dwarf problem’ (van den Bergh, 1962; Schmidt, 1963; Tinsley, 1980) was solved by relaxing the hypothesis of a closed-box evolution of the solar neighborhood and allowing the accretion of pristine gas onto the disk, which acts in diluting the abundances; in this way, one can reconcile the predicted frequency of metal-poor Galactic disk stars (which are too many in the framework of the simple closed-box model) with the observed one. Large scale galactic winds and outflows are also necessary to reproduce the overall properties of the observed galaxy population and to match the observed chemical enrichment of the intergalactic medium (IGM; see, for example, Finlator & Davé 2008; Erb 2008; Fabian 2012; Hopkins et al. 2012). Several observations of galactic outflows in the literature have demonstrated the ubiquity of the outflow phenomenon, both locally and at high redshift (see, for example, Pettini et al. 2001; Bolatto et al. 2013; Geach et al. 2014; Erb 2015; Cicone et al. 2014, 2015), however understanding their impact on galaxy properties over cosmic time remains a daunting task.

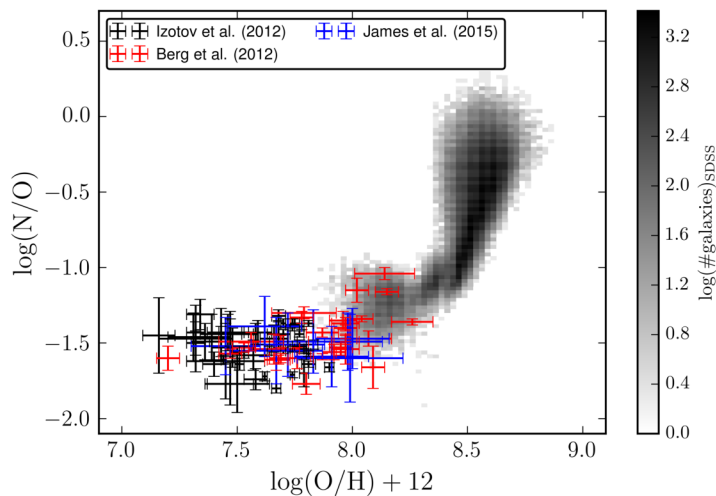


Figure 7.1: In this figure, the SDSS data sample for the (N/O) vs. (O/H) abundance pattern (density plot in greyscale) is compared with a data sample which includes the (N/O) and (O/H) abundances as observed in blue, diffuse star forming dwarf galaxies by [Berg et al. \(2012, red data\)](#), [Izotov et al. \(2012, black data\)](#) and [James et al. \(2015, blue data\)](#).

Since metals are a direct product of star formation in galaxies, chemical abundances are a powerful probe of the feedback processes driving the evolution of galaxies. Oxygen occupies a key role in this type of studies, since its gas phase abundance can be inferred from strong nebular lines easily observed in the optical wavelength range in the low redshift Universe. Since oxygen is the most common metal by mass, its abundance is also an excellent proxy for the total metallicity of the gas. Moreover, since oxygen is mostly produced by massive stars, dying as core-collapse supernovae (SNe), its enrichment is relatively simple to model and does not require, to first approximation, taking into account the effect of stellar lifetimes (under the so-called instantaneous recycling approximation, IRA).

The study of the relation between oxygen abundance and other fundamental galaxy parameters like stellar mass ([Lequeux et al., 1979](#); [Tremonti et al., 2004](#)), star formation rate (SFR, [Mannucci et al. 2010](#); [Andrews & Martini 2013](#)), gas content ([Hughes et al., 2013](#); [Bothwell et al., 2013](#)) and environment ([Pasquali et al., 2010](#); [Peng & Maiolino, 2014](#)) has paved the way to the development of a new generation of chemical evolution models ([Davé et al., 2012](#); [Lilly et al., 2013](#); [Peng & Maiolino, 2014](#); [Lu et al., 2015](#); [Belfiore et al., 2016](#)), which succeed, to various extents, at reproducing the general trends observed in the data with cosmological inflow rates and various simple outflow prescriptions.

Since different chemical elements are released in the interstellar medium (ISM) on different time-scales, the study of abundance ratios of some key elements can provide tighter constraints on the star formation and gas flow history of a system. For example, large galaxy surveys have demonstrated that the [O/Fe] ratios in elliptical galaxies are consistent with the paradigm requiring these objects to form stars vigorously over a short timescale at high redshift ([Matteucci, 1994](#); [Bernardi et](#)

al., 2003; Pipino & Matteucci, 2004; Thomas et al., 2005, 2010). Moreover, detailed analysis of chemical abundance ratios of n-capture, α - and iron-peak elements in individual stars in the Milky Way (MW) have been instrumental in showing that the various components of our Galaxy (halo, bulge, thick and thin disk) have had different chemical evolution histories with respect to each other (see, for example, Pagel 2009; Matteucci 2001, 2012).

In the context of star forming galaxies, strong nebular lines in the optical range allow reliable measurement of the (N/O) abundance ratio when both the [OII] λ 3726,3729 and [NII] λ 6548,6584 doublets are measured. The (N/O) abundance ratio has been studied by several authors (Vila-Costas & Edmunds, 1992; Thuan et al., 1995; Henry et al., 2000; Chiappini et al., 2003, 2005; Pérez-Montero & Contini, 2009; Pérez-Montero et al., 2013; Belfiore et al., 2015) since it is a promising tool to shed light on the relative role of pristine gas inflows and outflows, which appear degenerate when only the abundance of one chemical element is traced (see Köppen & Hensler 2005, but also the discussion in the Appendix of Belfiore et al. 2016).

Unlike oxygen, nitrogen is a chemical element mostly produced by low- and intermediate-mass stars (LIMS), with the nucleosynthetic yields depending on metallicity in a complex fashion. In particular, a stellar generation can release into the galaxy ISM both primary and secondary N. The secondary N component increases with metallicity, being a product of the CNO cycle and formed at expenses of the C and O already present in the star. Concerning LIMS, the primary N component is produced during the third dredge-up, occurring along the asymptotic giant branch (AGB) phase, if nuclear burning at the base of the convective envelope is efficient (Renzini & Voli, 1981). The latter is particularly important for very metal-poor LIMS, which would not be capable otherwise of synthesizing significant amounts of secondary N. On the other hand, the computation of the N stellar yields for massive stars still suffers of large uncertainty, especially at very low metallicity, and none of the current existing stellar evolutionary codes is able to provide the right amount of primary N which is needed to reproduce the observed (N/O) plateau at very low metallicities.

All the aforementioned complications prevent one from using IRA and a constant yield for the study of nitrogen abundances in galaxies, and have prevented the community so far from taking full advantage of the large nitrogen abundance datasets now available both through large spectroscopic surveys of local (like SDSS, York et al. 2000, or GAMA, Driver et al. 2011) and high-redshift (e.g. zCOSMOS, Lilly et al. 2009) galaxies.

In this Chapter, we critically revise the different assumptions affecting the interpretation of the (N/O) versus (O/H) abundance patterns, making use of a large dataset of star forming galaxies from the SDSS, complemented by data from metal-poor dwarf galaxies to explore the low-metallicity regime. While considerable uncertainties still persist in some of the basic model parameters (nitrogen yields, stellar initial mass function, IMF) we aim here at setting new constraints on pristine gas inflows and the models of outflows.

This Chapter is structured as follows. In Section 7.2, we present the dataset for the (N/O) vs. (O/H) abundance diagram. In Section 7.3, we summarize the

current knowledge about the nucleosynthetic origin of nitrogen in stars. In Section 7.4, we describe the basic equations and the assumptions of our numerical model of chemical evolution. Our results are presented in Section 7.5 and 7.6; in particular, in Section 7.5, we focus on the results of our models for the (N/O) vs. (O/H) abundance pattern of the ensemble of the SDSS galaxies; in Section 7.6, we present the results of our models for the low metallicity plateau, which a complementary sample of metal-poor, diffuse and star-forming dwarf galaxies exhibit in the (N/O) vs. (O/H) diagram. Finally, in Section 7.7, we end with our conclusions. All the results of this Chapter have been published in Vincenzo et al. (2016b).

7.2 Overview of the data

In order to study the characteristic gas-phase oxygen and nitrogen abundances in local galaxies, we make use of the data from SDSS Data Release 7 (Abazajian et al., 2009, DR7) and the emission line fluxes, stellar masses and SFR estimates presented in the MPA-JHU catalogue* (Brinchmann et al., 2004; Tremonti et al., 2004; Kauffmann et al., 2003) released as part of DR 8 (Aihara et al., 2011).

We select galaxies to have $0.023 < z < 0.3$ and $S/N > 3$ on the following emission lines: [OII] $\lambda\lambda$ 3726,28; [OIII] λ 5007; H β ; H α ; [NII] λ 6584, and [SII] $\lambda\lambda$ 6717,31. We use the standard Baldwin-Philippis-Terlevich (BPT) diagram (Baldwin et al., 1981; Veilleux & Osterbrock, 1987; Kauffmann et al., 2003) to exclude sources where the gas ionisation is not dominated by star formation, since available metallicity calibrations are only tailored to star forming regions. In this work we use the [OIII]/H β versus [SII]/H α diagnostic diagram and the demarcation curve of Kewley et al. (2001). We do not make use of the popular [OIII]/H β versus [NII]/H α to avoid a bias against nitrogen enriched HII regions (Sánchez et al., 2015; Belfiore et al., 2015).

Emission line fluxes are then corrected for dust extinction using the Balmer decrement and the Calzetti (2001) reddening curve with $R_V = 4.05$. The theoretical value for the Balmer line ratio is taken from Osterbrock & Ferland (2006), assuming case B recombination (H α /H β = 2.87). We note that the use of extinction curves of Cardelli et al. (1989) or Charlot & Fall (2000) yield very similar results for the wavelength range considered in this work.

Inferring gas phase oxygen abundance from strong nebular line ratios is a difficult problem, since the line ratios depend not only on ionic abundances, but also on other parameters, such as ionisation parameter, density and hardness of ionisation field. It is well known in the literature that different oxygen abundance calibrations based on strong nebular lines can lead to systematic discrepancies of up to 0.6 dex (Kewley & Ellison, 2008; López-Sánchez et al., 2012; Blanc et al., 2015). In particular, strong line calibrations based on an extrapolation to high metallicity of abundances measured with the τ_e method (which makes use of the faint oxygen auroral line [OIII] λ 4363 to directly infer the electron temperature of

*The MPA-JHU catalogue is available online at <https://www.sdss3.org/dr8/spectro/galspec.php>

the nebula) generally lead to lower abundances than calibrations based on photoionisation models.

Moreover, several metallicity calibrators make use of the nitrogen line fluxes, thus implicitly assuming that the relationship between the (N/O) ratio and metallicity varies monotonically with oxygen abundance.

In this work, we infer the oxygen and nitrogen abundances using the self-consistent framework presented in Pilyugin et al. (2010), which calibrates various strong line ratios through the electron temperature method. An alternative calibration taking both oxygen and nitrogen abundance into account has been recently presented in Pérez-Montero (2014).

In order to sample the low metallicity regime, which is poorly populated in SDSS, we make use of the data from Izotov et al. (2012); Berg et al. (2012); James et al. (2015) for a collection of blue, diffuse and star forming dwarf galaxies. We note that the abundances reported by Izotov et al. (2012); Berg et al. (2012); James et al. (2015) correspond to the chemical abundances as measured using the direct method and hence should fall onto the same scale of chemical abundances we inferred from the SDSS data with the adopted calibration.

In Fig. 7.1 we show the trend of the observed (N/O) ratios as a function of the (O/H) abundances. The density plot in greyscale represents the abundance pattern as observed in the ensemble of the SDSS galaxies, whereas the data with error bars represent the compilation of star forming dwarf galaxies from Berg et al. (2012); Izotov et al. (2012); James et al. (2015). The latter data extend towards lower (O/H) abundances than the SDSS data and clearly exhibits the well-known low metallicity plateau. The SDSS data show an abrupt change of the slope at oxygen abundances higher than $12 + \log(\text{O}/\text{H}) \sim 8.4$ dex .

7.2.1 Estimating the dust depletion

Oxygen abundance calibrations based on nebular lines only trace the oxygen abundance of the gaseous phase of the ISM. However, chemical elements in real galaxies are partially depleted on to dust grains. Since chemical evolution models only predict the total metallicity, depletion onto dust grains must be taken into account when comparing models with our data. From an observational point of view, the dust content can differ among galaxies of different metallicity and SFR (da Cunha et al., 2010; Fisher et al., 2014; Hjorth et al., 2014). In the framework of chemical evolution studies, the most important physical process affecting the dust cycle in galaxies is the star formation history, which regulates the main feedback processes responsible for the dust production and destruction and hence the run of the galaxy dust-to-gas ratio with metallicity (Wang, 1991; Dwek, 1998; Lisenfeld & Ferrara, 1998; Edmunds, 2001; Calura et al., 2008; Dwek & Cherchneff, 2011; Feldmann, 2015).

In the literature a mean oxygen depletion[†] of $D(\text{O}) \approx -0.1$ dex is often assumed (see also Whittet 2003; Jenkins 2009; Whittet 2010). Although oxygen depletion

[†]The depletion factor $D(X)$ is the logarithmic decrement between the observed abundance of a chemical element and its predicted total abundance, $A(X)$, namely $D(X) \equiv \log(N_X/N_H)_{\text{obs}} - A(X)$.

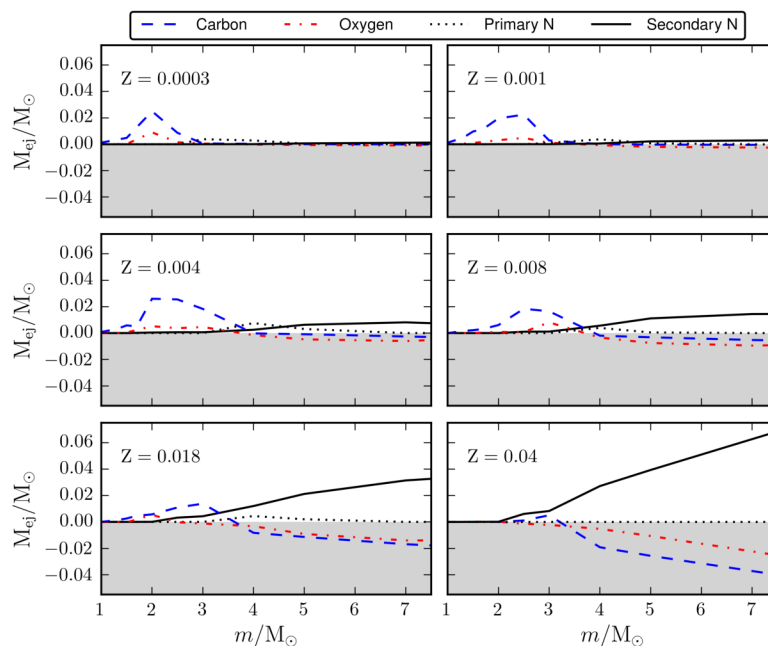


Figure 7.2: In this figure, we show the Ventura et al. (2013) stellar yields of LIMS for carbon (dashed blue line), oxygen (dashed-dotted red line), primary nitrogen (dotted black line) and secondary nitrogen (solid black line), as computed at $Z = 0.0003, 0.001, 0.004, 0.008, 0.018,$ and 0.04 . The various quantities do not include the amount of ejected mass which was initially present in the star and has not been nucleary processed; so the finding of negative values for the stellar yields means that the final total ejected amount of the generic element X is smaller than the one which was initially present in the star at its birth and has been later ejected into the ISM without any nuclear processing.

is likely to have a dependance on metallicity (differential depletion), for simplicity we do not consider this effect in this work. Although Jenkins (2009) suggests an average nitrogen depletion of ~ -0.1 dex, the large uncertainty in this estimate means that nitrogen is also consistent with zero depletion. Indeed most of the studies indicate that nitrogen is not a refractory element and does not deplete onto grains even in the densest molecular clouds (e.g. Meyer et al. 1997; Caselli et al. 2002). In light of this, in our work, we do not consider any nitrogen depletion onto dust. While the depletion corrections applied in this work are rather arbitrary, none of our conclusions depend on the exact values of the depletion factors.

7.3 The nucleosynthetic origin of nitrogen

According to its mass and initial chemical composition, each star pollutes the ISM with different amounts of a given chemical element. Since stellar lifetimes primarily depend upon the stellar mass, each chemical element is expected to enrich the ISM of galaxies on different typical timescales.

7.3.1 Primary and secondary nucleosynthetic products

A fundamental aspect to take into account in chemical evolution models is the nature of the physical processes which give rise to the production of the various chemical elements in stars. In particular:

- If a sequence of nuclear reactions involves as initial seed only the H and He present in the gas mixture of the star at its birth, then the nucleosynthetic products of that sequence do not depend upon the initial stellar metallicity. The chemical products of these reactions are then named *primary* elements.
- If the presence of metals in the initial gas mixture of the star is necessary for some nuclear reactions to occur, then the nucleosynthetic products of those nuclear reactions depend on the metallicity. These chemical products are named *secondary* elements.

In modern chemical evolution studies, the importance of distinguishing between the secondary and primary nature has been simplified for most of the chemical elements, since their yields are computed as a function of the initial metallicity. Nevertheless, for chemical elements like nitrogen, which have both a primary and secondary origin (see, for example, [Edmunds & Pagel 1978](#); [Alloin et al. 1979](#); [Renzini & Voli 1981](#); [Matteucci 1986](#); [Gavilán et al. 2006](#); [Mollá et al. 2006](#)), it can be conceptually useful to separate the two components, even in the presence of yields computed for different metallicities.

7.3.2 The production of nitrogen in the CNO cycle

Nitrogen is mainly produced during the CNO cycle, whose main branch consists in a series of *p*-captures and β^+ decays starting from an atom of ^{12}C and converting four protons into a nucleus of He (with two e^+ and two ν_e as byproducts). Since the inner reaction $^{14}\text{N}(p, \gamma)^{15}\text{O}$ proceeds with the slowest rate among the other in the sequence, when the equilibrium condition is reached (namely, when the rate of production of each CNO nucleus equals its rate of destruction), the ultimate effect of the CNO cycle is to convert most of the CNO isotopes into ^{14}N . The origin of the initial ^{12}C seed in the CNO cycle is a discriminating factor. In fact, if the atom of ^{12}C was initially present in the gas mixture from which the star originated, then the synthesized nitrogen behaves as a secondary element. On the other hand, if some physical mechanism is able to carry the C and O nuclei produced in the He-burning zones out to the H-burning zones, then the synthesized nitrogen behaves like a primary element.

7.3.3 Nitrogen yields in low- and intermediate-mass stars

Low- and intermediate-mass (LIM) stars during the AGB phase eject into the ISM significant amounts of He, C and N. The ejected masses reflect important abundance variations. The main physical mechanism for the transport of the C and O nuclei to the outer zones of the star is given by the so-called third dredge-up, which is the transfer of the nucleosynthetic products of the triple- α process by

Table 7.1: In this Table, the various columns report the following quantities: i) Z , metallicity; ii) $\overline{M}_{O,R10}$, the IMF-averaged stellar yield of oxygen in the mass range $M = 11-100 M_{\odot}$, by assuming the stellar yields of [Romano et al. \(2010, R10\)](#) and the [Kroupa et al. \(1993\)](#) IMF; iii) $\overline{M}_{N,R10}$, the IMF-averaged stellar yield of nitrogen, defined as in the previous column; iv) predicted average $\log(N/O)$ ratios, when considering only the contributions of massive stars; v) average stellar yield of primary N which should be provided by massive stars to reproduce the observed low-metallicity plateau with $\log(N/O) \approx -1.6$ dex. This empirically-derived yield is used as the reference stellar yield for primary nitrogen at low metallicity in this work.

Z	$\overline{M}_{O,R10} [M_{\odot}]$	$\overline{M}_{N,R10} [M_{\odot}]$	$\log(N/O)_{R10}$	$\overline{M}_{N,prim} [M_{\odot}]$
1.0×10^{-10}	3.025	0.014	-2.27	0.066
1.0×10^{-8}	3.105	0.082	-1.52	0.068
1.0×10^{-5}	1.995	0.0005	-3.53	0.043
1.0×10^{-3}	1.999	0.005	-2.55	0.044
4.0×10^{-3}	2.013	0.018	-1.99	0.044

the surface convection which proceeds after each thermal pulse. Primary nitrogen can then be produced when the hot-bottom burning (CNO burning at the base of the convective envelope) occurs in combination with the third dredge-up (see, for example, [Ventura et al. 2013](#)).

In [Fig. 1.5](#), we show how the stellar yields of [Ventura et al. \(2013\)](#) for C, O, and primary and secondary N vary as a function of the initial stellar mass, for different metallicities. The stellar yield of a given chemical element X is defined as the ejected amount of mass of the newly formed X . By looking at the figure, the stellar yields of secondary N increase with metallicity, by means of the consumption of the C and O nuclei originally present in the star. In fact, during the CNO cycle, the global abundance of the CNO nuclei remains constant, while the relative abundances of each CNO element can significantly vary. By looking at [Fig. 1.5](#), the stellar producers of primary N have masses in the range between $\sim 3 M_{\odot}$ and $6 M_{\odot}$. Furthermore, the production of primary N does not show any correlation with the consumption of the original C and O in the star, as expected.

7.3.4 Nitrogen yields in massive stars

In order to reproduce the observed plateau in the (N/O) ratio for the MW halo stars, [Matteucci \(1986\)](#) proposed that massive stars should produce only primary N at all metallicities, at variance with standard nucleosynthesis models predicting only secondary N from massive stars. This plateau was also later observed in damped Ly α (DLA) systems ([Pettini et al., 2002, 2008](#)) and blue, low metallicity star forming dwarf galaxies ([Thuan et al., 1995](#); [Izotov et al., 2012](#); [Berg et al., 2012](#); [James et al., 2015](#), see [Fig. 7.1](#)), thus confirming that there should be primary N production in massive stars.

[Maeder & Meynet \(2000\)](#) and [Meynet & Maeder \(2002b\)](#) found that primary N can be produced in rapidly rotating massive stars, but only at very low metallicity.

Their proposed main physical mechanism is given by the so-called rotational mixing, particularly efficient at very low metallicity, where stars are expected to rotate faster and to be much more compact than their metal-rich counterparts. Rotational mixing allows the nucleosynthetic products of the triple- α reaction (mainly C and O nuclei) to efficiently diffuse towards the outer CNO burning zone, where a pure primary nitrogen can then be synthesized (Chiappini et al., 2008; Maeder, 2009).

This unfortunately cannot solve the problem of the observed (N/O) plateau, which extends all over the metallicity range of MW halo stars. In fact, Geneva stellar evolutionary models predict fast rotating massive stars to produce primary N only in a narrow range at very low metallicity; as the metallicity $Z > 10^{-8}$, these stars resume producing only secondary N. Therefore, by assuming the theoretical stellar yields of the Geneva group, chemical evolution models predicted a ‘dip’ in the (N/O) ratio at low (O/H) abundances, which is never observed (see, for example, Chiappini et al. 2005, and the further discussion in Section 7.3.5 and 7.6). To solve this discrepancy and be able to explain the observed trends in the data, all previous chemical evolution models (Matteucci, 1986; Chiappini et al., 2005) had to assume artificially a pure primary N yield from massive stars.

7.3.5 Empirically fixing the nitrogen yield from massive stars at low metallicity

In order to re-assess the problem of primary nitrogen production in massive stars, we suggest a revised primary N stellar yield at low metallicity.

In Table 7.1 we report the IMF-averaged stellar yields of N and O from massive stars, $\overline{M}_{N,R10}$ and $\overline{M}_{O,R10}$, respectively, as computed by using the Romano et al. (2010) compilation of stellar yields and assuming the Kroupa et al. (1993) IMF. We also report how the values of $\log(\text{N/O})$ are predicted to vary for different metallicities, when considering only the contributions of massive stars to the nitrogen and oxygen chemical enrichment of the ISM. We observe that the Geneva stellar models predict a dip in the (N/O) ratios for $Z > 10^{-8}$. This dip is never observed and it stems from the lack of primary N production by massive stars for $Z > 10^{-8}$.

In order to reproduce the low-metallicity plateau, we therefore calculate the average amount of primary N that massive stars should provide to reproduce the observed (N/O) plateau at very low metallicities. We assume that the oxygen yields in this regime are reliable and we require the predicted (N/O) ratios to match the observed $\log(\text{N/O}) \approx -1.6$ dex at low metallicity. In particular, we empirically derive the needed average stellar yield of primary nitrogen by massive stars as

$$\overline{M}_{N,\text{prim}}(Z) = \overline{M}_{O,R10}(Z) \times 10^{-1.6} \times \frac{A_N}{A_O}, \quad (7.1)$$

where A_N and A_O represent the atomic weight of N and O, respectively. The calculated values of $\overline{M}_{N,\text{prim}}(Z)$ are reported in the last column of Table 7.1. Interestingly, at extremely low Z , the latter are of the same order of magnitude as the value of $0.065 M_\odot$ originally adopted in chemical evolution models to reproduce the low-metallicity plateau (see also Chiappini et al. 2005, and references therein).

For the rest of this work, in our reference chemical evolution models, we assume a pure primary N production by massive stars, with the stellar yields at the various metallicities being the quantity $\overline{M}_{\text{N,prim}}(\text{Z})$, as given in Eq. (7.1) and reported in the last column of Table 7.1. We remark on the fact that, because of the way we have defined it, this quantity depends on the assumed IMF and stellar yields of oxygen.

7.4 Summary and reminder of the chemical evolution framework

We study the nitrogen and oxygen evolution in the ISM of galaxies by adopting a chemical evolution model in which the galaxy is assumed to be composed of a single zone within which the various chemical elements are assumed to mix instantaneously and uniformly. The basic ingredients of the model are described in detail in [Matteucci \(2012\)](#). In summary, the model is capable of following the temporal evolution of the abundances of various chemical elements within the ISM of galaxies, by taking into account the main physical processes driving chemical evolution, such as star formation, inflows and outflows of gas.

In this Section, we remind the reader the main assumptions of our chemical evolution model (see also Chapter 1.3 for a more detailed description).

7.4.1 Star formation and chemical evolution

By defining $M_{\text{g},i}(t)$ as the gas mass in the galaxy which is in the form of the i -th chemical element at time t , its temporal evolution follows:

$$\frac{dM_{\text{g},i}(t)}{dt} = \underbrace{-X_i(t) \text{SFR}(t)}_{\text{SF}} + \underbrace{R_i(t)}_{\text{yields}} - \underbrace{\Psi_i(t)}_{\text{outflow}} + \underbrace{\Phi_i(t)}_{\text{infall}}, \quad (7.2)$$

where $X_i(t) = M_{\text{g},i}(t)/M_{\text{g}}(t)$ is the abundance by mass of the i -th chemical element, defined such that $\sum_i X_i(t) = 1$, and $M_{\text{g}}(t)$ is the total gas mass in the galaxy at time t . In our models, we assume the stellar lifetimes of [Padovani & Matteucci \(1993\)](#).

We assume a star formation law of the form $\text{SFR}(t) = \nu M_{\text{g}}(t)$, with ν being the star formation efficiency (SFE), a free parameter of our models.

The term $R_i(t)$ in equation 7.2 represents the rate at which stars return the i -th chemical element back to the ISM at their death. This term subsumes all our prescriptions about the stellar yields as well as the assumptions concerning SN progenitors. In particular, for Type Ia SNe, we assume the ‘single degenerate scenario’ with the same prescriptions as in [Matteucci \(2001,?, 2012\)](#), however the details of the treatment of Type Ia SNe are largely irrelevant to this work, since they only have a very minor effect in the enrichment of oxygen and nitrogen.

7.4.2 The infall rate

In our model, the galaxy is assumed to assemble by means of accretion of gas from an external reservoir into the potential well of an underlying dark matter (DM) halo.

The gas infall rate, $\Phi_i(t)$, follows an exponential form with time given by

$$\Phi_i(t) = \frac{X_{\text{inf},i} M_{\text{inf}} e^{-t/\tau_{\text{inf}}}}{\tau_{\text{inf}} (1 - e^{-t_{\text{G}}/\tau_{\text{inf}}})}, \text{ with } \sum_i \int_0^{t_{\text{G}}} \Phi_i(t) dt = M_{\text{inf}}, \quad (7.3)$$

where t_{G} is the age of the galaxy and $X_{\text{inf},i}$ is the abundance by mass of the i -th chemical element in the infalling gas (M_{inf}), whose chemical composition is assumed to be primordial.

7.4.3 The outflow model

In equation 7.2 the outflow rate is modelled by $\Psi_i(t) = \omega_i \text{SFR}(t)$, where ω_i is the so-called *mass loading factor*. Observations generally suggest that star-forming galaxies experience time-averaged outflow loading factors of order unity (Lilly et al., 2013; Peng et al., 2015; Belfiore et al., 2015; Lu et al., 2015) at stellar masses around $\log(M_{\star}/M_{\odot}) \sim 10$, close to the knee of the luminosity function. It is, however, likely that less massive galaxies experience much higher loading factors.

In this work, we assume the galactic wind to be *differential*; namely, the outflow carries only the main nucleosynthetic products of core-collapse SNe (mainly α -elements), for which ω_i is a constant value. For chemical elements such as nitrogen and carbon, which have a very minor contribution from SNe, we assume a null mass loading factor, i.e. $\omega_i = 0$. We recall here that the assumption of a differential outflow is justified by the fact that massive stars (the progenitors of core-collapse SNe and the most important oxygen producers in the Universe) are observed to be highly clustered and so, as they explode, they create a region of the ISM in which the filling factor closely approaches to unity (see Marconi et al. 1994; Recchi et al. 2001).

Interestingly, the first works suggesting a differential metal-enhanced galactic wind in the context of the study of chemical evolution of galaxies were those of Pilyugin (1993) and Marconi et al. (1994), which addressed also the issue of explaining the (N/O) vs. (O/H) abundance pattern observed in dwarf irregular galaxies (see Recchi et al. 2008 for a detailed study and references). We are aware that our assumption of a differential galactic wind is highly uncertain and it does not rely on firm theoretical and observational findings.

Following the formalism of Bradamante et al. (1998), the time for the onset of the galactic outflow is calculated by requiring the thermal energy of the gas (supplied by SNe and stellar winds to the galaxy ISM) to be larger than the binding energy of the gas to the galaxy potential well.

7.4.4 Summary of the stellar yields for O and N

In this work we assume for oxygen and nitrogen the following set of stellar yields.

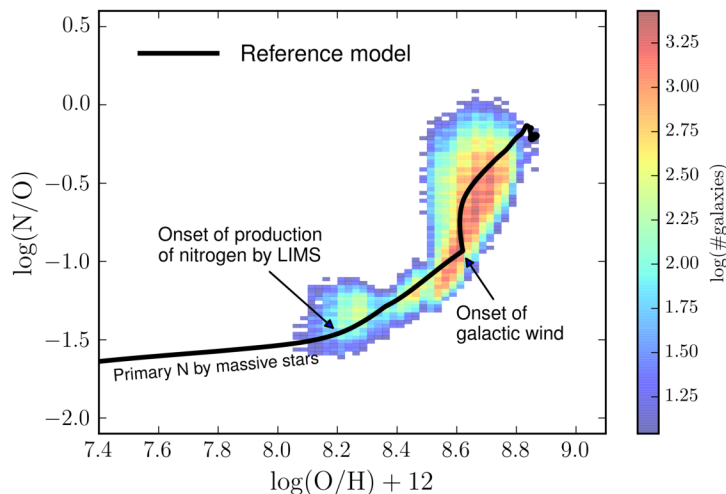


Figure 7.3: The reference chemical evolution model used in this work to reproduce the abundance pattern in the (N/O) vs (O/H) plane (black solid line). The distribution of SDSS galaxies is shown as a 2D histogram, with the bin size in both the (N/O) and (O/H) dimensions being 0.025 dex, and the colour-coding represents the number of galaxies in each bin. The changes in slope of the observed (N/O) vs (O/H) relation are linked to different physical properties of the model. The plateau at low metallicity is due to the pure primary N production by massive stars. The slope of the (N/O) vs (O/H) relation increases when LIMS start dying, producing both primary and secondary nitrogen. A further steepening of the relation is obtained after the onset of a differential galactic wind, which here is assumed to expel oxygen preferentially.

- For massive stars, we assume the metallicity-dependent compilation of stellar yields of [Romano et al. \(2010\)](#), see also Chapter 2.5 of this Thesis), in which the nitrogen and oxygen yields have been computed by the Geneva group, by including the combined effect of rotation and mass loss (see, for more details, [Meynet & Maeder 2002](#); [Hirschi et al. 2005](#); [Hirschi 2007](#); [Ekström et al. 2008](#)). For $Z < 10^{-3}$ we make use of the empirically-motivated nitrogen yield of massive stars derived in Sec. 7.3.5.
- For low- and intermediate-mass (LIM) stars, we assume the stellar yields at the various metallicities computed by means of the ATON numerical code of stellar evolution (see, for a detailed description, [Mazzitelli 1989](#); [Ventura et al. 1998](#); [Ventura & D’Antona 2009](#); [Ventura et al. 2013](#)). We have chosen the [Ventura et al. \(2013\)](#) stellar yields because they provide separately the primary and secondary components of the nitrogen stellar yield for a large range of metallicities ($3.0 \times 10^{-4} \leq Z \leq 0.04$; see the discussion in Sec 7.3.1). Other works which also separate the two components are those of [Gavilán et al. \(2005, 2006\)](#), however they span a too narrow metallicity range for the purpose of our work.

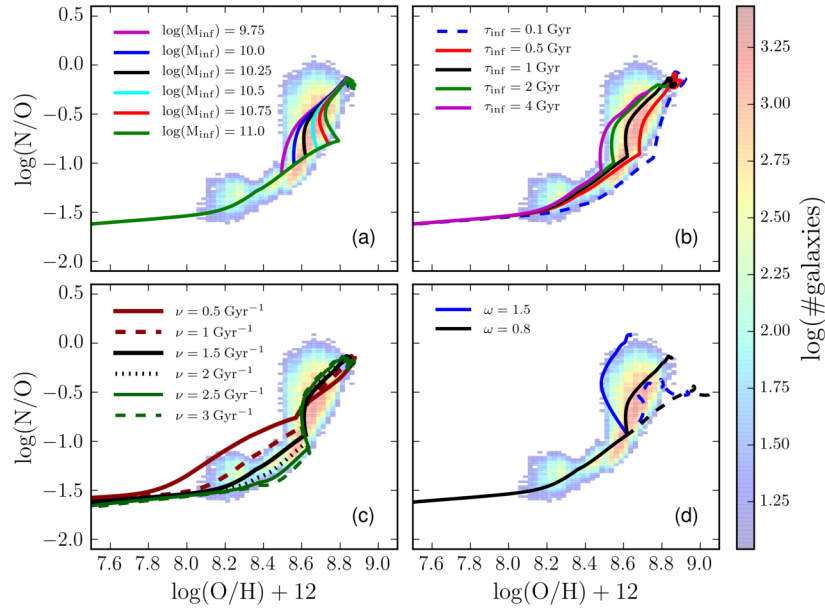


Figure 7.4: Chemical evolution model track in the (N/O) vs (O/H) plane. Abundances for SDSS galaxies are shown as a 2D histogram, with the colour-coding corresponding to the number of galaxies in each bin, with the bin size in both the (N/O) and (O/H) dimensions being 0.025 dex. The reference model is always plotted in black solid line. In different panels we vary different free parameters of the chemical evolution model. In panel a) we change the infall mass M_{inf} , in panel b) the infall timescale τ_{inf} , in panel c) the SFE ν and in panel d) the outflow loading factor ω . In panel d) the dashed lines correspond to a non-differential outflow (where both N and O are expelled with the same efficiency) while the solid lines refer to the reference assumption of a differential outflow where N is not expelled (with $\omega_N = 0$).

7.5 Modelling the SDSS data

In this section, we compare the predictions of our chemical evolution models with the set of data discussed in Sec. 7.2 (see Fig. 7.1) focusing on reproducing the high-metallicity regime of the (N/O) versus (O/H) diagram. We will address the question of reproducing the low metallicity tail of the (N/O) distribution in the next section.

7.5.1 The reference model

Given the relatively large number of free parameters in our detailed chemical evolution model, we take a qualitative, staged approach. We first choose a set of reference parameters. We then investigate the effect of changing each of them, while keeping the other ones fixed. Our reference model assumes:

- fixed SFE $\nu = 1.5 \text{ Gyr}^{-1}$,
- fixed mass loading factor $\omega = 0.8$ for oxygen,

- differential galactic outflow, with $\omega = 0.0$ for nitrogen,
- infall mass $\log(M_{\text{infall}}/M_{\odot}) = 10.25$,
- infall time-scale $\tau_{\text{infall}} = 1$ Gyr,
- [Kroupa et al. \(1993\)](#) IMF,

and the star formation history is assumed to be extended over all the galaxy lifetime (i.e. we do not introduce a quenching phase). In Fig. 7.3 we plot this reference model in the (N/O) versus (O/H) plane, together with the distribution of SDSS galaxies. The observed (N/O) vs. (O/H) abundance pattern is shown as a density plot, with the bin size in both the (N/O) and (O/H) dimensions being 0.025 dex; we show only the bins which contain more than ten galaxies and the colour-coding represents the number of galaxies within each bin.

It is remarkable to note that our simple reference model in Fig. 7.3 can well reproduce the main features of the data. The predicted low-metallicity plateau is the effect of our assumption of a pure primary N production by massive stars. The increase of the (N/O) ratios from $12 + \log(\text{O}/\text{H}) \sim 8.0$ dex is due to the delayed chemical feedback of LIMS, which pollute the ISM with primary *and* secondary nitrogen; we will refer to this change in slope as the ‘first break point’. By definition, the production of secondary nitrogen by LIMS increases as the metallicity increases. Although the production of primary N is smaller than the one of secondary N (see Fig. 1.5), the main primary N producers turns out to be, on average, less massive and hence more long-living than the bulk of the secondary N producers. In this way, the pollution of the ISM with primary N by LIMS mimics and amplifies the secondary N component. At $12 + \log(\text{O}/\text{H}) \sim 8.6$ dex, we see in Fig. 7.3 a new change in slope (‘second break point’), which is caused by the onset of the galactic wind. Since we assume a differential outflow, the loss of oxygen per unit time is more efficient than the loss of nitrogen (which is set to zero). In this way, the accumulation of oxygen within the galaxy ISM slows down and the net effect of the galactic wind is to steepen the (N/O) ratios as the chemical evolution proceeds. We remark that the increase of the (N/O) ratios after the second break point is also crucially bolstered by the larger amounts of secondary N which LIMS are able to synthesize at higher Z .

7.5.2 Exploring the parameter space

In this Section we discuss the effect of varying the free parameters in the reference model. In particular, we show that the main parameters influencing the shape of the (N/O) vs (O/H) relation are the star formation efficiency, the outflow loading factor and the assumptions regarding the differential outflow loading for N and O. Other parameters, such as the infall mass and the infall timescale do not have a significant effect on the abundance trends studied.

The infall mass

In Fig. 7.4a), we explore the effect of varying the infall mass, in the range defined by $\log(M_{\text{infall}}/M_{\odot}) = 9.75\text{-}11.0$. The common evolution of all the galaxies before

the onset of the galactic wind stems from the fact that all these models assume a fixed SFE ($\nu = 1.5 \text{ Gyr}^{-1}$). The models developing the galactic wind first are the ones with the smallest infall mass, which depart from the common track at the lowest (O/H) abundances; in fact, such models are characterized by a lower galaxy potential well, and hence they develop the outflow at earlier times. Overall the infall mass in our models does not play a key role in defining the shape of the (N/O) vs (O/H) relation.

The infall timescale

The infall time-scale regulates the rate of accretion of the gas into the system. In particular, by fixing the values of the other parameters, models with longer infall time-scales predict the galactic wind to develop at earlier times, since the binding energy of the gas to the whole galaxy is lower, at any time of the galaxy evolution. This can be appreciated by looking at Fig. 7.4b), where models assuming different infall time-scales are compared. Before the onset of the galactic wind, all the models evolve on the same track in the (N/O) vs. (O/H) diagram because the SFE is kept fixed.

The star formation efficiency

The SFE (ν) is a key parameter in driving the star formation history of the system and has a complex effect on the balance of the different stellar populations that contribute to the nitrogen and oxygen abundance in galaxies. Increasing the SFE speeds up the production of oxygen per unit time by massive stars in the earliest stages of the galaxy chemical evolution. Since we assume that nitrogen is synthesized by massive stars as a pure primary element, the increasing of the SFE does not affect much the (N/O) ratio in the low metallicity regime.

In Fig. 7.4c), we explore the effect of varying the SFE in the range $\nu = 0.5 - 3 \text{ Gyr}^{-1}$. The first large effect in the (N/O) vs (O/H) diagram can be seen at the first break point; in particular, the higher the SFE, the larger is the metal content within the galaxy as first LIMS die, causing the (N/O) ratios to increase. In conclusion, an increase of the SFE determines a wider range in metallicity of the initial (N/O) plateau due to the chemical enrichment of massive stars. This is a sort of application of the ‘time-delay model’ (Tinsley, 1979; Greggio & Renzini, 1983; Matteucci & Greggio, 1986) to the (N/O) vs. (O/H) diagram. We remind the reader that by *time-delay model* we mean the classical way of interpreting the trend of the observed $[\alpha/\text{Fe}]$ vs. $[\text{Fe}/\text{H}]$ abundance patterns in galaxies, where key roles are played by the assumed SFE and the delayed chemical enrichment by Type Ia SNe; in particular, the higher the SFE in galaxies, the larger is the $[\text{Fe}/\text{H}]$ abundance of the ISM as first Type Ia SNe explode and hence the $[\alpha/\text{Fe}]$ ratios steeply decrease.

In Fig. 7.5a), we show the relations between the age of the galaxy and the metallicity of the ISM, as predicted by our models with varying SFEs. Galaxies with very low SFEs struggle to reach high (O/H) abundances, spending most of their evolutionary time at low metallicities. Conversely, models with higher SFEs

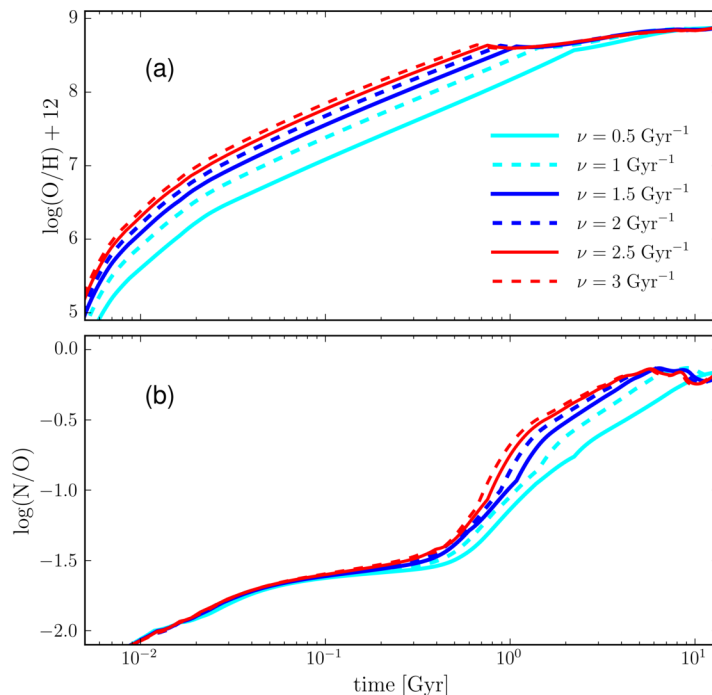


Figure 7.5: In this figure, in panel a) and b), we show how the (O/H) abundances and the (N/O) ratios, respectively, are predicted to vary as functions of the galaxy time. The various curves correspond to models with different star formation efficiency, with the reference model being the blue solid line.

predict galaxies to reach the (O/H) abundances of the SDSS data at earlier times. Once the galactic wind develops, there is an interplay between the rate of restitution of oxygen into the galaxy ISM by dying stars and the rate of removal of oxygen by galactic wind and star formation; this causes the (O/H) abundances to increase more gradually with time than before the onset of the galactic wind.

In Fig. 7.5b), we show how the predicted (N/O) ratios vary as a function of the time, when varying the SFE. In the earliest stages of the galaxy evolution, all the models tend towards $\log(\text{N}/\text{O}) \sim -1.6$ dex, which corresponds to the nitrogen-to-oxygen ratio of the low metallicity plateau. As first LIMS die, the (N/O) ratio is predicted to suddenly increase, because of the large amounts of both primary and secondary N which LIMS are capable of synthesize. In summary, the higher the SFE, the earlier and the higher are the metallicities (as discussed above) when LIMS start dying, causing the (N/O) ratio to increase. The effect of the onset of the galactic wind is less visible in this figure, and it corresponds to the gradual change in the slope of the (N/O) vs. time relation occurring at later times.

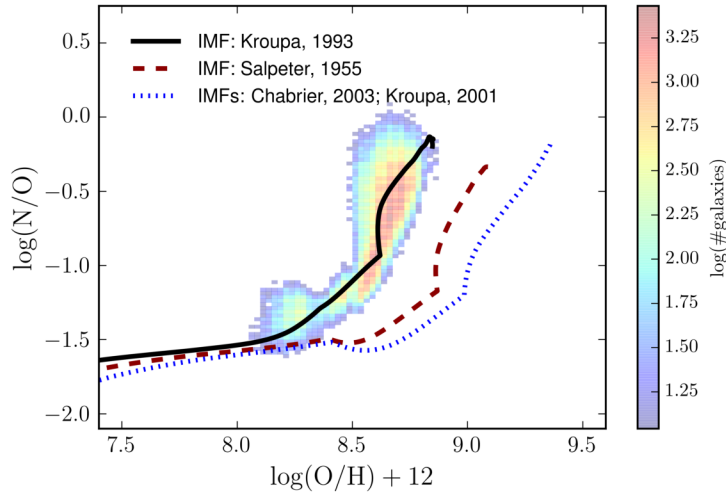


Figure 7.6: In this figure, we explore the effect of changing the IMF on the predicted (N/O) vs. (O/H) diagram. The black solid curve corresponds to our reference model with the [Kroupa et al. \(1993\)](#) IMF, the dashed curve in dark red to the [Salpeter \(1955\)](#) IMF, and the dotted curve in blue to the [Chabrier \(2003\)](#) and [Kroupa \(2001\)](#) IMFs, which provide very similar final results.

The outflow loading factor

Our reference model assumes a differential outflow, which carries only the nucleosynthetic products of core-collapse SNe (mainly α -elements) out of the galaxy potential well. Hence the mass loading factor, ω , quoted in the reference model only refers to oxygen, since nitrogen is assumed not to be expelled. Obviously, in reality, some nitrogen would be lost to the IGM, but here we consider its mass loading factor to be much lower than the one of oxygen, since core-collapse SNe are minor contributors of N in galaxies and the galactic wind (mainly triggered by SN explosions) develops when LIMS have already heavily polluted the ISM with nitrogen, overcoming the N enrichment from massive stars.

In Fig. 7.4d), we show the effect of almost doubling the mass loading factor on the (N/O) vs. (O/H) abundance pattern. By definition this parameter only has an effect after the galactic wind has started; this occurs at $12 + \log(\text{O}/\text{H}) \sim 8.6$ dex in our reference model. The requirement of a differential outflow to reproduce the observed trend of the (N/O) vs. (O/H) abundance pattern can be appreciated by comparing the solid and dashed curves in Fig. 7.4d), corresponding to models with differential and non-differential outflow, respectively. Concerning the model with a differential outflow, ω has the clear effect of changing the slope of the (N/O) vs. (O/H) relation at high metallicity. Importantly, even in the case of the reference model, this slope is much steeper than unity, which is the naive prediction for the secondary nitrogen enrichment. By looking at Eq. 7.2, the slope is crucially determined by the balance between the loss of oxygen via galactic winds (and star formation) and the restitution of oxygen by massive stars. If the latter exceeds the

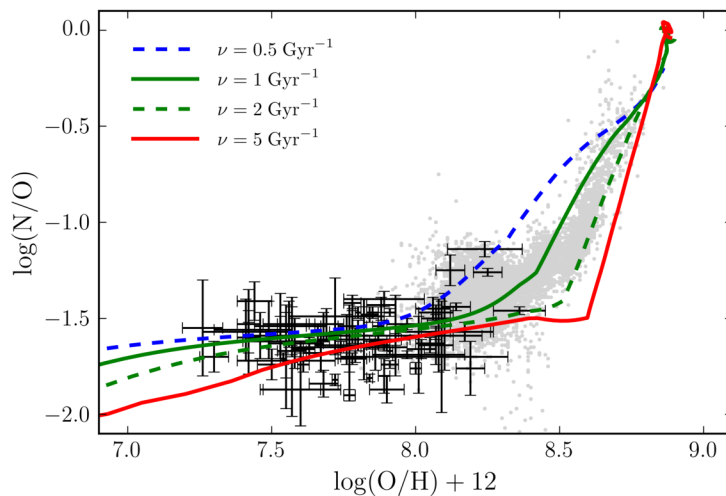


Figure 7.7: In this figure, we show chemical evolution models for dwarf galaxies. We assume $M_{\text{inf}} = 10^9 M_{\odot}$, varying SFEs, an infall timescale $\tau_{\text{inf}} = 0.1$ Gyr and the IMF of [Kroupa et al. \(1993\)](#). The grey points correspond to the SDSS galaxies with $M_{\star} \leq 10^9 M_{\odot}$, in the same range of stellar mass as the metal-poor, star forming dwarf galaxies from [Berg et al. \(2012\)](#); [Izotov et al. \(2012\)](#); [James et al. \(2015\)](#), which are represented by the data with error bars.

former, the slope is positive, otherwise it is negative. Concerning the model with a non-differential outflow, the transition between the SF-dominated regime and the outflow-dominated regime is smooth, since both oxygen and nitrogen are lost from the galaxy potential well with the same efficiency ω .

The IMF

In Fig. 7.6, we explore the effect of changing the IMF on the (N/O) vs. (O/H) abundance diagram. Our reference IMF, which is [Kroupa et al. \(1993\)](#), the best IMF for the MW disk; see [Romano et al. 2010](#)), hosts a large number of LIMS and a much smaller number of massive stars than the [Salpeter \(1955\)](#) IMF, and it provides the best agreement with the observed dataset among the classical IMFs considered in this work. IMFs like [Chabrier \(2003\)](#) and [Kroupa \(2001\)](#), which are very similar among each other, host a larger number of massive stars and hence an enhanced oxygen-production is predicted at the early stages of galaxy evolution; so the first break point occurs at higher metallicities when the [Chabrier \(2003\)](#) or the [Kroupa \(2001\)](#) IMF are assumed. The main effect of the IMF is to shift the chemical evolution tracks along the (O/H) axis. In fact, the main role of the IMF is to assign different weights to stars in different mass ranges.

7.6 Modelling the low metallicity tail

In this subsection, we present chemical evolution models for star forming, metal-poor dwarf galaxies, in order to reproduce the observed low metallicity tail of the (N/O) ratios. The data of [Berg et al. \(2012\)](#); [Izotov et al. \(2012\)](#); [James et al. \(2015\)](#) clearly exhibit a plateau in the (N/O) ratios, which extends towards low (O/H) abundances. None of the models developed in the past has been capable of reproducing this trend (see [Chiappini et al. 2005](#)).

In [Fig. 7.7](#), we show the predictions of models with $M_{\text{inf}} = 10^9 M_{\odot}$, $\tau_{\text{inf}} = 0.1$ Gyr and SFEs in the range $\nu = 0.05 - 5 \text{ Gyr}^{-1}$, with the purpose of reproducing the trend of the (N/O) vs. (O/H) abundances which are observed in metal-poor star forming dwarf galaxies (data with error bars) and in the SDSS galaxies with stellar mass $M_{\star} \leq 10^9 M_{\odot}$. The other parameters are the reference ones, as described at the beginning of [Section 7.5](#). In these models, we assume that massive stars produce pure primary N; our stellar yields for N are summarized in [Table 7.1](#), and they have been computed as a function of the metallicity, starting from the observational constraint that metal-poor dwarf galaxies share a common nitrogen-to-oxygen ratio which is $\log(\text{N/O}) \approx -1.6$ dex.

The trend of the various models in [Fig. 7.7](#) can be explained by means of the same mechanism which has been mentioned throughout all the text: very low SFEs cause a slow production of oxygen by massive stars; this fact allows the ISM to be quite metal-poor when LIMS begin to highly pollute the ISM with nitrogen. Therefore, lowering the SFEs causes the plateau of the (N/O) ratios to be less extended in metallicity and hence the first break to occur at lower Z . This explanation is a sort of application of the time-delay model to the (N/O) vs. (O/H) diagram. By comparing models and data, we can obtain a good qualitative agreement, clearly suggesting that a pure primary N production by massive stars is needed to explain and reproduce the low-metallicity plateau.

By assuming the N stellar yields of massive stars collected by [Romano et al. \(2010\)](#), which include the results of the stellar evolutionary code of the Geneva group taking into account the effects of mass loss and rotation, all our chemical evolution models predict a dip in the (N/O) ratios when going towards low (O/H) abundances (see also [Table 7.1](#)), at variance with observations.

This can be appreciated by looking at [Fig. 7.8](#), where the predictions of a model with pure primary N production by massive stars is compared with a similar model assuming the Geneva stellar yields for massive stars, as given in [Romano et al. \(2010, their model 15\)](#). Both models assume $\nu = 1.5 \text{ Gyr}^{-1}$, $M_{\text{inf}} = 10^9 M_{\odot}$ and $\tau_{\text{inf}} = 0.1$ Gyr. [Fig. 7.8](#) clearly points out the still open problem of standard stellar nucleosynthesis calculations as well as of stellar evolutionary models to predict the right amount of pure primary N which massive stars should provide to reproduce the observed (N/O) plateau at very low metallicity.

7.7 Conclusions

In this Chapter, we have presented a set of chemical evolution models with the purpose of reproducing the (N/O) vs. (O/H) abundance pattern, as observed in a sample of SDSS galaxies (Abazajian et al., 2009) and metal-poor, star forming dwarf galaxies (Izotov et al., 2012; Berg et al., 2012; James et al., 2015). Our collection of data spans a wide metallicity range ($7.1 \text{ dex} \lesssim \log(\text{O}/\text{H}) + 12 \lesssim 8.9 \text{ dex}$), enabling us to recover the trend of the observed (N/O) vs. (O/H) relation with a precision never reached before. At very low metallicity, the data clearly demonstrate the existence of a plateau in the (N/O) ratio, followed by an increase of this ratio which steepens as the metallicity increases. We summarize our main conclusions in what follows.

- The low metallicity plateau in the nitrogen-to-oxygen ratio represents the imprint of pure primary N from massive stars, as originally suggested by Matteucci (1986). Such plateau is also observed all over the metallicity range of MW halo stars and in low metallicity DLAs. From a theoretical point of view, standard nucleosynthesis calculations have shown that the rotational mixing in very-metal poor massive stars can allow a pure primary N production (see Maeder & Meynet 2000, and subsequent papers from the Geneva group); nevertheless, as the metallicity becomes $Z > 10^{-8}$, massive stars resume producing only secondary N. This still represents an open problem in stellar nucleosynthesis calculations, since all the chemical evolution models with the current stellar yields of massive stars, including standard mass loss and rotation, predict a “dip” in the (N/O) ratios for $Z > 10^{-8}$, at variance with observations (see, for example, Chiappini et al. 2005; Romano et al. 2010).
- We have computed the primary N stellar yields of massive stars which are needed, as functions of the metallicity, to reproduce the observational constraint suggesting that $\log(\text{N}/\text{O}) \approx -1.6 \text{ dex}$ in metal-poor, star forming dwarf galaxies. Our results are given in the last column of Table 7.1. In this way, we have been able to reproduce the observed flat trend of the data.
- A fundamental aspect to take into account for explaining the trend of the observed (N/O) vs. (O/H) abundance pattern is the time-delay with which LIMS start enriching the ISM with both primary and secondary N. In fact, before the first LIMS die, massive stars are the only nitrogen and oxygen producers in galaxies. When LIMS start dying, the N abundance within the galaxy ISM steeply increases. Since the stellar yields of the secondary N component by LIMS increase with metallicity, then the (N/O) ratios continuously grow as a function of the (O/H) abundance.
- The range in metallicity of the initial (N/O) plateau in the (N/O) vs. (O/H) abundance diagram is determined by the SFE; in particular, the higher the SFE, the larger is the extension in metallicity of the plateau. In fact, the SFE is the main parameter driving the rate of metal production from massive stars, hence regulating the metallicity of the system when LIMS begin to

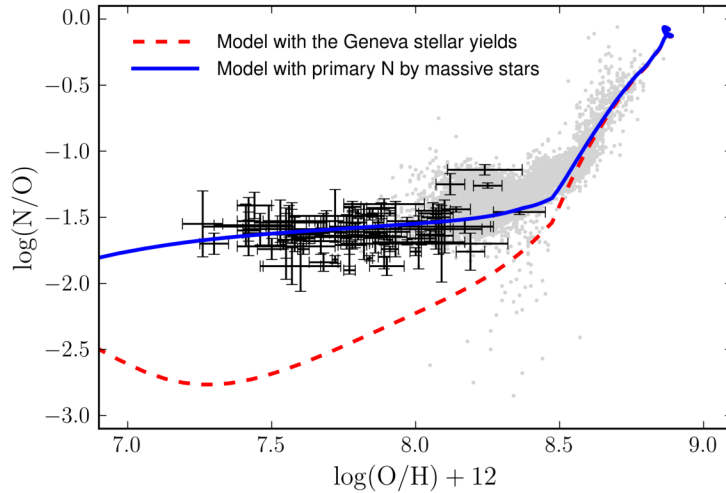


Figure 7.8: In this figure, we compare the predictions of a model with pure primary N production by massive stars with a similar model assuming the Geneva stellar yields for massive stars, as given in Romano et al. (2010, their model 15). Both models assume $\nu = 1.5 \text{ Gyr}^{-1}$, $M_{\text{inf}} = 10^9 M_{\odot}$ and $\tau_{\text{inf}} = 0.1 \text{ Gyr}$. The data are same as in Fig. 7.7.

heavily pollute the ISM with nitrogen. Therefore, if the SFE is high, the change in slope of the (N/O) ratio occurs at higher metallicity than in the case with low SFE. This is a consequence of the so-called time-delay model on the (N/O) vs. (O/H) diagram. In conclusion, the position of the galaxies along the observed (N/O) vs. (O/H) sequence is mostly determined by the SFE.

- Only by assuming differential galactic winds, removing exclusively chemical elements produced in core-collapse SNe, we have been able to reproduce the steep increasing trend of (N/O) ratios at high metallicity. Nevertheless, the larger amounts of secondary N provided by LIMS as the metallicity increases is necessary to reach the high observed (N/O) ratios at high metallicity. In our reference model, we have assumed a mass loading factor of the order of the unity; the variation of this parameter crucially determines the slope with which the (N/O) ratios are observed to increase at high metallicity. On the other hand, all our models with normal galactic wind – in which all the chemical elements are carried out of the galaxy potential well with the same efficiency – fail in explaining the observed trend of the (N/O) vs. (O/H) abundance pattern.
- The role of the IMF consists in giving different weights to stars as functions of their mass, when the star formation process takes place. If the IMF is rich in massive stars, then an enhanced O production is predicted (see also Vincenzo et al. 2016), letting the (N/O) ratios start to increase at high (O/H) abundances. So the main effect of the IMF is to shift the (N/O) vs. (O/H) relations over the (O/H) axis. Our chemical evolution models with

the [Kroupa et al. \(1993\)](#) IMF provide the best agreement with the observed dataset.

References

- Abazajian K. N., Adelman-McCarthy J. K., Agüeros M. A., et al., 2009, *ApJ*, 182, 543
Aihara H., Allende Prieto C., An D., et al., 2011, *ApJ*, 193, 29
Alloin D., Collin-Souffrin S., Joly M., Vigroux L., 1979, *A&A*, 78, 200
Andrews B. H., Martini P., 2013, *ApJ*, 765, 140
Arimoto N., Yoshii Y., 1987, *A&A*, 173, 23
Baldwin J. A., Phillips M. M., Terlevich R., 1981, *PASP*, 93, 5
Belfiore F., Maiolino R., Bundy K., et al., 2015, *MNRAS*, 449, 867
Belfiore F., Maiolino R., Bothwell M., 2016, *MNRAS*, 455, 1218
Berg D. A., Skillman E. D., Marble A. R., et al., 2012, *ApJ*, 754, 98
Bernardi M., Sheth R. K., Annis J., et al., 2003, *AJ*, 125, 1882
Bertin G., Saglia R. P., Stiavelli M., 1992, *ApJ*, 384, 423
Blanc G. A., Kewley L., Vogt F. P. A., Dopita M. A., 2015, *ApJ*, 798, 99
Bolatto A. D., Warren S. R., Leroy A. K., et al., 2013, *Nature*, 499, 450
Boselli A., Gavazzi G., 2014, *A&AR*, 22, 74
Bothwell M. S., Maiolino R., Kennicutt R., et al., 2013, *MNRAS*, 433, 1425
Bradamante F., Matteucci F., D’Ercole A., 1998, *A&A*, 337, 338
Brinchmann J., Charlot S., White S. D. M., et al., 2004, *MNRAS*, 351, 1151
Calura F., Pipino A., Matteucci F., 2008, *A&A*, 479, 669
Calura F., Gilli R., Vignali C., et al., 2014, *MNRAS*, 438, 2765
Calzetti D., 2001, *PASP*, 113, 1449
Cardelli J. A., Clayton G. C., Mathis J. S., 1989, *ApJ*, 345, 245
Caselli P., Walmsley C. M., Zucconi A., et al., 2002, *ApJ*, 565, 344
Chabrier G., 2003, *PASP*, 115, 763
Charlot S., Fall S. M., 2000, *ApJ*, 539, 718
Chiappini C., Romano D., Matteucci F., 2003, *MNRAS*, 339, 63
Chiappini C., Matteucci F., Ballero S. K., 2005, *A&A*, 437, 429
Chiappini C., Ekström S., Meynet G., et al., 2008, *A&A*, 479, L9
Cicone C., Maiolino R., Sturm E., et al., 2014, *A&A*, 562, A21
Cicone C., Maiolino R., Gallerani S., et al., 2015, *A&A*, 574, A14
da Cunha E., Eminian C., Charlot S., Blaizot J., 2010, *MNRAS*, 403, 1894
Davé R., Finlator K., Oppenheimer B. D., 2012, *MNRAS*, 421, 98
de Blok W. J. G., Keating K. M., Pisano D. J., et al., 2014, *A&A*, 569, A68
Dekel A., Zolotov A., Tweed D., et al., 2013, *MNRAS*, 435, 999
Driver S. P., Hill D. T., Kelvin L. S., et al., 2011, *MNRAS*, 413, 971
Dwek E., 1998, *ApJ*, 501, 643
Dwek E., Cherchneff I., 2011, *ApJ*, 727, 63
Edmunds M. G., Pagel B. E. J., 1978, *MNRAS*, 185, 77P
Edmunds M. G., 2001, *MNRAS*, 328, 223
Ekström S., Meynet G., Chiappini C., Hirschi R., Maeder A., 2008, *A&A*, 489, 685
Erb D. K., 2008, *ApJ*, 674, 151
Erb D. K., 2015, *Nature*, 523, 169
Fabian A. C., 2012, *ARA&A*, 50, 455
Faucher-Giguère C.-A., Kereš D., Ma C.-P., 2011, *MNRAS*, 417, 2982
Feldmann R., 2015, *MNRAS*, 449, 3274

- Finlator K., Davé R., 2008, *MNRAS*, 385, 2181
- Fisher D. B., Bolatto A. D., Herrera-Camus R., et al., 2014, *Nature*, 505, 186
- Fraternali F., van Moorsel G., Sancisi R., Oosterloo T., 2002, *AJ*, 123, 3124
- Fraternali F., Binney J. J., 2008, *MNRAS*, 386, 935
- Fraternali F., Marasco A., Armillotta L., Marinacci F., 2015, *MNRAS*, 447, L70
- Gavilán M., Buell J. F., Mollá M., 2005, *A&A*, 432, 861
- Gavilán M., Mollá M., Buell J. F., 2006, *A&A*, 450, 509
- Geach J. E., Hickox R. C., Diamond-Stanic A. M., et al., 2014, *Nature*, 516, 68
- Gentile G., Józsa G. I. G., Serra P., et al., 2013, *A&A*, 554, A125
- Gibson B. K., 1994, *J. R. Astron. Soc. Can.*, 88, 383
- Gibson B. K. 1994, *MNRAS*, 271, L35
- Greggio L., Renzini A., 1983, *Mem. Soc. Astron. Ital.*, 54, 311
- Heald G., Józsa G., Serra P., et al., 2011, *A&A*, 526, A118
- Henry R. B. C., Edmunds M. G., Köppen J., 2000, *ApJ*, 541, 660
- Hopkins P. F., Quataert E., Murray N., 2012, *MNRAS*, 421, 3522
- Hirschi R., Meynet G., Maeder A., 2005, *A&A*, 433, 1013
- Hirschi R., 2007, *A&A*, 461, 571
- Hjorth J., Gall C., Michałowski M. J., 2014, *ApJL*, 782, L23
- Hughes T. M., Cortese L., Boselli A., Gavazzi G., Davies J. I., 2013, *A&A*, 550, A115
- Izotov Y. I., Thuan T. X., Guseva N. G., 2012, *A&A*, 546, A122
- James B. L., Kuposov S., Stark D. P., et al., 2015, *MNRAS*, 448, 2687
- Jenkins E. B., 2009, *ApJ*, 700, 1299
- Jenkins E. B., 2014, preprint (arXiv:1402.4765)
- Karakas A. I., 2010, *MNRAS*, 403, 1413
- Kauffmann G., Heckman T. M., White S. D. M., et al., 2003, *MNRAS*, 341, 33
- Kewley L. J., Dopita M. A., Sutherland R. S., Heisler C. A., Trevena J. 2001, *ApJ*, 556, 121
- Kewley L. J., Ellison S. L., 2008, *ApJ*, 681, 1183
- Köppen J., Hensler G., 2005, *A&A*, 434, 531
- Kroupa P., Tout C. A., Gilmore G., 1993, *MNRAS*, 262, 545
- Kroupa P., 2001, *MNRAS*, 322, 231
- Lequeux J., Peimbert M., Rayo J. F., Serrano A., Torres-Peimbert S., 1979, *A&A*, 80, 155
- Lilly S. J., Le Brun V., Maier C., et al., 2009, *ApJS*, 184, 218
- Lilly S. J., Carollo C. M., Pipino A., Renzini A., Peng Y., 2013, *ApJ*, 772, 119
- Lisenfeld U., Ferrara A., 1998, *ApJ*, 496, 145
- López-Sánchez Á. R., Dopita M. A., Kewley L. J., et al., 2012, *MNRAS*, 426, 2630
- Lu Y., Blanc G. A., Benson A., 2015, *ApJ*, 808, 129
- Maeder A., Meynet G. 2000, *A&A*, 361, 159
- Maeder A., 2009, *Physics, Formation and Evolution of Rotating Stars*, Astronomy and Astrophysics Library. ISBN 978-3-540-76948-4. Springer Berlin Heidelberg, 2009
- Mannucci F., Cresci G., Maiolino R., Marconi A., Gnerucci A., 2010, *MNRAS*, 408, 2115
- Marconi G., Matteucci F., Tosi M., 1994, *MNRAS*, 270, 35
- Matteucci F., 1986, *MNRAS*, 221, 911
- Matteucci F., Greggio L., 1986, *A&A*, 154, 279
- Matteucci F., Brocato E., 1990, *ApJ*, 365, 539
- Matteucci F., 1992, *ApJ*, 397, 32
- Matteucci F., 1994, *A&A*, 288, 57
- Matteucci F., 2001, *Astrophysics and Space Science Library*, 253
- Matteucci F., Recchi S., 2001, *ApJ*, 558, 351

- Matteucci F., 2012, *Chemical Evolution of Galaxies: , Astronomy and Astrophysics Library*. ISBN 978-3-642-22490-4. Springer-Verlag Berlin Heidelberg, 2012,
- Mazzitelli I., 1989, *ApJ*, 340, 249
- Meynet G., Maeder A., 2002, *A&A*, 390, 561
- Meynet G., Maeder A., 2002, *A&A*, 381, L25
- Meyer D. M., Cardelli J. A., Sofia U. J., 1997, *ApJL*, 490, L103
- Mollá M., Vílchez J. M., Gavilán M., & Díaz A. I. 2006, *MNRAS*, 372, 1069
- O'Donnell J. E., 1994, *ApJ*, 422, 158
- Osterbrock D. E., Ferland G. J., 2006, *Astrophysics of gaseous nebulae and active galactic nuclei*, 2006, 2nd edn. University Science Books, Mill Valley, California
- Oosterloo T., Fraternali F., Sancisi R., 2007, *AJ*, 134, 1019
- Pasquali A., Gallazzi A., Fontanot F., et al., 2010, *MNRAS*, 407, 937
- Padovani P., Matteucci F., 1993, *ApJ*, 416, 26
- Pagel B. E. J., 2009, *Nucleosynthesis and Chemical Evolution of Galaxies*, Cambridge, UK, Cambridge University Press, 2009
- Peng Y.-j., Maiolino R., 2014, *MNRAS*, 443, 3643
- Peng Y., Maiolino R., Cochrane R., 2015, *Nature*, 521, 192
- Pérez-Montero E., Contini T., 2009, *MNRAS*, 398, 949
- Pérez-Montero E., Contini T., Lamareille F., et al., 2013, *A&A*, 549, A25
- Pérez-Montero E., 2014, *MNRAS*, 441, 2663
- Pettini M., Shapley A. E., Steidel C. C., et al., 2001, *ApJ*, 554, 981
- Pettini M., Ellison S. L., Bergeron J., Petitjean P., 2002, *A&A*, 391, 21
- Pettini M., Zych B. J., Steidel C. C., Chaffee F. H., 2008, *MNRAS*, 385, 2011
- Pilyugin L. S., 1993, *A&A*, 277, 42
- Pilyugin L. S., Vílchez J. M., Thuan T. X., 2010, *ApJ*, 720, 1738
- Pipino A., Matteucci F., 2004, *MNRAS*, 347, 968
- Pipino A., Calura F., & Matteucci F., 2013, *MNRAS*, 432, 2541
- Prochaska J. X., Wolfe A. M., 2009, *ApJ*, 696, 1543
- Putman M. E., Peek J. E. G., Jounge M. R., 2012, *ARA&A*, 50, 491
- Recchi S., Matteucci F., D'Ercole A., 2001, *MNRAS*, 322, 800
- Recchi S., Spitoni E., Matteucci F., Lanfranchi G. A., 2008, *A&A*, 489, 555
- Renzini A., Voli M., 1981, *A&A*, 94, 175
- Romano D., Karakas A. I., Tosi M., Matteucci F., 2010, *A&A*, 522, A32
- Sánchez S. F., Pérez E., Rosales-Ortega F. F., et al., 2015, *A&A*, 574, A47
- Saito M., 1979, *Publ. Astron. Soc. Japan*, 31, 181
- Salpeter E. E., 1955, *ApJ*, 121, 161
- Schmidt M., 1963, *ApJ*, 137, 758
- Talbot R. J., Jr., Arnett W. D., 1973, *ApJ*, 186, 51
- Thomas D., Maraston C., Bender R., Mendes de Oliveira C., 2005, *ApJ*, 621, 673
- Thomas D., Maraston C., Schawinski K., Sarzi M., Silk J., 2010, *MNRAS*, 404, 1775
- Tinsley B. M., 1979, *ApJ*, 229, 1046
- Tinsley, B. M. 1980, *Fundamentals of Cosmic Physics*, 5, 287
- Thuan T. X., Izotov Y. I., Lipovetsky V. A., 1995, *ApJ*, 445, 108
- Tremonti C. A., Heckman T. M., Kauffmann G., et al., 2004, *ApJ*, 613, 898
- van den Bergh S., 1962, *AJ*, 67, 486
- van den Hoek L. B., Groenewegen M. A. T., 1997, *A&AS*, 123, 305
- van de Voort F., Schaye J., Booth C. M., Haas M. R., Dalla Vecchia C., 2011, *MNRAS*, 414, 2458
- Veilleux S., Osterbrock D. E., 1987, *ApJ*, 63, 295
- Ventura P., Zeppieri A., Mazzitelli I., D'Antona F., 1998, *A&A*, 334, 953

- Ventura P., D'Antona F., 2009, *A&A*, 499, 835
- Ventura P., Di Criscienzo M., Carini R., D'Antona F., 2013, *MNRAS*, 431, 3642
- Vila-Costas M. B., Edmunds M. G., 1992, *MNRAS*, 259, 121
- Vincenzo F., Matteucci F., Belfiore F., Maiolino R., 2016, *MNRAS*, 455, 4183
- Vincenzo, F., Belfiore, F., Maiolino, R., Matteucci, F., & Ventura, P. 2016, *MNRAS*, 458, 3466
- Wang B., 1991, *ApJ*, 374, 456
- Whittet D. C. B., 2003, *Dust in the galactic environment* (2nd ed.; Institute of Physics Publishing: Bristol)
- Whittet D. C. B., 2010, *ApJ*, 710, 1009
- Woosley S. E., Weaver T. A., 1995, *ApJ*, 101, 181
- York D. G., Adelman J., Anderson J. E., Jr., et al., 2000, *AJ*, 120, 1579

8

Characterizing the local population of star-forming and passive galaxies with analytical models of chemical evolution

8.1 Introduction

In this Chapter, we present the results of the analytical chemical evolution model, which we have presented in Chapter 2.4; in particular, this model assumes a decaying exponential infall rate of gas as a function of time and, in Chapter 2.4, we have shown that analytical solutions for the evolution of the galaxy metallicity, gas mass and total mass can be found under this assumption. Here we apply this new analytical model to investigate and explain the observed mass-metallicity relation (MZ relation, hereafter), as derived in a sample of galaxies from the Sloan Digital Sky Survey (SDSS) by Peng et al. (2015).

We extend and update the methods and the results obtained by Spitoni et al. (2010), which reproduced the observed MZ relation in 27730 local SDSS star-forming galaxies (Kewley & Ellison, 2008) with an analytical model of chemical evolution. In particular, we aim at characterizing the two distinct MZ relations, which Peng et al. (2015) derived for the local actively star forming (we refer to them as *star-forming*) galaxies and the passively evolving (*passive*) ones. Such a tight relation between the stellar mass and the gas-phase metallicity, as displayed by a large sample of galaxies like the one provided by the SDSS, can be used to constrain the various fundamental parameters playing a role in any galaxy formation theory, such as the infall time scale, wind loading factor parameters, infall mass values, and the star formation efficiencies.

On the one hand, the analytical model of [Spitoni et al. \(2010\)](#) assumed both the gas outflow rate and the gas infall rate to be directly proportional to the galaxy SFR; when making this simplifying assumption, one can find that the analytical solution for the metallicity of the system does not explicitly depend upon the time variable, which indeed turns out to be hidden in the galaxy gas mass fraction entering in the equations (see also Chapter 2.3). Also [Kudritzki et al. \(2015\)](#) assumed constant ratios of galactic wind mass-loss and accretion mass gain to star formation rate (SFR) in the instantaneous recycling approximation (IRA); in particular, they investigated the radially averaged metallicity distribution of the interstellar medium of a sample of 20 local star-forming disc galaxies by means of analytical chemical evolution model.

On the other hand, in this work, the analytical solutions for the evolution of the galaxy metallicity explicitly depends upon the time variable; this fact will allow us to give also an estimate for the age of the galaxies and characterize them in terms of their infall time-scale.

[Mannucci et al. \(2010\)](#) added a further dimension to the observed MZ relation of local galaxies; in particular, they found that local galaxies place themselves on a tight surface in the 3D space defined by gas phase metallicity, star formation rate and stellar mass, with a small residual dispersion of about 0.05 dex and hence showing an underlying “fundamental” relation. In this work, we test whether our new analytical model is able to recover a similar fundamental relation for the local population of passive and star-forming galaxies.

This Chapter is organized as follows. In Section 8.2 we discuss the observed MZ relation in the population of local passive and star-forming galaxies by [Peng et al. \(2015\)](#) and present the method we employ to reproduce it. In Section 8.3, we summarize the analytical solutions for the galaxy metallicity, gas mass and total mass of our analytical chemical evolution model; in this Section, we present the methods used to reproduce the MZ relation. In Section 8.4 we report our results and, in Section 8.5, we discuss whether the population of galaxies drawn by our analytical model follow the fundamental relation of [Mannucci et al. \(2010\)](#). Finally, our conclusions are drawn in Section 8.6.

We remind the reader that all the results of this Chapter have been published in [Spitoni, Vincenzo & Matteucci \(2017\)](#).

8.2 The MZ relation of the SDSS sample of star-forming and passive galaxies

By analyzing a sample of local galaxies from SDSS data, [Peng et al. \(2015\)](#) were able to disentangle the local population of actively star-forming and gas-rich galaxies from the passive and gas-poor ones. In Fig. 8.1 we report the data by [Peng et al. \(2015\)](#), showing that these two populations of galaxies present distinct relations in the MZ plane, with the passive galaxies having on average larger stellar metallicities than the star-forming ones.

For a given stellar mass, there is a gap in metallicity between the two galaxy populations, which is observed to diminish as the stellar mass increases. At $M_{\star} \approx$

8.2. The MZ relation of the SDSS sample of star-forming and passive galaxies

Table 8.1: Principal characteristics of the computed “passive” and “star-forming” galaxies. In each column is indicated the range spanned by the values related of the infall time scale τ , the ages of the computed local galaxies, the wind parameter λ and the infall mass M_{inf} . Moreover, the range the values at which the 75% of galaxies are found is presented. Results are also indicated for two different IMFs: a [Chabrier \(2003\)](#) and [Salpeter \(1955\)](#).

Results: Properties of local star-forming and passive galaxies

		Salpeter (1955)				Chabrier (2003)			
		<i>Passive Galaxies</i>		<i>Star-Forming galaxies</i>		<i>Passive Galaxies</i>		<i>Star-Forming galaxies</i>	
		<i>Range</i>	<i>75%</i>	<i>Range</i>	<i>75%</i>	<i>Range</i>	<i>75%</i>	<i>Range</i>	<i>75%</i>
Infall time-scale	τ [Gyr]	0.07 – 4.8	≤ 1.8	0.07 – 7.8	≤ 6	0.07 – 4.2	≤ 2.4	0.07 – 7.8	≤ 6.6
Age	[Gyr]	1.8 – 13.1	≤ 9.6	0 – 4.8	≤ 2.4	0.6 – 13.1	≤ 10.2	0 – 3	≤ 1.8
Wind parameter	λ	0 – 1.5	≤ 0.9	0 – 5.8	≤ 2.25	0.6 – 3	≤ 2.2	0.6 – 10.2	≤ 5.3
Infall Mass	$\log(M_{\text{inf}}[M_{\odot}])$	9.5 – 11.5	≤ 10.5	10.1 – 11.5	≤ 11.43	10.2 – 11.8	≤ 10.9	10.8 – 12.5	≤ 12.05

$10^{11} M_{\odot}$ and beyond, star-forming and passive galaxies share almost the same average stellar metallicities. In Fig. 8.1 we also show the fits of the passive and star-forming sequences by means of third order polynomial functions that we will use in this paper.

In order to explain the observed MZ relation of the star-forming and passive galaxy populations in the SDSS data, [Peng et al. \(2015\)](#) suggested that galaxies ceased to accrete gas from the outside and kept forming stars only by exhausting the remaining available cold gas reservoir within their potential well. In this way, as soon as the galaxy is “strangulated” and stops accreting gas, the concentration of metals in the galaxy can steeply increase and similarly the metallicity of all the subsequent stellar generations. The average time needed for star-forming galaxies to reach the high metallicity stripe of passive galaxies in the MZ relation is predicted by [Peng et al. \(2015\)](#) to be of the order of ~ 4 Gyr.

Here we do not invoke any a priori “strangulation” scenario and aim at reproducing the two observed sequences of star-forming and passive galaxies by using our new analytical model with an “exponential” infall law and by varying the important parameters of galaxy evolution. In particular, we characterize the local SDSS galaxies in terms of their age, infall time-scale of formation, infall mass and wind parameter.

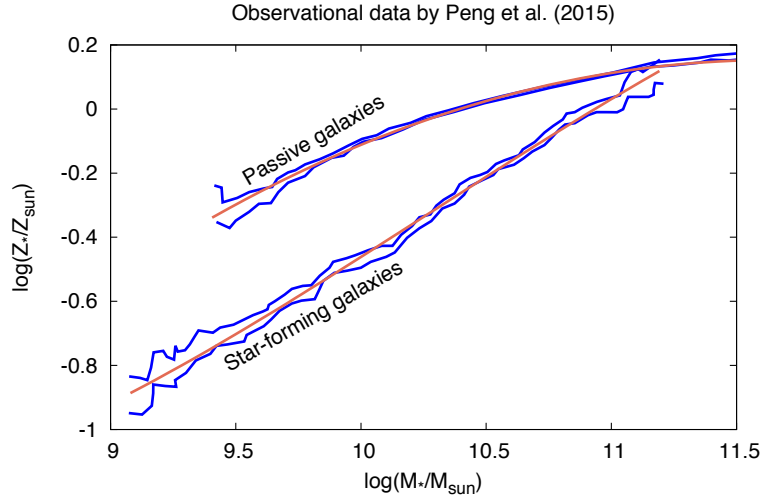


Figure 8.1: The observed uncertainties of the MZ relations for star-forming and passive galaxies by Peng et al. (2015) are reported with blue lines. We show with orange lines the third order polynomial fits for the passive and star-forming galaxies adopted in this work.

8.2.1 Summary of the analytical solutions

8.3 In this Section, we briefly summarize the analytical solutions for the system of differential equations, characterizing the chemical evolution of galaxies under the IRA approximation and the assumption of a decaying exponential infall of gas; this system of equations is the following one:

$$\begin{cases} \dot{M}_{\text{tot}}(t) = Ae^{-t/\tau} - \lambda\psi(t) \\ \dot{M}_{\text{gas}}(t) = -(1-R)\psi(t) + Ae^{-t/\tau} - \lambda\psi(t) \\ \dot{M}_Z(t) = (-Z(t) + y_z)(1-R)\psi(t) - \lambda Z(t)\psi(t) + Z_{\text{inf}}Ae^{-t/\tau} \end{cases} \quad (8.1)$$

where M_{tot} and M_{gas} are the total mass and gas mass of the galaxy, respectively; $Z = M_Z/M_{\text{gas}}$ represents the gas metallicity of the system and Z_{inf} the metallicity of the infalling gas. The total stellar mass of the system can be retrieved by means of the following formula: $M_{\star}(t) = M_{\text{tot}}(t) - M_{\text{gas}}(t)$.

We assume for equation (8.1) the following initial conditions:

- At $t = 0$, we assume $M_{\text{tot}}(0) = M_{\text{gas}}(0) \ll M_{\text{inf}}$. For the integration of equation (8.1), an initial gas mass different from zero is required; we consider it as negligible with respect to the infall mass.
- The metallicity of the gas infall is constant: $Z_{\text{inf}} = 0$;
- The metallicity of the galaxy is primordial at the formation of the galaxy: $Z(0) = Z_{\text{inf}} = 0$.

The solution for the gas mass is:

$$M_{\text{gas}}(t) = e^{-\alpha t} \left(\frac{A [e^{-t/\tau + \alpha t} - 1] \tau}{\alpha \tau - 1} + M_{\text{gas}}(0) \right); \quad (8.2)$$

the solution for the total galaxy mass ($M_{\text{gas}}(t) + M_{\star}(t)$) is given by the following formula:

$$\begin{aligned} M_{\text{tot}}(t) = & M_{\text{gas}}(0) \frac{S}{\alpha} (\lambda e^{-\alpha t} + 1 - R) + \\ & + \frac{S}{\alpha} (1 - R) A \tau - A \tau e^{-t/\tau} + \frac{S \lambda A \tau (\tau \alpha e^{-t/\tau} - e^{-\alpha t})}{\alpha (\alpha \tau - 1)}; \end{aligned}$$

finally, the solution for the galaxy gas-phase metallicity is:

$$\begin{aligned} Z(t) = & \frac{y_z S (1 - R)}{\alpha \tau - 1} \times \\ & \times \frac{M_{\text{gas}}(0) t (\alpha \tau - 1)^2 + A \tau [t - \tau (1 + \alpha t) + \tau e^{\alpha t - t/\tau}]}{A \tau (e^{\alpha t - t/\tau} - 1) + M_{\text{gas}}(0) (\alpha \tau - 1)}. \end{aligned}$$

In the previous equations, we have defined the parameter α as follows:

$$\alpha = (1 + \lambda - R) S, \quad (8.3)$$

where S is the star formation efficiency, with units Gyr^{-1} , R is the return mass fraction and λ is the mass loading factor. In our model, we assume that the SFR is directly proportional to the galaxy gas mass through the S parameter (linear Schmidt-Kennicutt law); finally, we assume that the outflow rate is proportional to the SFR through the λ parameter.

8.3 Methods

For the MZ relation, [Peng et al. \(2015\)](#) make use of the average stellar metallicity, $Z_{\star}(t)$; we recover this quantity from our models by averaging the gas metallicity of each galaxy in the following way:

$$\langle Z_{\star}(t) \rangle = \frac{\int_0^t dt' Z(t') \psi(t')}{\int_0^t dt' \psi(t')}, \quad (8.4)$$

where the metallicity of the various galaxy stellar populations is weighted with the total number of stars formed with that metallicity (the latter quantity is directly proportional to the SFR). This expression represents the so-called mass-weighted average metallicity of all the stellar populations ever born in the galaxy (see [Pagel 1997](#)).

8.3.1 Passive galaxies

In order to define a galaxy as “passive”, we adopt the following criterium introduced by [Fossati et al. \(2015\)](#), which takes into account the galaxy specific star formation rate (sSFR), i.e. the star formation rate per unit galaxy stellar mass:

$$\text{sSFR}_{\text{pass}} < \frac{b}{t_z}, \quad (8.5)$$

where b is the birthrate parameter $b = \text{SFR}/\langle \text{SFR} \rangle$ as defined by [Sandage \(1986\)](#), and t_z is the age of the Universe at redshift z . As done in [Fossati et al. \(2015\)](#), we assume the value proposed by [Franx et al. \(2008\)](#): $b = 0.3$.

Since the SDSS sample of galaxies considered by [Peng et al. \(2015\)](#) has an average redshift $\langle z \rangle = 0.05$, the passive galaxy population is characterized by $\text{sSFR}_{\text{pass}} < 2.29 \times 10^{-11} \text{yr}^{-1}$.

8.3.2 Star-Forming galaxies

For star-forming galaxies, we adopt the following scaling relation between μ_* and M_* found by [Boselli et al. \(2014\)](#) for a sample of the Herschel Reference Survey: SDSS galaxies:

$$\log(\mu_*) = -0.74 \log(M_*/M_\odot) + 7.03, \quad (8.6)$$

where μ_* is the ratio between M_{gas} and M_* : $\mu_* = M_{\text{gas}}/M_*$. Molecular gas masses are estimated from the H -band luminosity-dependent conversion factor of [Boselli et al. \(2002\)](#), while the galaxy stellar masses are derived from the galaxy i -band luminosities, by assuming a [Chabrier \(2003\)](#) IMF and using the $g - i$ color-dependent stellar mass-to-light ratio relation from [Zibetti et al. \(2009\)](#).

A further scaling relation found by [Boselli et al. \(2014\)](#) is the following one between the typical galaxy gas depletion time scale, τ_{gas} , and the galaxy stellar mass:

$$\log(\tau_{\text{gas}}) = -0.73 \log(M_*/M_\odot) + 16.75. \quad (8.7)$$

with $\tau_{\text{gas}} = M_{\text{gas}}/\text{SFR}$ is defined as the inverse of our SFE, namely $\tau_{\text{gas}} = 1/S$. From equation (8.7), galaxies with larger stellar mass would consume their available gas mass on shorter and shorter typical time scales if only star formation activity were taking place in the galaxy; this means that larger galaxies are expected to experience, on average, higher SFEs (see [Matteucci 2012](#)). In our work, we adopt equation (8.7) to constrain the galaxy SFE (which is kept fixed during the galaxy evolution), given an initial value for the galaxy infall mass, M_{inf} .

8.3.3 Summary of the free parameters and constraints

The free parameters entering in the analytical solutions of our chemical evolution model are the following:

- the infall time-scale τ ;
- the infall mass M_{inf} ;

- the wind parameter λ .

We create a set of chemical evolution models, by varying the aforementioned free parameters with a very fine resolution. The assumed infall time-scale τ spans the range between 0.1 and 8 Gyr, with a resolution of the grid values of $\Delta\tau=0.05$ Gyr. The wind parameter λ is defined between 0 and 10, with a resolution of $\Delta\lambda=0.5$. The infall masses are in the range between $10^{5.5}$ and $10^{12.5} M_{\odot}$.

The SFE is determined by means of equation (8.7), where M_{\star} is replaced with M_{inf} . Indeed, we cannot vary the SFE of the galaxy according to its stellar mass, since the system of equation (8.1) is solved by keeping constant the SFE.

The observational constraints that we assume to characterize the star-forming and passive populations of galaxies in the SDSS sample of Peng et al. (2015) are the following.

- Our models for passive and star-forming galaxies have average stellar metallicities defined such that $|\log(Z_{\star,\text{mod}}) - \log(Z_{\star,\text{obs}})| < 0.001$ dex, where $Z_{\star,\text{mod}}$ are computed with equation (8.4) and $Z_{\star,\text{obs}}$ are the stellar metallicities obtained with the fit reported in Fig 8.1 for the observed values by Peng et al. (2015).
- Our models for star-forming galaxies have $|\mu_{\star,\text{mod}} - \mu_{\star,\text{obs}}| < 0.001$, where $\mu_{\star,\text{obs}}$ are computed by means of equation (8.6).
- Our models for passive galaxies must have $\text{sSFR}_{\text{mod,passive}} < 2.29 \times 10^{-11} \text{ yr}^{-1}$, where sSFR_{mod} is the predicted specific SFR;
- Our models for star-forming galaxies must have $\text{sSFR}_{\text{mod,star-forming}} > 2.29 \times 10^{-11} \text{ yr}^{-1}$.

In this way, we are able to select and discriminate which chemical evolution model best represents the Peng et al. (2015) sample. We follow the chemical evolution of our entire galaxy sample with a fixed time resolution $\Delta t = 0.0065$ Gyr. There is not physical motivation behind our chosen time resolution; we remark on the fact that we are able to predict – at each time of the galaxy evolution – the galaxy stellar and gas mass and the metallicity of the galaxy ISM, thanks to our analytical solutions. Hence the time resolution simply determines how fine the evolution of the predicted galaxy properties is sampled with our analytical solutions. The ages of allstar-forming and passive galaxies are defined as the galactic time when all the observational constraints for a given population are fulfilled.

As stressed before, we study the case of primordial infall of gas (i.e. $Z_{\text{inf}} = 0$). Although Lehner et al. (2013) studying the circumgalactic medium of galaxies recently demonstrated the presence of metal enriched infalls, previous papers (Tosi 1988; Matteucci 2012) have already shown that an infall enriched with metallicity $Z \leq 0.4 Z_{\odot}$ does not produce differences in the evolution of the solar neighborhood. Moreover, assuming an infall with metallicity larger than $0.4 Z_{\odot}$ requires very specific situations. Recently, in Spitoni, Vincenzo & Matteucci (2017) we consider the effects of an enriched infall of gas with the same chemical abundances as the matter ejected and/or stripped from dwarf satellites of the Milky Way on the chemical evolution of the Galactic halo. We found that α -elements are only slightly affected by such an enriched infall of gas.

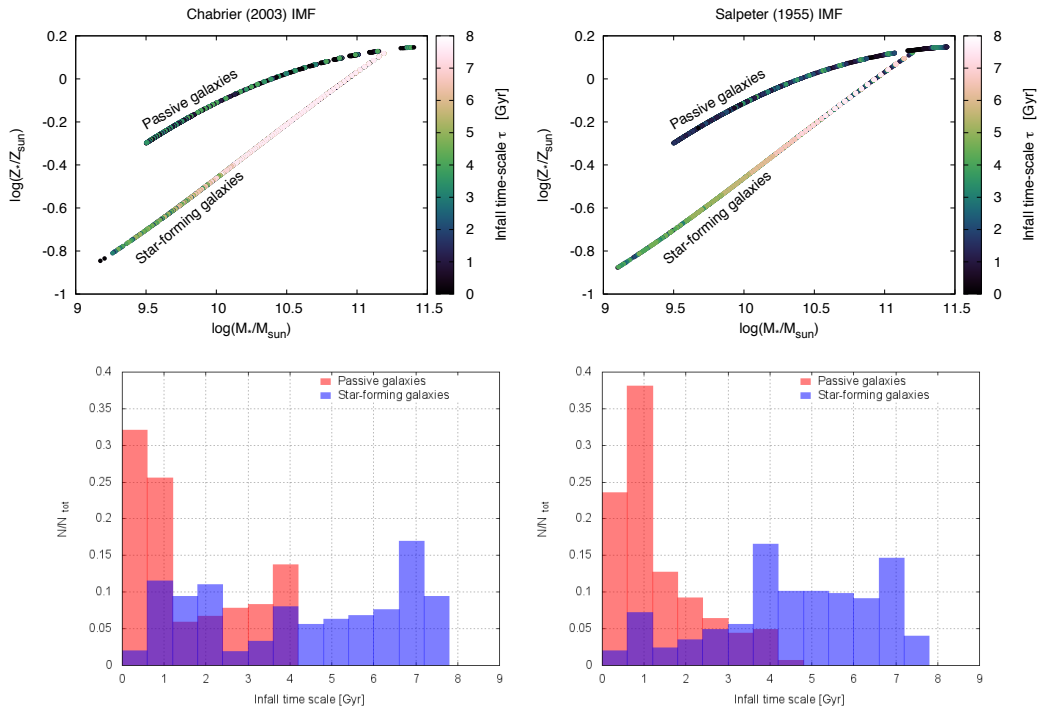


Figure 8.2: *Upper panels:* The MZ relation by Peng et al. (2015) (fitted by third order polynomial functions shown in Fig. 8.1) for passive and star forming galaxies. We reproduce it using the new analytical solution presented in this paper varying different parameter models. In this figure we focus on the time scale parameter τ , and the color code indicates different τ values of the computed galaxies which reside along the MZ relations. In the left panel we adopt a Chabrier (2003) IMF, whereas in the right one the Salpeter (1955) one. *Lower panels:* The distribution of the predicted passive galaxies (red histogram) and star-forming galaxies (blue histogram) which reproduced the MZ relation in terms of the time-scale parameter τ with a Chabrier (2003) IMF (left panel) and a Salpeter (1955) IMF (right panel).

8.4 Results

In this Section we present our results concerning the characterization of the local passive and star-forming galaxies of the SDSS sample of Peng et al. (2015), by making use of the new analytical solutions presented in Section 8.2.1 in presence of an exponential infall of gas. We remark on the fact that we select the best chemical evolution models characterizing the SDSS sample of Peng et al. (2015), by imposing the set of constraints presented in the previous Section 8.3.3 and by varying all the free parameters simultaneously.

In Table 8.1, we summarize the main results of our work. We report the range of values spanned by the main free parameters of our models in order to reproduce the observed MZ relation of the local star-forming and passive galaxies. For each parameter we also report the value within which 75 per cent of the galaxies are expected to reside. We show in the table our results for both the Salpeter (1955) and the Chabrier (2003) IMFs. A fundamental quantity which we can predict

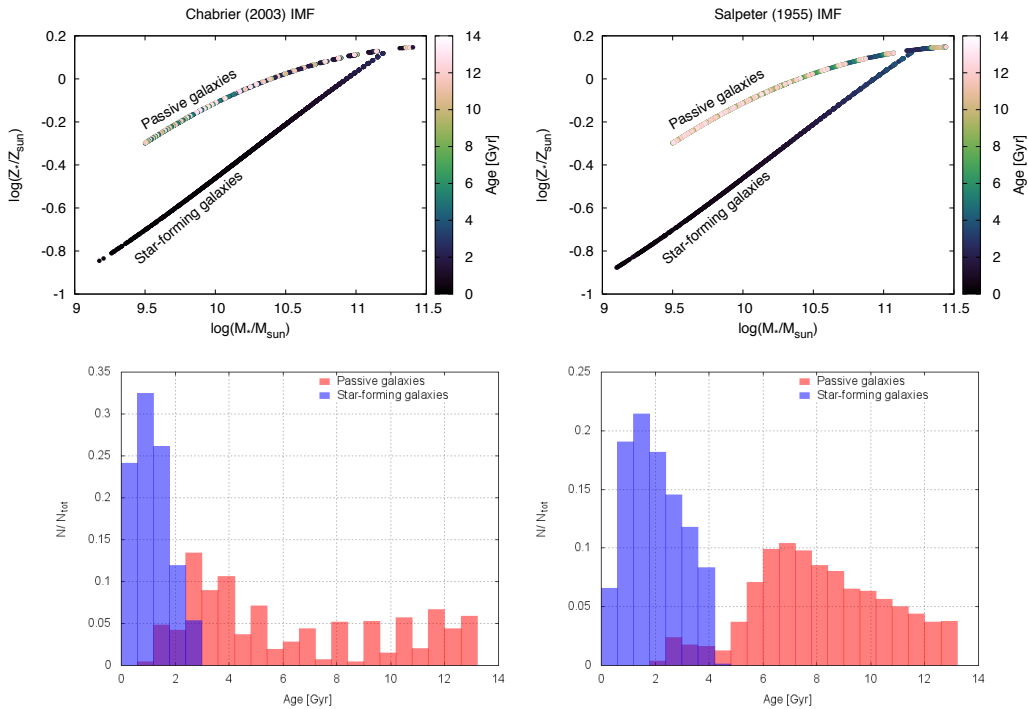


Figure 8.3: *Upper panels:* As in Fig. 8.2 but here, the color code indicates different ages of the galaxies which reproduce the MZ relations. *Lower panels:* The distribution of the predicted passive galaxies (red histogram) and star-forming galaxies (blue histogram) which reproduced the MZ relation in terms of the age of galaxies. In the left panel we adopt a Chabrier (2003) IMF, whereas in the right one the Salpeter (1955) one.

is the age distribution of the passive and star-forming galaxy SDSS population, corresponding to the second row in the table.

In this work we assume that galaxies can form at different times, and by age we mean the galaxy evolutionary time, namely the difference between the time corresponding to redshift $z = \langle 0.05 \rangle$ and the formation epoch.

In order to visualize better our results, in Figs. 8.2, 8.3, 8.4 and 8.5 we show how local star-forming and passive galaxies are expected to distribute in the MZ relation (upper panels) and in relative number (lower panels), for different values of the infall time scale, age, wind parameter and infall mass, respectively. In the lower panels of the Figures we indicate as N/N_{tot} , the ratio between the number of the computed star-forming (or passive) galaxies in the considered bins of infall time-scale, age, wind parameter and infall mass values over the total number of the computed star-forming (passive) galaxies. The plots on the left correspond to our results with a Chabrier (2003) IMF, while on the right we show our results with a Salpeter (1955) IMF.

By looking at Fig. 8.2, our models for the local passive galaxies are characterized by shorter typical formation time scales than the star-forming ones. This is mainly due to the requirement of very low sSFRs for these galaxies at the present time. Therefore, they had the time to consume or remove most of their total infall

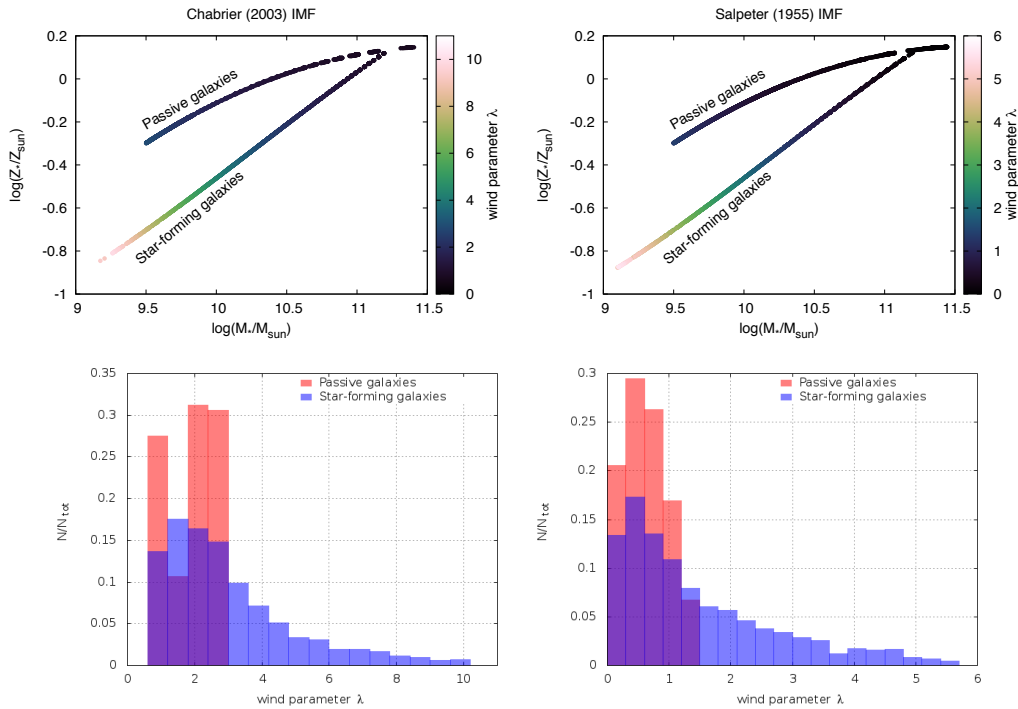


Figure 8.4: *Upper panels:* As in Fig. 8.2 but here, the color code indicates different wind parameter λ of the galaxies which reproduce the MZ relations. *Lower panels:* The distribution of the predicted passive galaxies (red histogram) and star-forming galaxies (blue histogram) which reproduced the MZ relation in terms of wind parameter λ of galaxies. In the left panel we adopt a Chabrier (2003) IMF, whereas in the right one the Salpeter (1955) one.

gas mass through the star formation activity or galactic wind. The short typical formation time scales also enhance the star formation activity and hence the metal production in the earliest epochs of the galaxy evolution. According to the predictions of our models, local passive galaxies are undergoing at the present time the declining, fading phase of their SFR evolution.

In our analytical model of chemical evolution, the IMF only enters in the calculation of the yield of metals per stellar generation and the returned mass fraction. Top-heavy IMFs determine larger yields of metals per stellar generation and hence a more effective chemical enrichment of the galaxy ISM, fixed all the other model parameters. Therefore, passive galaxies with a top-heavy IMF which reach their relatively high observed stellar metallicity –on average– are characterized by longer time-scales of formation (a SFR less intensive at early times). We find that, when assuming [Salpeter \(1955\)](#) IMF, the distribution of the formation time-scales of passive galaxies turns out to be narrower than when assuming a [Chabrier \(2003\)](#) IMF, which contains a larger number of massive stars. We find that almost 75 per cent of all passive galaxies are expected to assemble on $\tau \leq 1.8$ Gyr with a [Salpeter \(1955\)](#) IMF, while $\tau \leq 2.4$ Gyr with a [Chabrier \(2003\)](#) IMF (see also Table 8.1).

In Fig. 8.3, we show the results of our models for the age distribution of local galaxies. Our main result is that passive galaxies are – on average – much older

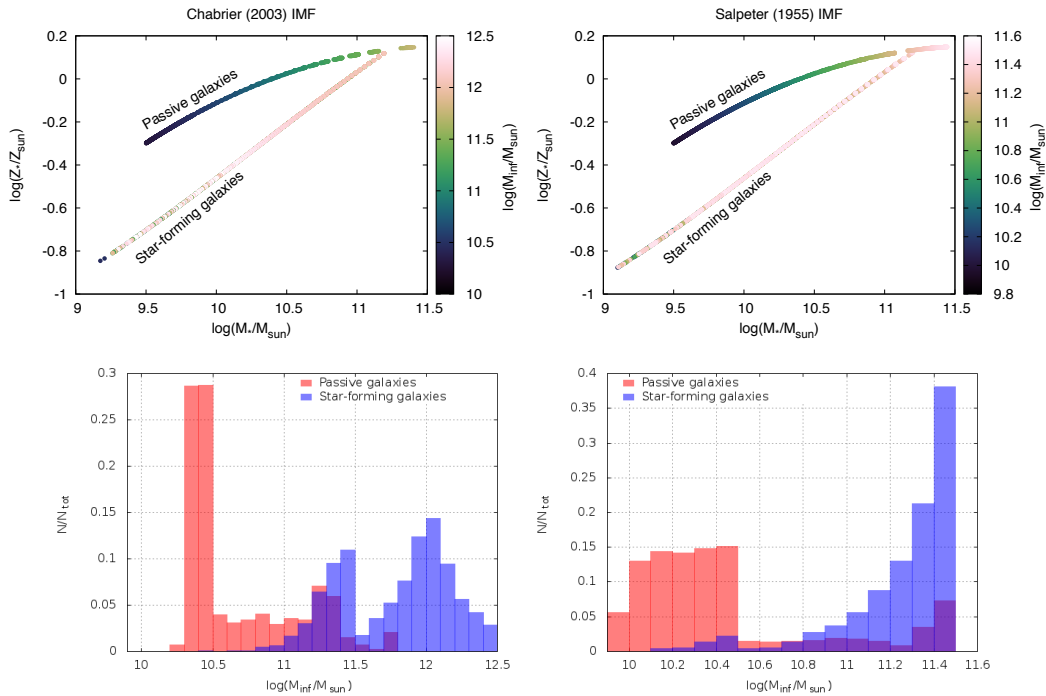


Figure 8.5: *Upper panels:* As in Fig. 8.2 but here, the color code indicates different infall mass M_{inf} of the galaxies which reproduce the MZ relations. *Lower panels:* The distribution of the predicted passive galaxies (red histogram) and star-forming galaxies (blue histogram) which reproduced the MZ relation in terms of infall mass M_{inf} of galaxies. In the left panel we adopt a Chabrier (2003) IMF, whereas in the right one the Salpeter (1955) one;

than the star-forming ones. In fact, as aforementioned, the passive galaxies need a longer evolution in order to exhaust their total reservoir of gas, and to be observed as quiescent objects at the present time.

In the case of star-forming galaxies the larger mass star-forming galaxies show generally older ages and longer typical formation time-scales compared with the smaller mass star-forming galaxies.

To reach their higher observed stellar metallicities with respect to the less massive ones, the more massive galaxies must be older. On the other hand, longer formation time scales can ensure more massive galaxies to be still observed as star forming at the present time, since large amounts of gas may be still available for star formation at later epochs.

Peng et al. (2015) were able to derive also luminosity-weighted stellar ages for their galaxy sample. Their main finding is that passive galaxies are – on average – about 4 Gyr older than the star-forming ones, with this difference remaining almost constant when considering different bins for the galaxy stellar mass.

Considering the difference between the median age values of our computed star-forming and passive galaxies we find that our results are in agreement with the data by Peng et al. (2015). Indeed, with the Chabrier (2003) IMF, we find that the median stellar ages for star-forming and passive galaxy are 0.9 Gyr and

5.1 Gyr, respectively; therefore the Δ age = 4.2 Gyr. We find a larger difference between the median ages adopting the [Salpeter \(1955\)](#) IMF, indeed in this case the median stellar ages for star-forming and passive galaxy are 2.1 Gyr and 7.5 Gyr, respectively; therefore Δ age = 5.4 Gyr.

Models of galaxies with a top-heavy IMF, because of the chemical enrichment driven by a larger number of massive stars, are expected to need less time to reach their relatively high observed stellar metallicity; in fact the minimum age we found for passive galaxies with the [Chabrier \(2003\)](#) IMF is 0.6 Gyr, much lower than the value we found using the [Salpeter \(1955\)](#) IMF (1.8 Gyr).

In Fig. 8.4, we present our results for the distribution of the wind parameter, λ , associated to our best models for the star-forming and passive galaxy populations of the SDSS sample of [Peng et al. \(2015\)](#). According to our results, the population of galaxies which suffer more prominent wind episodes is given by the star forming ones. In order to reproduce the observed average stellar metallicity of star-forming galaxies at smaller stellar mass, stronger winds are needed. On the other hand, the wind parameters, λ , is predicted to decrease when going towards star-forming galactic systems with larger stellar mass. In summary, the observed MZ relation can be well reproduced by assuming a variable mass loading factor, which increases when passing from more to less massive galactic systems. This conclusion has been discussed by several authors in the past (see, for example, [Spitoni et al. 2010](#), and references therein). This correlation between the mass loading factor, λ , and the galaxy stellar mass is also valid for passive galaxies, although the galactic winds for these systems is predicted to be much weaker than for the star-forming ones.

Also the IMF choice can affect the typical values of the wind parameter which best reproduce the observed MZ relation. Our best models for low mass and metal-poor star-forming galaxies with a [Salpeter \(1955\)](#) IMF require weaker galactic winds than similar models with a [Chabrier \(2003\)](#) IMF, which predict a faster and hence more effective chemical enrichment of the galaxy ISM. By looking at Table 8.1 and Fig. 8.4, the distribution of the wind parameters for star-forming galaxies with a [Salpeter \(1955\)](#) IMF span the range $0 \lesssim \lambda \lesssim 5.8$, and the 75 per cent of star-forming galaxies are expected to have $\lambda \lesssim 2.25$, while the models of star-forming galaxies with a [Chabrier \(2003\)](#) IMF span the range $0.6 \lesssim \lambda \lesssim 10.2$, and the 75 per cent of star-forming galaxies are expected to have $\lambda \lesssim 5.3$.

We remark on the fact that we are able to find models capable of fitting the data also when the galactic winds are included, at variance with the results of [Peng et al. \(2015\)](#), which had to suppress the galactic outflows from all their models to reproduce the observed MZ relation.

In Fig. 8.5, we show our results for the distribution of the infall mass of our best models for the local population of star-forming and passive galaxies. We find that passive galaxies are characterized by smaller infall masses than the star-forming ones. indeed, passive galaxies in the Local Universe must be characterized by very low sSFRs, which can be obtained – in the framework of our analytical model with an exponential infall of gas – by assuming small infall gas masses together with short typical time-scales (as we discussed above for the passive population). In this way, nearly most of the infall gas mass is converted into stars at the later epochs of the galaxy evolution. Typical values of the infall mass of our best models for

8.5. The predicted Fundamental Relation of the local star-forming and passive galaxies

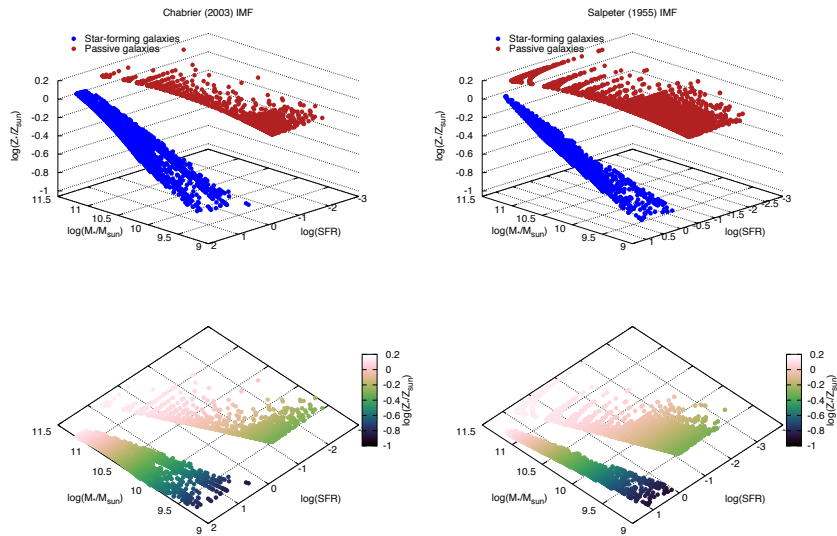


Figure 8.6: *Upper panels:* Simulated “passive” and “star-forming” galaxies which are able to reproduce the MZ relations of Peng et al. (2015) in the 3D plot to test a more general relation between stellar M_* , average stellar metallicity Z and the SFR using a Chabrier (2003) IMF (left panel) and a Salpeter one (right panel). *Lower panels:* The 2D projection in the M_* - SFR plane.

the passive and star-forming galaxies can be found in Table 8.1.

The results for the infall mass distribution of the local population of star-forming and passive galaxies are strongly affected by the adopted IMF. Indeed, larger infall masses are requested with a [Chabrier \(2003\)](#) IMF. We recall here that we are assuming a primordial infall of gas. Because a top-heavy IMF leads to a more efficient chemical enrichment than a [Salpeter \(1955\)](#) one, a larger dilution of metals and therefore larger infall masses are requested to obtain the observed MZ relation.

8.5 The predicted Fundamental Relation of the local star-forming and passive galaxies

In this Section, we analyze the correlations which local galaxies are predicted to show by our chemical evolution model in the 3D space defined by stellar mass, gas-phase metallicity and SFR. [Mannucci et al. \(2010\)](#) showed that local galaxies lie on a tight surface in such a space and named the resulting correlation as “fundamental relation” implying that it is valid at all redshifts.

Since we do not possess gas-phase metallicities for the passive galaxies in the sample of [Peng et al. \(2015\)](#), we use the average galaxy stellar metallicity instead of the gas-phase metallicity to study the MZ relation. Usually the gas metallicity turns out to be larger than the stellar one for evolved galactic systems. Our results are shown in Fig. 8.6, where we show that local star-forming and passive galaxies

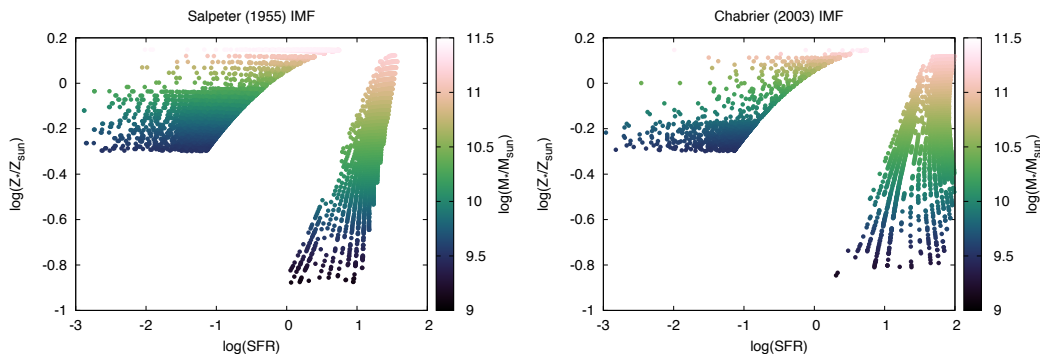


Figure 8.7: The stellar metallicity as a function of the star formation rate for the computed “star-forming” and “passive” galaxies. The color code indicates the stellar mass. In the *upper panel* model results with a Salpeter (1955) IMF are drawn in the *Lower panel* a Chabrier (2003) IMF is adopted.

lie on a tight surface when considering their stellar mass, M_* , mass-weighted stellar metallicity, $\langle Z_* \rangle$, and SFR. The projection of this 3D diagram onto the M_* - Z_* plane gives rise to the MZ relation discussed in the previous sections. By looking at the figure, the two populations of galaxies are separated by a discontinuity, which is due to the different metallicity distributions of star-forming and passive objects.

The discontinuity is also visible in Fig. 8.7, where we show the projection of the predicted “fundamental relation” onto the Z_* -SFR plane. In this figure, the color-coding corresponds to the galaxy stellar mass. The local galaxy populations are predicted to show a similar trend as the one presented by Mannucci et al. (2010, see the right panel of their figure 1), where higher stellar masses are found for galaxies with larger SFRs and metallicities.

8.6 Conclusions

We have developed a new analytical model of chemical evolution, in which an exponential infall of gas and galactic winds are assumed. We have applied this model to reproduce the observed MZ relation for local SDSS galaxies (Peng et al. 2015); in particular, we have characterized the populations of gas-rich and star forming and passive (gas-poor and quiescent) galaxies, by showing how their ages, formation time-scales, mass loading factors and infall masses must be related to each other. Finally, we have analyzed the “fundamental relation” for these local galaxies in the 3D space, defined by stellar mass, average stellar metallicity and SFR. Our main conclusions can be summarized as follows.

- We assume that all galaxies form by gas accretion with an exponential law. We find that passive galaxies are characterized by shorter typical time scales of formation and are older objects than the star-forming ones.
- Galactic winds in star-forming galaxies are found – on average – to be stronger than in passive galaxies. The intensity of the galactic winds de-

depends on the adopted IMF, with the larger values of the mass loading factor corresponding to top-heavy IMFs. This is a consequence of the fact that top-heavy IMFs lead to a more efficient metal enrichment of the galaxy ISM than bottom-heavy IMFs.

- The observed MZ relation of Peng et al. (2015) can be reproduced by our models without invoking any strangulation effects. This is due to the fact that the assumption of an exponential infall of gas, coupled also to galactic winds, naturally reduces the gas accretion after the assumed infall time scale, hence mimicking the effect of strangulation. Nevertheless, we conclude that strangulation is not the main physical mechanism driving the transition of galaxies towards the passive evolution.
- We have shown that our models for star-forming and passive galaxies imply that they obey to the so-called “fundamental relation” of Mannucci et al. (2010), which is a more general relation between stellar mass, metallicity and SFR. We remind the reader that the fundamental relation of Mannucci et al. (2010) adopts the gas-phase metallicity, but we find that it is still valid when adopting the average galaxy stellar metallicity (M_{\star} - SFR - Z_{\star}).

References

- Boissier, S., & Prantzos, N., 1999, MNRAS, 307, 857
 Boselli, A., Cortese, L., Boquien, M., et al., 2014, A&A, 564, A66
 Boselli, A., Lequeux, J., Gavazzi, G. 2002, A&A, 384, 33
 Brusadin G., Matteucci F., Romano D., 2013, A&A, 554, A135
 Chabrier, G., 2003, PASP, 115, 763
 Chiappini C., Matteucci F., Gratton R., 1997, ApJ, 477, 765
 Chiosi, C., 1980, A&A, 83, 206
 Clayton, D. D., 1988, MNRAS, 234, 1
 Clayton, D. D., Pantelaki, I., 1986, ApJ 307, 441
 Clayton, D. D., Pantelaki, I., 1993, PhR 227, 293)
 Colavitti, E., Matteucci, F., Murante, G., 2008, A&A, 483, 401
 Edmunds, M. G., 1990, MNRAS, 246, 678
 Edmunds M. G., Greenhow R. M., 1995, MNRAS, 272, 241
 Erb, D. K. 2008, ApJ, 674, 151-156
 Fossati, M., Wilman, D. J., Fontanot, F., et al., 2015, MNRAS, 446, 2582
 Franx M., van Dokkum P. G., Förster Schreiber N. M., et al., 2008, ApJ, 688, 770-788
 Hartwick F. D. A., 1976, ApJ, 209, 418
 Kewley, L. J., Ellison, S. L. 2008, ApJ, 681, 1183
 Kroupa, P., 2001, MNRAS, 322, 231
 Kudritzki, R.-P., Ho, I.-T., Schrubba, A., et al., 2015, MNRAS, 450, 342
 Lacey, C. G., Fall, M., 1985, ApJ, 290, 154
 Lanfranchi G. A., Matteucci F., Cescutti G., 2008, A&A, 481, 635
 Lehner, N., Howk, J. C., Tripp, T. M., et al., 2013, ApJ, 770, 138
 Mannucci, F., Cresci, G., Maiolino, R., Marconi, A., Gnerucci, A., 2010, MNRAS, 408, 2115
 Martinelli A., 1998, A&A, 335, 847
 Matteucci, F., Chiosi, C., 1983, A&A, 123, 121

Chapter 8. Characterizing the local population of star-forming and passive galaxies with analytical models of chemical evolution

- Matteucci, F. 2001, *The Chemical Evolution of the Galaxy*, ASSL, Kluwer Academic Publisher
- Matteucci F., 2012, *Chemical Evolution of Galaxies*. Springer-Verlag, Berlin
- Micali A., Matteucci F., Romano D., 2013, *MNRAS*, 436, 1648
- Pagel, B. E. J., Patchett, B. E. 1975, *MNRAS*, 172, 13
- Pagel B. E. J., 1997, in Bernard E. J. P., eds, *Nucleosynthesis and Chemical Evolution of Galaxies*, ISBN: 0521550610. Cambridge Univ. Press, Cambridge, p. 392
- Peng, Y., Maiolino, R., Cochrane, R., 2015, *Nature*, 521, 192
- Peng, Y., Maiolino, R., 2014, *MNRAS*, 443, 3643
- Pezzulli, G., Fraternali, F., 2015, *MNRAS*, 455, 2308
- Portinari, L., Chiosi, C. 2000, *A&A*, 355, 929
- Recchi, S., Kroupa, P, *MNRAS*, 2015, 446, 4168
- Recchi, S., Spitoni, E., Matteucci, F., Lanfranchi, G. A., 2008, *A&A*, 489, 555
- Recchi, S., & Hensler, G., 2013, *A&A*, 551, A41
- Romano D., Karakas A. I., Tosi M., Matteucci F., 2010, *A&A*, 522, A32
- Salpeter, E. E. 1955, *ApJ*, 121, 161
- Sandage A., 1986, *A&A*, 161, 89
- Schmidt, M. 1963, *ApJ*, 137, 758
- Schmidt, M. 1959, *ApJ*, 129, 243
- Searle, L., Sargent, W. L. W. 1972, *ApJ*, 173, 25
- Spergel, D. N., Bean, R., Dor, O., et al. 2007, *ApJS*, 170, 377
- Spitoni, E., 2015, *MNRAS*, 451, 1090
- Spitoni E., Calura F., Matteucci F., Recchi S., 2010, *A&A*, 514, A73
- Spitoni E., Matteucci F., 2011, *A&A*, 531, A72
- Spitoni, E., Vincenzo, F., Matteucci, F., Romano, D., 2016, *MNRAS*, 458, 2541
- Spitoni, E., Vincenzo, F., & Matteucci, F., 2017, *A&A*, 599, A6
- Springel, V., 2005, *MNRAS*, 364, 1105
- Tinsley B. M., 1974, *ApJ*, 192, 629
- Tinsley B. M., 1980, *Fundamentals of Cosmic Physics*, 5, 287
- Tosi, M., 1988, *A&A*, 197, 33
- Twarog B. A., 1980, *ApJ*, 242, 242
- Vincenzo, F., Matteucci, F., Belfiore, F., Maiolino, R., 2016, *MNRAS*, 455, 4183
- Vincenzo F., Matteucci F., Vattakunnel S., Lanfranchi G. A., 2014, *MNRAS*, 441, 2815
- Weinberg, D.H., Andrews, B.H., Freudenburg, J. 2016, arXiv:1604.07435
- Zibetti, S., Charlot, S., Rix, F. 2009, *MNRAS*, 400, 1181

Part IV

Concluding remarks

9

Conclusions and perspectives

In this Thesis, I have shown how chemical evolution models are currently used to study and investigate the main physical processes which determine the evolution of the chemical elements within the interstellar medium of galaxies of different morphological type through cosmic epochs. All my models start by assuming a galaxy gas mass assembly history, which typically follows a decaying exponential law with time, an initial mass function, and a set of stellar nucleosynthetic yields. Finally, my models take into account the stellar lifetimes and assume that galaxies are composed of a single zone within which all the chemical elements are well mixed at any time of the galaxy evolution. By making these assumptions, I have developed chemical evolution models to characterize the classical and ultra-faint dwarf spheroidal galaxies, satellites of the Milky Way, and to reproduce the oxygen and nitrogen abundances, as inferred in a sample of star forming galaxies in the Local Universe by the Sloan Digital Sky Survey.

I have shown what is the effect of varying the main assumptions in the models – namely, the gas infall history, the initial mass function, the set of stellar yields and the prescriptions for the star formation activity and galactic outflow – to explain the present-day physical and chemical properties of galaxies.

I have tried to give an answer to the following scientific questions, which have been triggered by observations:

- ***How did classical and ultra-faint dwarf spheroidal galaxies evolve, by looking at their present-day physical and chemical properties?***

The observed chemical abundance patterns – as well as the present-day stellar and gas mass, and the metallicity distribution function – require that the Milky Way dwarf spheroidal galaxy satellites evolved with low typical efficiencies of star formation and were characterized by strong galactic outflows, which were also favored by the shallow potential wells of these systems.

These characteristics are even more marked in the ultra-faint dwarfs.

At extremely low metallicities, all galaxies share a common $[\alpha/\text{Fe}]$ -plateau, which is determined by the cumulative effect of massive stars, exploding as core-collapse Supernovae and producing both α -elements and iron; in particular, the effect of massive stars is expected to be the same everywhere, regardless the galaxy morphological type.

As the metallicity slightly increases, the $[\alpha/\text{Fe}]$ ratios in the dwarf spheroidal and ultra-faint dwarf galaxies steeply decrease, at variance with the observed $[\alpha/\text{Fe}]$ ratios in the Milky Way halo, which are still flat; such a decrease seems to occur at lower $[\text{Fe}/\text{H}]$ abundances in systems with lower dynamical mass. Therefore, at low metallicities, ultra-faint dwarfs exhibit lower $[\alpha/\text{Fe}]$ ratios than the more massive dwarf spheroidals.

The different $[\text{Fe}/\text{H}]$ - $[\alpha/\text{Fe}]$ relations in the Milky Way halo and its dwarf galaxy satellites can be explained as mainly due to star formation efficiencies in the dwarf spheroidal galaxies, which are roughly one order of magnitude lower ($\nu_{\text{dSph}} \sim 0.1 \text{ Gyr}^{-1}$) than the typical star formation efficiency in the Milky Way halo ($\nu_{\text{MW}} \sim 1 \text{ Gyr}^{-1}$); the ultra-faint dwarfs are characterized by even much lower star formation efficiencies ($\nu_{\text{UFD}} \ll 0.1 \text{ Gyr}^{-1}$). In particular, the decrease in the $[\alpha/\text{Fe}]$ ratios is determined by the large amounts of iron deposited by Type Ia Supernovae, which explode with a wide distribution of delay times from the star formation event.

If the star formation efficiency is low, then the rate of production of iron by core-collapse Supernovae is slow and hence Type Ia Supernovae pollute an interstellar medium which is still characterized by low $[\text{Fe}/\text{H}]$ abundances. In summary, lower star formation efficiencies cause the $[\alpha/\text{Fe}]$ ratios to decrease at lower $[\text{Fe}/\text{H}]$ abundances.

The shallow potential wells of the dwarf spheroidal and ultra-faint dwarf galaxies favour the occurrence of very strong galactic winds, which efficiently remove most of the gas within these systems and determine a steepening of the decrease of the $[\alpha/\text{Fe}]$ ratios as functions of the $[\text{Fe}/\text{H}]$ abundances. The occurrence of strong galactic outflows also suddenly halt the galaxy star formation activity; this fact – coupled with the low star formation efficiencies in these systems – causes the galaxy not to build large amounts of stellar masses; in particular, the typical stellar mass of a dwarf spheroidal galaxy is $M_{\star, \text{dSph}} \sim 10^6$ - $10^7 M_{\odot}$, while the most massive ultra-faint dwarfs typically have $M_{\star, \text{UFD}} \lesssim 10^4$ - $10^5 M_{\odot}$.

To confirm the aforementioned scenario, we need more accurate spectroscopic data for these systems, which have been very difficult to study in the past because of the very low luminosities of their stars. Photometric metallicity estimates are available for the most recently discovered (very low-mass) ultra-faint dwarfs but they are not as accurate and precise as the spectroscopic ones.

- ***Do the actual classical and ultra-faint dwarf spheroidal galaxies, satellites of the Milky Way, correspond to the (evolved) building***

blocks of the Galaxy stellar halo? The chemical abundances of the α -elements and barium in the dwarf spheroidal and ultra-faint dwarf galaxies are systematically different than in the Milky Way halo. although the scatter in the data is still very large to draw firm conclusions. Nevertheless, the observed $[\text{Fe}/\text{H}]$ - $[\text{Ba}/\text{Fe}]$ relation might be discriminant in this sense.

The $[\text{Ba}/\text{Fe}]$ ratios in the Milky Way halo stars are observed to increase as functions of the $[\text{Fe}/\text{H}]$ abundances, while they suggest a decreasing trend in the ultra-faint dwarfs, which – incidentally – host stars as old as the Milky Way halo stars. Both observations and our models discard the hypothesis that the Galaxy stellar halo formed by accreting stars, gas and metals from the actual dwarf spheroidal galaxy satellites.

Finally, the RR Lyrae in the MW halo globular clusters show peculiar pulsation properties (the so-called “Oosterhoff dichotomy”) which are not observed when studying the RR Lyrae in the dwarf spheroidals and in the majority of the ultra-faint dwarfs.

- ***Is the initial mass function in the Sagittarius dwarf galaxy deficient in the most massive stars?*** We have applied the so-called “integrated galactic initial mass function theory” to the chemical evolution of Sagittarius. This theory predicts less massive stars (the main oxygen producers) in the regime of low star formation rates of dwarf spheroidals.

Our results suggest a truncated initial mass function in Sagittarius, causing the $[\alpha/\text{Fe}]$ ratios to shift systematically towards lower values, providing a better agreement with data, although the latter are still too uncertain to draw firm conclusions.

The integrated galactic initial mass function has been applied in the past to reproduce also the chemical abundance patterns in elliptical galaxies and in the Milky Way. It naturally predicts a variation of the initial mass function as a function of the galaxy morphological type. In particular, when passing from early type to late type galaxy morphological types, the integrated galactic initial mass function predicts the initial mass function to become top-heavier (namely, more rich in massive stars), in agreement with what seems to be suggested by observations.

- ***Is Eu synthesized by core-collapse Supernovae, whose progenitors were stars with lower mass than the main O-producing stars?*** This question arises because the Sagittarius and the Milky Way disc stars share similar $[\text{Eu}/\text{Fe}]$ ratios, while they have different $[\text{O}/\text{Fe}]$ ratios; in particular, the $[\text{O}/\text{Fe}]$ ratios in Sagittarius are systematically lower than the Milky Way thick disc stars.

If the initial mass function in Sagittarius is truncated, as suggested by our results with the Integrated Galactic Initial Mass Function (see the previous point), then the truncation would act not only on the oxygen producers but also on the europium producers. Since the Eu/Fe ratios in the Milky Way and in Sagittarius are similar, we hypothesize that Eu is synthesized as an

r-process element by core-collapse Supernovae, whose progenitors have lower masses than the main O producers.

We have assumed different nucleosynthesis scenarios for the Eu production by core-collapse Supernovae, including a scenario where Eu is synthesized by low-mass core-collapse Supernovae; none of these models was able to reproduce at the same time the Eu and O abundances in the Sagittarius dwarf spheroidal galaxy.

- ***Can neutron star mergers explain the observed Eu abundances in the Sagittarius dwarf spheroidal galaxy?*** We have proposed a completely alternative scenario for the Eu nucleosynthesis in a dwarf spheroidal galaxy. In particular, we have tested whether neutron star mergers can provide the right amount of Eu to explain the observed chemical abundances in Sagittarius. We conclude that this is the best scenario for the Eu nucleosynthesis in Sagittarius.

Many uncertainties still rely in the assumptions of our models about neutron star mergers. For example, *which is the typical delay time for the coalescence of a binary system of neutron stars?* Our best model assumes a fixed delay time $\tau_{\text{NSM}} = 1$ Myr. Nevertheless, we can ask whether *there is a distribution of delay times*, as currently assumed to model the progenitors of Type Ia Supernovae. Moreover, *which is the typical fraction of massive stars – both giving rise to neutron stars – which lie in binary systems?* Our best model assumes $\alpha_{\text{NSM}} = 0.02$. *Which is the maximum stellar mass for the formation of a neutron star?* We assume $M_{\text{max,NS}} = 40\text{-}50 M_{\odot}$. *How much Eu is synthesized by each neutron star merger event?* Our best model assumes $M_{\text{Eu,NSM}} = 10^{-5} M_{\odot}$ per neutron star merger event, but more recent studies suggest slightly larger values.

In conclusion, neutron star mergers are an intriguing mechanism for the nucleosynthesis of r-process elements like Eu, but a lot of progress has to be made from a theoretical point of view in the next years.

- ***How is nitrogen produced in galaxies?*** Nitrogen can be synthesized both by massive and by low- and intermediate-mass stars. On the one hand, massive stars are the only N producers before the first low- and intermediate-mass stars start dying. On the other hand, low- and intermediate-mass stars are the most important N producers; they have both larger typical lifetimes and higher weights in the initial mass function than massive stars.

From an observational point of view, galaxies in the Local Universe are observed to exhibit a plateau in the (N/O) ratios at very low metallicity, which is followed by an increase of this ratio, which steepens as the metallicity increases.

To interpret and understand the observed behavior of the (N/O) vs. (O/H) abundance patterns, we distinguish between two different nucleosynthetic channels for the N production; in particular, we distinguish between “primary” and “secondary” nitrogen, according to the origin of the C and O

nuclei which are used to synthesize nitrogen in the CNO cycle of the H-burning.

Secondary nitrogen. If the C and O nuclei were originally present in the gas mixture at the stellar birth, then the synthesized nitrogen is secondary; the secondary N component increases as a function of the stellar metallicity and it is necessary to explain the high (N/O) ratios which the SDSS galaxies exhibit at high metallicities.

Primary nitrogen. If the C and O nuclei have been synthesized by the star itself and later destroyed to produce N, then the synthesized nitrogen is primary. The primary N nucleosynthesis by low- and intermediate-mass stars is predicted to occur when the “third dredge-up” during the Asymptotic Giant Branch (AGB) phase occurs in conjunction with the so-called “hot-bottom burning”. The invoked physical mechanism to produce primary N in massive stars is given by the so-called “rotational mixing”; nevertheless, this mechanism is efficient in producing primary N only at very low metallicities; in fact, as $Z > 10^{-8}$, massive stars resume producing only secondary N.

The primary N component by low- and intermediate-mass stars mimics the behavior of a secondary N component because the main AGB primary N producers have – on average – lower mass than the main AGB secondary N producers; hence the main primary N producers in the low- and intermediate-mass range typically have higher weights in the initial mass function and longer lifetimes than the main secondary N producers in the same mass range. In summary, the primary N production by AGB stars bolsters the observed steepening of the (N/O) ratios at high metallicities, which – nevertheless – is mainly determined by the secondary N nucleosynthesis.

Pure primary N by massive stars at low metallicity is necessary to explain the observed initial plateau in the (N/O) ratios, which low-mass, blue and diffuse dwarf galaxies clearly exhibit at low metallicities; nevertheless, none of the existing stellar models is able to predict the right amount of primary N by massive stars. In our models, we derive an empirical stellar yield of primary N by massive stars to reproduce the low metallicity plateau of the (N/O) ratios.

A further study to understand the origin of nitrogen in galaxies is to develop models aimed at reproducing the observed radial profiles of the (N/O) ratios, which are going to be released as a result of the MANGA survey. This work of modelling is in progress at the present time. We could put stronger constraints on how the galaxies grow in mass as a function of their galactocentric radius and on variations of the star formation efficiency with radius.

- ***Do galactic winds preferentially carry the nucleosynthetic products of core-collapse Supernovae?*** In order to reproduce the very steep increase of the observed (N/O) ratios at high metallicities in the SDSS galaxies a large secondary N production by low- and intermediate-mass stars is necessary, together with “differential” galactic winds, which preferentially remove

oxygen and other α -elements, namely the main nucleosynthetic products of massive stars.

This scenario might be justified by the fact that massive stars preferentially form in clusters; as they explode, they create a region of the interstellar medium where the filling factor closely approaches to unity. Hence the nucleosynthesis products of core-collapse Supernovae can gain the right amount of thermal energy to escape from the galaxy potential well (or to spread into the diffuse hot phase of the galaxy interstellar medium). We remark on the fact that this is an hypothesis which still does not rely on firm theoretical and observational grounds.

Since chemical abundances usually suffer of large systematic uncertainties, I have developed a new galaxy photo-chemical evolution model, extending the number of observables which can be reproduced at the same time by the model, beyond the chemical abundances. In particular, my model is capable of predicting also the photometric properties of the galaxy stellar populations. In this way, I can draw a synthetic galaxy Color-Magnitude Diagram, which can be directly compared with the observed one. This new galaxy photo-chemical evolution model has been applied to reproduce the chemical and photometric properties of the stellar populations in the Sculptor dwarf spheroidal galaxy.

A further possible application would be to study the photo-chemical evolution of the recently discovered ultra-faint dwarfs; to do that (and that is also the main reason why this kind of works has not been done so far), we need a more extended library of stellar isochrones, computed also for extremely low stellar metallicities. Unfortunately, we still do not possess this kind of libraries. Finally, it would be interesting to apply this new photo-chemical model to reproduce the chemical and photometric properties of the various Milky Way stellar components, for which very new and accurate data from the Gaia-ESO survey are going to be released.

Chemical evolution models can be coupled also with a library of stellar spectra (either empirical or theoretical) to study the spectro-photometric evolution of galaxies in a more theoretical framework. During my PhD activity, I have developed a preliminary version of such a numerical code, which I intend to use to study unresolved stellar populations in the Local Universe and at high redshift, by taking into account also the twisting effect of dust. Finally, this kind of models can be used to study radial variations of the chemical and spectral properties of the stellar populations in galaxies, which recent surveys like MaNGa or Muse are able to determine observationally; this study could put a stronger constraints on how the dynamical mass of the system is distributed.

Finally, in this Thesis, I have shown how to develop a simplified (but effective) method to solve the chemical evolution of galaxies, which can be easily exploited by other groups in the community, willing to integrate a module of chemical evolution within their galaxy population synthesis model. My method assumes the so-called “instantaneous recycling approximation” for chemical elements like oxygen – which are mainly produced by massive stars, having negligible lifetimes – and the Delay Time Distribution formalism for the iron produced by Type Ia Supernovae. In particular, for oxygen, I assume a net yield per stellar generation which I have

computed by taking into account a recent compilation of stellar nucleosynthetic yields and the effect of the metallicity and initial mass function. I have successfully applied my new simplified chemical evolution model to reproduce the observed chemical abundance patterns in the Milky Way. A further study would be to include in this theoretical framework also the effect of stellar migrations and radial gas flows. In particular, it would be interesting to study the effect of migration of Type Ia Supernovae on the chemical evolution of galaxies.

List of publications

- Vincenzo F., Matteucci F., Vattakunnel S., Lanfranchi G. A., “*Chemical evolution of classical and ultra-faint dwarf spheroidal galaxies*”, 2014, MNRAS, 441, 2815
- Vincenzo F., Matteucci F., Recchi S., Calura F., McWilliam A., Lanfranchi G. A., “*The IGIMF and other IMFs in dSphs: the case of Sagittarius*”, 2015, MNRAS, 449, 1327
- Vincenzo F., Matteucci F., Belfiore F., Maiolino R., “*Modern yields per stellar generation: the effect of the IMF*”, 2016, MNRAS, 455, 4183
- Vincenzo F., Belfiore F., Maiolino R., Matteucci F., Ventura P., “*Nitrogen and oxygen abundances in the Local Universe*”, 2016, MNRAS, 458, 3466
- Spitoni E., Vincenzo F., Matteucci F., Romano D., “*Are ancient dwarf satellites the building blocks of the Galactic halo?*”, 2016, MNRAS, 458, 2541
- Vincenzo F., Matteucci F., de Boer T. J. L., Cignoni M., Tosi M., “*Lighting up stars in chemical evolution models: the CMD of Sculptor*”, 2016, MNRAS, 460 (2), 2238
- Spitoni E., Vincenzo F., Matteucci F., “*New analytical solutions for chemical evolution models: characterizing the population of star-forming and passive galaxies*”, 2017, A&A, 599, A6
- Vincenzo F., Matteucci F., Spitoni, E., “*A simple and general method for solving detailed chemical evolution with delayed production of iron and other chemical elements*”, 2017, MNRAS, 466, 2939

“Come in,” she said “I’ll give you shelter from the storm”

“Shelter From The Storm”, Bob Dylan

Acknowledgments

I thank Francesca Matteucci, for her generosity and the many opportunities and constant support she has given. We have travelled some road together, but I will never meet again a great travel companion like her in the future, always triggering and stimulating my (rational) spirit and (scientific) passion with new ideas.

I thank all my collaborators, Roberto Maiolino, Francesco Belfiore, Simone Recchi, Gustavo Lanfranchi, Emanuele Spitoni, Donatella Romano, Francesco Calura, Andrew McWilliam, Thomas De Boer, Michele Cignoni, and Monica Tosi.

I want to mention here all my PhD colleagues, Matteo Costanzi, Emanuele Pomante, Marianna Annunziatella, David Goz, Chiara Mongardi, Erik Romelli, Manuel Colavincenzo, Lorenzo Gioannini, Matteo Pinamonti, Anna Zoldan, Carlo De Masi, Eda Gjergo, and Lorenzo Pizzuti. We have shared the same troubles and handed down the same tricks though years and, maybe, generations. I hope that our roads will cross again in the future.

I thank the friends who I have unexpectedly met during my PhD; I mean Francesco Belfiore, Stefano Carniani, Claudia Cicone, Emanuele Spitoni, Lorenzo Gioannini, Eda Gjergo, and Alan Alves-Brito. I have felt less lonely and blind in my journey, gazing at the window, while seated beside you. Each of us jumps off the train at different stations, at the end, to take new trains (and airplanes) bringing very far away. I hope to find persons and young astronomers like you in the future.

I am grateful to my old friends, both truly physicists, Salvatore Salis and Antonio Pittelli, because they filled my life with philosophy and literature, music and art. I thank my very old friends, Massimo Rossi and Stefano Rossi, because their only friendship defines my homeland.

I want to remember my grandfather, Francesco Stifano, his eyes and smile, his words of wisdom; I want to remember my grandmother, Grazia Madaio, her voice, love and sweetness. They died during my PhD, leaving a deep sign in my life.

I thank my parents, Mario and Antonietta, and my brother, Graziano, for always being present in the most difficult moments.

I want to conclude with a mention to Maddalena, because her will to live and intelligence, her unbelievable strength and irony have taught me the courage to face the difficult moments which can always happen in life; the example of her life has completely changed my scale of values.